UNIVERSIDAD DE BUENOS AIRES

Facultad de Ciencias Exactas y Naturales

Departamento de Física

Medición de la vida media del mesón $B^{\pm}$ e identificación de quarks top a partir de la reconstrucción de decaimientos de quarks b

por Ariel Schwartzman

Director de Tesis: Ricardo Piegaia

Director Asistente: Meenakshi Narain

Lugar de Trabajo: FCEyN, UBA

Trabajo de Tesis para optar por el título de

Doctor de la Universidad de Buenos Aires

2004

Dedication

To my parents.

Medición de la vida media del mesón $B^{\pm}$ e identificación de quarks top a partir de la reconstrucción de decaimientos de quarks b

Ariel Schwartzman

Director de Tesis: Ricardo Piegaia

Director Asistente: Meenakshi Narain

Esta Tesis presenta una medición preliminar de la vida media de mesón $B^{\pm}$ a través de la reconstrucción de su cadena de decaimiento, y de la producción de quarks top en el canal de electrón más jets, usando el método de vértices desplazados para la identificación de jets-b. Su principal contribución es el desarrollo, implementación y optimización del algoritmo de filtros de Kalman para la reconstrucción de vértices, y del método de vértices desplazados para identificar jets provenientes de la fragmentación de quarks b. Estos dos algoritmos forman ahora parte del paquete estándar de reconstrucción del experimento DØ, y explotan al máximo la tecnología de punta de los nuevos detectores de trazas recientemente instalados. El análisis está basado en datos tomados hasta abril de 2003 en el Colisionador Hadrónico $p\bar{p}$ de Fermilab, corespondiente a una luminosidad integrada de $60\,pb^{-1}$. La medición de τ=1.57$\pm$0.18 ps para el bosón B está de acuerdo con el valor aceptado de su vida media, y permite esperar un nivel de precisión altamente competitivo para el final de la toma de datos.

Palabras claves: Modelo Estándar, Mesones B, Identificación de jets-b, Producción de quark top

Resumen

El detector de particulas DØ fue diseñado para el estudio de colisiones proton-antiproton a altas energias en el colisionador de hadrons Tevatron ubicado en el Fermi National Accelerator Laboratory, en USA. Hasta el ano 2007, cuando el colisionador LHC entre en funcionamiento, el Tevatron es el unico acelerador de particulas en el mundo que produce colisiones de hadrons con una energia de centro de masa de $1.96 TeV$. Una descripcion mas detallada del detector como asi tambien del acelerados de particulas puede encontarse en los capitulos 2 y 3 de esta tesis. DØ consiste de tres sub-detectores concentricos: detector de trazas, calorimetro y detector de muones. El detector de trazas, que es el mas proximo a la region de interaccion, es responsable de la medicion tridimensional de las trayectorias de las particulas cargadas que lo atraviesan como resultado de cada colision. Consiste de tres componentes principales: un detector de silicio de alta resolucion (SMT), un detector de fibras opticas (CFT) y un solenoide superconductor. El detector de silicio permite la determinacion precisa de vertices de interaccion, mientras que el detector de fibras opticas agrega mediciones que permiten la reconstruccion eficiente de trazas y, en conjuncion con el alto campo magnetico generado por el solenoide de 2 Teslas, una mejora en la determinacion del momento (curvatura) de las particulas. Rodeando el detector de trazas, un calorimetro mide la energia depositada por todas las particulas cargadas y neutrales que lo atraviesan. Consiste de aproximadamente 50.000 celdas acad una conteniendo un material absorbente (uranio) y un centellador (argon liquido). Cuando una particulas interactua con el calorimetro, produce una lluvia de particulas secundarias en el material absorbente. La energia de la particula incidente es determinada mediante el tamano de la lluvia, mientras que la forma y desarrollo de la lluvia permite la identificacion de distinto tipo de particulas (como electrones, fotones, y hadrones). Neutrinos no puede detectarse ni en el detector

de trazas ni en el calorimetro. Su presencia es deducida indirectamente mediante el imbalance de la energia transversa medida en el calorimetro, es decir: un neutrino es identificado como la energia faltante para satisfacer la conservacion de energia transversa en el evento. Debido a que muones penetran el calorimetro, estos son identificados mediante un detector de trazas adicional localizado inmediatamente despues del calorimetro.

Dado que el acelerador de particulas provee colisiones $p\overline{p}$ con una frecuencia de $4.7MHz$ por segundo, seria imposible reconstruir y almacenar en discos cada evento. Sin embargo, loseventos fisicos de interes poseen una seccion eficaz muchos ordenes de magnitud menor, de modo que el detector cuenta con un sofisticado sistema de disparo (trigger) que consiste en el agorithmos rapidos que examinan cada uno de los eventos (usando informacion parcial de los sub-detectores) y deciden desacartar o almacenar el evento para su reconstruccion precisa ofline. El sistema de disparo consiste en tres niveles. El primer nivel consiste de un sistema de disparo electronico, basado en algoritmos muy simples, que selecciona eventos de interes con una frecuencia de $5 - 10kHz$. En general, el nivel 1 selecciona eventos con significante depositos de energia en al calorimetro, senales en el detector de muones, etc. El nivel 2 es tambien un sistema de disparo electronico que refina y combina la informacion proventiente del nivel 1, aceptando eventos con una frecuencia de $1kHz$. Finalmente, el trecer nivel de disparo es basado en complejos programas de computacion que corren en un conjunto de procesadores comerciales y aceptan 50 eventos por segundo. Existen diversos algoritmos de disparo, cada uno adecuado para distintos tipos de analisis.

Los eventos aceptados por el sistema de disparo consisten en las senales digitales registradas por cada uno de los sub-detectores. Un complejo programa de computacion orientado a objectos (C++) transforma la informacion digital en objectos fisicos tales como electrones, neutrinos, muones, trazas y jets. Durante el desarrollo

de esta tesis, la universidad de Buenos Aires tomo parte en el desarrollo e implementacion de una varios compententes de DØreco. Una descripcion general de la reconstruccion e identificacion de objetos fisicos es dada en el Capitulo 3.

Una parte fundental de esta tesis fue la implementacion y optimizacion del algoritmo para la reconstruccion de vertices primarios y secundarios usando la informacion de los detectores de trazas. La reconstruccion de vertices consiste de dos pasos principales relacionados entre si: la identificacion de conjuntos de trazas pertenecientes a distintos vertices de decaimiento, y la estimacion precisa de los parametros que describen al vertice y el momento de todas sus trazas asociadas con la restriccion que provienen del vertice.

Como trabajo de tesis, implemente un algoritmo para la recontruccion de vertices basado en el Filtro de Kalman [33]. En esta tecnica de ajuste de datos permite incorporar la informacion de cada medicion (traza) iterativamente. El filtro de Kalman posee un modelo para la propagacion de trazas cargadas en un campo magnetico que permite predecir los parametros del vertice. Cada vez que una nueva traza es incorporada, el filtro compara su predicion con el valor observado de los parametros de la traza y actualiza la estimacion de la poscion del vertice. El proceso se repite hasta que todas las trazas son incorporadas. Como paso final, el Filtro de Kalman iterativamente corrije los momentos de todas las trazas usando la informacion mas acualiza de los parametros del vertice. Esta idea es ilustrada en la figura 1 para el caso de la estimacion de un vertice de tres trazas. El algoritmo comienza con la primer traza una predicion para la posicion del vertice. Esta predeccion es simplemente la distancia minima entre la traza y el origien de coordenadas. La prediccion es combinada con la siguiente traza dando lugar a una nueva estimacion de la posicion del vertice y del momento de la traza con la condicion de que provenga del vertice. El proceso es repetido con la tercer traza. Como ultimo paso, el Filtro de Kalman acualiza el momento de todas sus trazas utilizando el ultimo valor obtenido

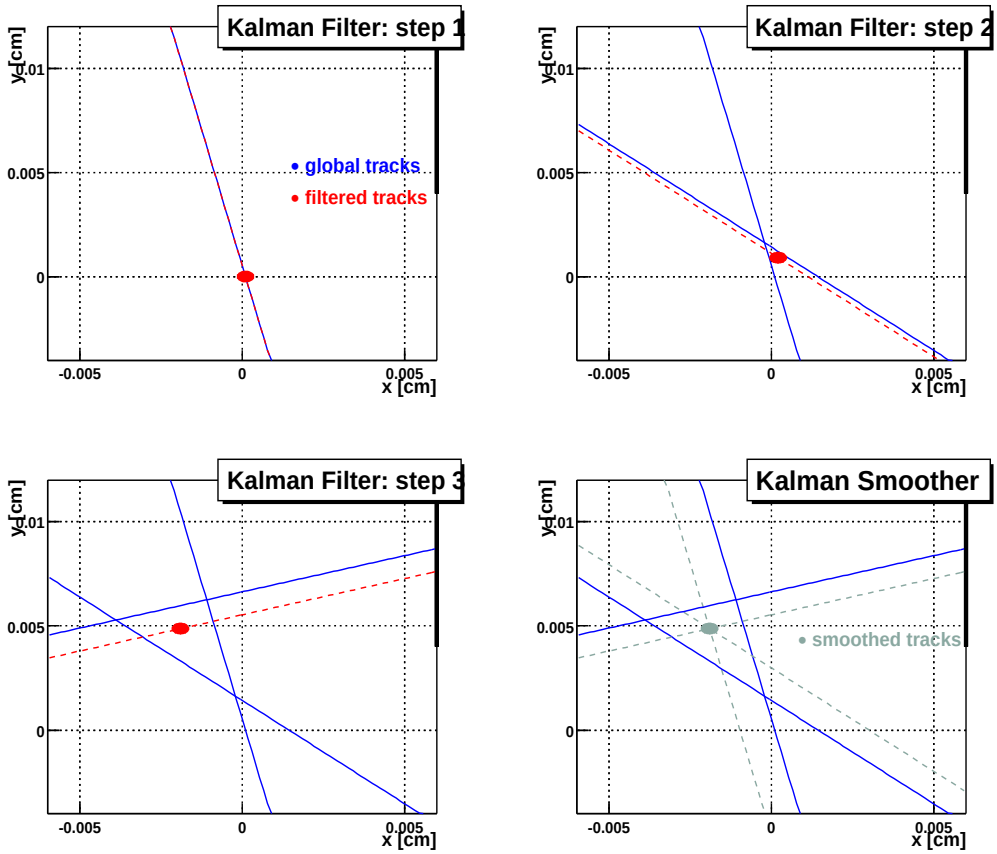

Figura 1: Example of 3-track vertex fit using the Kalman Filter

para la posicion del vertice.

La identificacion de vertices primarios consiste de dos pasos: la reconstruccion de todos los vertices de interaccion y la seleccion de la interaccion fuerte entre las adicionales interacciones suaves. El algoritmo de para la reconstruccion de vertices comienza formando grupos de trazas proximas entre si a lo largo de la direccion z. Luego trazas con parametro de impacto pequeno, compatibles con provenir de la interaccion principal, son seleccionadas. El Filtro de Kalman es utilizado para estimar la posicion del vertice para cada grupo de trazas seleccionadas. Finalmente, la contribucion de cada traza al chi^2 del vertice es examindo. Mientras el χ^2 total del vertice es mayor que 10, la traza que mas contribuye al χ^2 es removida, y el

vertice es nuevamente calculado.

La seleccion de la interaccion fuerte se basa en un algoritmo probabilistico basado en la diferencia de momento de las particulas provenientes interacciones fuertes y suaves. A partir de la distribucion de momento transverso de trazas provenientes de interacciones suaves en la simulacion, se define la probabilidad de que una traza provenga de una interaccion suave integrando la distribucion de $\log_{10} p_T$ desde su momento transverso hasta infinito. Por cada vertice, las probabilidades de cada una de sus trazas son combinadas para determinar la probabilidad de que un dado vertice provenga de una interaccion suave. El vertice con la menor probabilidad de provenir de una interaccion suave es seleccionado como el vertice fuerte.

Basado en la caracteristicas cinematicas del decaimiento $B^{\pm} \rightarrow J/\psi K^{\pm}$, el algoritmo desarrollado para su identificacion consiste de tres pasos: la reconstruccion e identificacion del vertice primario, la seleccion de trazas, la reconstruccion del vertice J/ψ y la identifiacion del decaimiento $J/\psi K^{\pm}$ mediante la combinacion del vertice J/ψ y trazas compatibles con particulas $K^{\pm}$.

El vertice primario es reconstruido mediante el Filtro de Kalman. Dado que los dos muons provenientes del decaimiento del J/ψ son originados en la interaccion fuerte, el vertice primario mas cercano en el eje z a la posicion promedio de los muones, es seleccionado.

La identificacion de mesones $B^{\pm}$ comienza preselecionando las particulas del estado final. Los dos muones deben poseer como un segmento en el detector de muones y estar asociados a un track central conteniendo al menos 3 mediciones en el detector de silicio y momento transverso mayor que $1.5\,GeV/c$. Todas las trazas restantes, con al menos 3 mediciones en el SMT y momento transverso mayor a $1.5\,GeV/c$ son considerados posibles K candidatos. El decaimiento $J/\psi \rightarrow \mu^+\mu^-$ es reconstruido mediante la aplicacion del Filtro de Kalman a los dos muones (de carga opuesta) seleccionados en el evento. Si hubieran mas de dos muones en el evento, todas las

combinaciones son consideradas. El χ^2 del vertice J/ψ es requirido ser menor que 10 de modo de asegurar que los dos muones provienen de la misma interaccion. Solo J/ψ con masa invariante en el rango $2.9 - 3.3\,GeV/c^2$ son seleccionados. Por cada J/ψ vertice y cada candidato kaon, un vertice de tres trazas es formado. La Table 1 sumariza el criterio de seleccion de los mesones $B^{\pm}$ reconstruidos.

μ p_T	$> 1.5\,GeV/c$
μ SMT hits	> 2
K p_T	$> 1.5\,GeV/c$
K SMT hits	> 2
J/ψ χ^2_{vtx}	< 10
J/ψ σ_{Lxy}	$< 0.02\,cm$
χ^2_K	< 10
χ^2_{vtx}	< 20

Table 1: Summary of $B^{\pm} \to J/\psi\, K^{\pm}$ vertex reconstruction and selection criteria.

La Figura 3 muestra la distribucion de masa invariante de los $B^{\pm}$ mesones incluyendo un requiriemento en su longitud de decaimiento mayor a $200\mu m$.

La vida media es calculada como:

$$c\tau = L^B_{xy}\; M_{B^{\pm}} \;/\; |\vec{p}_T| \tag{1}$$

donde $M_{B^{\pm}}$ es la masa promedio del meson B^+ y $\vec{p}_T$ es su momento transverso.

La medicion de la vida media fue llevada a cabo mendiante un unbinned maximum log-likelihood definido mediante la siguiente ecuacion:

$$L = \prod_{i=1}^{N} [F g^i_{sig} + (1 - F)\, g^i_{bck}\,] \tag{2}$$

donde N es el numero de eventos de senal, F la fraccion de senal, y g^i_{sig} y g^i_{bck} son la funcion densidad de probabilidad para senal y fondo respectivamente. Eventos

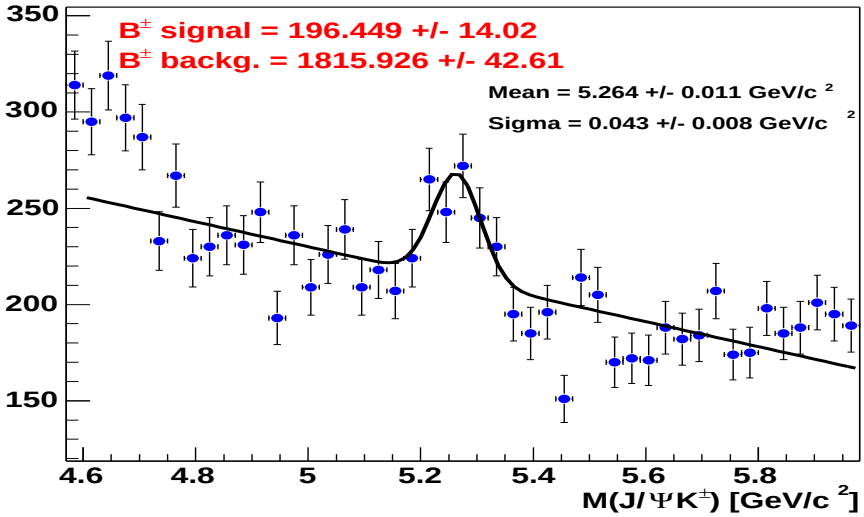

Figura 2: Invariant mass distribution of $B^{\pm}$ candidate vertices.

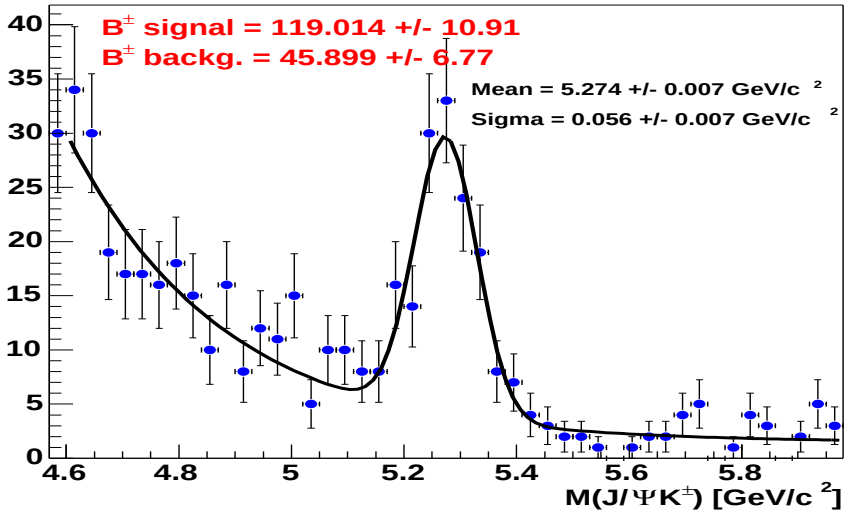

Figura 3: Invariant mass distribution of $B^{\pm}$ candidate vertices, but including a $L_{xy} > 200\,\mu m$ requirement.

que contaminan la distribucion de vida media y dan lugar al fondo incluyen: decaimientos $J\psi$ originidos como produccion $c\bar{c}$, otros canales de decaimiento de B mesons en donde una o mas trazas no fueron identificadas, y vertices falsos. Basado estas fuentes de contaminacion, la distribucion de vida media para el fondo fue parametrizada como una distrubucion normal para eventos con vida media cero (vertices con vida media cero pero que son reconstruidos con una cierta vida media debido a efectos de resolucion y falsa identificacion), y dos fuciones exponencial para eventos con vida media negativa y positiva respectivamente. Las funciones exponenciales describen posibles colas no-normales'3.

$$g^i_{bck} = \begin{cases} (1 - f_+ - f_-)\, \frac{e^{-\lambda_i^2/2(\epsilon\sigma_i)^2}}{\sqrt{2\pi}\,\epsilon\sigma_i} + \frac{f_+}{\lambda_+}\, e^{-\lambda_i/\lambda_+} & \lambda_i \leq 0 \\ (1 - f_+ - f_-)\, \frac{e^{-\lambda_i^2/2(\epsilon\sigma_i)^2}}{\sqrt{2\pi}\,\epsilon\sigma_i} + \frac{f_-}{\lambda_-}\, e^{+\lambda_i/\lambda_-} & \lambda_i > 0 \end{cases} \tag{3}$$

where ϵ is the error scale factor, f_+ and f_- the fractions of right and left side exponentials, λ_+ and λ_- the respective coeficients for the positive and negative background exponential tails, and λ_i and σ_i are the lifetime and its uncertainty for the i^{th} event.

La distribucion de vida media para la senal, g^i_{sig}, es descripta por una funcion exponencial convolucionada con una funcion normal de resolucion:

$$g^i_{sig} = \frac{1}{\sqrt{2\pi}\,\epsilon\sigma_i\lambda_B} \int_0^\infty e^{-\frac{(c\tau-\lambda_i)^2}{2(\epsilon\sigma_i)^2}}\, e^{-\frac{c\tau}{\lambda_B}}\; d(c\tau) \tag{4}$$

where λ_B is the mean $B^\pm$ proper decay length.

El resultado del fit, mostrado en la Figura 4 y Tabla 2 es:

$$c\tau(B^+) = 471 \pm 53\,(stat)\,\mu m \tag{5}$$

$$\tau(B^+) = 1.57 \pm 0.18\,(stat)\,ps \tag{6}$$

que es consistente con otras mediciones de la vida media del meson $B^\pm$ [1]. El valor presente para el promedio de la vida media del meson $B^\pm$ es $1.674 \pm 0.018\,ps$.

Parameter	Value
ϵ	1.176 ± 0.035
F	$9.2 \pm 1.3\%$
λ_B	$0.0471 \pm 0.0053\, cm$
λ_-	$0.0077 \pm 0.0018\, cm$
λ_+	$0.0079 \pm 0.0012\, cm$
f_-	$5.2 \pm 1.7\%$
f_+	$15.4 \pm 2.0\%$

Table 2: Fit parameters for the $B^{\pm}$ lifetime measurement

El algoritmo para la identificacion de b-jets se basa en la habilidad para reconstruir vertices secundarios -desplazados del vertice primario- provenientes de decaimientos inclusivos de mesones B. La vida media promedio de mesones B en b-jets provenientes del decaimiento de top quarks es de $3mm$.

La reconstruccion de vertices secundarios consiste de los siguientes pasos: primero, trazas son agrupadas en jets usando un algoritmo de cono. Este algoritmo basicamente combina en un jet, todas las trazas halladas dentro de un area πR^2 en el espacio $\eta - \phi$. El segundo paso es la seleccion de trazas desplazadas -no compatibles con provenir de la interaccion primaria-. Esta seleccion se basa en la significancia del parametro de impacto ($S = dca/\sigma(dca)$) de los tracks con respecto al vertice primario. Solo trazas con $S > 3$ en cada jet son seleccionadas. Luego, el Filtro de Kalman es utlizado para encontar todos los posibles vertices combinando pares de trazas (semillas). A partir de cada semilla, el Filtro de Kalman es utilizado para eveluar la compatibilidad de las restantes trazas con cada una de las semillas. Si una traza es los suficientemente cercana a una semilla de modo de formar un vertice con $\chi^2 < 10$, es agragada a la semilla. Este proceso es repetido hasta que no es posible agregar mas trazas a semillas. Notar que este procedimiento es tal que los resultantes vertices pueden comparir trazas. El ultimo paso para la identificacion

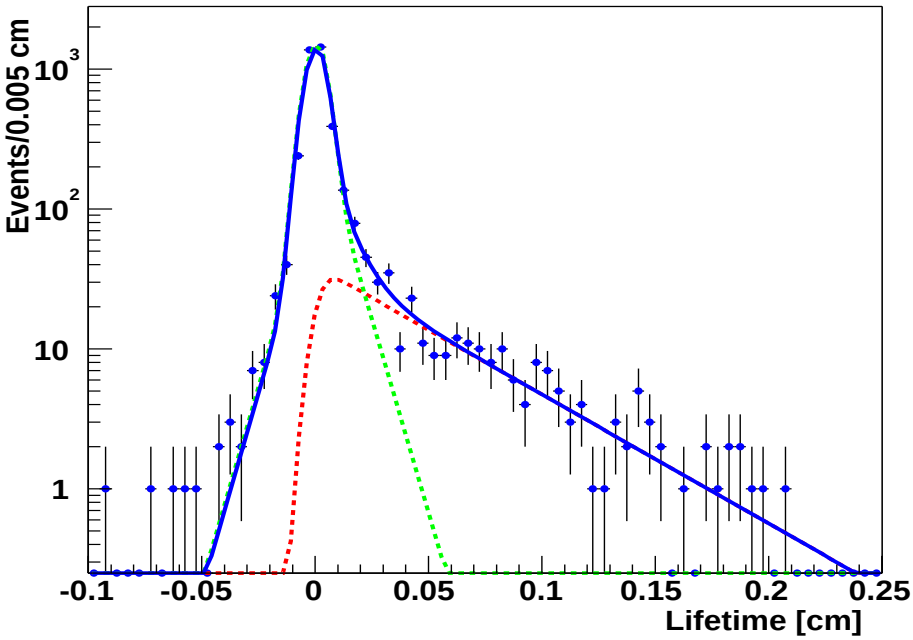

Figura 4: Proper decay length $c\tau$ of $B^{\pm}$ candidates. The background (signal) contribution is shown in light (dark) dashed lines. The sum of background and signal contribution is shown with the solid line.

de vertices secundarios es la seleccion final de vertices, basado en sus propiedades cinematicas. Si alguno de los vertices secundarios es compatible con un decaimiento K^0_S, es removido debido a que K^0_S son mayoritariamente producidos en la interaccion primaria. La Tabla 3 resume el criterio de seleccion.

Tanto el criterio de seleccion como la metodologia adoptada para la busqueda de vertices secundarios es el resultado de detallados estudios con eventos simulados. La Figura 5 sumariza la eficiencia de identificacion de quarks b en funcion de la la longitud de vida media del decaimiento B. La eficiencia es definida como la fraccion de b quarks correctamente identificados con al menos un vertice secundario satisfaciendo los requirimientos en 3. En la literatura de fisica de altas energias, la

Variable	Cut
Decay length, $\|\vec{L}_{xy}\|$	$< 2.6\,cm$
Decay length significance, $\|L_{xy}/\sigma(L_{xy})\|$	> 5
Collinearity, $\vec{L}_{xy} \cdot \vec{p}_T / \|\vec{L}_{xy}\|\|\vec{p}_T\|$	> 0.9
Multiplicity, N	≥ 2
K^0_S rejection	see text

Table 3: Selection criteria for secondary vertices

tecnica de identifacion de b jets se denomina marcado de b.

Dos aspectos fundamentales de cualquier algoritmo de marcado de b quarks son la frecuencia con la cual jets provenientes de quarks u, d, y s son erroneamente identificados como b quarks a traves de la reconstruccion de vertices falsos, y la eficiencia para identificar b quarks en datos reales.

Jets provenientes de quark livianos pueden ser erroreamente marcados debido a efectos de resolucion y errores en la reconstruccion de trazas. Estos efectos son responsables de que trazas originadas en el vertice primario sean reconstruidos como desplazados. La longitud de decaimiento de vertices secundarios asociados con vertices falsos se distribuye simetricamente alrededor de $L_{xy} = 0$.

Se midio la frecuencia de marcado erronea (identificado por su sigla en ingles: TRF, por Tag rate Function) como la fraccion de jets en las cuales su vertice asociado posee longitud de decaimiento negativa (vertice negativo). Existen diversas fuentes de vertices positivos en datos: vertices falsos, y produccion de b quarks por medio de distintos mecanismos. El estudio de vertices positivos y negativos en datos reales se llevo a cabo en dos muestras de jets: **qcd_em** y **qcd_jet**. La primera consiste de eventos con al menos un electron de $p_T > 20\,GeV/c$, uno o mas jets, y energia faltante menor a $10 GeV/, GeV$. Esta muestra fue subdividida de acuerdo al numero de jets en **qcd2_em** (dos jets) y **qcdINCL_em** (dos o mas jets). La segunda muestra

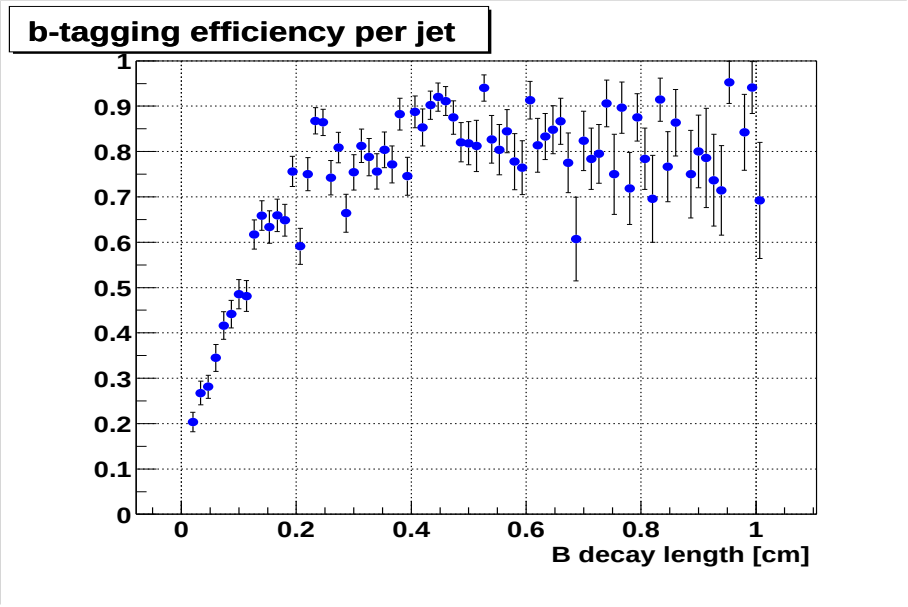

Figura 5: b-tagging efficiency as a function of the B hadron decay length.

consiste simplemente de eventos conteniendo uno o mas jets y que hayan disparado el nivel 1 como eventos con al menos un jet hadronico.

Las Figuras 6 y 7 muestran la distribucion de longitud de decaimiento de vertices en la muestra **qcd_em**. El exceso de vertices positivos is debido mayoritariamente a vertices provenientes de quarks pesados.

La Figura 8 muestra la parametrizacion de TRFs para vertices positivos y negativos en la muestra **qcd_jet**. Una comparasion de las TRFs derivadas en distintas muestras se muestra en la Figura 9

En los datos, la eficiencia para identificar b quarks fue medida en un muestra de de muones. Una fraccion significante de esta muestra se espera que provenga de produccion directa de b quarks en le cual uno de los b quarks produce el muon y el otro un jet hadronico. El muon es no aislado sino que se requiere que este asociado con un jet. El contenido de b quarks de esta muestra es obtenido mediante el uso de parametrizaciones del momento transverso del muon relativo al eje del jet. (p_T^{rel}) para muones provenientes de b, c y quarks livianos. La Figura 10 muestra la forma

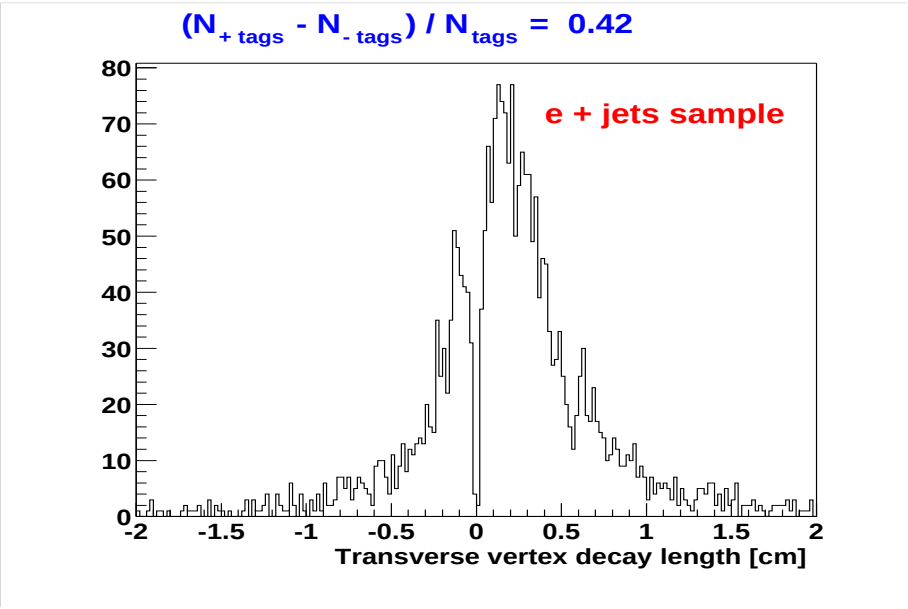

Figura 6: Secondary vertex decay length distribution in the **qcd_em** data sample. The excess of events with positive tags is mostly from heavy flavor.

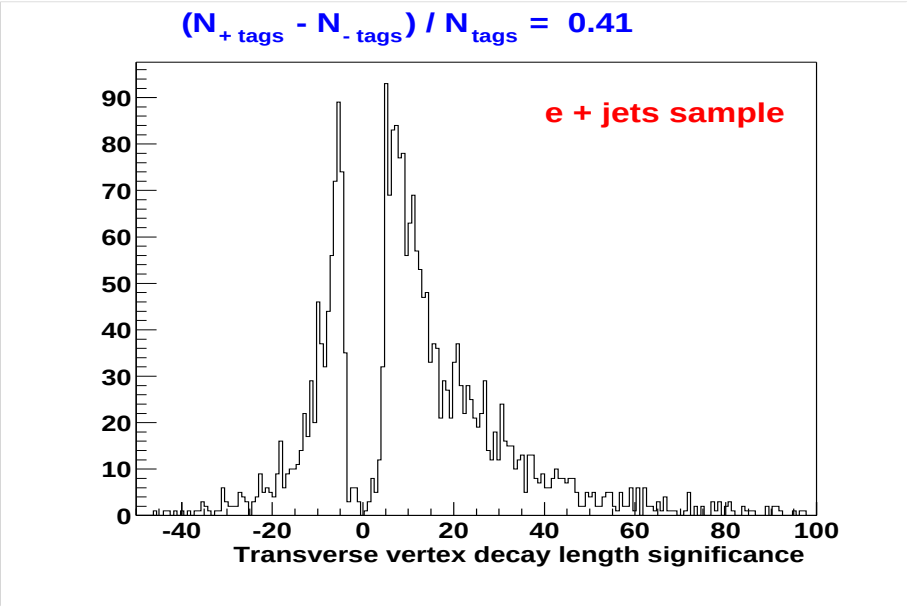

Figura 7: Secondary vertex decay length significance distribution in the **qcd_em** data sample.

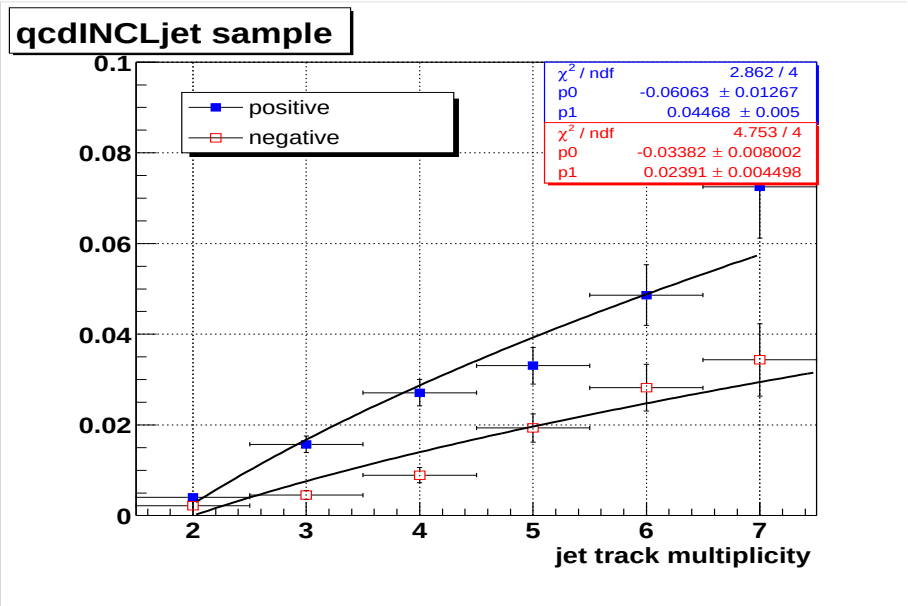

Figura 8: Tag rate function parametrization in the qcdINCL_jet sample for jet $|\eta| < 1.0$.

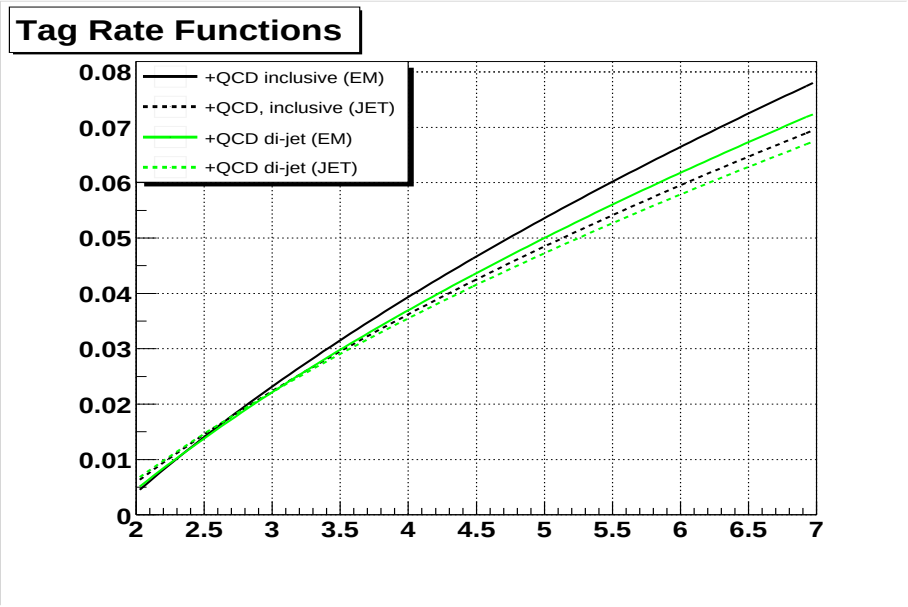

Figura 9: Tag rate function parametrizations in the 4 qcd data samples for jet $|\eta| < 1.0$.

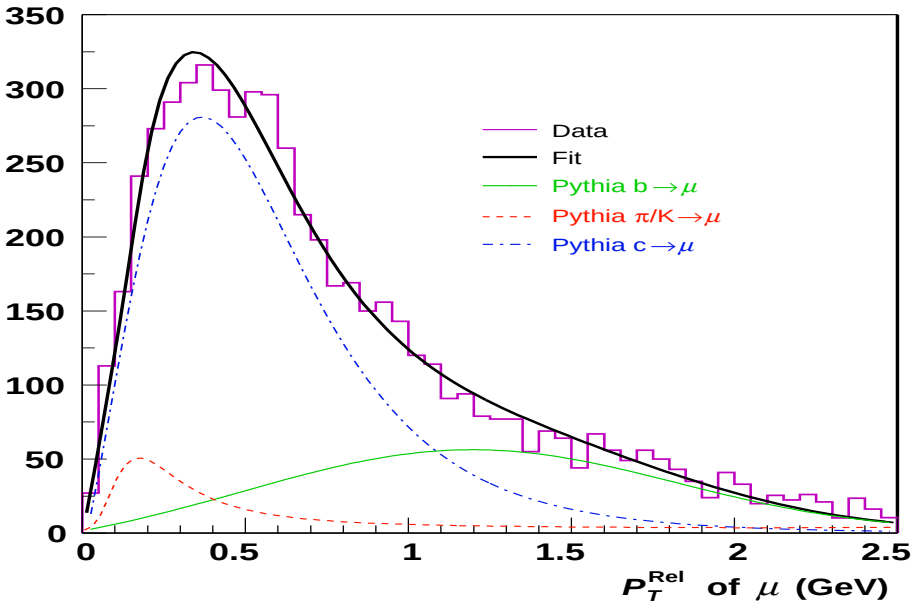

Figura 10: Distribution of muon p_T^{rel} in the data and simulation.

de estas parametrizaciones obtenida en la simulacion.

El numero total de vertices positivos puede ser expresado en termino de la eficiencia de identificacion de quarks b, c y quarks livianos y la fraccion de cada tipo de quark en la muestra (obtenido mediante p_T^{rel})

$$+Tags = N_b\epsilon_b + N_c\epsilon_c + N_{qcd}\epsilon_{qcd} \tag{7}$$

Esta equacion puede ser resulta para ϵ_b permitiendo estimar la eficiencia de marcado de jets en datos reales. La Figura 11 muestra la eficiencia de identificacion de b quarks en funcion del numero de trazas en el jet semileptonico.

La resolucion de energia transversa faltante es determinada por varios efectos: incorrecta identificacion del vertice primario, resolucion de jets, electrones y muones, ruido electronico del calorimetro, etc. Dado un evento particular con cierta energia faltante, uno puede preguntar con que probabilidad esta energia es debida a una fluctuacion experimental debido a efectos de resolucion, teniendo en cuenta la topologia particular y todos los objectos fisicos medidos en el evento. En otras palabras, cual

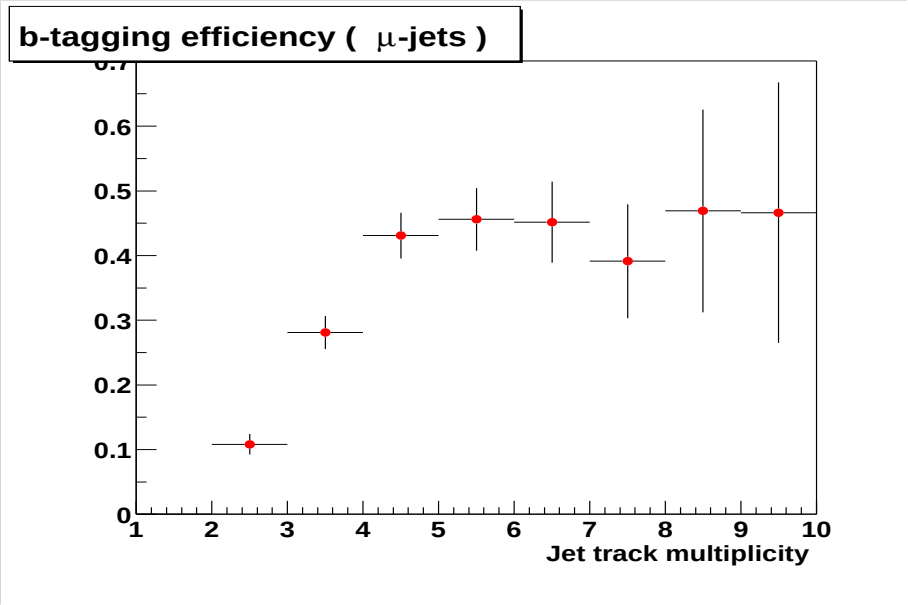

Figura 11: *b*-jet tagging efficiency in semileptonic mu-jet events as function of the number of tracks in the jet.

es la *relevancia* de la energia faltante medida en un evento particular. Como parte de esta tesis, se implemento y estudio un algoritmo que calcula, evento a evento, la distribucion de probabilidad de la energia faltante a partir del conocimiento de las resoluciones experimentales de jets, electrones y energia no asociada a obajectos fisicos. Esta distribucion de probabilidad es utilizada para evaluar con que probabilidad la energia faltante medida, en un evento particular, es consistente con una fluctuacion experimental.

El algorithm the [[[Relevancia de energia faltante]]] fue desarrollado en RunII [40] con el objeto de discriminar entre eventos con energia faltante real, proveniente de un neutrino, y eventos en los cuales la energia faltante es falsa, producto de efectos de resolucion. Este metodo mostro ser muy efectivo en muchas busquedas de nueva fisica que involucran gravitones y gluinos en el estado final. En esta tesis, implente y optimize este algoritmo para ser usado en los analisis fisicos de RunII.

En cada evento, la distribucion de probabilidad de energia faltante, en la direccion de la energia faltante observada se calcula como:

$$p(\not\!\!E_{Ta}) = \not\!\!E_T - N\left(0, \sqrt{\sum_{j=1}^{N-1} \sigma_j^2 \cos^2(\vec{j}, \vec{a}) + \sigma_{U.E}^2}\right) \tag{8}$$

donde se asume que la resolucion de energia de jets y electrones es normal con dispersion σ, $\not\!\!E_T$ es la energia faltante medida, y $U.E.$ es la energia no asociada con ningun objecto fisico (en ingles: Unclustered Energy).

Basado en la definicion anterior, la [[[Relevancia de energia faltante]]] se define como

$$L = \log \frac{p(\not\!\!E_{Ta})_{max}}{p(\not\!\!E_{Ta} = 0)} = 2 \log \frac{\not\!\!E_T{}^2}{2\sigma} \tag{9}$$

donde σ es la variancia de la distribucion de probabilidad $p(\not\!\!E_{Ta})$.

Para enteder el poder de discriminacion de este metodo entre eventos con energia faltante real y eventos con energia faltante falsa, producto de efectos de resolucion, se estudiaron dos samples, una con energia faltante real proveniente del decaimiento leptonico $W \to e\nu$, y otra con energia faltante falsa. La primera es una muestra de $W+ \geq 1$ jets y la segunada es una muestra de eventos con uno o mas jets, donde la energia faltante es con gran certeza proveniente de efectos de resolucion.

Por un dado corte en valor de energia faltante total $\not\!\!E_T$ y L, la Figura 12 muestra el numero de eventos de W (con energia faltante real) en funcion del numero de eventos QCD (con energia faltante falsa) que sobreviven el corte. Se observa que un corte en L que retiene el 80% de eventos W retiene 13% de eventos con energia faltante falsa. Para lograr la misma discriminacion de eventos conteniedo energia faltante falsa mediante un corte en $\not\!\!E_T$, solo 65% de eventos W son seleccionados. Esto muestra como este metodo es superior al metodo tradicional de seleccion basado en el modulo de la energi faltante observada.

Finalmente, la Figura 13 muestra la distribucion de la variable L en eventos conteniendo dos fotones (donde la energia faltante medida es falsa) y en eventos

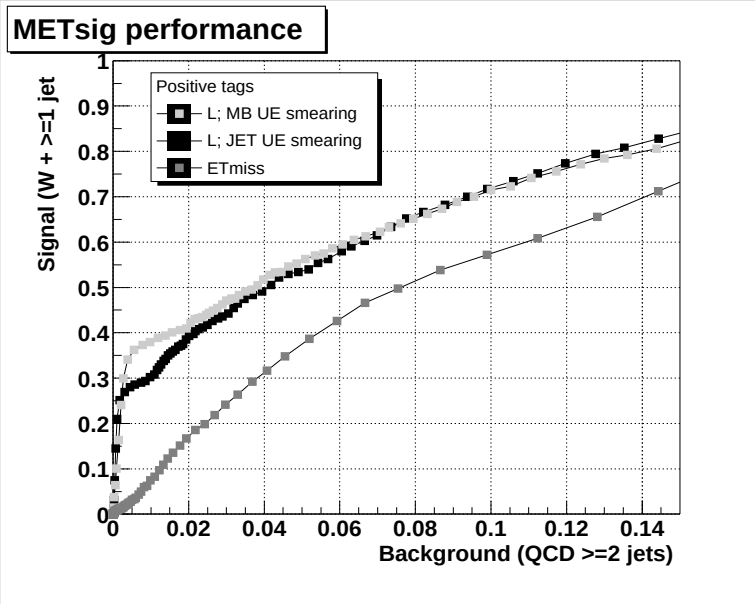

Figura 12: Signal vs. background efficiencies for the $\not\!\!E_T$ *qcd* likelihood (blue), $\not\!\!E_T$ *mb* likelihood (green) and standard $\not\!\!E_T$ cut (red).

conteniendo $W \to e\nu$ en el mismo grafico, de modo de poner en evidencia el poder de discriminacion de este metodo.

Aproximadamente 30% de los eventos $t\bar{t}$ decaen en el canal de electron y jets, donde uno de los W decae leptonicamente, $l\nu_l$, y el otro hadronicamente en dos quarks dando lugar a dos jets. La topologia para este canal es entonces un electron, imbalance de energia transversa debido al neutrino, y cuatro jets, dos de los cuales originados de b quarks. La mayor fuente de contaminacion en este canal consiste en produccion de W+jets que da la lugar a la misma topologia, con la diferencia fundamental que, en general, b-quarks no se encuentran presentes. El metodo mas eficaz para identificar al quark top se basa en la eficiente identificacion de quarks b. Esta tesis presenta el desarrollo, implemenation y optimizacion del metodo de identificacion de quarks b mediante la reconstruccion de vertices secundarios en jets y su aplicacion a la identificacion del quark top.

El primer paso para identificar eventos top consiste en seleccionar un subconjunto de los datos basado en cortes cinematicos. La seleccion consite en requerir un

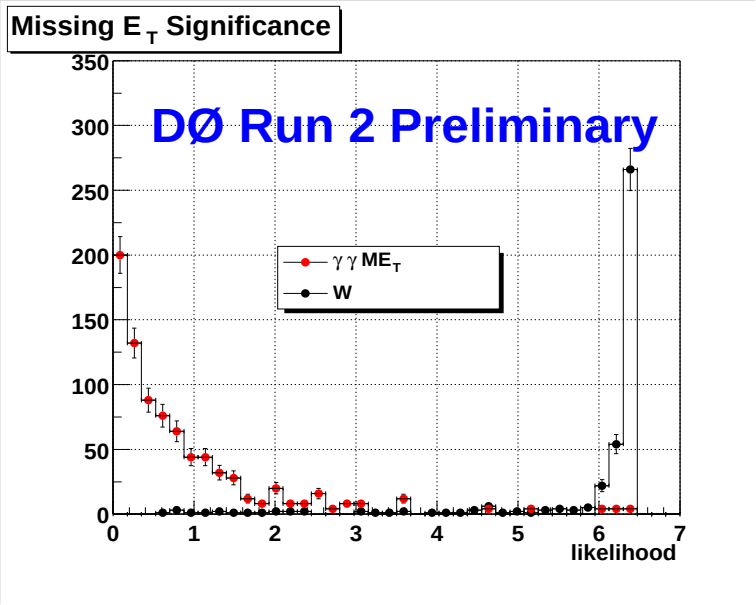

Figura 13: $\not\!\!E_T$ significance likelihood distribution for $\gamma\gamma\not\!\!E_T$ and W events.

electron central ($|\eta| < 1.1$) con momento transverso $E_T^2 > 20\,GeV/c$ y asociado a un track, momento imbalance $\not\!\!E_T > 20\,GeV$ y $\Delta\phi(\not\!\!E_T, e) > 0.5$, uno o mas jets con $E_T > 15\,GeV/c$ y el requirimiento del trigger "EM15_2JT15".

El algoritmo para identificacion de b es aplicado en los eventos que sobreviven la seleccion cinematica. Jets son considerados como provenientes de b quarks si existe al menos un vertice secundario dentro de $\Delta R(jet, vtx) < 0.3$.

El siguiente paso consiste en estimar el mumero de jets marcados provenientes del los procesos contaminantes en los datos. Un exceso en el numero de jets marcados sera interpretado como provenientes de eventos top.

Existe una variedad de procesos, diferentes del top, que pueden dan lugar a jets identificados como b quarks. Los mas importantes son: vertices secundarios falsos en jets, produccion de quarks b y c en asociacion con Ws ($Wb\bar{b}$, $Wc\bar{c}$, Wc) y produccion directa de b quarks, siendo el primero el proceso dominante con una contribucion de aproximadamente 90% del total. La contribucion proveniente de distintos procesos en funcion del numero de jets reconstruidos se muestra en la Tabla 4.

Source	$W+1$ jet	$W+2$ jets	$W+3$ jets	$W+4$ jets
$Wb\bar{b}$		$(0.88 \pm 0.04)\%$	$(1.57 \pm 0.09)\%$	$(3.17\pm)\%$
$Wc\bar{c}$		$(1.25 \pm 0.13)\%$	$(2.33 \pm 0.26)\%$	$(3.34 \pm 0.88)\%$
$W(b\bar{b})$	$(0.50 \pm 0.11)\%$	$(1.70 \pm 0.48)\%$	$(1.40 \pm 0.44)\%$	$(0.92 \pm 0.83)\%$
$W(c\bar{c})$	$(1.21 \pm 0.16)\%$	$(2.16 \pm 0.55)\%$	$(5.52 \pm 0.88)\%$	$(9.28 \pm 2.66)\%$
Wc	$(2.96 \pm 0.07)\%$	$(6.51 \pm 0.69)\%$	$(3.84 \pm 0.83)\%$	$(3.86 \pm 1.69)\%$

Table 4: Summary of the fraction of different W+jets flavor processes as a function of exclusive jet multiplicity obtained from ALPGEN simulation. We distinguish cases in which the two heavy flavor jets are resolved ($Wb\bar{b}$) from the cases where both heavy flavor jets are reconstructed as a single jet ($W(b\bar{b})$) The remained background corresponds to mistags.

En lugar de un calculo explicito del numero esperado de jets marcados en cada uno de estos procesos, se uso la parametrizacion positiva del las TRFs en la muestra **em_qcd** la cual tiene en cuenta todos las posibles fuentes de produccion de b jets. La precision de este metodo depende de hasta que punto la composicion de quark pesados en la muestra **em_qcd** se corresponde con la muestra pre-seleccionada de electron+jets. Esta forma de estimacion de la contaminacion no puede ser utilizada para una medida precisa de la seccion eficaz, pero consituye un metodo sencillo de observar una senal de $t\bar{t}$ en los datos [46].

El numero esperado de eventos conteniendo como minimo un jet marcado proveniente de la contaminacion es calculado a partir de la funcion de marcado erronea positiva ($f(\eta, ntrk)$) mediante la siguiente ecuacion:

$$P(n \geq 1\, tags; N\, jets) = 1 - \prod_{i=1}^{N} (1 - f_i(\eta, ntrk)) \tag{10}$$

La idea es comparar el numero observado de eventos marcados en funcion del numero inclusivo de jets (uno o mas, dos o mas, etc.) con el numero esperado de eventos marcados provenientes de la contaminacion. La presencia de eventos top

deberia ser observada como un exceso en el numero de eventos marcados en los bines $N_{jets} \geq 3$ y $N_{jets} \geq 4$.

La Figura 14 y Table 5sumariza el numero observado de eventos marcados y la estimacion de la contaminacion para distintas multiplicidades de jets. Puede notarse como el numero de eventos marcados para $e + 3$jets y $e + 4$jets, excede a la expectacion de la contaminacion. Esta es la primera evidencia de produccion de quark tops usando el metodo de vertices desplazados en el experimento DØ. Se espera que este metodo sea la herrmienta mas importante para identificacion de top quarks en el futuro. El exceso observado puede transformarce en una seccion eficaz a traves de un estudio detallado de la contaminacion y la inclusion de eficiencias de identificacion y luminosidad.

Source	$W+ \geq 1$ jet	$W+ \geq 2$ jets	$W+ \geq 3$ jets	$W+ \geq 4$ jets
Background	15.2	5.7	1.3	0.5
Data	12	5	3	2

Table 5: Summary of the expected and observed number of tagged events in the $W+$jets sample as a function of jet multiplicity. The number of background events is expected to be an overestimate.

La Figura 15 muestra un evento candidato de produccion de top con 3 jets en el estado final en el que puede observarse la presencia de dos vertices secundarios en uno de los jets.

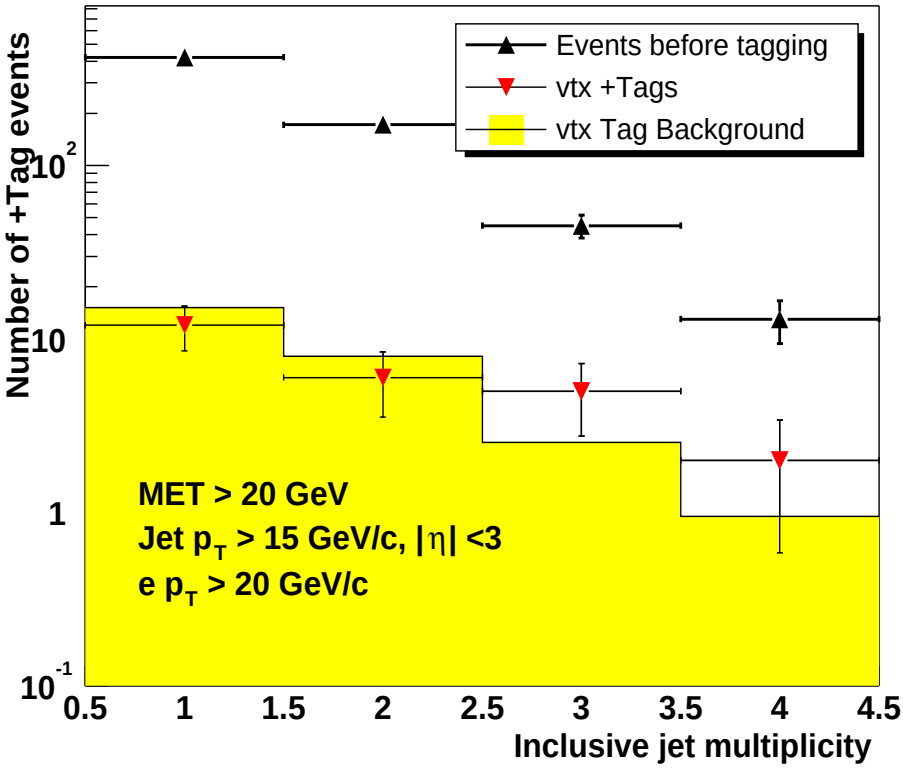

Figura 14: Observed number of tagged events (dots), and total predicted background (error band including the statistical uncertainty) in the e+jets sample.

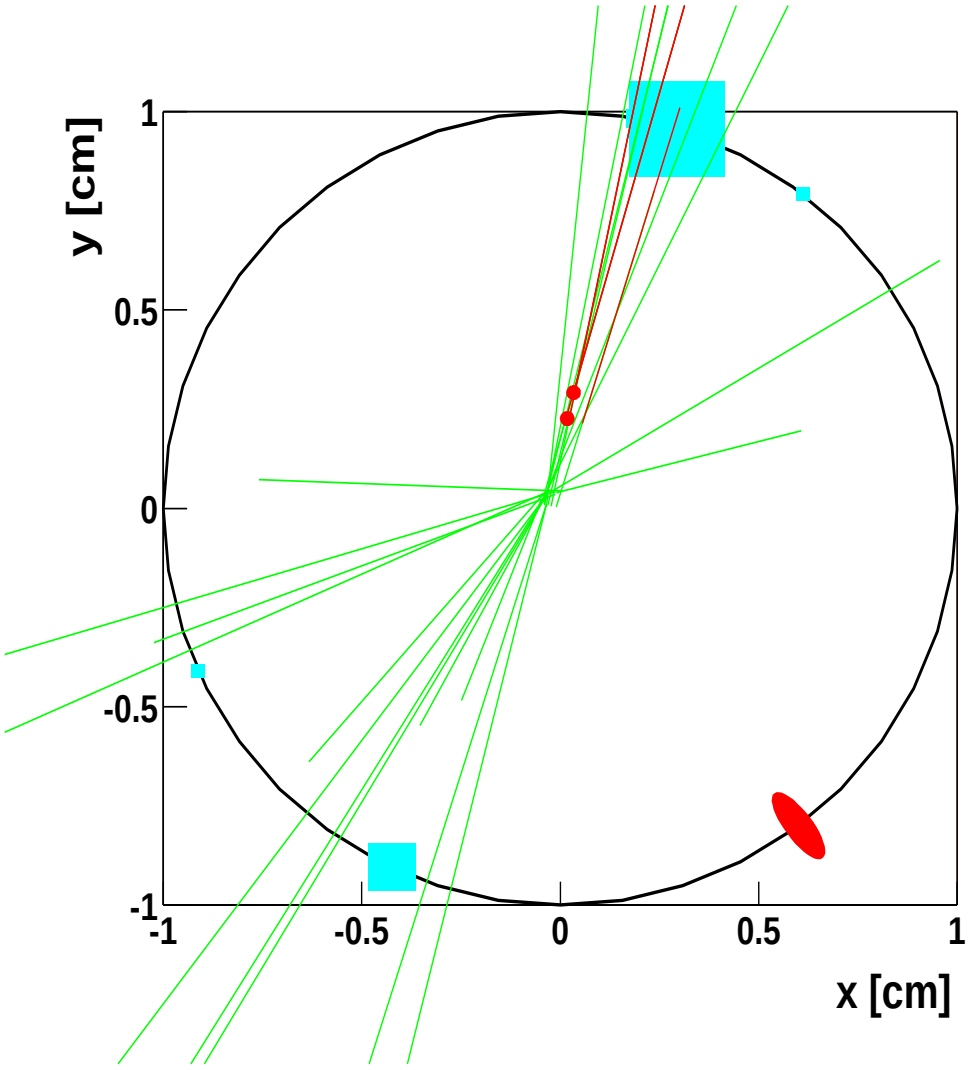

Figura 15: Event display of a single tagged event. Calorimeter jets are drawn as light grey boxes with its size proportional to p_T. Black lines correspond to all tracks within track-jets. Two secondary vertices are shown as dark circles and its attached tracks are plotted as dark lines. The dark ellipse corresponds to the electron.

Measurement of the $B^{\pm}$ Lifetime and Top Quark Identification using Secondary Vertex b-tagging

Ariel Schwartzman

Thesis Advisor: Ricardo Piegaia

Assistant Advisor: Meenakshi Narain

This dissertation presents a preliminary measurement of the $B^{\pm}$ lifetime through the full reconstruction of its decay chain, and the identification of top quark production in the electron plus jets channel using the displaced vertex b-tagging method. Its main contribution is the development, implementation and optimization of the Kalman filter algorithm for vertex reconstruction, and of the displaced vertex technique for tagging jets arising from b quark fragmentation, both of which have now become part of the standard DØ reconstruction package. These two algorithms fully exploit the new state-of-the-art tracking detectors, recently installed as part of the Run 2 DØ upgrade project. The analysis is based on data collected during Run 2a at the Fermilab Tevatron $p\bar{p}$ Hadron Collider up to April 2003, corresponding to an integrated luminosity of $60\,pb^{-1}$. The measured B meson lifetime of τ=1.57$\pm$0.18 ps is in agreement with the current world average, with a competitive level of precision expected when the full data sample becomes available.

Keywords: Standard Model. Jet b-tagging. B lifetime. Top quark production.

Acknowledgments

Working in the DØ experiment at Fermilab was a fascinating experience. I had the unique opportunity to work with exceptional physicists from whom I learned and shared the excitement of working in such a special place. This thesis is the result of the work of a great number of people and institutions and I am grateful to all of them.

First of all, I would like to express my gratitude to my thesis advisor Ricardo Piegaia. He gave the opportunity to work in Fermilab and provided guidance and support through my Ph.D. He spent an incredible amount of time helping me during the development of this thesis. Without his help and advice, this thesis would not have been possible.

I would like to thank my co-advisor, Meenakshi Narain. She is responsible for almost all the accomplishments in this thesis and I own her huge gratitude. She guided me through all my Ph.D giving me support, advice and a lot of work!. She has been not only a brilliant physicist, but also an extraordinary human being who did not hesitate to help and support me every time I asked for her advice.

I would like to thank Mark Strovink, who has been an example through my career. I am grateful for his support on my work, and his advice.

I want to express my gratitude to Greg Landsberg. Working with him was fascinating. Every discussion with Greg was a source of inspiration and new ideas.

I spent a significant amount of time working in the vertex and b-id groups and I

own a huge thanks to many people with whom I collaborated. In particular I would like to thank Maria Roco, Norman Graf, Rick Van Kooten, Gullerme Lima, Suyong Choi, Frank Filthauth, Flera Rizatdinova, Harry Melanson and Alice Bean among others. Working with them was exciting and wonderful.

I would like to thank Brad Abbott and Vivek Jain for giving me the opportunity to work in the B physics group. I will never forget the excitement to find the first K_S^0 and Λ particles in RunII data with Brad.

In addition, I would like to thank all the members of the top group with whom I worked, in particular Aurelio Juste.

I would also like to thank Gaston Gutierrez. Working with him in the construction of the fiber tracker was an invaluable experience.

Finally, I would like to thank John Womersley and Boaz Klima for providing support, advice and wisdom throughout my years at DØ.

Contents

Chapter 1

Physics of Bottom and Top Quarks

This dissertation presents the measurement of the exclusive $B^{\pm}$ meson lifetime and the identification of top quark production in the electron plus jets channel, using the first Run 2a data collected at the Fermi National Accelerator Laboratory Tevatron, up to April 2003, corresponding to an integrated luminosity of $60\,pb^{-1}$. The B meson lifetime is obtained through the full reconstruction of the secondary vertices in its $J/\psi\,K$ decay channel, where the J/ψ gives rise to a $\mu^{+}\mu^{-}$ pair. The identification of top quark pairs decaying to a lepton, neutrino, and several hadronic jets is accomplished using the displaced vertex b-tagging method.

This Thesis is organized as follows. After a brief introduction, this Chapter summarizes the theory of the bottom and top quarks, and the recent results obtained by the CDF and DØ collaborations. Chapters 2 and 3 respectively introduce the DØ detector, and the reconstruction and particle identification algorithms. Chapter 4 describes the method developed to reconstruct primary and secondary vertices, and Chapter 5 details its application to the identification of jets originating from b quarks. Chapter 6 presents an algorithm designed to identify events with genuine missing transverse energy, the signature of neutrino production. Chapter 7 discusses the reconstruction of exclusive $B^{\pm}$ meson decays and the measurement of its life-

time. Finally, in Chapter 8, we apply the above tools to the identification of top quark production in the electron plus jets channel.

1.1 The Standard Model

The Standard Model of particle physics is the most successful attempt to date to describe nature at very small distance scales. It is a theory of interacting quantum fields, whose excitations correspond to particles, with one separate field for each type (or flavor) of particle.

There are two categories of particles based on their spin: fermions and bosons. Particles in the first category, quarks and leptons, have spin 1/2, and are the building blocks of matter. Those in the second category have spin 0, 1 or 2, like photons, gluons and massive *gauge bosons*. They are the carries of the forces between quarks and leptons. The interaction between two particles can be viewed, at the lowest order in perturbation theory, as the exchange a virtual intermediator. Table 1.1 lists the Standard Model particles and their main properties.

We know of four fundamental forces in the universe: gravitational, electromagnetic, weak and strong. Forces in gauge theories arise from certain *local* symmetry invariances in the Lagrangian, and are each proportional to a constant, or "charge". In the electromagnetic interactions, this is the usual Coulomb electric charge, whereas in strong interactions it is called "color". Each quark carries one of three colors, conventionally called "red", "green" and "blue".

Quantum Chromodynamics (QCD) and the Electroweak Theory (EWK), which unifies the electromagnetic and the weak interactions, constitute the Standard Model of particle interactions. The remaining force is gravity, which is mediated by the *graviton*. Gravitation is described by the classical General Theory of Relativity and, at present, there is no quantum version of it. However, since gravity is much weaker than all the other three forces, it is ignorable in almost all high-energy experiments.

	Symbol	Name	Mass (GeV)	Charge (e)
Quarks	u	up	0.003	2/3
($spin = \frac{1}{2}$)	d	down	0.006	$-1/3$
	s	strange	0.1	2/3
	c	charm	1.3	$-1/3$
	b	bottom	4.3	2/3
	t	top	175	$-1/3$
Leptons	e	electron	0.511	-1
($spin = \frac{1}{2}$)	ν_e	electron neutrino	$< 3 \times 10^{-9}$	0
	μ	muon	0.105	-1
	ν_μ	muon neutrino	$< 2 \times 10^{-10}$	0
	τ	tau	1.777	-1
	ν_τ	tau neutrino	$< 2 \times 10^{-8}$	0
Gauge bosons	γ	photon	0	0
($spin = 1$)	W	W	80	± 1
	Z	Z	91	0
	g	gluon	0	0
Higgs	H	Higgs	?	0,?

Table 1.1: Particles of the standard model [1].

1.1.1 The Electroweak Theory

In the Standard Model, electroweak interactions are described by a local gauge theory based on the $SU(2)_L \otimes U(1)_Y$ symmetry group, with four interaction mediators, or gauge bosons: the massless photon and the massive W^-, W^+ and Z bosons.

Quarks and leptons, which transform as specific representations under $SU(2)_L$, are mass-ordered into three generations of two particles each. The bottom and top quarks belong to the third and most massive quark generation. All normal matter in nature (protons, neutrons and electrons) is formed of particles from the first generation. Higher generations can be produced in high-energy interactions, but they are unstable and decay into first generation particles or photons. Each

	T_3	Q	**1**	**2**	**3**
Quarks	$+1/2$	$+2/3$	u	c	t
	$-1/2$	$-1/3$	d_c	s_c	b_c
Leptons	$+1/2$	0	ν_e	ν_μ	ν_τ
	$-1/2$	-1	e	μ	τ

Table 1.2: The three generations of quarks and leptons in the Standard Model. Q and T_3 are the charge and third component of the weak isospin, respectively.

generation of leptons consists of one charged and one uncharged particle. They are the electron, the muon, the tau, and their corresponding neutrinos (ν_e, ν_μ and ν_τ). Each generation of quarks consists of two particles of *weak isospin* (charge) $+\frac{1}{2}$ $(+\frac{2}{3})$ and $-\frac{1}{2}$ $(-\frac{1}{3})$. Table 1.2 summarizes the three families of quarks and leptons.

The c subscript on the negatively charged quarks denotes that the eigenstates with respect to the weak interaction are not the same as the mass eigenstates. Instead, weak eigenstates are rotated according to the Cabibbo-Kobayashi-Maskawa (CKM) matrix, shown in equation 1.1. The non-diagonal elements in the CKM matrix allow for transitions between different quark generations, and complex terms accomodate CP violation within the Standard Model.

$$\begin{pmatrix} d_c \\ s_c \\ b_c \end{pmatrix} = \begin{pmatrix} V_{ud} & V_{us} & V_{ub} \\ V_{cd} & V_{cs} & V_{cb} \\ V_{td} & V_{ts} & V_{tb} \end{pmatrix} \begin{pmatrix} d \\ s \\ b \end{pmatrix} \tag{1.1}$$

The local gauge invariance method for introducing interactions in a Lagrangian requires massless gauge bosons. The Standard Model introduces however a new scalar particle, the Higgs boson, to endow the W and Z bosons with mass via the so-called spontaneously broken symmetry mechanism. Quarks and leptons also acquire mass via interaction with the Higgs boson.

1.1.2 Quantum Chromodynamics

Quantum Chromodynamics is the quantum theory of the strong force between quarks and gluons. In what concerns this Thesis, it is the base for the understanding of the bottom and top quark production mechanisms in $p\overline{p}$ collisions, and is also key in the formation of *jets*, B hadrons, and the top quark decay products.

Quantum Chromodynamics is based on the $SU(3)$ symmetry group. The eight generators of $SU(3)$ correspond to the carriers of the strong force, the gluons. Quarks come in three colors, the components of an $SU(3)$ triplet. Since gluons carry color, they may also interact among themselves. Leptons are colorless, and do not participate in the strong force.

QCD is an *asymptotic free* theory, in which the value of the coupling α_s slowly tends to zero as the energy of the interaction increases, i.e. at shorter distances. This is described at leading order by equation 1.2, valid for $Q \gg \Lambda$, where f is the number of quark flavors and Λ is a characteristic energy scale of the order $100 - 200\,MeV$.

$$\alpha_s(Q^2) = \frac{12\pi}{(33 - 2f)\ln Q^2/\Lambda^2} \tag{1.2}$$

As a consequence, at the high energies reached in modern particle accelerators, quarks and gluons behave like free particles.

On the other hand, the strength of the strong interaction tends to increases at low energies, or equivalently, with increasing distance scales. This suggests an *infrared slavery* domain, with quarks always appearing as bound states in the low energy regime. It is indeed an experimental fact that all observable free particles are colorless. Isolated quarks have never been observed, but they appear as quark-antiquark (*mesons*) and three-quark (*baryons*) bound states, collectively called as *hadrons*.

1.1.3 Hadronization and Jets

The intermediate process, between the free quarks and gluons produced as a result of the primary high energy interaction and the final state hadrons observed in the detector, is called *hadronization*. This a low Q^2 process, so perturbative calculations are not applicable.

One common semi-empirical model for hadronization is *string fragmentation*, in which the quark-antiquark interaction is pictured as a $V(r) \propto kr$ potential, analogous to the elastic potential in classical mechanics, where the string models the cloud of gluons. As a quark-antiquark pair separates, the string stretches, until it breaks and a new quark-antiquark pair pops out of the vacuum to form the new ends of a new shorter string. These new strings also stretch and break, producing more quark-antiquark pairs. The hadronization process stops when there is not enough energy to generate new pairs.

As result of the hadronization, initial partons (quarks and gluons) are converted into showers of hadrons, or *jets* that travel more or less in the direction of the initial parton. Experimentally jets are identified as large energy deposition in localized calorimeter cells in a particle detector.

1.1.4 $p\overline{p}$ Collisions

At the Tevatron, b and t quarks are produced as a result of proton-antiproton collisions. Protons (antiprotons) are made of three uud ($\bar{u}\bar{u}\bar{d}$) "valence" quarks and a "sea" of virtual gluons and quark-antiquark pairs which can be of any flavor. Quarks and gluons are collectively called *partons*. Our knowledge of the internal structure of a hadron is encompassed by the Parton Distribution Functions, $f_i^H(x)$, defined such that in a hadron H, with momentum $P \gg M_H$, the number of partons of type i carrying a fraction of the parent hadron momentum in the range $[x, x+\mathrm{d}x]$, is given by $f_i^H(x)\,\mathrm{d}x$. These Parton Distribution Functions (PDFs) cannot be calculated

from first principles, and have to be empirically determined from data, mainly from measurements of electron, muon and neutrino deep inelastic scattering structure functions, and Drell-Yan lepton-pair production in hadron collisions [2].

Cross sections involving partons in the initial state are calculated by the convolution of the parton distribution functions and the perturbatively computed respective partonic process, summed over all contributing partons and integrated over all values of x. The initial state infrared divergences present in all partonic cross sections above tree level are partially absorbed in the PDFs in a procedure called *factorization*, which separates the perturbative (high energy) from the non-perturbative (low energy) processes. The PDFs are therefore dependent, in addition to x, on an energy parameter called the factorization scale μ_F, that determines the separation between the long- and short-distance physics [3]. Although the PDF's are extracted from data taken at a finite number of energy scales, the Gribov-Lipatov-Altarelli-Parisi (GLAP) [4] equations are used to evolve the parton distribution functions to other momentum regions.

There are different sets of PDFs, depending on the assumptions done on their parametrization, the data sets taken into account, and the relative weight assigned to each experiment in the fits. For example, in their CTEQ3 [5] set, the CTEQ group considers fixed target direct photon data and lepton asymmetries in $p\overline{p}$ W production, in addition to Drell-Yann and DIS experiments. In their CTEQ4 [6] set, they add the inclusive jet energy spectrum from CDF and DØ, while the MRST [7] parametrization incorporates instead charm data in lepton-hadron scattering and neutrino production of dimuons. Figure 1.1 shows, as an example, a CTEQ parametrization of the quark and gluon distribution functions in the proton at two factorization scales. It is interesting to remark that the quark over gluon dominance changes at about $x \sim 0.1$ which, as will be shown below, it implies that the main contributing channels are different for bottom and top production.

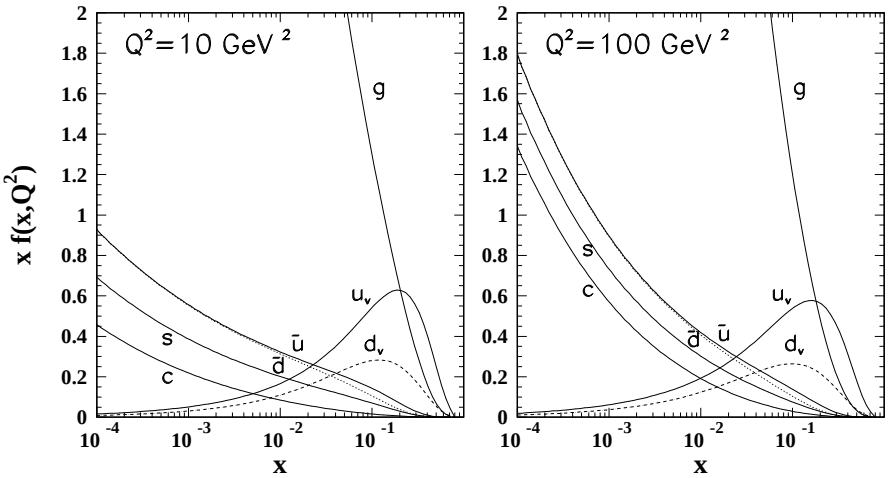

Figure 1.1: The CTEQ4M PDF's for quarks and gluons inside the proton at $\mu_F^2 = Q^2 = 10$ and 100 GeV^2.

When the momentum fractions of the two colliding partons are x_1 and x_2, the partonic center-of-mass frame will have a total available energy of $E_{CM}^2 = 4\,x_1 x_2\,E_p^2$, where E_p is the energy of the proton and antiproton beams, and it will be boosted by $\beta = (x_1 - x_2)/(x_1 + x_2)$ along the beam direction.

Since these fractions are different from event to event, every $p\overline{p}$ collision occurs with a different and unknown CM energy and longitudinal boost. For this reason collider physics, and in particular this Thesis, heavily relies on boost invariant quantities along the beam direction, like the transverse momentum $\vec{p}_T$ (or transverse energy E_T, for calorimetric measurements) and position variables like ϕ, the azimuthal angle, and η, the pseudorapidity , related to the polar angle θ through $\eta = -\ln\tan(\theta/2)$ for massless particles.

1.2 The Bottom Quark

The section discusses b quark production and decay in $p\overline{p}$ collisions, and some aspects of its physics relevant to the design of algorithms suited for its identification, This is important not only for the purpose of measuring B hadron properties, but also in the light of its relevance in top production. In effect, given that top quarks decay with 99% probability into a Wb pair, $t\bar{t}$ events will always contain two b quarks in their final state.

The b quark was discovered in 1977 at Fermilab, in a fixed target experiment [8] which collided high energy protons on nuclei. The experiment showed an enhancement in the rate of $\mu^+\mu^-$ pairs with an invariant mass $\sim$9.5 GeV/c^2 which was interpreted as a $b\bar{b}$ bound state called Υ, now known to be the first of a family of the bottonium $b\bar{b}$ bound states, the strong force analog of the electromagnetically bound positronium.

1.2.1 $b\bar{b}$ Production Mechanisms

The b quarks in $p\overline{p}$ collisions are produced predominantly in pairs, as the result of the strong interaction between one parton from the proton and another parton from the antiproton. The cross section for producing a b quark in a $p\overline{p}$ collision is calculated by convoluting the perturbative parton cross section with the proton distribution functions:

$$\frac{\mathrm{d}^2\sigma}{\mathrm{d}p_T\,\mathrm{d}\eta}(p\overline{p} \rightarrow bX) = \sum_{ij} \int dx_i dx_j f_i^p(x_i,\mu_F) f_j^{\bar{p}}(x_j,\mu_F) \frac{\mathrm{d}^2\sigma(ij \rightarrow bX,\mu_F)}{\mathrm{d}p_T\,\mathrm{d}\eta} \qquad (1.3)$$

where i and j are the incoming partons, $f_{i,j}^{p,\bar{p}}$ the proton and antiproton PDFs, and $\mathrm{d}^2\sigma\,(ij \rightarrow bX)/\mathrm{d}p_T\mathrm{d}\eta$ is the parton-level cross section for the $ij \rightarrow bX$ process, which is calculated perturbatively in powers of the strong coupling constant $\alpha_s(\mu_R)$, at renormalization and factorization scales μ_R and μ_F, usually chosen of the order of the energy scale of the event.

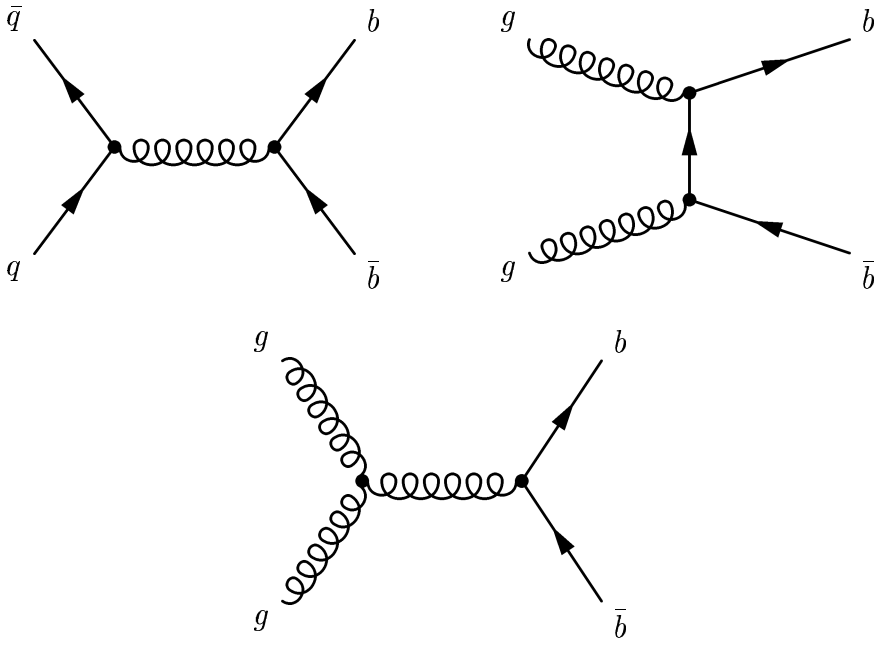

Figure 1.2: Leading order diagrams for $b\bar{b}$ production.

Figure 1.2 shows the leading order (LO) Feynman diagrams for $b\bar{b}$ pair production and Figure 1.3 illustrates some of the processes entering the next-to-leading order (NLO) QCD calculation. The contribution to the total $b\bar{b}$ cross section from higher order production mechanisms is comparable to that of direct production. This can be qualitatively understood because, for instance, the $gg \to gg$ cross section is about a factor 100 larger than $gg \to b\bar{b}$, and the rate of gluon splitting to bottom quarks ($g \to b\bar{b}$) is proportional to α_s, which is of the order of 0.1.

The gluon-gluon initial states dominate the $b\bar{b}$ production cross section since the gluon PDF is higher than the quark's at low momentum fractions[1], as it can be seen on Figure 1.1.

In hadron colliders, the $b\bar{b}$ production mechanisms have been traditionally grouped into three categories: direct production, flavor excitation and gluon splitting. In

[1]At least $\sim$10 GeV/c are required to create a $b\bar{b}$ pair. Since the proton momentum at the Tevatron Run 2 is $\sim$1000 GeV/c, typical parton momentum fractions for $b\bar{b}$ production are in the range $x \sim 0.01, 0.1$

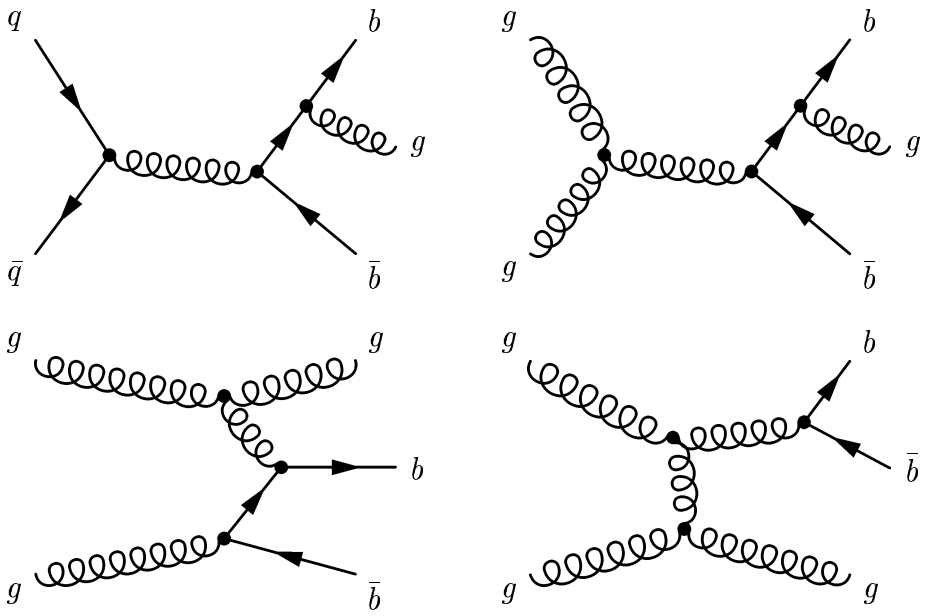

Figure 1.3: Next-to-leading order diagrams for $b\bar{b}$ production: Top: Direct production processes with gluon radiation, Bottom: (left) flavor excitation, (right) gluon splitting.

perturbation theory, the three processes are not independent due to interference between them.

At next-to-leading order, direct production is basically a $2 \rightarrow 2$ parton subprocess with the addition of gluon radiation in the final state. Flavor excitation consists in an initial state gluon splitting into a $b\bar{b}$ pair before interacting with a parton from the other hadron. In gluon splitting, a gluon in the final state splits into a $b\bar{b}$ pair.

In Monte Carlo event simulators (such as PYTHIA [9], HERWIG [10] and ISAJET [11]) based on a leading-order matrix element calculation, the three categories are generated separately without interference. Higher order is mimicked by allowing initial and final partons to radiate according to the Altarelli-Parisi evolution kernels, and the final showered partons are hadronized using empirical fragmentation models tuned to experimental results. In the Monte Carlo, direct production, flavor excitation and gluon splitting, are defined by the number of b quarks entering and leaving

the leading-order matrix element. Direct production has no b quarks in the initial state and two of them in the final state. Flavor excitation has one b quark in both the initial and final states. The initial b quark belongs to the proton sea and is described by the parton distribution functions. Gluon splitting has no b quarks in neither the initial nor final state. The $b\overline{b}$ pair is created during the parton showering process.

Final state b quarks hadronize into B hadrons. During the fragmentation process, other particles will also be produced along with the B hadron, giving rise to b-jets. The partons from the proton and antiproton remnants, not directly involved in the b quark production, also undergo hadronization generating the so-called *underlying event*, conformed by low p_T particles which tend to have small angles with respect to the beam pipe. In general, the momentum of the underlying event particles are uncorrelated with the final B hadron direction.

Directly produced b-jets are p_T balanced and back-to-back in the azimuthal angle ϕ. However they are not 3-D balanced because b-jets may be boosted in the z direction due to the different proton momentum fractions carried by the initial partons. In the flavor excitation process, the b quark which does not participate in the hard scatter belongs to the underlying event, resulting in a forward (large η) b-jet. The angular $\Delta\phi$ separation between the two b-jets is therefore expected to be flat. Gluon splitted b-jets are expected to be collinear since they originate from the splitting of a gluon and will tend to be identified as a same hadronic jet. The azimuthal separation between the two gluon splitted b-jets thus peaks at small angles.

1.2.2 Heavy Flavor Hadrons

B hadrons are produced as result of the hadronization process of b quarks. Since the probability for pair quark-antiquark creation from the vacuum depends on the

Hadron	**Composition**	**Mass** $[MeV/c^2]$	**Lifetime** $[ps]$
B^+	$b\bar{u}$	5279.1 ± 0.5	1.674 ± 0.018
B^0	$b\bar{d}$	5279.3 ± 0.7	1.542 ± 0.016
B_s^0	$b\bar{s}$	5369.6 ± 2.4	1.461 ± 0.057
B_c^+	$b\bar{c}$	6400 ± 520	0.46 ± 0.21
Λ_b^0	bud	5624 ± 9	1.229 ± 0.080

Table 1.3: Summary of B hadron properties [1].

Hadron	**Composition**	**Mass** $[MeV/c^2]$	**Lifetime** $[ps]$
D^+	$c\bar{d}$	1869.4 ± 0.5	1.051 ± 0.013
D^0	$c\bar{u}$	1864.1 ± 1.0	0.474 ± 0.028
D_s^+	$c\bar{s}$	1969.0 ± 1.4	0.490 ± 0.09
Λ_c^+	cud	2284.9 ± 0.6	0.200 ± 0.006

Table 1.4: Summary of D hadron properties [1].

quark-antiquark mass, the most common B hadrons are $B^+(\bar{b}u)$ and $B^0(\bar{b}d)$. Each comprises approximately 38% of the produced B hadrons. B_s^0 $(\bar{b}s)$ is the next most common B meson, comprising 11% of the cases. The B_c^+ meson is made of a c and a b quark and, the c quark being much more massive than the u-d-s, they amount to only $\sim$0.001% of the B hadrons produced in $p\overline{p}$ collisions. The remaining 13% is basically comprised of Λ_b baryons. The hadronization process for c quarks is similar to that of the b, the resulting mesons are generically called D, Λ_c being the most common baryon. Tables 1.3 and 1.4 summarize some properties of the B and D hadrons.

B hadrons decay via the weak interaction. The simplest description is provided by the *spectator* model, in which the heavy quark decays via an electroweak diagram into a virtual W and a c quark, and the lighter quark (the spectator) plays no role. B hadron decays are classified in semi-leptonic or hadronic depending on the W decay, which can respectively give rise to a charged lepton and its associated

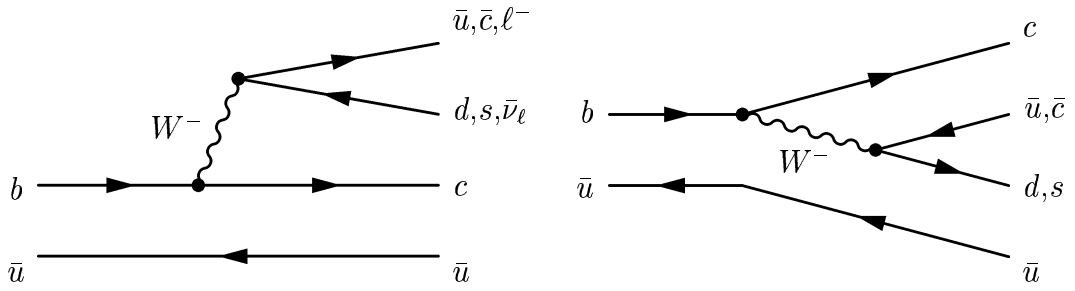

Figure 1.4: Diagrams for simple B^- decays in the spectator model.

neutrino, or a quark-antiquark pair. Figure 1.4 shows a few simple examples for B^- decay within the spectator model. Depending on the choice for the W^- decay vertex, the final states illustrated are semileptonic, $D^0 \ell\, \bar{\nu}_\ell$, where ℓ can be e^-, μ^- or τ^-; or hadronic, $D^0\pi^-$, $D^0 D_s^-$, $D^0 K^-$, $J/\psi\, K^-$ and $J/\psi\, \pi^-$.

1.2.3 *B* Hadron Lifetimes

Precise measurements of the B lifetimes are key to the determination of the CKM matrix elements involved in CP violation, as well as to understand B hadron decay mechanisms beyond the simple spectator model. According to it, the naive expectation would be that all B hadron lifetimes are equal. This is in fact to first order true, as the experimental values are 1.65, 1.55, 1.49, 0.46 and 1.23 $\times 10^{-12}$ *sec*, for $B^+\,(\bar{b}u)$, $B^0\,(\bar{b}d)$, $B_s^0\,(\bar{b}s)$, $B_c^+\,(\bar{b}c)$, $\Lambda_b^0\,(bud)$, respectively. The shorter B_c^+ lifetime can be understood in the light that both b and c quarks can decay weakly. And the slightly lower value for B_s^0 is accomodated because of the larger phase space available for the decay products due to the higher mass of the s quark, $m_s > m_{u,d}$. However, the fact that $\tau(B^\pm) > \tau(B^0)$ can only be explained via non-spectator mechanisms, such as Pauli interference effects between contributing diagrams. For example, both diagrams on Figure 1.4 contribute to the $B^- \to D^0\rho^-$ decay, while only the left one does for $B^0 \to D^+\rho^-$.

B meson lifetimes have been measured in several e^+e^- collider experiments, such

as BABAR, BELL, LEP and SLD, as well as in $p\overline{p}$ collisions, by the CDF collaboration. At BELL and BABAR, e^+e^- beams are tuned at the $\Upsilon(4S)$ resonance so that only $B^{\pm}$ and B^0 mesons are produced as a result of the $\Upsilon(4S)$ decay. The relative error on the $B^{\pm}$ and B^0 lifetimes is of the order of $\sim$3% in both experiments. At LEP, $B^{\pm}$, B^0 and B_s^0 are produced via $e^+e^- \to Z$. The relative measurement error for $B^{\pm}$ and B^0 mesons is close 5.0%, whereas it is $\sim$12% for B_s^0.

CDF measured all B meson lifetimes, and is the only one to have produced the heavier members of the family. The measurement precision for $B^{\pm}$ and B^0 mesons is similar to LEP, while the relative error for the B_c^0 lifetime is $\sim$45%. CDF used fully reconstructed B decays to measure the individual B lifetimes while an average inclusive B hadron lifetime was obtained via partially reconstructed $B \to J/\psi X$ events. The measured average B lifetime is smaller than that of the $B^{\pm}$ or B^0, as expected form the contribution from B hadrons with shorter lifetimes.

The upgraded DØ detector is expected to measure B meson lifetimes with a precision better than 5% by the use of a completly new silicon vertex detector, central fiber tracker and trigger system as well as an improved muon system with large η coverage.

The main advantage for measuring B lifetimes at hadron colliders is that the $b\overline{b}$ production cross section is very large. At the Tevatron, it is approximately four orders of magnitude larger than in e^+e^- experiments. However, the background is higher because less than one in a thousand $p\overline{p}$ collisions results in b quark production, whereas this fraction is $\sim\frac{1}{4}$ for e^+e^-. Furthermore, the presence of multiple interactions and underlying event particles from the proton-antiproton remnants, render the identification of B hadrons even more difficult experimentally.

1.3 The Top Quark

This section addresses the physics of the top quark and a summary of the recent results obtained at the two Tevatron Collider experiments.

The top quark was discovered in 1995 at Fermilab by the CDF and DØ collaborations. However, even prior its discovery, the Standard Model provided several compelling theoretical and experimental arguments for its existence. Some of them are briefly summarized below:

1. **Results from precision electroweak measurements:** The comparison between high precision electroweak measurements at LEP, SLC and Fermilab, with their corresponding Standard Model predictions, allowed to set limits on the top and Higgs boson masses, because their values enter the calculations via virtual loop corrections. Some of these measurements include the Z/W mass and width, branching ratios and asymmetries. Prior to its discovery, the best indirect limit on the top quark mass was $m_t = 178 \pm 8^{+27}_{-20}\, GeV/c^2$.

2. **Cancellation of anomaly diagrams:** The divergence introduced by the chiral anomaly in the triangle diagram shown in Figure 1.5 cannot be solved by renormalization techniques. In the electroweak theory, however, the fermion contributions from each generation add up to zero, demanding the existence of a top quark to complete the cancellation in the third generation, thus rendering the theory anomaly free.

3. **$B^0 - \bar{B}^0$ mixing:** Within the Standard Model B^0 and $\bar{B}^0$ mesons can mix with each other through box diagrams, as shown in Figure 1.6. A heavy top quark becomes necessary in the internal lines of these diagrams to explain the experimental level of mixing.

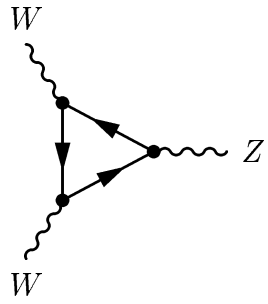

Figure 1.5: Example of anomaly triangle diagram.

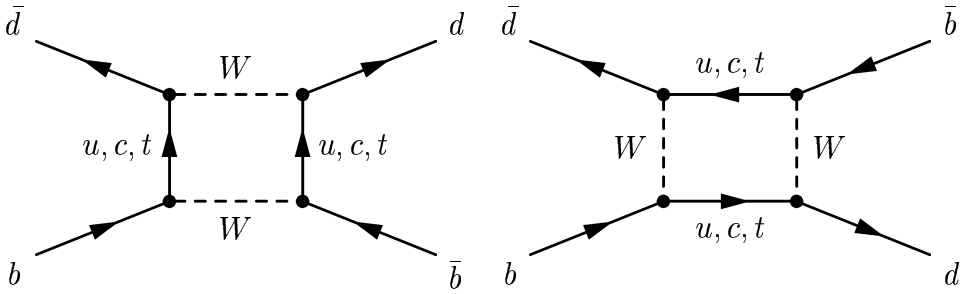

Figure 1.6: $B^0 - \bar{B}^0$ mixing diagrams.

1.3.1 Top Quark Production

There are two mechanisms that yield top quarks in $p\overline{p}$ collisions: pair ($p\overline{p} \rightarrow t\bar{t}\ X$) and single top ($p\overline{p} \rightarrow tX$) production. The dominant process is the former, and its leading order Feynman diagrams are shown in Figure 1.7: $q\overline{q} \rightarrow t\bar{t}$ (quark annihilation) and $gg \rightarrow t\bar{t}$ (gluon fusion). At the Tevatron, approximately 90% of $t\bar{t}$ production proceeds through the $q\overline{q}$ channel. The preeminence of the $q\overline{q}$ contribution can be understood from inspection of Figure 1.1, and of equation $E^2_{CM} = 4\,x_1 x_2\,E^2_p$ in Section 1.1.4. In effect, the minimum center-of-mass energy needed to create a $t\bar{t}$ pair is 350 GeV, requiring a value of $x \gtrsim 0.18$, which is in fact usually larger if the event is boosted and/or the $t\bar{t}$ pair is created with kinetic energy. In this range of proton momentum fractions, the quark contribution dominates over the gluon's.

The theoretical $t\bar{t}$ production cross-sections are in the range of $\sim 6.7 - 7.5\,pb$ for $m_t = 175\,GeV/c^2$ and $\sqrt{s} = 2\,TeV$, with an expected uncertainty of ~5%. At next-

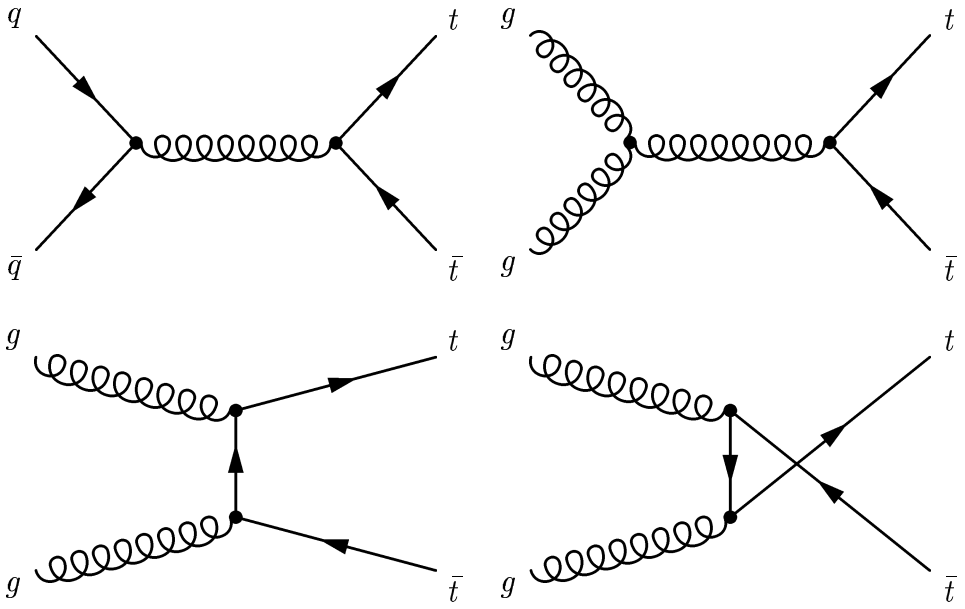

Figure 1.7: Leading order $t\bar{t}$ production diagrams.

to-leading order, the predicted cross section is $\sim$8.8 pb. It should be noted that the total inelastic cross section in $p\overline{p}$ collisions is approximately ten orders of magnitude higher than that for $t\bar{t}$ production. rendering the subtracion of the background a formidable task, that will be addressed in Chapters 5 and 8.

There are two dominant processes for single top production, Wg fusion and W^* production, whose lowest order diagrams are shown in Figure 1.8. The respective cross sections for a top quark mass of $m_t = 175\,GeV/c^2$ are $1.44 \pm 0.43\,pb$ and $0.74 \pm 0.04\,pb$. Single top production is however very difficult to disentangle from the background, and has not been observed yet in DØ. In this thesis, we only consider top quarks produced in pairs.

1.3.2 Top Quark Decay

Given its high mass, the top quark decays before it hadronizes. The top quark lifetime is of the order of $10^{-24}s$, whereas typical timescales for hadronization are about one order of magnitude shorter.

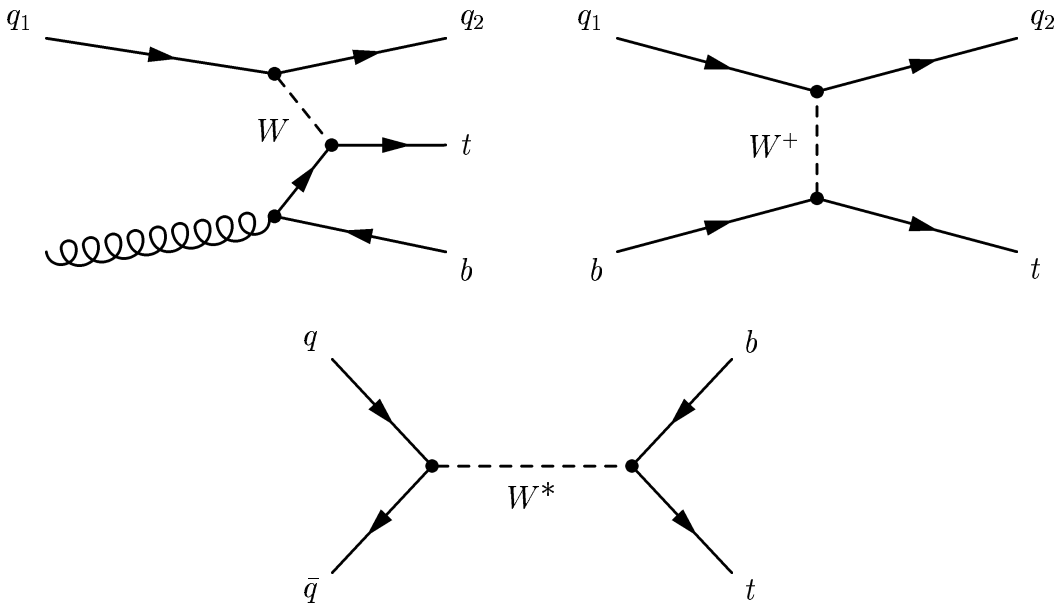

Figure 1.8: Leading order diagrams for single top production in $p\overline{p}$ collisions.

According to the Standard Model, the top quark decays predominantly to bW since the decay modes $t \to sW$ and $t \to dW$ are suppressed by the CKM matrix factors $|V_{ts}|$ and $|V_{td}|$.

The decay mode of the $t\overline{t}$ pair is determined by the fate of the two W bosons, as shown in Figure 1.9. Each W boson may decay hadronically or leptonically. All three ($e\nu_e$, $\mu\nu_\mu$, $\tau\nu_\tau$) leptonic W decays are kinematically allowed. The hadronic decay of the W produces first and second generation $q\overline{q}$ pairs, and since every quark comes in three colors, there are six possible hadronic decay modes. Hence, as Table 1.5 shows, the probability for a W boson to decay in each of the two available quark final states is approximately 1/3, while for each leptonic channel it is 1/9.

Since the t and $\bar{t}$ decay independently, events can be classified according to the different W decay modes as follows (see Table 1.6).

- **dilepton events**, in which both W decay leptonically. Despite its low branching ratio, this channel is characterized by very low background (especially in the $e\mu$ channel). Its final state signature consists of two b-jets, two leptons

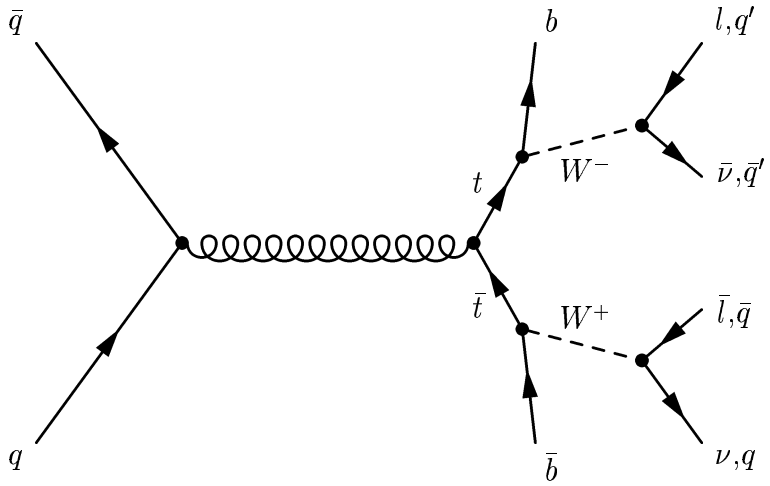

Figure 1.9: Standard Model decay modes of $t\bar{t}$ pairs.

	decay mode	**branching ratio**	
leptonic	$t \to be\nu_e$	1/9	33%
	$t \to b\mu\nu_\mu$	1/9	
	$t \to b\tau\nu_\tau$	1/9	
hadronic	$t \to bq\bar{q}'$	2/3	67%

Table 1.5: Possible decay modes of the top quark and approximate branching ratios.

and large momentum imbalance in the plane transverse to the beam from the two unobserved neutrinos.

- **lepton+jets events**, in which one W decays leptonically and the other hadronically. This channel has larger branching ratio compared to the dilepton channel, but it also suffers from a larger background from QCD multijet events and single W production with associated jets.

- **all-jets events**, in which both W decay hadronically. Its signature consists of six jets in the final state. This is the channel with the largest cross section but it also has a huge background from QCD multijet process which makes its identification very difficult. from QCD multijet processes which makes its

	decay mode	branching ratio	
dilepton	$t\bar{t} \rightarrow bbe\nu_e e\nu_e$	1/81	
	$t\bar{t} \rightarrow b\bar{b}\mu\nu_\mu\mu\nu_\mu$	1/81	
	$t\bar{t} \rightarrow b\bar{b}e\nu_e\mu\nu_\mu$	2/81	5%
lepton + jets	$t\bar{t} \rightarrow b\bar{b}e\nu_e jj$	12/81	
	$t\bar{t} \rightarrow b\bar{b}\mu\nu_\mu jj$	12/81	30%
all-jets	$t\bar{t} \rightarrow b\bar{b}jjjj$	36/81	44%
τ *channels*	$t\bar{t} \rightarrow b\bar{b}\tau X$	17/81	21%

Table 1.6: Possible decay modes of $t\bar{t}$ events

identification very challenging.

Tau channels are classified in a different category since tau leptons are difficult to identify experimentally.

1.3.3 The Lepton + Jets channel

The signature of this channel consists of two b-jets, a lepton and a neutrino from the leptonic W decay, plus two additional quark-jets from the hadronic W vertex. There may also be additional jets from QCD radiation from the initial (ISR) or final (FSR) state. Since the neutrino does not interact with the detector, we infer its presence from the momentum imbalance in the plane transverse to the beam, which we measure through the event missing transverse energy, $\not\!\!E_T$, to be discussed in detail in Chapter 6. From an experimental point of view, $t\bar{t}$ events are characterized by a high p_T lepton, $\not\!\!E_T$, and 4 or more jets, two of which originate from b fragmentation.

The dominant background sources are QCD multijet production, and single W production with additional radiated jets.

In the first case, one of the jets is misidentified as an electron and fake $\not\!\!E_T$ is produced by energy resolution fluctuations in the calorimeter. Consider for instance 2 balanced back-to-back jets of $p_T = 100\,GeV/c$ each. If the energy resolution

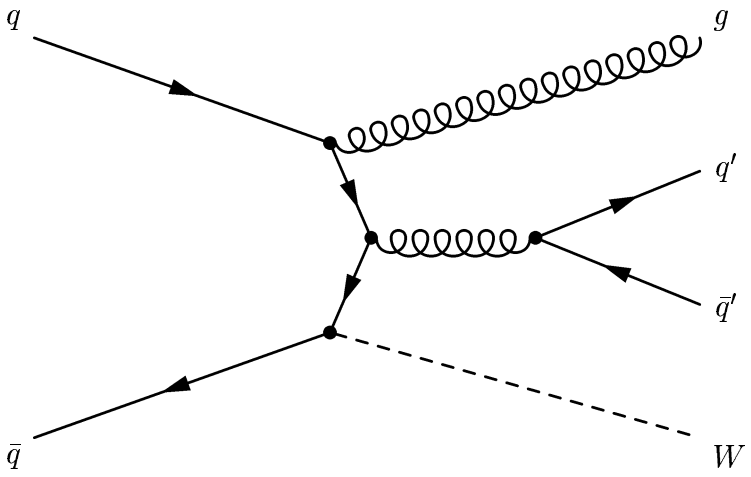

Figure 1.10: Example of $QCD\ W + jets$ production.

is $\Delta p_T/p_T = 0.1$, there is then a 17% probability for the $\not\!\!E_T$ to be greater than $20\,GeV/c$ due to energy resolution fluctuations. This probability increases if there are more than 2 jets in the event. Since lepton+jets events contain several hadronic jets, the probability to fake $\not\!\!E_T$ from jet energy resolutions in QCD multijet events is not negligible.

Figure 1.10 shows an example of W+jets production, which has a similar signature than $t\bar{t}$ events, with the exception that in general there are no jets from b fragmentation.. This is an important point, for all top decay channels contain two b-jets. The identification of b-jets (*b-tagging*) is therefore an essential technique (to be discussed in detail in Chapter 5) to separate top from background events, since none of the main top backgrounds contain heavy flavor.

1.4 Recent Experimental Results

This section summarizes the current knowledge and the latest cross section and mass measurement results from CDF and DØ experiments.

1.4.1 CDF Top Quark Results

CDF employed b-tagging as the main technique to isolate the top quark signal from background. Two different methods were used: secondary vertex b-tagging (SECVTX) and soft lepton tagging (SLT). The first method searches for secondary vertices -displaced from the primary event vertex- within jets from the decay of long lived B hadrons. This is the same method developed and used in this Thesis for the first time in DØ. The second method searches for the presence of a soft lepton (electron or muon) within jets, indicative of a semileptonic b decay. The b-tagging efficiency of the SLT method is limited by the branching ratio, which is roughly 5% for each of the two leptonic modes.

In the lepton+jets channel, the $t\bar{t}$ cross section measurement is determined by comparing the total number of observed events with at least one tagged jet (single tagged events) with its prediction computed from all background contributions in the $W + 3, 4$ jets sample. The main sources of backgrounds are the $p\overline{p} \rightarrow Wg$ with $g \rightarrow b\overline{b}$, $g \rightarrow c\overline{c}$, $p\overline{p} \rightarrow Wc$ physics processe, and mistags, tagged events which do not contain heavy flavor. Smaller background contributions are QCD multijet production, single top, WW, WZ, ZZ and $Z \rightarrow \tau\tau$.

With an integrated luminosity of $105.1\, pb^{-1}$, CDF observed 29 (25) SECVTX (SLT) single tagged events with 8.0 ± 1.0 (13.2 ± 1.2) expected background events. This excess yields a cross section of $\sigma_{t\bar{t}} = 5.08 \pm 1.54\, pb$ for the SECVTX method and $\sigma_{t\bar{t}} = 9.18 \pm 4.26\, pb$ for the SLT, for $m_t = 175\, GeV/c^2$. In the dilepton channel, CDF observed nine candidate events. The predicted number of background, estimated using a combination of data and Monte Carlo, was 1.3 ± 0.4 (0.8 ± 0.2) yielding a cross section of $\sigma_{t\bar{t}} = 8.5^{+4.4}_{-3.4}\, pb$. Finally, in the all-jets channel, CDF measured $\sigma_{t\bar{t}} = 7.6^{+3.5}_{-2.7}\, pb$. The all channels combined result is $\sigma_{t\bar{t}} = 6.5^{+1.7}_{-1.4}\, pb$

The top quark mass was measured in the dilepton, lepton+jets and all-jets channel by means of a constrained kinematic fit. The method consists in fitting a com-

bination of background and $t\bar{t}$ signal for different top quark mass hypothesis, and extractig the mass by maximizing a likelihood function. The all-channel combined result is $m_t = 176.1 \pm 6.6\, GeV/c^2$.

1.4.2 DØ Top Quark Results

DØ identified top quark events by means of two methods: a topological analysis based on the kinematics of the $t\bar{t}$ final state and a soft muon b-tagging analysis similar to the SLT CDF method. The DØ experiment did not have a silicon detector during Run 1 to perform secondary vertex tagging.

In the dilepton analysis, DØ combined the ee, $\mu\mu$, $e\mu$ and $e\nu$ channels observing 9 candidates events over a background of 2.69 ± 0.66 events resulting in a $\sigma_{t\bar{t}} = 6.02 \pm 3.21\, pb$.

In the combined lepton+jets channel, 39 candidate events were observed with a background prediction of 13.97 ± 2.22 events, yielding $\sigma_{t\bar{t}} = 5.31 \pm 1.72\, pb$.

The all-jets channel analysis consisted of 41 observed events over 24.80 ± 2.37 predicted background events, resulting in $\sigma_{t\bar{t}} = 7.33 \pm 3.20\, pb$.

The combined DØ cross section result is $\sigma_{t\bar{t}} = 5.69 \pm 1.60\, pb$.

The top quark mass was also determined using a constrained fit method using dilepton and lepton+jets events. The final combined top quark mass is $m_t = 172.1 \pm 5.2 \pm 4.9\, GeV/c^2$

Chapter 2

Experimental Apparatus

This chapter describes the upgraded Fermilab Tevatron accelerator and the DØ detector during its second period of operation, Run II. The accelerator upgrade [12] allowed a decrease in the bunch crossing time from the Run I value of $3.5\,\mu s$ to $396\,ns$, with a consequent increase in instantaneous luminosity. The DØ detector upgrade [13] consisted of the addition of a superconducting magnet, a completely new high resolution tracking system, the upgrade of the muon system, the addition of preshower detectors and improvements on the trigger, electronics and data acquisition systems.

2.1 The Accelerator

The Tevatron collider accelerates protons and antiprotons at a center-of-mass energy of $2.0\,TeV$. Until the finalization of the Large Hadron Collider (LHC) at CERN, The Tevatron will continue to be the highest energy hadron collider.

2.1.1 Accelerator Concepts

Particle accelerators consist of two main components: Radio Frequency (RF) cavities and Magnets. RF cavities are used to increase the kinetic energy of the charged particles and Magnets are used to bend particles into a circular orbit -in the case of collider accelerators-, focalize the particle beam and transfer particle beams from one system to another.

RF cavities

In an RF cavity, oscillating electric currents are used to create time dependent electric fields in the longitudinal direction of a particle beam in order to increase their kinetic energy. RF cavities are resonant structures with a natural resonant frequency. Given the oscillating nature of the generated electric field, an RF cavity will accelerate particles only during half a period of oscillation, when the electric field points in the direction of the beam momentum. In order to obtain a net gain of kinetic energy, particles must be shielded during the second half period, when the electric field would decelerate them. There are basically two methods of shielding particles from decelerating fields inside an RF cavity: by means of drift tubes and by changing the RF frequency. The former can only be used in linear accelerators while the latter is the acceleration method of synchrotron circular accelerators.

In the first case, grounded drift tubes are inserted inside the cavity so that when the electric field points in the wrong direction, the particle is hiding inside the drift tube and is not accelerated, it simply drifts. If the RF cavity has a constant frequency, as particles gain kinetic energy, the time particles take to pass each drift tube shortens. Thus, the drift tubes need to be longer after each RF cavity. This is the structure of the Tevatron Linac accelerator DTL.

One important characteristic of RF cavity acceleration is that a continuous beam of particles will emerge in discrete packets of particles called *bunches*. This bunch

structure appears from the fact that particles that enter the cavity when the electric field is correct, get accelerated through the drift tubes. Particles slightly behind in time, will enter the cavity when the electric field points in the opposite beam direction and will not be accelerated.

In a synchrotron circular machine, the RF frequency and the strength of the magnetic bending field are synched to the beam momentum and revolution frequency. As the particle kinetic energy increases in each lap, the synchrotron increases the RF resonant frequency of its cavities, such that the beam is always accelerated when it passes through them.

Another characteristic of RF accelerating cavities is *phase focusing*. A bunch of particles arriving in an RF cavity with a distribution of phases will receive different kinetic energy depending on the time they arrive with respect to the synchronous phase. A particle arriving earlier in time, will receive less of an increase, whereas particles arriving later, will receive a larger boost, than synchronous particles. This effect is illustrated in Fig 2.1. Particles arriving earlier to the RF cavity do so because they have more energy relative to others in their bunch. Since particles at point "E" in Fig 2.1 will receive a smaller increase in energy, they will slowly move toward point "S". Similarly, particles at point "L" will slowly move toward "S" as well, by receiving a larger amount of energy. These longitudinal (parallel to the direction of the beam) motions are called *synchrotron oscillations* and are usually represented as a rotation in the $\Delta E - \Delta\phi$ phase space as shown in Figure 2.2.

Magnets

Magnets have several uses in particle accelerators. In this section, two primary application of magnets are briefly discussed: Bending and focusing.

Bend magnets are used to keep the particles around a circle so that the same RF cavities can increase the kinetic energy of the beam at each revolution. Since

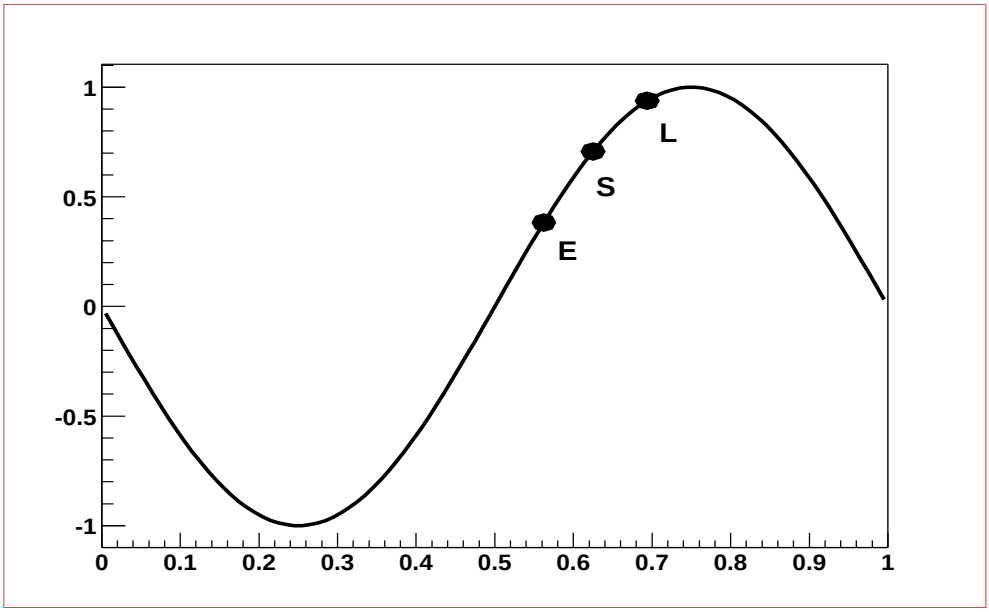

Figure 2.1: RF phase focusing: Particles arriving in the cavity at different phases perceive a different magnitude of the accelerating electric field. Point "S" is the synchronous phase. Point "E" indicates particles in the bunch arriving earlier and receiving less kinetic energy than synchronous particles. Point "L" indicates later particles, receiving more energy than synchronous particles.

the particle momentum increases during acceleration, the strength of the bending magnetic field has to be increased in order to keep the charged particles confined to the same radius. Thus, in a synchrotron accelerator, the frequency of the RF cavities and the strength of the magnetic bending field are changed according to the beam's changing momentum and revolution frequency. A bend magnet consist of a superconducting *dipole* electromagnet. The field intensity is controlled by the intensity of its electric current. For a synchronous particle, the increasing energy of the particle during acceleration, is exactly accounted for by the increasing magnetic bending field created by the dipole. Therefore, a synchronous particle always follows a perfect circular path or *ideal orbit*. In a real beam, particles momenta are not the same as the synchronous case. Higher momentum particles will be slightly less bent and will follow an orbit radially outside of the ideal orbit. Similarly, particles with

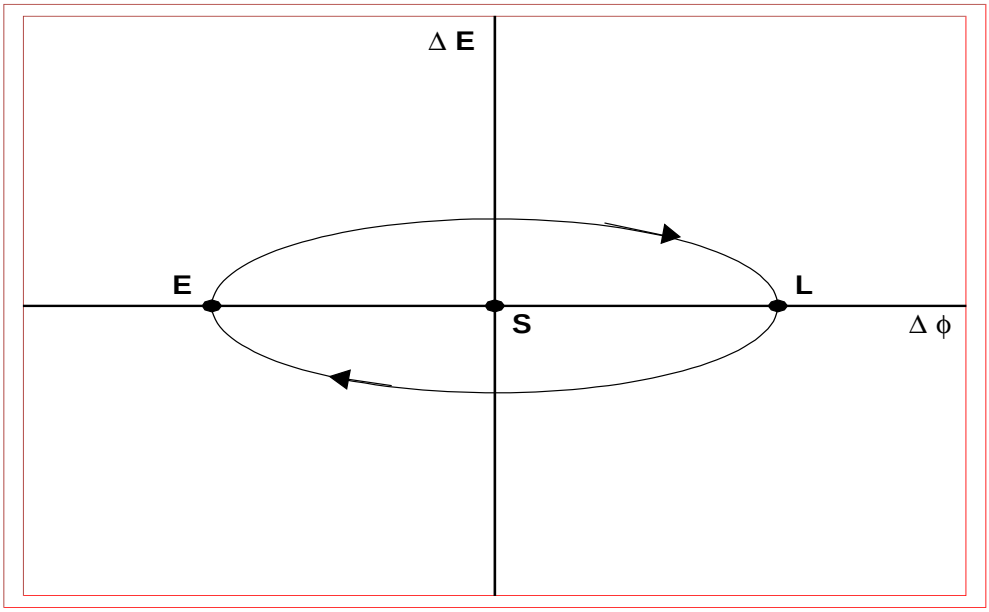

Figure 2.2: Phase space diagram for synchrotron oscillations. The labeled points represent various initial beam phases.

lower momentum relative to the synchronous particle, will travel radially inside of the ideal orbit. This distribution in orbit radia due to the beam momentum spread is called *dispersion*. Due to dispersion and Coulomb interaction among the particles beam, it is necessary to focus the beam in the transverse plane, as RF focuses the particles in the longitudinal plane.

Beam focusing in the transverse plane is achieved by the use of *quadrupole* magnets consisting of four magnetic poles created by four current loops arranged in the vertices of a rectangle with faces $N - S - N - S$. A quadrupole magnet focuses the beam in one plane and defocuces it in the other. In order to focus the beam in both horizontal and vertical planes, two quadrupole magnets, 90 degrees rotated with respect to each other, are required. The restorative forces created by the quadrupole focusing magnets produce stable transverse oscillations of the particles around the ideal orbit called *betatron oscillations*. The area in the phase space defined by the distance and the deviation angle of the particles from the ideal orbit, is called *emmitance* and defines the beam size. The number of betatron oscillations that the

beam undergoes in each revolution is called the *tune* of the accelerator.

2.1.2 Overview of the Tevatron Collider

The Tevatron collider is an accelerator complex composed of many systems which are briefly described below. Figure 2.3 shows a general layout of the Tevatron accelerator chain.

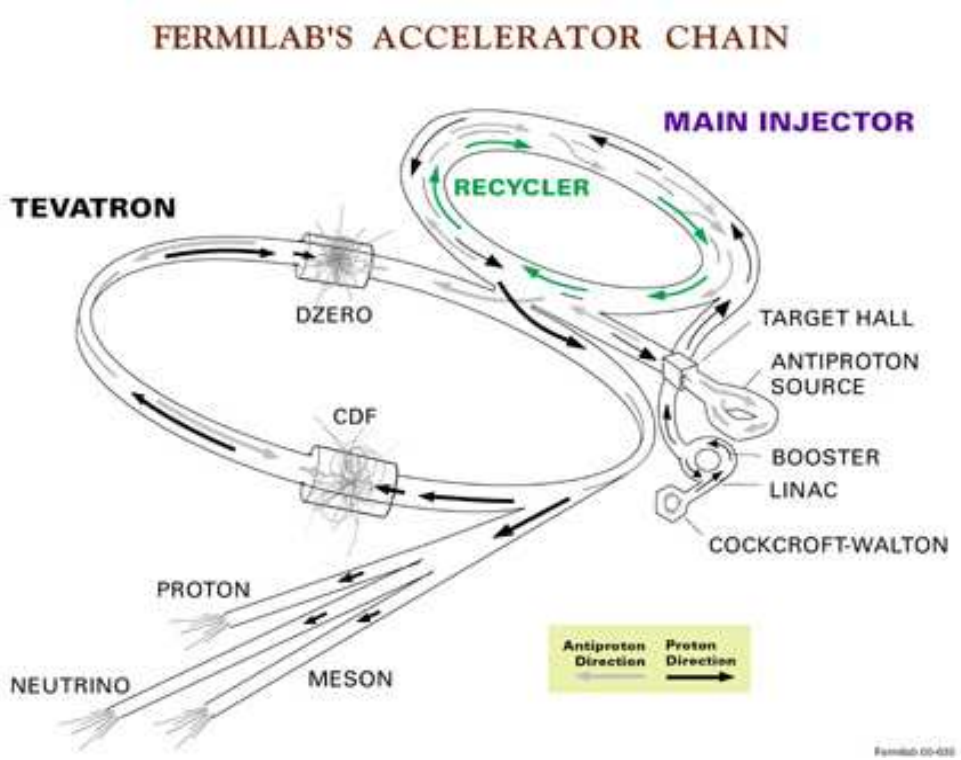

Figure 2.3: Fermilab Tevatron collider complex.

The Preaccelerator

The beam originates at the Preaccelerator with the production of negatively charged hydrogen ions (H^-) from hydrogen gas. The ion source is located within a static electric field which accelerates the H^- ions to an energy of $750\,KeV$. After the beam exits the Preaccelerator, it is transferred to the the Linac.

The Linac

The Linear Accelerator or "Linac" accelerates the $750\,KeV$ H^- ions to an energy of $400\,MeV$ and sends the beam to the Booster. The Linac is made of two main sections with different geometries, the low energy drift tube Linac (DTL) and the high energy side coupled cavity Linac (SCL) which operate at $201\,MHz$ and $805\,MHz$ respectively. It can accelerate beam once every $66\,ms$.

The Booster

The Booster takes the $400\,MeV$ H^- ions from the Linac, passes them through a carbon foil which strips off both electrons leaving only protons, and accelerates the protons to $8\,GeV$. The Booster is the first synchrotron in the Tevatron complex. It consists of a $75\,m$ radius circle with 18 RF cavities and a series of magnets interspersed in a FOFDOOD lattice configuration. A pulse train of 5 to 7 bunches, containing 5-6 $\times 10^{10}$ protons each is delivered from the Booster to the Main injector.

The Main Injector

The Main Injector is a circular synchrotron seven times the circumference of the Booster and slightly more than half the circumference of the Tevatron. The Main Injector is made of 18 RF cavities and can accelerate $8\,GeV$ protons from the Booster to either $120\,GeV$ or $150\,GeV$ depending on their destination: the antiproton production (stacking) or the Tevatron proton beam injection. As well as accelerating protons from the Booster, it can also accelerate $8\,GeV$ antiprotons from the Antiproton source to $150\,GeV$.

The Main Injector has two main operation modes *Pbar production* and *Shot Setup*. In Pbar mode, the Main Injector sends $120\,GeV$ protons to the Antiproton Source. In Shot Setup mode, the Main Injector extracts $8\,GeV$ antiprotons from the Accumulator Source, accelerates them to $150\,GeV$ and loads the Tevatron with

$150\,GeV$ proton and antiproton beams.

For proton injection to the Tevatron, the Main Injector coalesces the 7 proton bunches exiting the Booster into a single high intensity bunch and repeats this process 36 times in a row to load the Tevatron with the protons necessary for a 36×36 store. When loading antiprotons, 4 sets of 7 bunches are coalesced into 4 bunches and this process is repeated nine times in a row to load the Tevatron with the 36 $\bar{p}$ bunches.

The Antiproton Source

The Antiproton Source consists of three components: the Target and two synchrotron: the Debuncher and the Accumulator. $120\,GeV$ protons coming from the Main Injector strike a nickel/copper target producing antiprotons and all sort of secondary particles. Magnets are used to select $8\,GeV$ antiprotons from the spray of particles produced in the collision. These antiprotons are directed to the Debuncher.

The Debuncher is a rounded triangular-shaped synchrotron with a mean radius of $90\,m$. Its purpose is to reduce the momentum spread of the antiprotons coming off the target by means of an RF manipulation technique called *bunch rotation*. The antiprotons are also stochastically cooled in order to reduce their transverse oscillation. The Debuncher does not accelerate beam, but maintains it at a constant energy of $8\,GeV$ until it can be transferred to the Accumulator.

The Accumulator is also a triangular-shaped synchrotron of $75\,m$ radius housed in the same tunnel as the Debuncher. It is the storage ring for the antiprotons which are further cooled and stored until needed. The beam from the Accumulator is transferred to the Recycler ring.

The Recycler

The purpose of the Recycler is to recover antiprotons left from a previous store, cooling them and storing them alongside those sent from the Antiproton Source. When an $8\,GeV$ antiproton beam is formed, it is first transferred to the Main Injector, to raise its energy to $150\,GeV$, and then injected into the Tevatron accelerator.

The Tevatron

The Tevatron is the largest Fermilab accelerator, with a circumference of approximately 4 miles. It is a circular synchrotron with eight accelerating cavities. The Tevatron accepts both protons and antiprotons from the Main Injector and accelerate them, in opposite directions, from $150\,GeV$ to $980\,GeV$. The Tevatron uses superconducting niobium/titanium alloy magnets to produce the 4 Tesla magnetic fields needed for the beams to reach their maximum energy. Once the final energy is reached, the beams are focalized to small transverse dimensions by means of quadrupole magnets to produce collisions at the two experimental areas: CDF and DØ.

2.2 The DØ Detector

The DØ detector [14, 13] is a general purpose collider detector designed and optimized to study interactions originating from $p\overline{p}$ collisions measuring final states containing electrons, muons, jets and neutrinos and providing b-jet identification.

Particle detectors for high energy hadron colliders consist of three main components: tracking, calorimeter and muon systems.

Closest to the interaction region is the tracking system, responsible of the measurement of the three dimensional trajectories (*tracks*) of charged particles passing through it. Tracking detectors are located inside a magnetic field to provide momen-

tum and charge determination. Modern tracking detectors consist of an inner high resolution silicon vertex detector, to provide precise primary and secondary vertex determination, and a larger outer tracking system, to provide efficient track pattern recognition and improved momentum resolution.

Surrounding the tracking system, the calorimeter measures the energy of most particles (charged and neutrals) that hit it. A calorimeter is made of an absorber material so that a particle hitting it produces a shower of secondary particles. The measurement of the shower size allows determination of the particle energy, and the shower shape provides a way to identify between different types of particles, such as electrons, photons and hadrons.

Neutrinos cannot be detected in the tracking nor the calorimeter detector. Their presence is inferred from an imbalance in the total transverse energy measured by the calorimeter, denoted $\not\!\!E_T$. Excellent $\not\!\!E_T$ resolution is crucial for a wide range of searches, like for instance new physics involving supersymmetric particles.

Since muons are not stopped by the calorimeter, they are identified by means of additional tracking detectors beyond them.

The DØ detector is shown in Figure 2.4. The tracking system consists of a Silicon Microstrip Tracker (SMT) and a Scintillating Central Fiber Tracker (CFT) enclosed within a 2 T superconducting solenoid magnet. The tracking system is surrounded by two scintillator based Central (CPS) and Forward (FPS) Preshower detectors to provide electron identification and to compensate for energy losses in the solenoid.

The calorimeter is made of four sampling Uranium-liquid Argon cryostats: a central cryostat covering the region $|\eta| < 1.2$, two forward cryostats extending the coverage to $|\eta| \sim 4$ and the Inter Cryostat Detector to cover the overlapping pseudorapidity region.

The muon system consists of a central and forward scintillating based tracking detector, a toroidal magnet and special shielding material surrounding the accelerator

beam pipe. The purpose of the shielding material is to reduce the presence of non-muon background particles originating from the beam halo and proton-antiproton fragments interacting with the beam pipe and the calorimeter.

The entire assembly of the detector is very large. It weights 5500 tons and measures $13\,m$ (height) $\times$ $11\,m$ (width) $\times$ $20\,m$ (length). It is supported by a platform mounted on rollers that allow to move the detector from the assembly area to the Collision Hall.

The next sections provide an overview of the different subsystems of the DØ detector. A much more complete treatment can be found in the different design reports and publications on the individual systems.

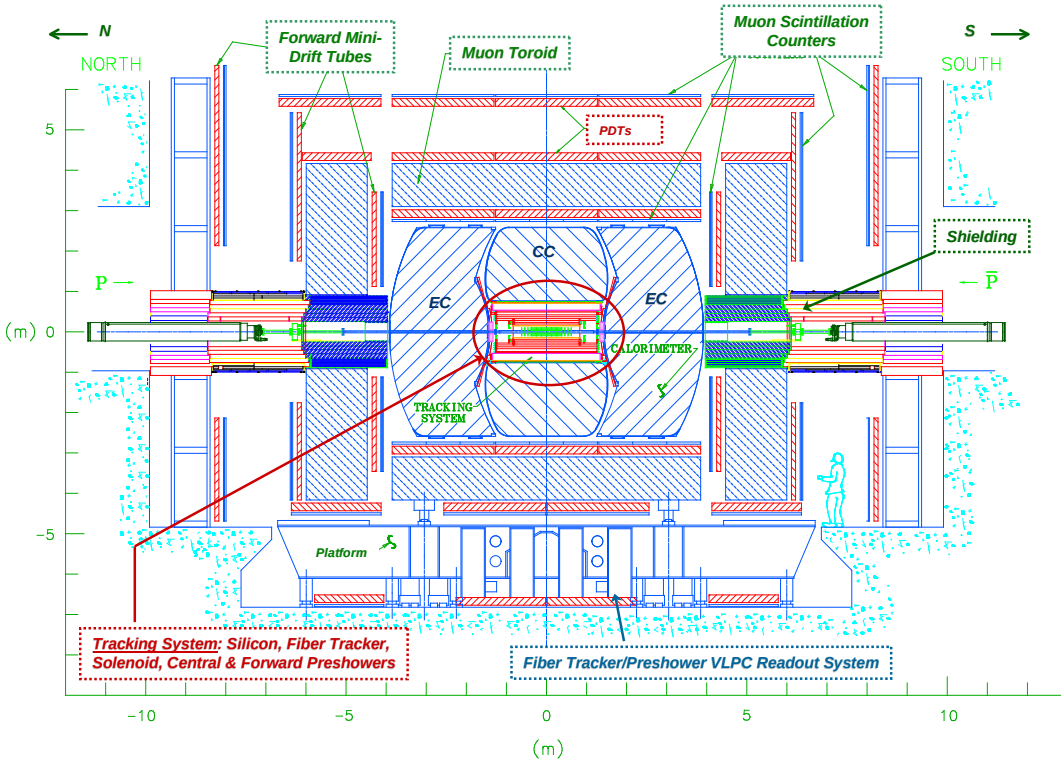

Figure 2.4: DØ detector layout.

2.2.1 Tracking System

The DØ tracker detector was designed to achieve several goals: momentum measurement and tracking over a large range in pseudorapidity ($|\eta| < 3$), electron identification, precise secondary vertex determination for identification of b-jets from top and B hadrons for B-physics, and fast tracking triggering. The tracking system, shown in Figure 2.5, is made of a silicon vertex detector and a scintillating fiber tracker surrounded by a 2T superconducting solenoid [15].

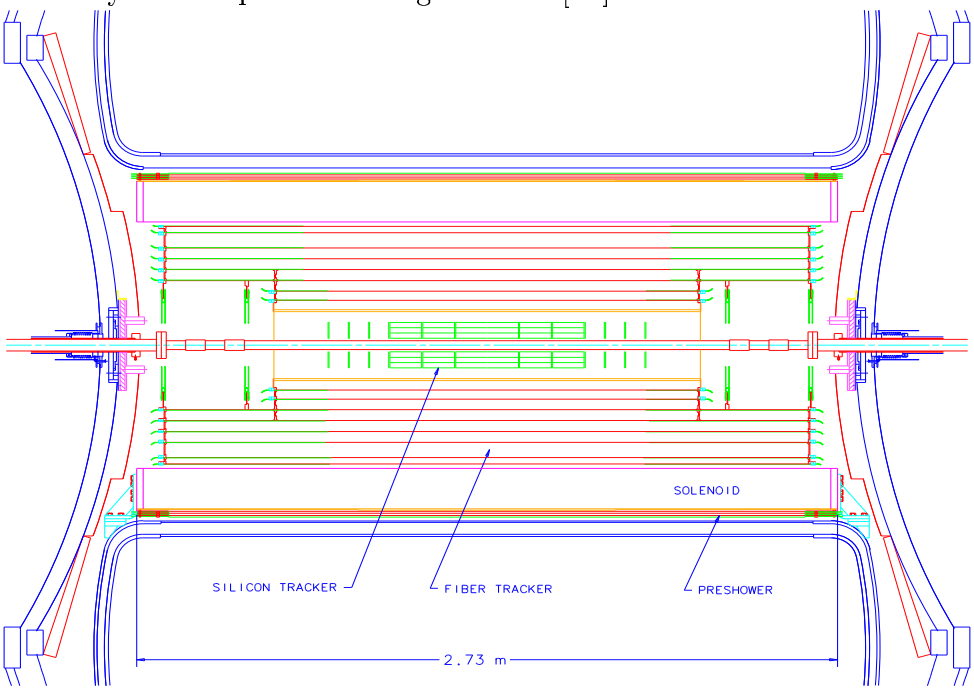

Figure 2.5: The DØ tracking system.

Silicon Microstrip Tracker

The Silicon Microstrip Tracker (SMT) [17] is the highest resolution tracking subsystem and is the first detector encountered by particles emerging from the collision. Since the collider interaction point is extended, with a $\sigma_z \sim 25\,cm$, the SMT consists of a hybrid system, with barrel detectors measuring primarily the $r - \phi$ coordinate,

and interspersed disk detectors providing $r-z$ as well as $r-\phi$ measurements. Thus, high η particles are reconstructed in three dimensions by the disks, and particles at small η are primarily identified by the barrels. Figure 2.6 shows the disk-barrel configuration of the SMT detector.

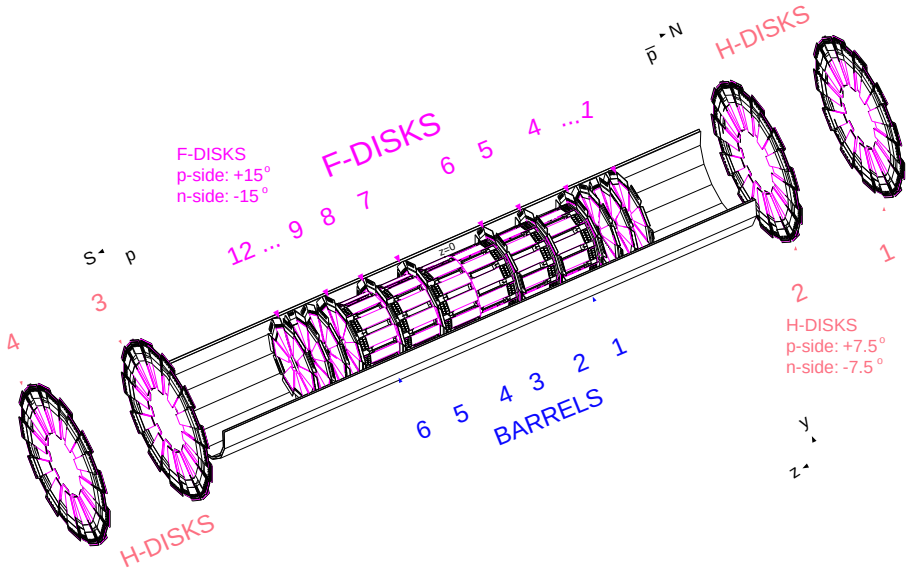

Figure 2.6: 3-D view of the SMT detector showing its barrel and disk structure.

Charged particles passing through a silicon sensor produce electron-hole pairs in the silicon bulk. In double sided detectors, holes are collected on the $p-side$ (axial) and electrons on the $n-side$ (stereo) layers. The energy deposited by the incident particle is proportional to its path in the silicon sensor.

The SMT detector is made of 6 barrel segments 12.4 cm long in z, consisting of 4 concentric layers of silicon ladder detectors each, 12 small diameter **F** disks, and 4 large diameter **H** disks. Together they provide a spacial resolution of approximately 10 μm in $r-\phi$ and 100 μm in $r-z$.

Layers 1 (innermost) and 3 consist of double-sided (axial and 90 deg stereo strips) detectors in the central four barrel segments and single-sided detectors (axial strips) in the outermost barrel segments. Layers 2 and 4 are double-sided detectors (axial

and 2 deg stereo strips). The layers extend radially from 2.7 cm to 9.4 cm and consist of 50 μm pitch silicon microstrips detectors, 300 μm thick. The election between 2 deg and 90 deg stereo strips resulted from a trade off between resolution and mechanical complexity. Monte Carlo studies [16] have shown that 90 deg stereo strips primary affects the $r - z$ resolution (improving it by a factor of 2), whereas the $r - \phi$ resolution is similar for both types of detectors.

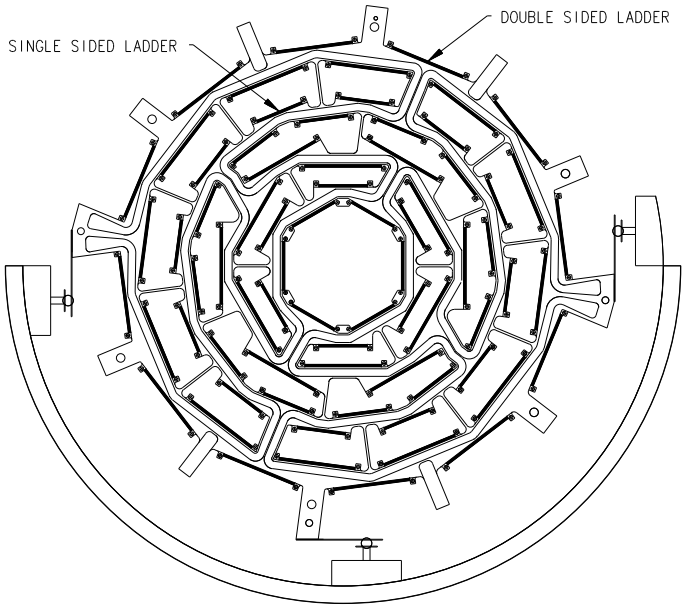

Figure 2.7: $x - y$ view of a silicon barrel.

Tracking in the forward region (up to $|\eta| < 3$) is performed with the F and H disks. F disks consist of double-sided (± 15 deg stereo strips) detectors consisting of overlapping $r-\phi$ wedges based on 62.5 μm pitch silicon microstrips. H disks are made of two back-to-back single-sided (± 7.5 deg stereo strips) detectors, at $|z| \sim 110\, cm$ and $|z| \sim 120\, cm$.

The individual number of channels for barrel layers 1,2,3 and 4 is roughly $46k$, $83k$, $92k$ and $166k$ respectively. It is $258k$ for F disks and $147k$ for H disks resulting in a total number of readout channels of $\sim 793k$

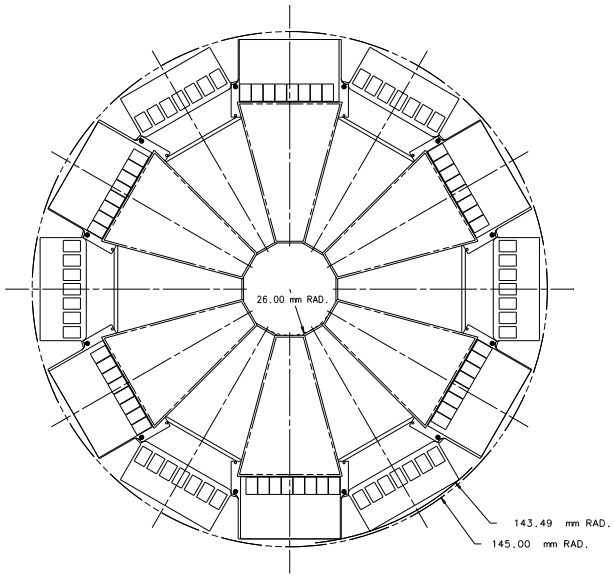

Figure 2.8: $x - y$ view of an F-disk.

Central Fiber Tracker

A scintillating fiber tracker (CFT) [18] surrounds the silicon vertex detector providing coverage in the central pseudorapidity region up to $|\eta| < 1.7$. With the SMT detector, the CFT enables track reconstruction and momentum measurement of all charged particles as well as fast "Level 1" triggering.

The detector, shown in Figure 2.9, consist of eight concentric carbon-fiber support cylinders extending radially from 19.5 cm to 51.5 cm. The two innermost cylinders are 1.7m long while the outer six are 2.5 m long in order to accommodate the silicon H disks at high η. Each Cylinder contains two ribbon layers of scintillating fiber doubles in a zu or zv configuration (z= axial fibers and u,v = ± 3 deg stereo fibers). Each doublet consist of two layers of 830 μm diameter fibers, offset by one half of the fiber spacing with respect to its partner. This configuration compensates for geometry gaps between adjacent fibers and improves the detection efficiency per doublet. Cosmic ray tests of CFT ribbons showed an spatial resolution per doublet of $\sim 100\,\mu m$ and detection efficiency per doublet $> 99\%$.

Fibers are composed of an inner polystyrene core surrounded by two acrylic

claddings with refraction indices of 1.49 and 1.42 respectively. The use of two claddings instead of one, increases the light trapped by the fiber. Each clading is 15 μm thick. The fiber scintillates in the yellow-green part of the visible spectrum, with a peak emission wavelength near $530nm$.

The about 77,000 CFT channels are grouped into ribbons of 256 fibers each. Eleven meter long clear multicad fiber waveguides transfers the scintillating light to Visible Light Photon Counter (VLPC) photodectors situated in cryostats on the DØ platform under the central calorimeter.

VLPCs are arsenic-doped silicon diodes with $\sim$ 70% single photon quantum efficiency at visible light wavelengths, gain of $\sim$ 40,000 electrons per converted photon and rate capability of at least 10 MHz. The level of noise is less than 0.1%. VLPCs photodectors operate with a bias voltage of $6.5-7.5\,V$ and at a temperature of $6.5-14\,K$ depending upon its version.

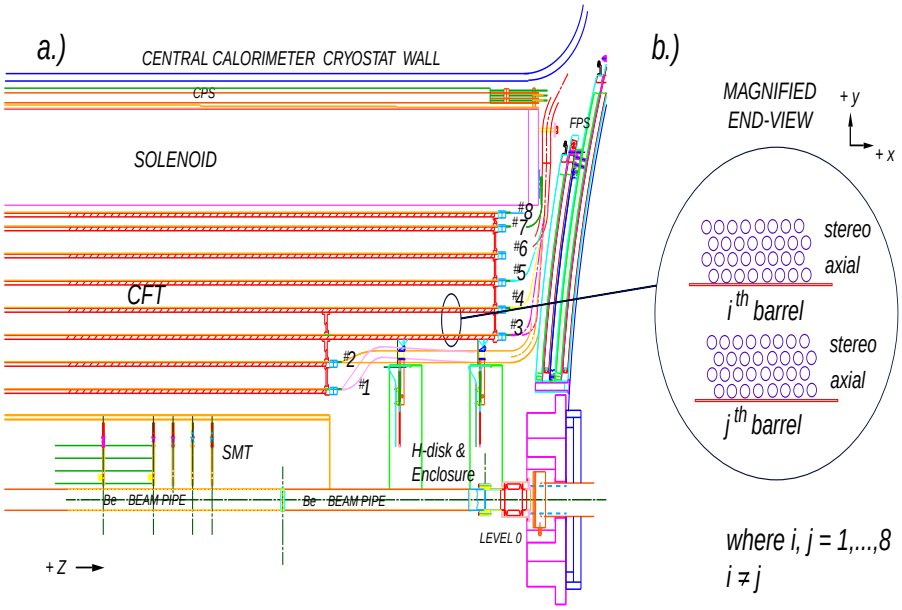

Figure 2.9: $r-z$ view of the DØ tracking system. The inset shows a detail of the two ribbon doublet layers per barrel.

Central Preshower System

The central preshower (CPS) [19], as Figure 2.10 shows, consist of a scintillator based cylindric detector placed in the $51\,mm$ gap between the solenoid and the central calorimeter at a radius of $72\,cm$, and covering the pseudorapidity region $|\eta| < 1.2$. The CPS functions as a calorimeter, participating in the early energy sampling of particles entering the central calorimeter, and as a tracker, providing precise position measurements added to the SMT and CFT detectors.

The detector is made of three concentric cylindrical layers of $\sim 6.1\,mm$ base triangular shape scintillating strips, with co-axially embedded $835\,\mu m$ diameter Wavelength Shifting (WLS) fibers read out by VLPC detectors. Wavelength shifting compounds absorb the primary scintillation light, emitting photons in the visible region of the spectrum. Strips in the innermost layer are axially oriented while the two outer layers are arranged in a $u - v$ stereo configuration with $\pm 22.5\,\text{deg}$ angles with respect to one another. An additional layer of lead radiator is located before the CPS detector. Thus, the solenoid and lead total 2 radiation lengths of material for all particle trajectories.

The triangular shape of the scintillator strips and its nesting allow to improve the position resolution when light-sharing information between adjacent strips is used. The cluster position can be determined by means of the charge-weighted mean of the strip centers. A detail of the triangular strip nesting can be seen in the inset of Figure 2.10 b).

Light from the scintillator WLS fibers is transported over $\sim 10\,m$ long clear light-guide fibers to the VLPCs readout system.

Forward Preshower System

The forward preshower detector (FPS) [20], shown in Figure 2.11, covers the pseudorapidity region $1.4 < |\eta| < 2.5$ and consists of two detectors mounted on the inner

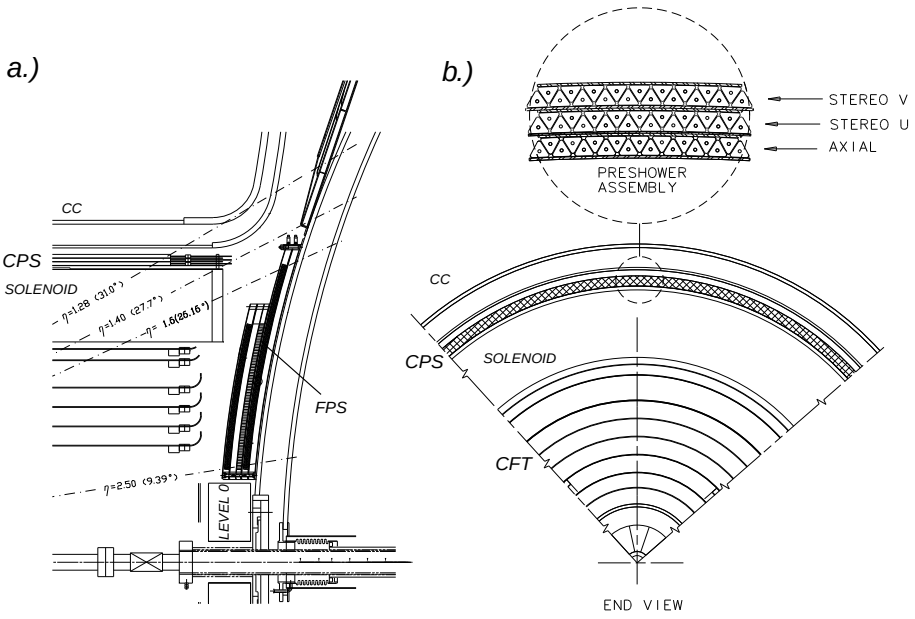

Figure 2.10: Central preshower detector in a) $r - z$ view, and b) $r - \phi$ view of the DØ tracking system.

face of each of the Endcap calorimeters. The detector is made of the same triangular scintillator strips and WLS fibers than the CPS detector.

The FPS consist of a lead absorber layer of 2 radiation length deep sandwiched between two scintillator planes consisting of $u - v$ sub-layers for charged particle tracking. The function of the lead absorber is to initiate showers of electrons and photons traversing it.

The innermost two layers are know as the *minimum ionizing particle* (MIP) layers whereas the outermost layers behind the lead are called shower layers. Since particles traversing the solenoid ($1.4 < |\eta| < 1.6$) are likely to shower before the FPS detector, the MIP layers in from of the lead absorber are not needed in this pseudorapidity region.

All charged particles traversing the detector will be detected in the MIP layers yielding a 3-dimensional space point. Electrons will shower in the lead absorber generating a collimated energy cluster in the shower layers. Charged pions and muons may not generate any type of shower, leaving a signature of two spacial

points in both the MIP and shower layers. Photons will only be detected in the shower layer due to the shower induced by the absorber, similar to that of the electrons.

Each of the four FPS layers is made of eight azimuthal wedges consisting of a $u - v$ configuration of scintillator fibers with 22.5 deg stereo angle with respect to one another. The strips in the stereo layers are oriented perpendicular to one of the edges of a wedge forming an angle of 78.75 deg with the vertical bisector of the wedge. Only the central 22.5 deg of each wedge consists of active scintillator volume. The remaining 11 deg on either side of the wedge is used for the mechanical support of the WLS fibers. Layers 1 and 3 are rotated 22.5 deg in ϕ with respect to layers 2 and 4 in order to cover the full azimuthal angle.

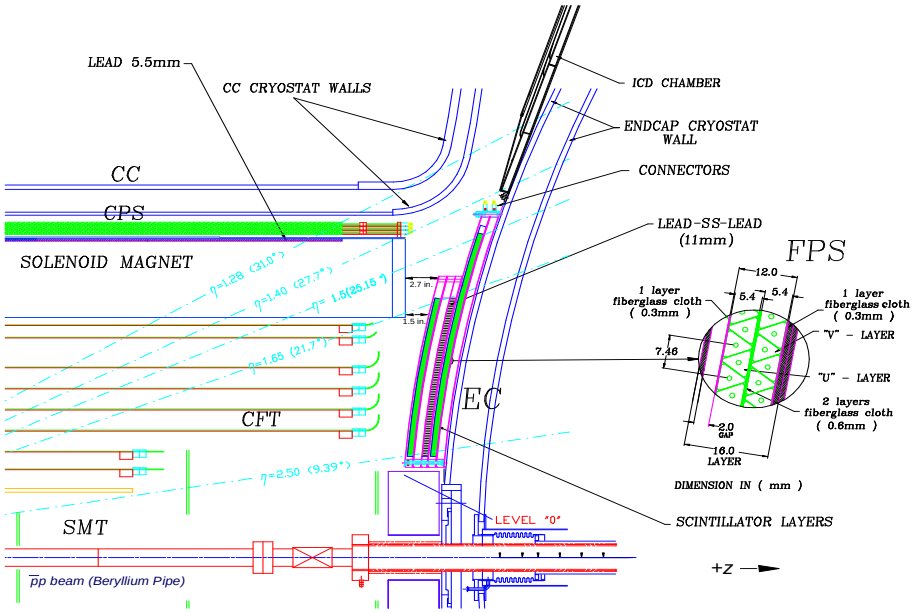

Figure 2.11: Forward preshower detector in an $r - z$ view. A detail of the triangular strip nesting is shown within the inset.

2.2.2 Calorimeter

The DØ calorimeter [21] is responsible for measuring the energy and direction of most particles that are incident to it. It is crucial for the identification of electrons, photons and jets as well as for inferring the presence of neutrinos and other non-interacting particles from the missing transverse momentum imbalance.

In a calorimeter, incident particles are made to interact with a large detector mass resulting in a shower of lower energy secondary particles. The energy of the secondary particles, which is proportional to the energy of the incident particle, is measured by their ionization loss within the calorimeter mass.

The interaction of electromagnetic particles (electrons and photons) with matter is very different than the interaction of hadronic particles. Electromagnetic particles interact with matter primarily by electron-positron photon conversion and Bremstrahlung mechanism [1]. As result of successive interactions of these two processes [2], and electromagnetic shower develops until the energy of all secondary particles reaches the level where ionization losses and atomic interactions become important. Since at high energies, the angle of emission of electrons and photons is small, the shower develops primary in the direction of the incident particle. Hadronic showers are produced from the inelastic collisions of hadrons with atomic nuclii or from multiparticle production of slow pions and kaons. Hadronic showers develop until ionization losses and nuclear absorption of secondary hadrons become dominant. Typical secondary hadron production occurs with a transverse momentum of $\sim 350\,MeV/c$. Hence, hadronic showers tend to be more spread out laterally than electromagnetic showers. The longitudinal development of electromagnetic (hadronic) showers scales with the radiation (interaction) length of the medium, X_0

[1] Emission of a photon due to the interaction between the Coulomb field surrounding a nucleus and a charged particle

[2] For instance, an incident electron losses energy by emitting a photon. The photon converts into an e^+e^- pair which in turn will lose energy by emitting photons

and λ_0 respectively. For uranium, $X_0 = 0.32\,cm$ and $\lambda_0 = 10.5\,cm$. Thus, hadronic showers are much larger than electromagnetic showers of similar energy.

The DØ Calorimeter is a highly segmented *sampling* calorimeter. In a sampling calorimeter, the shower development of incident particles is periodically sampled via the ionization of an active medium or the use of a scintillator. The sampling layers are interspersed with layers of an absorber material. Calorimeter segmentation in the transverse and longitudinal shower directions, allows to measure the shape of the shower development and determine the direction of the incident particles. The determination of the shower shape can also be used for the identification between different type of particles such as electrons, photons and hadrons.

The DØ Calorimeter uses liquid Argon (LAr) as active medium and uranium-238, stainless steel/copper plates as absorber materials. It consist of a Central Cryostat (CC) calorimeter covering the region $|\eta| < 1.2$, two Endcaps Cryostats (EC) extending the coverage to $|\eta| \sim 4$ and the Inter-Cryostat Detector (ICD) covering the overlapping region as shown in Figure 2.12. Each consist of an inner electromagnetic (EM) module, a fine hadronic (FH) module and a coarse hadronic (CH) module. Each module consist of alternating layers of absorber plates and signal boards filled with LAr as shown in Figure 2.13. The signal boards are made of a copper readout pad sandwiched by two $0.5\,mm$ thick G-10 insulator. The outer surfaces of the boards are coated with a highly resistive epoxy. An electric field is created by applying a positive high voltage of $2.0 - 2.5\,kV$ between the resistive surfaces of the signal boards and the grounded the absorber. Incident particles shower in the absorber plates, and the resulting particles ionize the LAr gap. The liberated electrons drift toward the signal boards inducing a signal on the copper pad. Signals from several boards in the same η and ϕ regions are grouped together in depth to form *readout cells*.

The calorimeter is transversely segmented into pseudo-projective towers in which

the cell boundaries are non-projective but their centers lie on lines which project back to the center of the detector as it is illustrated in Figure 2.14.

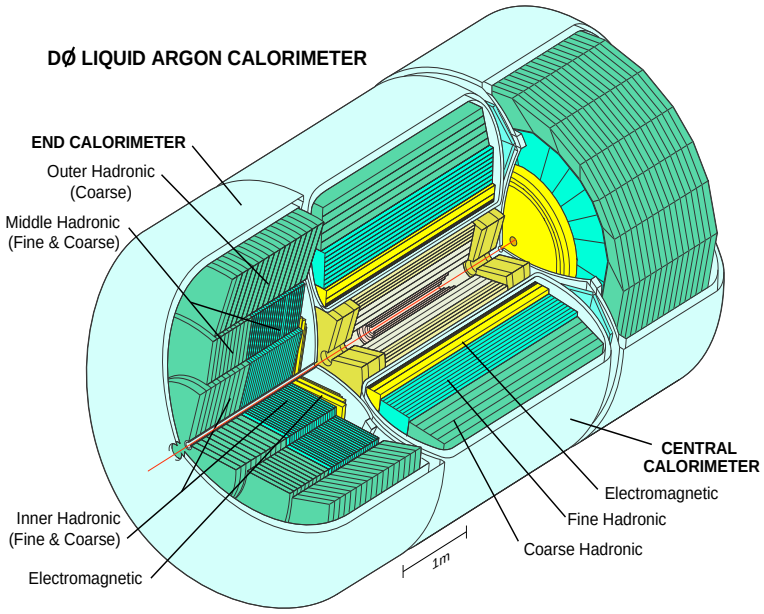

Figure 2.12: $3-D$ view of the DØ calorimeter.

Electromagnetic Calorimeter

The Electromagnetic calorimeter is 21 radiation length deep and it is arranged in four readout layers (EM1 through EM4). Each EM module is made of 21 (18) radial cells composed of $3(4)mm$ uranium absorber plates in the CC (EC) and $2.3\,mm$ LAr gap for a sampling rate fraction of 12.9%. In the Central cryostat, the transverse segmentation of the EM calorimeter in $\Delta\eta \times \Delta\phi$ is 0.1×0.1 in all layers except for the third, in which the maximum of electromagnetic showers is expected, which is segmented twice as finely into cells with $\Delta\eta \times \Delta\phi = 0.5 \times 0.5$. With this fine segmentation the azimuthal position resolution for electrons with energy above $50\,GeV$ is about $2.5\,mm$. In the Endcap cryostat, the segmentation is 0.1×0.1 except for $|\eta| > 3.2$, where the pad becomes too small and the segmentation is

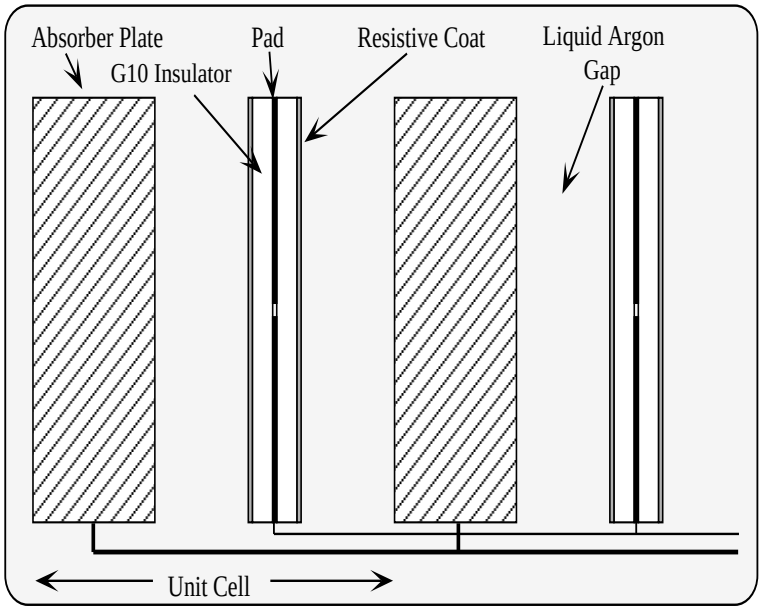

Figure 2.13: Structure of a calorimeter readout cell.

increased to 0.2×0.2.

Hadronic Calorimeters

The Hadronic calorimeter surrounds the EM calorimeter in both the ECs and CC cryostats and are $7-9$ interaction length deep. In the CC, it is composed of 16 fine hadronic (FH) modules and 16 coarse hadronic (CH) modules. The FH modules consist of 50 radial cells arranged in three readout layers (FH1 through FH3) with each cell made of $6\,mm$ uranium-niobium alloy absorber plates and $2.3\,mm$ LAr gap for a sampling fraction of 6.9%. The CH modules consist of 9 radial cells but only 1 readout layer. CH cells use $4.75\,cm$ copper absorber plates with $2.3\,mm$ LAr gap for a sampling fraction of 1.7%. The transverse segmentation of all hadronic modules is $\Delta\eta \times \Delta\phi \sim 0.1 \times 0.1$.

In the EC, the hadronic calorimeter is divided in three sections: the inner hadronic (IH), the middle hadronic (MH) and the outer hadronic (OH). Longitudinally, the IH is divided in four FH layers, each made of 16 cells, and one CH readout layer made from 13 cells, each using $4.65\,cm$ stainless steel absorber plates.

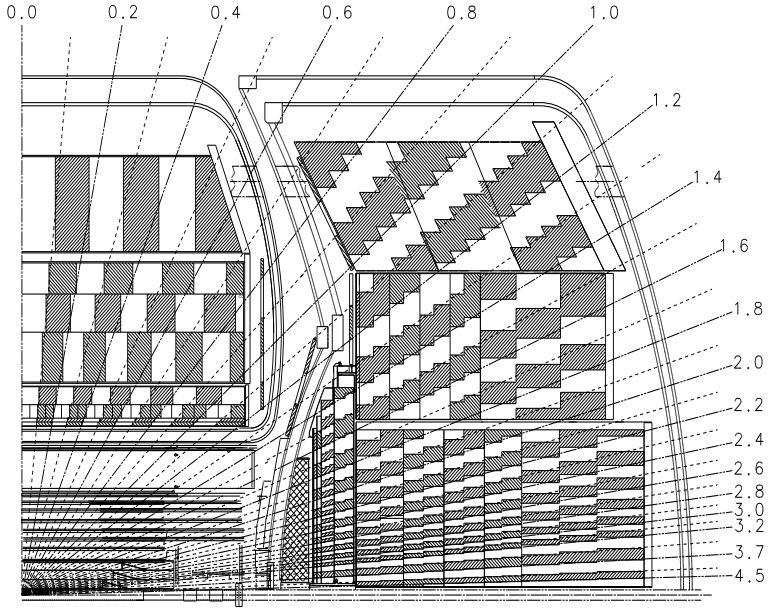

Figure 2.14: One quadrant view of the calorimeter detector projected in the $r-z$ plane. Radial lines illustrate the geometry of calorimeter towers. Each tower has size $\Delta\eta x\Delta\phi = 0.1x0.1$.

Surrounding the IH section, is the MH ring. This ring consist of 16 wedge shaped modules divided into four FH layers of 60 radial cells and a single readout layer consisting of 14 cells. The MH ring extends from an inner radius of $33\,cm$ to an outer radius of $152\,cm$ The OH ring surrounds the MH ring at an inner radius of $162\,cm$ and an outer radius of $226\,cm$. Each of its 16 coarse modules consist of 25 radial cells, read out in three layers.

Intercryostat Detectors and Massles Gaps

In the overlapping region between CC and EC cryostats, particles have to pass through several support structures before reaching the sampling calorimeter modules. To partially compensate for the energy loss in the support structures, two types of detectors were installed: Massles gap (MG) detectors and the Intercryostat detector (ICD). MG detectors are made of a sampling LAr layer covering the region $0.7 < |\eta| < 1.2$ with a typical segmentation of $\Delta\eta \times \Delta\phi \sim 0.1 \times 0.1$. The ICD consist

of two arrays of 384 scintillation counters mounted on the front surface of each EC cryostat.

Calorimeter Electronics

The signal from every calorimeter readout cell is brought to a feed-through port on a 30Ω coaxial cable. The signals are carried to preamplifiers which integrate the charged produced in the calorimeter cells producing proportional voltages. The impedance of the cables reading out the calorimeter cells has an impact on the rate at which the charge is extracted from the cells. Each readout channel looks like a capacitor with different capacitance depending on the calorimeter layers. This capacitance and the cable impedance form an integrating RC circuit that delays the transfer of the charge produced in the cell into the preamplifier. The 30Ω resistive cable reduces the delay time constant over the 115Ω cable cable used in Run I.

The preamplifier output consist of a step function with a rise time of $430\,ns$ (the drift time in the liquid argon gap) and a longer decay time constant of $15\,\mu s$. Therefore, over short time scales, the preamplifier is cumulative over successive bunch crossings. In order to extract the height of the voltage step due to a given bunch crossing, the preamplifier output is differentiated with a time constant of $250\,ns$. Thus, the output consist of a pulse of amplitude proportional to the integrated charge. The shaped output voltage is stored in an analog pipeline. The pipeline consist of an array of capacitors called the Switched Capacitor Array (SCA) and its function is to store analog information from calorimeter channels until a trigger decision is made. Signals from SCA are delivered to a Baseline subtructor (BLS) where signals before and after the bunch crossing are subtracted to remove slowly varying offsets in the input voltage. The baseline subtracted output is stored in an additional SCA pipeline awaiting the level-2 trigger decision. Following the level-2 accept, the sampled output is digitized by an ADC module. The DØ calorimeter

contains a total of 47,800 readout channels.

2.2.3 Muon System

Since muons do not initiate electromagnetic showers at Tevatron energies, they penetrate the calorimeter only depositing ionization energy. Therefore, muons are identified by matching CFT tracks with a separate muon tracking system outside the calorimeter detector.

The DØ muon detector [22] consists of four major parts as shown in Figure 2.15. A central Wide Angle MUon Spectrometer (WAMUS) detector covering $|\eta| < 1$, a Forward Angle MUon Spectrometer (FAMUS) covering $1 < |\eta| < 2$, a 1.8T toroidal iron magnet, and a shielding material. Both the central and forward muon detectors consist of three layers (normally called A,B,C) with the A-layer closer to the interaction region. The toroidal magnet separates the A-layer from the B and C-layers bending muon's trajectories in the $r - z$ plane.

The purpose of the shielding material is to block non-muon background particles from scattered proton and antiproton fragments which interact with the exist of the calorimeter or beam pipe and quadrupole magnets, as well as accelerator halo particles. Th shielding surrounds the accelerator beam pipe in the forward region behind the endcap cryostat wall.

The WAMUS detector is made of three layers of proportional drift tube (PDT) chambers, an inner layer of "A-ϕ" scintillation counters and an outer layer of cosmic ray scintillator detectors (Cosmic Cap). PDTs are filled with 80% Argon, 10%CF_4, and 10%CH_4 gas mixture, and are oriented along the field lines of the magnetic field. They consist of an anode sensor wire and a vernier pad used as cathode. Wires are separated 5 cm from each other. For each hit in the PDTs, the coordinate measurement is made combining the drift time perpendicular to the anode sensor wire, the difference time arrival of the hit at the two ends of the sensor wire, and

the charge deposition on the vernier pads. The "A-ϕ" scintillation counters are located between the central calorimeter and the WAMUS central A-layer PDT. Their purpose is to provide a ϕ measurement for matching with the central tracker detector for low and high p_T muon triggers and to reject out-of-time backgrounds originated at/near the exit of the calorimeter. The Cosmic Cap covers the top and sides of the central muon detector as well as part of the bottom. It is mounted outside the WAMUS C-layer PDTs. Their purpose is to provide a fast signal to identify cosmic rays and to assist in trigger and track matching with the CFT.

The forward muon system consist of three (A,B,C) planes of Iarocci mini-drift tube (MDT) chambers with (4,3,3) layers of tubes per plane as shown in Figure 2.16. Each plane consist of tubes oriented in a $r-\phi$ geometry, each having 8 cells. The individual cells have $9.4 \times 9.4\, mm^2$ internal cross section and have a $50\, \mu m$ tungsten-gold wire as anode. Each cell is filled with a gas mixture of $90\% CF_4$, and $10\% CH_4$. Three layers (A,B,C) of scintillation pixel counters, in a $r-\phi$ geometry, are mounted on the face of each MDT layer (see Figure 2.17). Pixel counters have a $\Delta\eta \times \Delta\phi = 0.12 \times 4.5\,\text{deg}$ segmentation for the outer nine rows of counters and $0.07 \times 4.5\,\text{deg}$ for the innermost two. They serve similar functions as the central 'A-ϕ" scintillation counters providing position measurements to be combined with the CFT/FPS detectors.

2.2.4 Luminosity Monitor

The primary goal of the luminosity monitor (LM) [23] is the determination of the DØ luminosity by detecting beam crossings containing non-difractive inelastic collisions. Secondary goals include the identification of multiple interactions and to provide diagnostic information regarding accelerator performance such as beam halo rates and measurement of the beam optics.

The DØ luminosity monitor consist of two hodoscopes located symmetrically

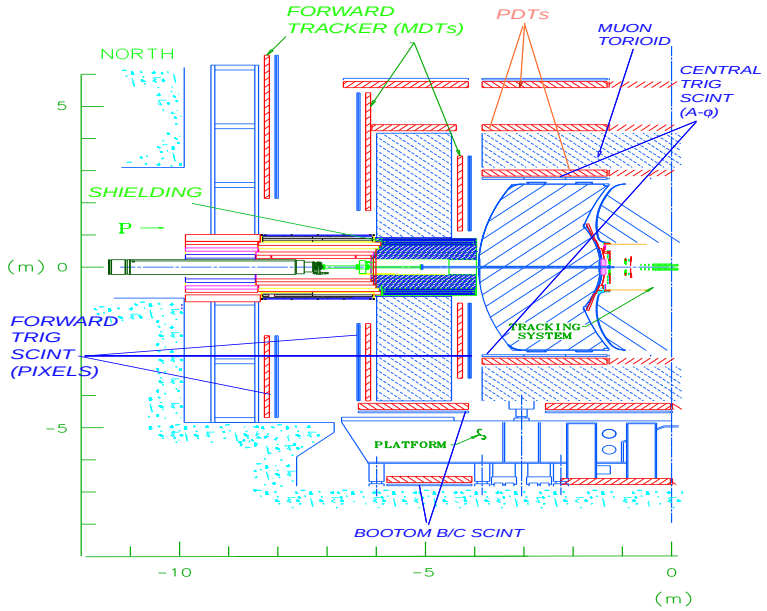

Figure 2.15: $r - z$ view of the DØ muon detector.

about the beam pipe and mounted on the face of the Endcap calorimeters. Each hodoscope is made of 24 identical 1.58 cm thick scintillator wedges with 27.9 cm diameter fine-mesh photomultiplier tubes mounted directly on the face of each scintillator wedge as shown in Figure 2.18. This unconventional placement of the photomultiplier tubes is necessary to align the photomultiplier axis with the magnetic field. The LM covers the region $2.7 < |\eta| < 4.5$ providing an acceptance of 0.980 ± 0.011 for all non-difractive inelastic collisions.

The LM measures the time difference between charged particles hitting the north and south detectors to determine the z coordinate of the interaction vertex and the instantaneous luminosity. The vertex position can be obtained with a resolution of $\sim 6\,cm$ and is calculated according to

$$z_{vtx} = \frac{1}{2}c(t_{-z} - t_{+z}) \tag{2.1}$$

The instantaneous luminosity is determined by counting beam crossings where $|z_{vtx}| < 100\,cm$ and applying multiple interaction corrections.

Proton and antiproton beam halo rates are obtained by counting crossings where

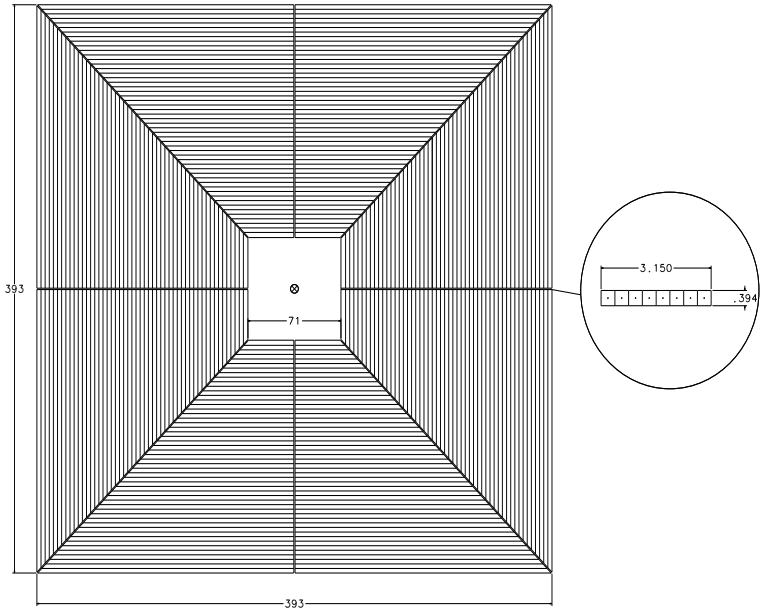

Figure 2.16: Forward muon mini-drift tube chambers.

$|z_{vtx}| \sim 140\,cm$, corresponding to a time difference for a particle to travel from one end of the detector to another.

Multiple interaction corrections are performed from the standard deviation of the time measurements in the two detectors.

The electronics of the LM provides two output paths: FASTZ and SLOWZ. The FASTZ path consist of the difference between the analog sum of the time signals at each of the two detectors. In the SLOWZ path, analog signals are digitized and calibrated to form the quantities N_{hit}, $\sum t_i$, $\sum t_i^2$, t_{min} and t_{max}. The L0VTX boards use these quantities to calculate the average and standard deviation of the times between each end of the detectors providing the SLOWZ vertex position and a multiple interaction flag.

2.3 The DØ Trigger System

Due to the very high rate of $4.7\,MHz$ $p\overline{p}$ collisions, it is not possible to record an analyze every event from every crossing at the DØ detector. The trigger system [24]

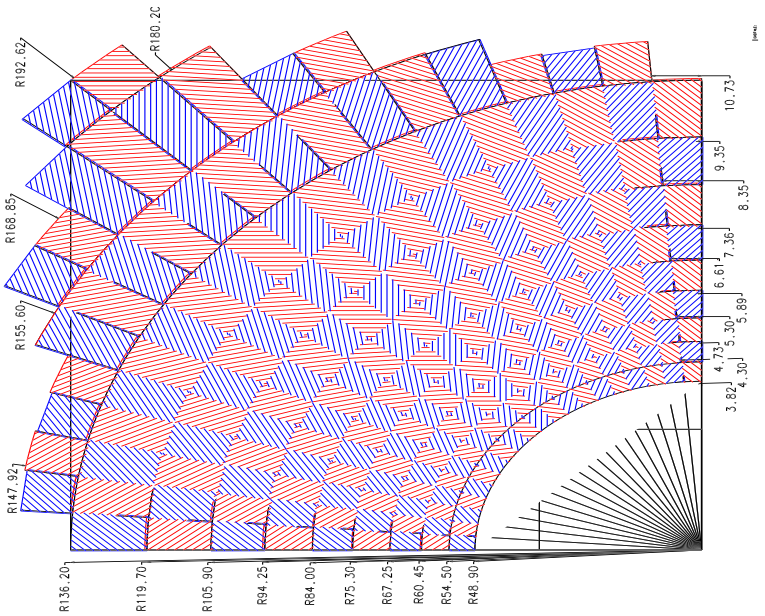

Figure 2.17: One quadrant $r-\phi$ view of the forward muon scintillation pixel counters.

allows to select only a small fraction of interesting events by means of series of hardware and software fast filters which partially reconstruct events and search for particular physics signals of interest. The trigger framework consist of three level of selection stages: Level 1 (L1), Level 2 (L2), and Level 3 (L3). The LM detector provides an initial Level 0 (L0) trigger detecting non-difractive inelastic collisions. The L1 consist of a hardware trigger based on simple algorithms implemented in Field Programmable Gate Arrays (FPGAs). L1 output rate is in the range $5 - 10\,kHz$. The L2 is a second hardware trigger which refines and combines the L1 outputs, accepting events with a rate of $1\,kHz$. L3 trigger is based on complex software algorithms running on a set of high performance commercial processors with an output rate of $50\,Hz$.

2.3.1 Level 1 Trigger

The L1 trigger decision is made based on the information from the calorimeter, the CFT, CPS, FPS and muon scintillation counters subsystems. The calorimeter, fiber

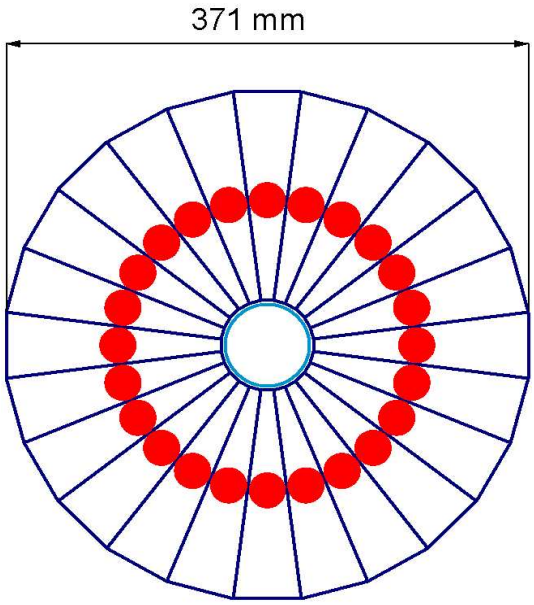

Figure 2.18: Luminosity wedge counters.

tracker and preshower detectors provide electron triggering for $|\eta| < 2.5$. The CFT and muon systems cover the region $|\eta| < 2.0$

Each L1 trigger subsystem process data from each subdetector and evaluates, for every beam crossing, a list of several trigger terms. Each trigger term indicates is a certain condition was satisfied in a particular subdetector. For instance: a hit pattern consistent with track momentum above a threshold, or a calorimeter trigger tower with transverse energy above a preset threshold.

For every beam crossing, the trigger system evaluates 128 trigger terms. If a specific L1 term has been satisfied, a "L1 accept" signal is issued and the event is digitized and pipelined to 16 event buffers for temporary storage awaiting for a L2 trigger decision.

2.3.2 Level 2 Trigger

The L2 trigger consist of two stages: a preprocessor stage and a global processor. In the first stage, each subsystem provides a list of candidate objects from that specific

detector such as electrons, muons, jets and tracks. In the second stage, the global processor combines the information from the various detector subsystems considering correlations between different objects. Examples of such correlations include matching between the calorimeter or the preshower and the tracker, estimation of dilepton and dijet masses, etc.

The L2 trigger provides a factor of 10 rejection, making the trigger decision at an accept rate of $1\,kHz$.

2.3.3 Level 3 Trigger

The L3 trigger is a software system running in a farm of parallel commercial processors. Each processor runs event filter algorithms that allow to the reconstruction of physics objects such us electrons and jet candidates and their relations, such us event topologies and transverse mass distributions.

The L3 system provides a trigger decision with an accept rate of $50\,Hz$. The selected events are stored on a robotic tape unit accessible for offline event reconstruction.

Chapter 3

Event Reconstruction and Particle Identification

The events recorded by the DØ detectors consist of digital signals from calorimeter cells, silicon detectors, drift tube times from the muon systems, etc. This chapter describes the high level algorithms used to transform the raw data into physics objects used for analysis such us jets, neutrinos, electrons, muons, and tracks. This task is performed by a extremely complex C++ program called *d0reco* [25].

3.1 Track Reconstruction

The trajectory of charged particles (tracks) are reconstructed from the energy they deposit in successive layers of the silicon and fiber tracker detectors.

Track reconstruction is performed with the GTR [26] algorithm which consist of a road-based finding algorithm and a Kalman Filter and Smoother fitter.

The observed signals in the detectors are called clusters. Signals from two or more nearby tracks may not be separable and be merged into a single cluster. Clusters consist of a position measurement and error and are the input to the tracking

algorithm.

The reconstruction of particle tracks consists of two related steps: track finding and fitting. The goal of track finding is to identify list of clusters corresponding to single particle trajectories. Track fitting consists of determining the kinematic track parameters based on the cluster measurements.

The GTR algorithm is divided an several components:

- Surfaces

  The detector is described as a collection of layers made of bounded surfaces. The Fiber tracker detector is described with cylindrical surfaces, and the SMT with $x - y$ and z planes. Each cluster is associated with a surface in a layer.

- Tracks

  A track is described by a list of clusters and a kinematic fit. Each track consists of a surface, a set of parameters at that surface, and an error matrix for those parameters. There are five parameters: two characterize the position on the surface, two describe the direction and one specifies the momentum.

- Paths

  A path is an ordered list of surfaces crossed by a track. Paths are used during track finding by searching for tracks which are only consistent with specified path maps. Other path-specific track properties, such as the number of missed surfaces are used to reject bad tracks.

- Propagators

  Propagators are used for track fitting. They propagate the track parameters and their errors from one surface to another. They account for material interactions (multiple scattering, dE/dx) and the magnetic field.

- Fitters

  Track fitting is done with a Kalman Filter algorithm. The mathematics beyond this technique will be explained in detail in Chapter 4. Here we only provide a brief description.

  Given the track parameters and errors at a given surface, the Kalman Filter allows to *add* the information from a cluster to generate a new set of track parameters and its error matrix. This procedure is done in two steps: in the first step (prediction) the Kalman Filter estimates the track parameters at the next surface by the use of a propagator. In the second step (update) the actual cluster measurement is combined with the predicted parameters and a new improved estimate is made. The process is repeated from the cluster in the inter-most surface to the cluster in the outermost layer.

- Filters

  Once paths have been selected, the procedure for adding clusters is straightforward. However, when the track density is high, it is necessary to identify and reject ghost tracks early in the track finding process. Tracks can be rejected if the fit χ^2 is too large, they have too many missed surfaces, they fall outside the kinematic range of interest, their fit is inconsistent with their paths, etc. It is also possible to reject tracks which share some specified number of clusters.

The GTR track reconstruction algorithm is based on four different paths, each covering a different the angular region. The central region is covered by the SMT and all layers of the CFT. In the overlap region, a particle can cross at least five fiber layers. The gap region has coverage by less than five fiber layers and the forward region includes additional coverage from the silicon H-disks detectors.

The next sections, describe briefly the track finding algorithm in the different regions.

3.1.1 Track Finding in the Central Region

Track reconstruction in the central region consist of three steps:

- Axial fiber tracking: A track is built in the $\phi - r$ plane from axial fiber clusters only. Such a track will have three parameters and so, only three measurements are required to measure these track parameters and associated errors. Seed tracks are made from combinations of clusters in these layers with the requirement that the track transverse momentum is greater than $0.5\,GeV/c$.

  A propagator is then used to extrapolate the seed tracks through the remaining five axial layers, and filters remove duplicate tracks.

- Stereo fiber tracking:

  Two additional clusters are required to measure the five track parameters. These measurements are required to come from clusters in the outer two stereo fiber layers.The track finding proceeds as before, with propagators and fitters used to build and reject bad tracks.

- Silicon extension:

  The last step of the track finding algorithm consist of adding clusters in the silicon detector to the already found tracks. At least four silicon clusters are required to be picked up by tracks.

3.1.2 Track Finding in the Overlap Region

In the overlap region, clusters from axial and stereo fibers in each layer are combined to speed up the process. The combined clusters are required to have a z position consistent with a track which exited the edge of the CFT. Tracks can begin in the fifth, sixth of seventh layers of the CFT, but are not allowed to miss any of the other layers.

3.1.3 Track Finding in the Gap and Forward Region

Since in these regions there is partial or no CFT information, track finding begins in the silicon barrels and F-Disks. Track finding begins in the outer layer of the barrels and works inward. In the forward region, candidate tracks are extended to the H-Disks where more clusters can be added.

3.1.4 Track parameters

The output of the GTR algorithm is a list of reconstructed track helices parametrized at the distance of closest approach to the origin (DCA). Each track is described by the following parameters:

- $h_0 = dca$ distance of closest approach, $(-\infty, +\infty)$
- $h_1 = zca$ z at DCA, $(-\infty, +\infty)$
- $h_2 = \phi$ azimuthal angle at DCA, $(-\pi, +\pi)$
- $h_3 = \tan\lambda$ dip angle, $(-\infty, +\infty)$
- $h_4 = e/p_T$ curvature, $(-2, 2)$

where e is the charge of the electron ($(-1, 1)$) and p_T is the transverse momentum of the particle ($p_T = p\sin\theta$) in GeV/c. ϕ is the angle between the transverse momentum at DCA and the x-axis. $\tan\lambda$ measures the slope of the helix. $\lambda + \theta = \pi/2$, and $\theta = arccos(dz/ds)$, where s is the path length along the helix, increasing when moving in the particle direction. dca is the distance of closest approach of the track to the z axis. The sign of dca is given by the vector product $(\vec{dca} x p_T)$, where $\vec{dca}$ is the the point of closest approach. Figure 3.1 shows an illustration of the track parameters in the transverse plane.

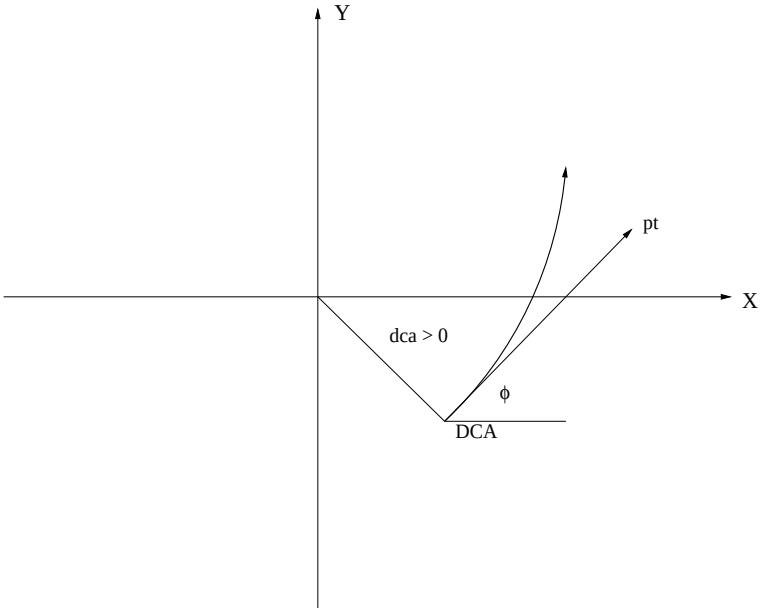

Figure 3.1: Track parameter defintions at the DCA.

3.2 Jet Reconstruction

Jets are reconstructed using the *improved legacy cone algorithm* [27] designed following the recommendations of the Run2 QCD workshop.

The jet reconstruction starts by clustering energy depositions in the calorimeter into towers seeds. Only towers with positive energy are considered as seeds. Starting from a $E_T > 0.5\,MeV/c$ ordered list of seed towers, jets are created by adding all towers within $R = \sqrt{\Delta^2\eta + \Delta^2\phi} < 0.5$ around the seed direction. The η and ϕ definition of the jets and their transverse energy are given by:

$$\eta = \frac{\sum_i E_T^i \eta^i}{\sum_i E_T^i} \tag{3.1}$$

$$\phi = \frac{\sum_i E_T^i \phi^i}{\sum_i E_T^i} \tag{3.2}$$

$$E_T = \sum_i E_T^i = \sum_i E_i \sin\theta_i \tag{3.3}$$

where the index i denotes the $i-th$ tower in the jet. If the new centroid is still within the seed tower, the calculation of the kinematic variables of the jet is re-iterated until

the centroid either falls outside the boundary of the original seed tower, or stabilizes within $R < 0.001$.

This process is repeated with the remained seed towers until all stable cone jets around seeds are found.

Next, the jet algorithm attempts to find stable cones around mid-points between previously found jets. Mid-points are defined as the vector sum of the momentum of pair of jets. Only mid-points within $\Delta R < 2R_{cone}$ are considered. The inclusion of mid-point jets removes the sensitivity of the cone jet algorithms to soft radiation.

This procedure produce a list of jets which may share energy. Ambiguities in the association of towers to jets is resolved with the following split and merge algorithm: If the shared energy between two jets is higher than half of the energy of the lowest E_T jet, both jets are merged. Otherwise, each of the shared towers is assigned to the closest jet. The final jets are required to have at least $8\,GeV/c$.

The following quality selection cuts are required to the reconstructed jets:

- In order to remove isolated electromagnetic particles, the fraction of energy deposited in the electromagnetic section of the calorimeter (EMF) is required to be between 0.05 and 0.95.

- To remove jets which predominantly deposit their energy in the coarse hadronic section of the calorimeter due to a higher detector noise, the fraction of energy deposited in this section of the calorimeter is required to be smaller than 0.4.

- To remove jets clustered from hot cells (noisy cells), the ratio of the highest to the next-to-highest transverse energy cell is required to be smaller than 10.

- Jets made from a single hot tower are removed by requiring the number of towers containing 90% of the jet energy to be greater than 1.

3.3 Missing Energy

The presence of neutrinos is inferred from the imbalance momentum measured in the calorimeter detector. Since events are produced by interaction of a parton from the proton and a parton from the antiproton, the longitudinal z component of the momentum is not known and it is not possible to constrain the p_Z. We use conservation of transverse momentum and energy to calculate the imbalance in E_T. We call this imbalance the $\not\!\!E_T$ and it is defined to be:

$$\not\!\!E_X = -\sum_k E_x^k \tag{3.4}$$

$$\not\!\!E_Y = -\sum_k E_y^k \tag{3.5}$$

$$\vec{\not\!\!E}_T = \not\!\!E_X \hat{x} + \not\!\!E_Y \hat{y} \tag{3.6}$$

where the sums are over all cells in the calorimeter and $\not\!\!E_X$ and $\not\!\!E_Y$ are the x and y components of $\vec{\not\!\!E}_T$, respectively. Only calorimeter cells with transverse energy greater than $100\,MeV$ are considered. Cells belonging to the coarse hadronic section of the calorimeter are treated differently due to high level of noise.Only coarse hadronic cells clustered within jets are accounted in the $\not\!\!E_T$ calculation.

3.4 Electron Identification

Electrons are identified by small isolated clusters of energy in the electromagnetic (EM) layers of the calorimeter with an associated matched track pointing back to the interaction vertex. Details of the algorithm can be found in [28].

3.4.1 Electromagnetic Cluster Reconstruction

EM candidates are identified by clustering electromagnetic towers in a cone of radius $R = \sqrt{\Delta^2\eta + \Delta^2\phi} = 0.2$ around initial tower seeds. The clusters are expected

to have large EM fraction $f_{EM} = E_{EM}/E_{tot}$ (where E_{EM} is the cluster energy in the electromagnetic calorimeter, and E_{tot} is the total energy in the cone), and its longitudinal and transverse shower shape to be compatible with those of an electron. Each cluster defines a χ^2 based on the comparison of the energy deposited at each EM layer and the expected energy deposited by an electron shower obtained from the simulation.

Electron candidates are selected based on its EM fraction, χ^2 and isolation:

$$f_{EM} > 0.9 \tag{3.7}$$

$$\chi^2 < 20 \tag{3.8}$$

$$f_{ISO} = \frac{E_{EM}(R < 0.4) - E_{EM}(R < 0.2)}{E_{EM}(R < 0.2)} < 0.15 \tag{3.9}$$

The EM cluster reconstruction efficiency was measured on an unbiased sample of electrons from Z decays where one is used for tagging purposes and the other to evaluate the efficiency. The fraction of electrons satisfying these cuts is [29] $\epsilon = (88.1 \pm 0.7 \text{ stat } \pm 0.7 \text{ syst })\%$.

3.4.2 Electron Reconstruction

Since photon and electron showers are very similar, a track is required to be associated with the cluster.

An EM cluster is associated to a track if the matching χ^2 probability is greater than 1%. The χ^2 in the CC, and EC regions is defined as

$$\chi^2 = \left(\frac{\delta\phi}{\sigma_\phi}\right)^2 + \left(\frac{\delta z}{\sigma_z}\right)^2 + \left(\frac{E_T/p_T - 1}{\sigma E/p}\right)^2 \qquad CC. \tag{3.10}$$

$$\chi^2 = \left(\frac{\delta\phi}{\sigma_\phi}\right)^2 + \left(\frac{\delta r}{\sigma_r}\right)^2 EC. \tag{3.11}$$

where

- $\delta\phi$ is the difference between ϕ of the track impact at the EM3 floor and ϕ of the cluster position.

- δz (δr) denotes the difference between z (r) of the track impact at the CC (EC) EM3 floor and z (r) of the cluster position.

- E_T/p_T is the ratio of the measured transverse energy of the cluster to the measured p_T of the track.

- σ_ϕ, σ_z, σ_r, and $\sigma_{E/P}$ are the root-mean-square (RMS) of the measured distributions of the associated quantities (ϕ, z, r and E_T/p_T).

The track matching efficiency, measured in Z events, is $\epsilon = 0.745 \pm 0.010$ stat.

3.5 Muon Identification

Muon reconstruction consists of three main steps. First, the time measured at the readout channels is transformed into positions and times of hits in scintillators and wires. Second, straight lines (segments) are reconstructed from scintillator and wire hits in each layer of the local muon system. Finally, segments reconstructed in the A-layer are fitted with segments in the B and C layers to measure the muon momentum. A detailed description of muon reconstruction can be found in [30] and [31].

Muons are selected according to the following requirements:

- At least 1 wire hit in the A segment.

- At least 1 scintillator hit in the A segment.

- At least 2 wire hits in the BC segment.

- At least 1 scintillator hit in the BC segment.

A veto on cosmic muons is applied by requiring the time difference between scintillator hits in B or C layers and the A layer to be consistent with a muon coming from the interaction region. The muon tracks are extrapolated to the point of closest approach (PCA) to the primary vertex and their parameters are compared with those of central tracks at PCA. For all central tracks within 1 radian in azimuthal and polar angle of a muon track at PCA a global fit is performed.

The muon reconstruction efficiency is measured in the data using the calorimeter detector, as its fine segmentation allows to identify muons by the signature of a minimally ionizing particle. Using $Z \rightarrow \mu\mu$ events, the reconstruction efficiency in the data was measured to be [29] $82.9 \pm 1.4\%$ and the muon-track matching efficieny is $76.8 \pm 0.2\%$.

Chapter 4

Vertex Reconstruction

This Chapter describes the development of algorithms for the reconstruction of primary and secondary vertices using the tracking information from the SMT and CFT sub-detectors. Vertex reconstruction consists of two main steps: vertex finding and fitting. Vertex fitting involves the estimation of the position and the momentum vectors of a set of tracks emanating from a unique interaction point. Vertex finding corresponds to the identification of sets of tracks belonging to a same decay vertex.

In the past, the most common method for vertex fitting has been the method of Least Squares. In this method, all candidate tracks are fitted *globally* in a single step, requiring the inversion of large matrices with dimension proportional to the number of tracks. In addition, this formalism is not flexible for adding or removing tracks from different vertex hypothesis.

The Kalman filter is a *local* recursive Least Squares algorithm that allows to incorporate the information of different particle trajectories about the vertex consecutively. The dimension of matrices to invert is proportional to the number of parameters to estimate. The Kalman Filter algorithm was originally developed to estimate the state of (linear) dynamic systems and has been applied to different areas such as tracking of ballistic missiles, satellite positioning and image recognition

among others. In High Energy Physics, the Kalman filter technique is applied for tracking and vertex fitting.

At $\mathcal{L} \sim 10^{32}\, cm^{-2} sec^{-1}$ an average of 2.5 additional minimum bias interactions per crossing is expected. Thus, at the Tevatron Collider, the vertex reconstruction procedure is involved because the algorithms must be able to deal not only with the hard scatter primary vertex, but also with additional minimum bias interactions and displaced secondary vertices produced in the decay of long-lived particles.

As part of this Thesis, I have analyzed the different vertex algorithms, written and implemented the Kalman Filter code within the DØ suite of reconstruction programs, and studied and optimized its performance with different MC and data samples. This chapter summarizes this work and is organized as follows: We briefly described the most common vertex fitting method and its disavantages in Section 4.1. Section 4.2 describes the general Kalman Filter formalism. Section 4.3 discusses the application of the Kalman filter technique to vertex fitting. Sections 4.4 and 4.5 describe the primary vertex finding algorithm and the identification of the hard scatter vertex from additional minimum bias interactions. Section 4.6 discusses algorithms for secondary vertex reconstruction.

4.1 The Least Squares Formalism

In the Least Squares formalism, the coordinates of the vertex are determined by minimizing the impact parameter (or distance of closest approach) of tracks with respect to the vertex. This technique is also known as the *Impact Parameter Algorithm.*

In the transverse plane, the distance of closest approach of a track a to a vertex V, can be written as:

$$\epsilon_a^d = |\eta_a - (\vec{E}_a \cdot \vec{V})| \tag{4.1}$$

where (see Figure 4.1) $\vec{V}$ is the vector from the origin to the vertex, $\vec{E}_a$ is the unit vector from the point of closest approach, $\vec{P}_a$, to the vertex, and η_a is the projection of $\vec{P}_a$ onto $\vec{E}_a$ ($\eta_a = \vec{P}_a \cdot \vec{E}_a$).

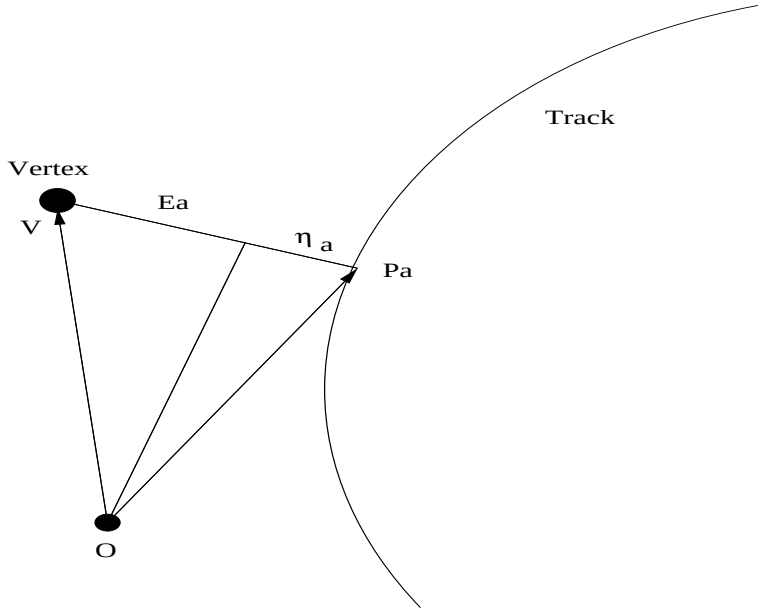

Figure 4.1: Transverse impact parameter definition.

In the longitudinal plane, the impact parameter ϵ_a^z is defined, in the linear track approximation, as:

$$\epsilon_a^z = |z_a - V_z + \cot\theta\,(\vec{u}_a \cdot \vec{V})| \tag{4.2}$$

where $\vec{u}_a$ is a unit vector in the transverse track direction, $\vec{u}_a = (\sin\phi_p, \cos\phi_p, 0)$, ϕ_p is the azimuth of the track at $\vec{P}_a$, θ is the polar angle of the track, and z_a is the projection along z of the vector from the origin to the point of closest approach of the track to the origin in the transverse plane.

The reason not to define a $3D$-impact parameter, but to work with separte $R\phi$ and z impact parameters, is due to the fact that the SMT resolution is significantly different in the transverse and longitudinal planes. Thus, in case of a poor z information for a given track, only the $R\phi$ information will be used.

The vertex position is obtained by minimizing the χ^2 function:

$$\chi^2(V_i) = \sum_a \frac{(\epsilon_a^d)^2}{(\sigma_a^d)^2} + \sum_a \frac{(\epsilon_a^z)^2}{(\sigma_a^z)^2} \tag{4.3}$$

where σ_a^d and σ_a^z are the uncertanties in the transverse and logitudinal impact parameters and the sums are taken over all the tracks used in the fit. The value of the χ^2 function can be calculated analytically as

$$\chi^2(V_i) = A - 2B_i + C_{ij}V_iV_j \tag{4.4}$$

The elements A, B_i and C_{ij} are defined in [32]. The values V_i which minimize the χ^2 can be obtained by:

$$V_i = (C^{-1})_{ij}B_j \tag{4.5}$$

Among the disavantages of this technique are the fact that it does not use the full tracking information, it is not flexible in adding or removing tracks from a vertex hyphothesis, and it does not constrain the track momenta to go through the final fitted position.

4.2 The Kalman Filter Formalism

The Kalman Filter allows to use the full track information, not only the impact parameter information, for the estimation of the vertex position. In addition, track momenta are re-computed with the constraint that the trajectories go through the fitted vertex position.

The Kalman Filter is the optimal recursive estimator of the state of a linear dynamic system. We consider that at time instant k, a dynamic system is described by a $n \times 1$ state vector x_k. The state vector normally cannot be observed directly. The quantities measured from the system are linear functions of the state vector described by the measurement equation

$$m_k = H_k x_k + \epsilon_k \tag{4.6}$$

where H_k is an $l \times n$ *measurement* matrix, the $l \times 1$ vector ϵ_k represents the measurement error, and m_K is an $n \times 1$ vector describing the measurement vector.

The evolution of the state vector with time is modeled as a Gauss-Markov process described by the system equation

$$x_k = F_{k-1}x_{k-1} + \omega_{k-1} \tag{4.7}$$

where F is a $n \times n$ *transition* matrix that relates the state vector at time k to the time $k-1$. It contains all the information about the dynamics of the system. The $n \times 1$ ω_{k-1} vector is called *process noise* and represents a random disturbance of the system between $k-1$ and k states. A typical example of process noise is the multiple scattering suffered by a particle traveling from layers $k-1$ to k of a silicon detector. In the case of vertex fitting,ω_{k-1} is zero.

The random variables ω_k and ϵ_k are assumed to be independent with normal probability distributions:

$$p(\omega_k) = N(0, Q_k) \tag{4.8}$$

$$p(\epsilon_k) = N(0, V_k) \tag{4.9}$$

$$Cov[\omega_k, \epsilon_k] = 0 \tag{4.10}$$

The Kalman Filter algorithm consist of three steps:

- **Prediction:** is the estimation of the state of the system at time k from the knowledege of the system at time $k-1$.

$$x_k^{k-1} = F_{k-1}x_{k-1} \tag{4.11}$$

$$C_k^{k-1} = F_{k-1}C_{k-1}F_{k-1}^T + Q_{k-1} \tag{4.12}$$

  where $C_k^{k-1} = cov(x_k^{true} - x_k^{k-1})$ is the predicted state vector covariance matrix.

- **Filtering:** is the estimation of the state vector at time k based on all previous measurements. It is computed as a linear combination of a prediction

estimate x_k^{k-1} and a weighted difference between the measurement m_k and a measurement prediction $H_k x_k^{k-1}$

$$x_k = x_k^{k-1} + K_k(m_k - H_k x_k^{k-1}) \tag{4.13}$$

$$C_k = (1 - K_k H_k) C_k^{k-1} \tag{4.14}$$

where K_k is the Kalman *Gain* matrix:

$$K_k = C_k^{k-1} H_k^T (V_k + H_k C_k^{k-1} H_k^T)^{-1} \tag{4.15}$$

derived by minimizing the trace of the covariance matrix C_k.

Equation 4.15 shows that when the measurement errors approaches zero, the gain matrix tends to H_k^{-1} and the actual measurements m_k are weigthed more than the prediction. On the other hand, when the predicted covariance matrix C_k^{k-1} approaches zero, the gain matrix tends to zero and the prediction is weighted more than the measurements.

- **Smoothing:** it consists in the estimation of the state vector at past times using the full available information. The final state vector estimate, containing the full information about the system, is propagated back to all previous estimates:

$$x_k^n = x_k + A_k(x_{k-1}^n - x_{k-1}^k) \tag{4.16}$$

$$C_k^n = C_k + A_k(C_{k-1}^n - C_{k-1}^k) A_k^T \tag{4.17}$$

where A_k is the *Smoother Gain* matrix:

$$A_k = C_k F_k^T (C_{k-1}^k)^{-1} \tag{4.18}$$

Kalman Filter equations can also be derived in a more symmetric form called *weighted means formalism*. In this equivalent representation, the filtering step is

given by a linear combination of the prediction estimate x_k^{k-1} and the system measurements m_k:

$$x_k = C_k[(C_k^{k-1})^{-1}x_k^{k-1} + H_k^T G_k m_k] \tag{4.19}$$

$$C_k = [(C_k^{k-1})^{-1} + H_k^T G_k H_k] \tag{4.20}$$

with $G_k = V_k^{-1}$

The χ^2 contribution is the sum of two terms: the distance between the measured and predicted state vector and the distance between the predicted and filtered state vector:

$$\chi^2 = (m_k - H_k x_k)^T G_k (m_k - H_k x_k) + (x_k - x_k^{k-1})^T (C_k^{k-1})^{-1}(x_k - x_k^{k-1}) \tag{4.21}$$

Figure 4.2 illustrates the idea behind the Kalman Filter in the case of estimating a particle trajectory. The Filter starts with the first track hit at layer $k-1$ and makes a prediction for the hit at layer k (x_k^{k-1}). The prediction is combined with the actual measurement at layer k, producing an updated estimator x_k. The light cones represent the predicted covariance matrix error for the hit position. This process is repeated until the last detector layer. During the smoothing, the process is reversed, and, starting from the last hit, the track is back propagated until the first layer by using the full available information.

4.2.1 The Extended Kalman Filter (EKF)

When the process to be estimated and or the measurement equations are non-linear, it is possible to apply the Kalman Filter by linearizing the equations around a previous estimate by means of a Taylor expansion. For instance, in the case of a non-linear measurement equation:

$$m_k = h_k(x_k) + \epsilon_k \tag{4.22}$$

$$h_k = h_k(x_k^0) + H_k(x_k - x_k^0) = c_k^0 + H_k x_k \tag{4.23}$$

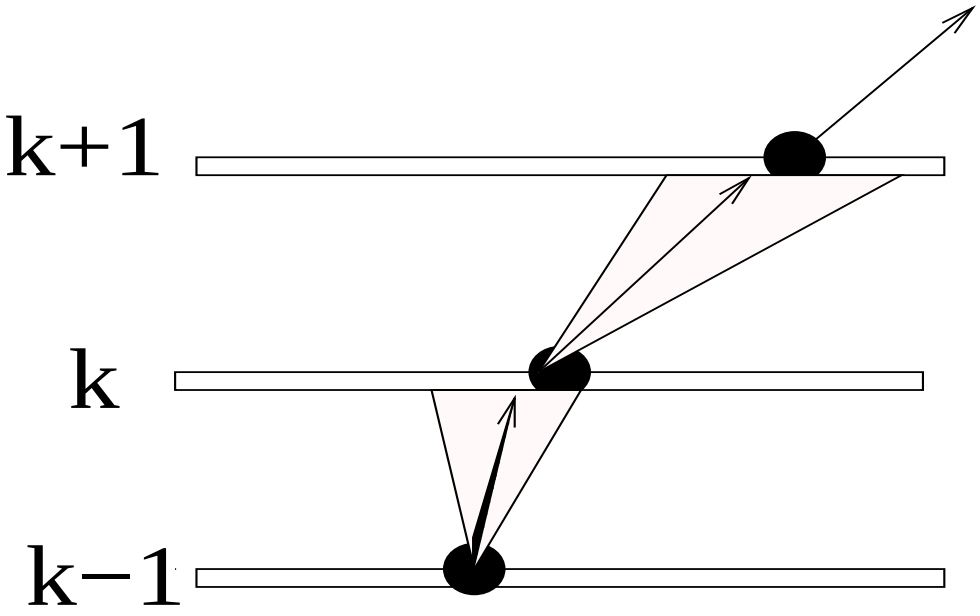

Figure 4.2: Kalman Filter example of track estimation.

with

$$c_k^0 = h_k(x_k^0) - H_k x_k^0 \tag{4.24}$$

and

$$H_k^{i,j} = \frac{\partial h_k^i}{\partial h_k^j} \tag{4.25}$$

is the Jacobian of the transformation.

Since

$$(m_k - c_k^0) = H_k x_k + \epsilon_k \tag{4.26}$$

all the Kalman Filter equations remain the same with the variable change:

$$m_k = (m_k - c_k^0) \tag{4.27}$$

The point of expansion is usually chosen as the previous filter estimate of the state vector x_{k-1}. However, if the current estimate x_k is very different from the true x_k, the first-orden expansion is not good any more and the final estimate may be significantly different from the current state of the system.

One approach to reduce the effect of non-linearities consists in applying iteratively the EKF around the previous estimate. This procees is called Iterated Extended Kalman Filter (IEKF) and can be implemented locally or globaly. The first case corresponds to re-linearizing the equations *in each step* until convergence. In the second case, the EKF is first applied to the full data starting with an initial estimate as linearization point and next, the process is repeated using the new estimate as expansion point until convergence is reached. The choice between the two methods depends on the stability of the solution for the particular system equations.

4.3 Vertex Fitting Using the Kalman Filter

Starting from a set of reconstructed tracks, the goal is to estimate the position of the vertex interaction and the momentum of the tracks at this point.

4.3.1 Definitions

In a uniform magnetic field, charged particles describe a helicoidal trajectory which is fully described by 5 parameters. The most commonly used set of helix parameters for a measured charged track is defined as

$$m_k = (dca, zdca, \phi, \tan\lambda, \frac{q}{p_T}) \tag{4.28}$$

The 5×5 track covariance matrix error is denoted by $V_k = G_k^{-1}$, and the parameter's description is:

- *dca* (distance of closest approach): minimal distance from the helix to the z axis. Its sign is given by the sign of the vector product $(\vec{dca} \times \vec{p_T})$, where $\vec{dca}$ is the vector from the origin of the coordinate system to *dca*.
- *zdca*: the z-coordinate of $\vec{dca}$.

- ϕ: angle between the transverse momentum p_T at $\vec{dca}$ and the x-axis.

- λ: the slope of the helix, defined by $\lambda = \sin(\mathrm{d}z/\mathrm{d}s)$.

- e/p_T: it measures the track curvature, being e the charge of the particle.

The first three parameters in (4.28) define a 3-dimensional point of the helix (the DCA point) in cylindrical coordinates and the last three parameters define the *geometric* momentum vector of the particle at the DCA, denoted by $q = (\phi, \tan\lambda, \frac{q}{p_T})$.

The conversion between geometric and kinematic momentum $\vec{p} = (p_x, p_y, p_z)$ is given by

$$p_x = \frac{|q|}{e/p_T}\cos\phi \quad p_y = \frac{|q|}{e/p_T}\sin\phi \quad p_z = \frac{|q|}{e/p_T}\tan\lambda \tag{4.29}$$

and the covariance matrix for the kinematic momentum is

$$C_p = JC_qJ^T \tag{4.30}$$

where C_q is the covariance matrix for the geometric momentum and J is the jacobian of the transformation, given by

$$J = \begin{pmatrix} -p_y & 0 & -p_x/(e/p_t) \\ p_x & 0 & -p_y/(e/p_t) \\ 0 & p_t & -ep_z/(e/p_t) \end{pmatrix} \tag{4.31}$$

The state vector x_k is defined as the vertex position, $\vec{x}_k$, and the geometric momentum of track k at $\vec{x}_k$

$$x_k = (\vec{x}_k, \vec{q}_k) \tag{4.32}$$

with $\vec{x}_k = (x, y, z)_k$ and $\vec{q}_k = (\phi, \tan\lambda, e/p_T)_k$

The covariance matrices for the vertex position and the geometric momentum are denoted by $\mathbf{C}_k$ and $\mathbf{D}_k$ respectively.

4.3.2 Measurement Equation

The measurement equation that relates the track parameters m with the state vector x is nonlinear due to the presence of a magnetic field:

$$m_k = h_k(\vec{x}_k, \vec{q}_k) + \epsilon_k \tag{4.33}$$

It can be linearized around $(\vec{x}_k^0, \vec{q}_k^0)$ as

$$m_k = c_k^0 + A_k\vec{x}_k + B_k\vec{q}_k \tag{4.34}$$

with

$$A_k = \frac{\partial h_k}{\partial \vec{x}}(\vec{x}_k^0, \vec{q}_k^0) \qquad B_k = \frac{\partial h_k}{\partial \vec{q}}(\vec{x}_k^0, \vec{q}_k^0) \tag{4.35}$$

$$c_k^0 = h_k(\vec{x}_k^0, \vec{q}_k^0) - A_k x_k^0 - B_k q_k^0 \tag{4.36}$$

The mathematical expresions for c, A and B are given in appendix ??.

4.3.3 Filter Equations

Since there is no dynamics involved in a vertex fit (the next track cannot be predicted from the previous one), the system equation is very simple:

$$x_k = x_{k-1} \tag{4.37}$$

Due to fact that there is no prior information about the track momentum $\vec{q}_k$, we assign an "infinite" covariance matrix to the "predicted" momenta q_k^{k-1}. So, the prediction equations are

$$\vec{x}_k^{k-1} = \vec{x}_{k-1} \qquad \vec{q}_k^{k-1} = \vec{q}_k \tag{4.38}$$

$$\mathbf{C}_k^{k-1} = \mathbf{C}_{k-1} \qquad \mathbf{D}_k^{k-1} = (1/\delta)^{-1}1 \tag{4.39}$$

Where we separated the vertex position $\vec{x_k}$ and the momentum $\vec{q_k}$ from the state vector x_k for clarity.

$\mathbf{C}_k = cov(\vec{x}_k^{true} - \vec{x}_k)$ is the vertex position covariance matrix and $\mathbf{D}_k = cov(\vec{q}_q^{true} - \vec{q}_k)$ is the track momentum covariance.

In the weighted means formalism, the filter equations are given by:

$$\vec{x}_k = \mathbf{C}_k[\mathbf{C}_{k-1}^{-1}\vec{x}_{k-1} + A_k^T G_k^B (m_k - c_k^0)] \tag{4.40}$$

$$\vec{q}_k = W_k B_k^T G_k (m_k - c_k^0 - A_k x_k)] \tag{4.41}$$

$$\mathbf{C_k} = (\mathbf{C}_{k-1}^{-1} + A_k^T G_k^B A_k)^{-1} \tag{4.42}$$

$$\mathbf{D}_k = W_k + W_k B_k^T G_k A_k \mathbf{C_k} A_k^T G_k B_k W_k \tag{4.43}$$

$$\mathbf{E}_k = -W_k B_k^T G_k A_k \mathbf{C_k} \tag{4.44}$$

with

$$W_k = (B_k^T G_k B_k)^{-1} \tag{4.45}$$

$$G_k^B = G_k - G_k B_k W_k B_k^T G_k \tag{4.46}$$

$$cov(\vec{x}_k) = \mathbf{C}_k, \quad cov(\vec{q}_k) = \mathbf{D}_k, \quad cov(\vec{x}_k, \vec{q}_k) = \mathbf{E}_k \tag{4.47}$$

The χ^2 is given by

$$\chi_k^2 = \chi_{k-1}^2 + \chi_+^2 \tag{4.48}$$

with

$$\chi_+^2(\vec{x}, \vec{q}) = (x - x_{k-1})^T (\mathbf{C}_{k-1})^{-1} (x - x_{k-1}) + (m_k - c_k^0 - A_k x - B_k q)^T G_k (m_k - c_k^0 - A_k x - B_k q) \tag{4.49}$$

The smoother equations constrain all tracks to the final vertex estimate:

$$\vec{x}_k^n = \vec{x}_N \tag{4.50}$$

$$\vec{q}_k^n = W_k B_k^T G_k (m_k - c_k^0 - A_k x_n)] \tag{4.51}$$

$$\mathbf{C}_k^n = \mathbf{C_N} \tag{4.52}$$

$$\mathbf{D}_k^n = W_k + W_k B_k^T G_k A_k \mathbf{C_N} A_k^T G_k B_k W_k \tag{4.53}$$

$$\mathbf{E}_k^n = -W_k B_k^T G_k A_k \mathbf{C}_N \tag{4.54}$$

The correlation between two tracks k and j is given by

$$\mathbf{Q}_{kj}^n = W_k B_k^T G_k A_k \mathbf{C_N} A_j^T G_j B_j W_j \tag{4.55}$$

4.3.4 The Concept of Vertex Fitting by Means of the Kalman Filter Techinque

Consider the case of fitting the 3 tracks shown in figure 4.3. The KF starts with a vertex estimation at the origin and an initial covariance matrix of the order of centimeters in order not to bias the final result. In the first step, one track is added to the filter and, according to (4.49), the first vertex estimate is the distance of closest approach to the origin. The track momentum at the vertex is simply the original track momentum.

When the second track is added, the new estimate is found by a compromise between the distance from the new to the previous vertex estimate and the difference between the new 5-helix parameters and the actual track parameters.

It is clear from figure 4.3 that the track direction remains basically unmodified at first order, most of the change being in the *dca* and *zdca* track parameters. It must also be noted that the full track information is used in the minimization, not only the impact parameter.

When the third track is added, a new estimate for the vertex position and the momentum of this track at the vertex is found by minimizing (4.49). In this stage, all the information has been incorporated to the Kalman Filter. Thus, the final vertex position is not dependent on the order the tracks were added.

The updated track momenta, however, do depend on the order in which the tracks were considered and this is why the smoother is necesary at the end of the process. In last picure of figure 4.3 all tracks were constrained to the final vertex

estimate using the smoothing equations.

Since the measurement equation is non-linear, the final vertex position may be track-order dependent and a re-iteration linearizing the equations around the last vertex estimate could be necessary until convergence (IEKF).

As was discussed above, the vertex estimate takes into account the full tracking error matrix, as opposed to the more standard vertexing methods based on the impact parameter information. In order to visualize the effect of the track errors in the fit, Figure 4.4 shows the same 3-track fit from Figure 4.3, when the third track covariance matrix has been increased by a factor of 10. The vertex position, as expected, turns out to be basically defined by the first two tracks. However, the parameters of the third track are still updated using the more precise information for tracks 1 and 2

4.3.5 Vertex Fitting Example

In this section, the Kalman Filter vertex algorithm is applied to 100 Monte Carlo simulated events of five muon particles generated at a vertex position $\vec{x} = (-0.3, 0.2, z)\, cm$, with z given by a Gaussian distribution of $\sigma = 30\, cm$.

Figure 4.5 shows the KF vertex position distributions. The RMS of the transverse position is of the order of $10\, \mu m$. It is important to note that this distributions are not biased by the inital starting point at $\vec{x} = (0, 0, 0)\, cm$.

Figures 4.6 and 4.7 show some of the track parameter distributions before and after the Kalman vertex constrained fit. Note the important improvement in the momentum resolution due to the use of the final vertex estimate information during the smoothing step.

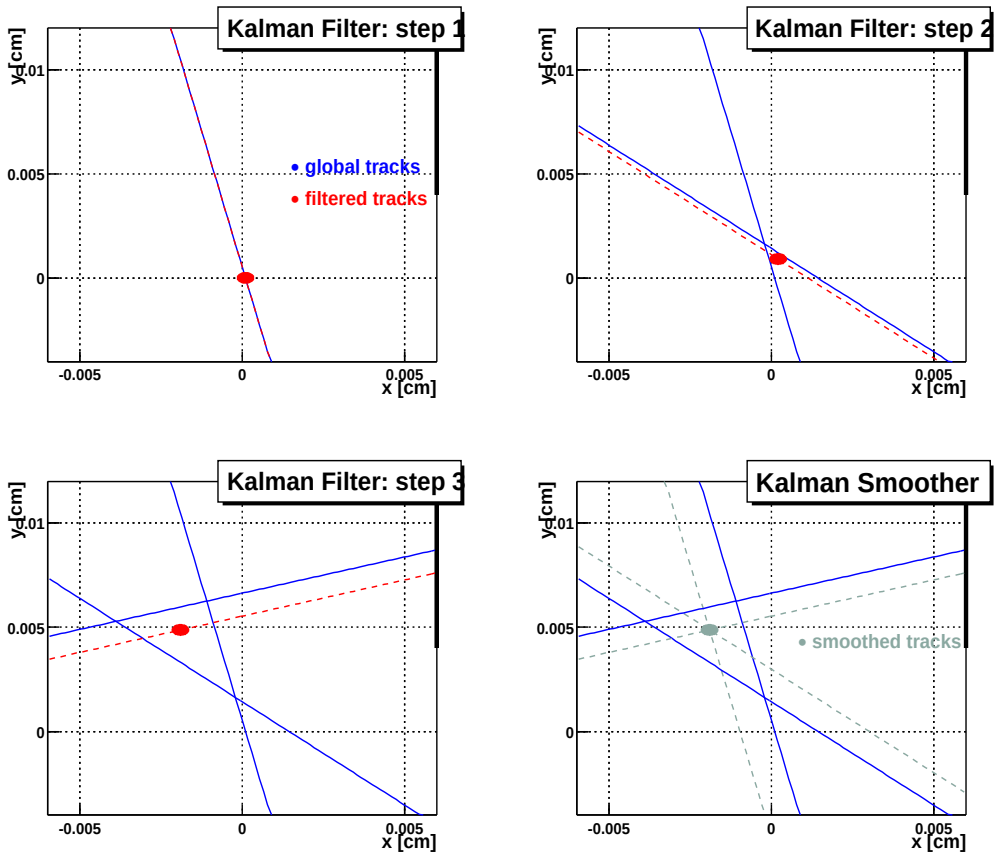

Figure 4.3: Example of 3-track vertex fit using the Kalman Filter

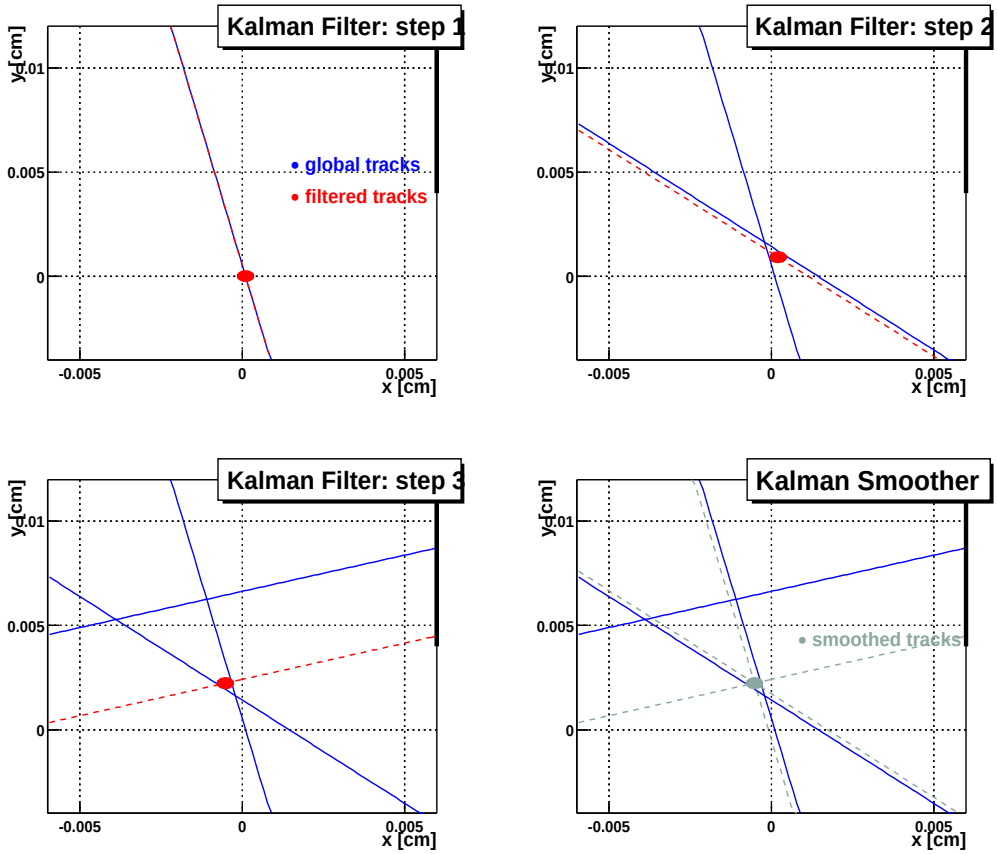

Figure 4.4: Example of 3-track vertex fit using the Kalman Filter when the covariance matrix of one of the tracks has been multiplied by 10.

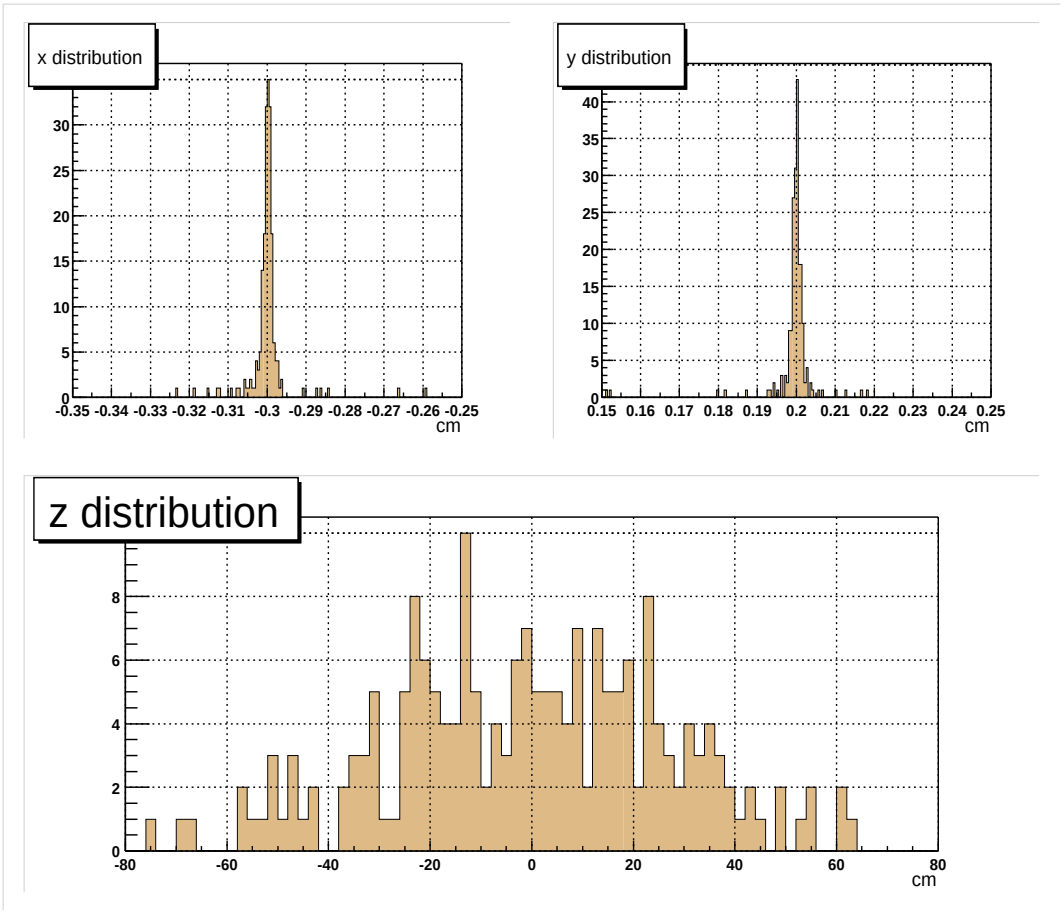

Figure 4.5: Kalman Filter reconstructed vertex distributions for 5-muon events.

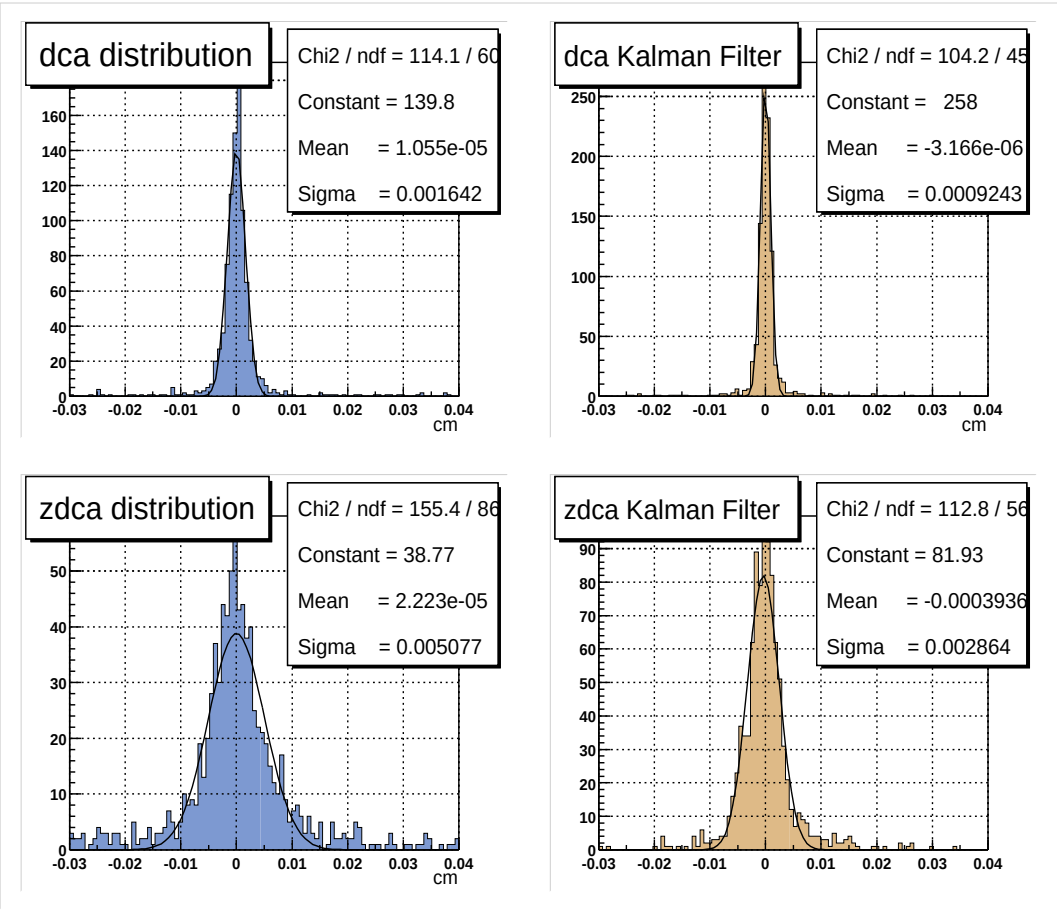

Figure 4.6: Track parameters before (left) and after (right) the Kalman Filter vertex fit. Plotted is the $(x_{reconstructed} - x_{generated})$ distribution for dca and $zdca$.

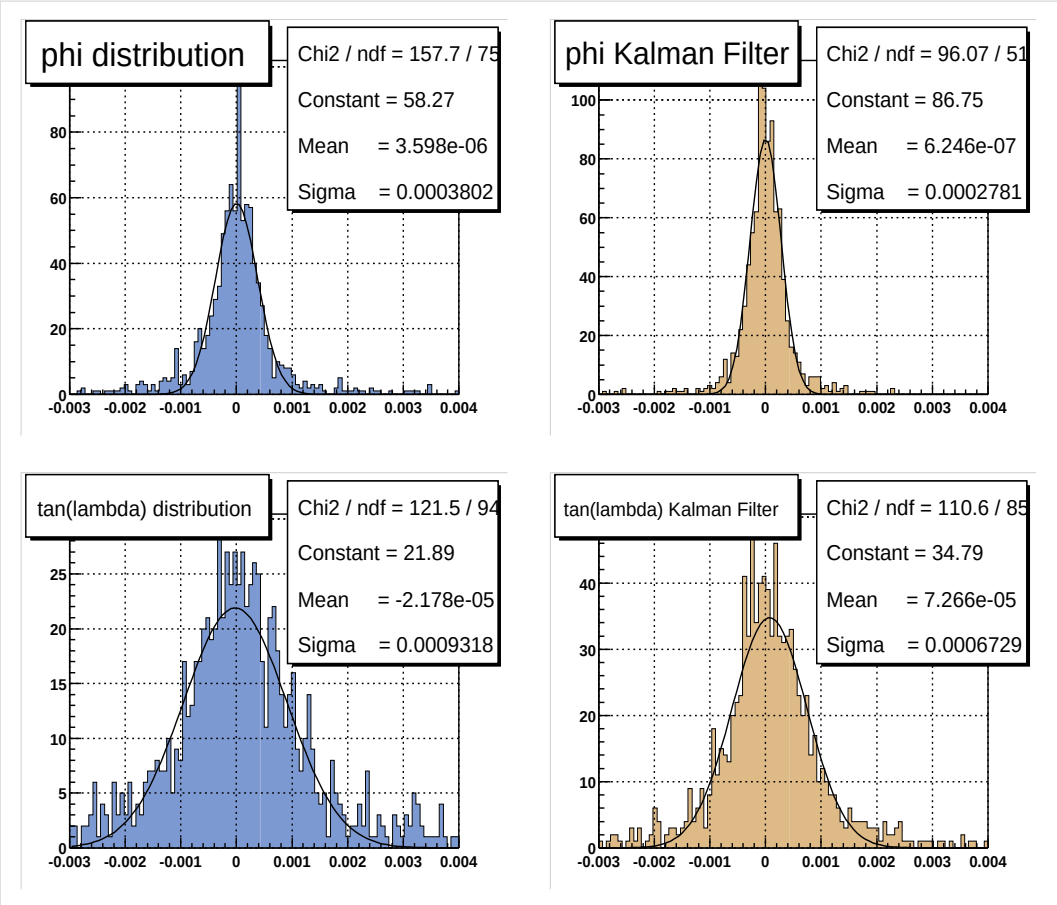

Figure 4.7: Track parameters before and after the Kalman Filter vertex fit.

4.4 Primary Vertex Reconstruction

The accurate determination of the primary vertex is essential for the reconstruction of physics objects such as electrons, jets, b-jets, $\not\!\!E_T$ and secondary vertices.

In general, one does not know in advance which tracks belong to the primary vertex. Thus, a pattern recognition (or vertex finding) algorithm is necessary to be able, by means of an iterative process, to identify the tracks coming from a same vertex. Since most of the particles produced in an interaction come from the primary vertex, the algorithm used to find these vertices is based on a "tear-down" approach.

The vertex search procedure consists of three steps: track clustering, track selection, and vertex finding and fitting.

First, tracks are clustered along the z axis by means of the following algorithm:

- Order tracks by p_T
- Looping in descendent order of track p_T, add tracks to the pre-cluster if $\Delta z < 2\,cm$, where Δz is the difference between the z of closest approach of the track, and the pre-cluster z average position.

The Δz parameter was chosen such that it is small enough to resolve multiple interactions and big enough to be able to cluster all tracks from each interaction taking into account track resolution. The particular value of $2\,cm$ was determined to optimize the primary vertex efficiency including SMT-only tracks with poor resolution. This parameter will be updated as newer versions of tracking are introduced.

Second, quality cuts are applied to the reconstructed tracks in every z-cluster in order to remove fake and badly reconstructed ones. In addition, tracks are required to be within 3 sigmas of the nominal transverse interaction position. The track-selection requirements are

- At least 2 hits in the SMT detector ($N_{smt} \geq 2$)

- $p_T > 0.5\,GeV/c$
- $|dca/\sigma(dca)| < 3$

For every z-cluster of N selected tracks $N^z_{trk} > 1$, the tear-down vertex search algorithm proceeds as follows:

- All selected tracks are fitted to a common vertex and the total χ^2 of the fit is computed, $\chi^2(N^z_{trk})$.
- Each track is excluded separately of the fit and a new $\chi^2(N^z_{trk}-1)$ is computed.
- The track which gives the maximum difference $\chi^2(N^z_{trk}) - \chi^2(N^z_{trk} - 1)$ is removed from the vertex, if the total vertex χ^2 per degree of freedom exceeds a threshold of 10.
- This procedure is repeated until the total vertex χ^2 per degree of freedom is smaller than 10.

The final list of vertices found will contain the primary (hard scatter) vertex, and additional minimum bias interactions.

4.4.1 Primary Vertex Performance in Simulated Events

In this section we check the primary vertex algorithm performance, and the basic properties of the reconstructed primary vertices in a sample of simulated $W(\rightarrow qq)H(\rightarrow b\bar{b})$ events.

The algorithm efficiency is defined as the number of events with a correctly identified vertex divided by the total number of events. A reconstructed vertex is considered *correct* according to the following matching algorithm:

- the χ^2 between the 3-dimensional position of the reconstructed and the generated vertex is smaller than 50.

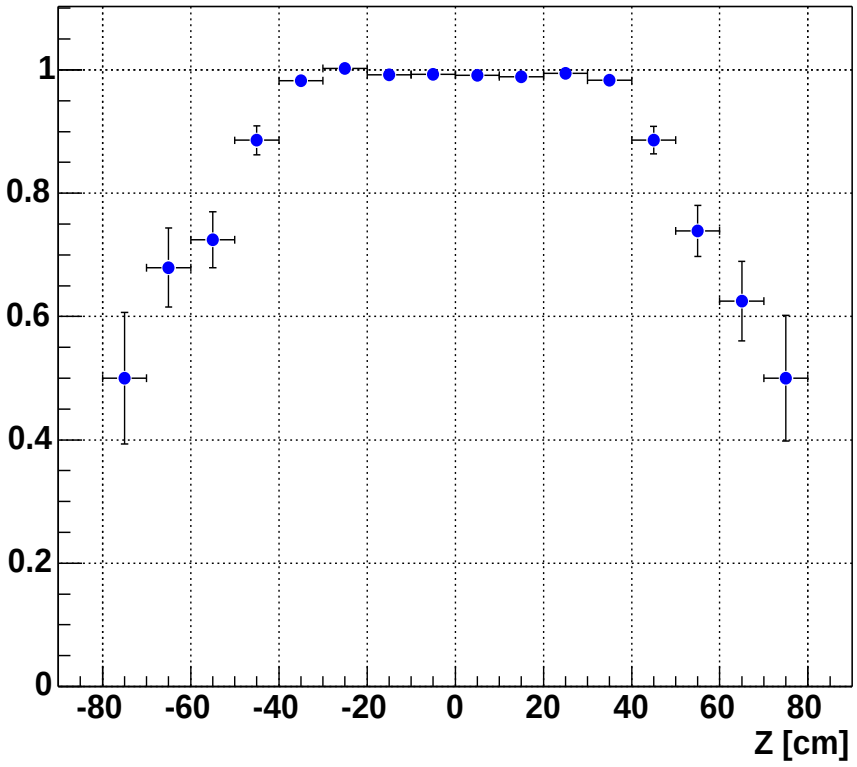

Figure 4.8: Primary vertex reconstruction efficiency in the simulation

- the reconstructed and generated vertices share at least 2 tracks.
- The simulated vertex has at least 2 tracks within the SMT acceptance, which are reconstructed. (i.e. at least 2 simulated particles are reconstructed by the tracking algorithm)

Figure 4.8 shows the primary vertex reconstruction efficiency as a function of the interaction z position. It is 99% in the central region. The efficiency drops significantly for $|z| > 40\,cm$ due to the lack of SMT hit information in the input tracks.

The number of attached tracks to the primary vertex is shown in Figure 4.9. This

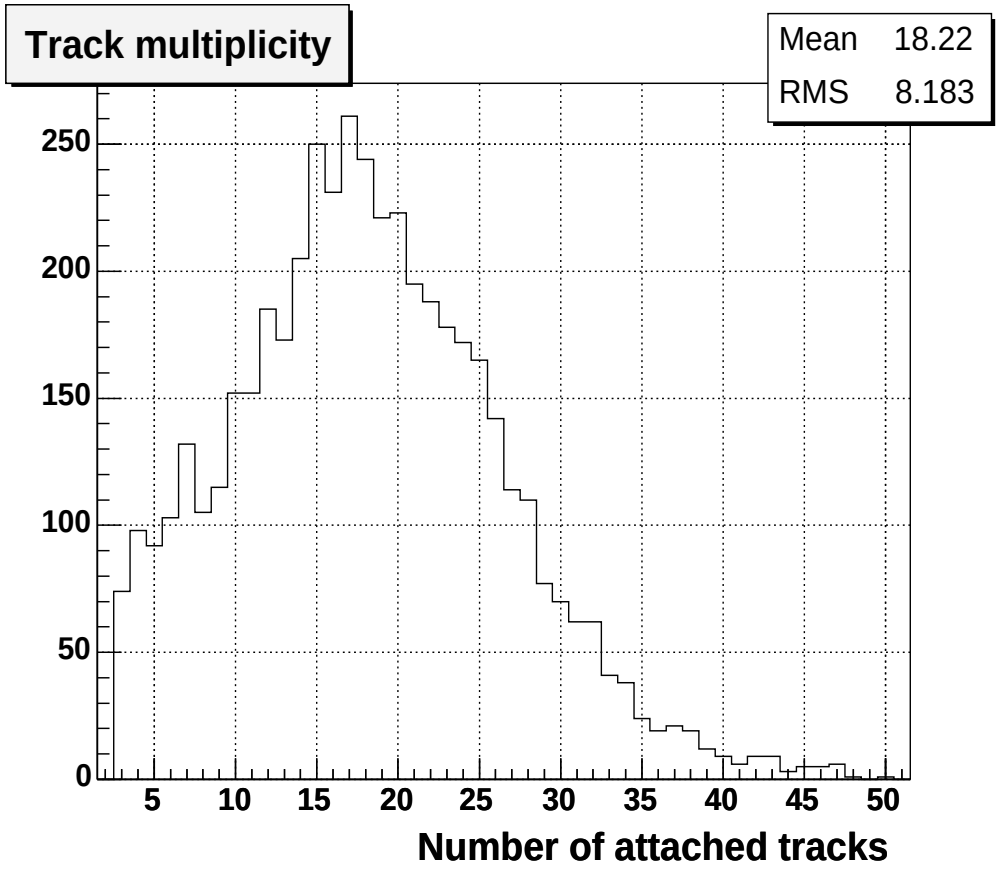

Figure 4.9: Primary vertex track-multiplicity in the simulation

magnitude strongly depends on the physics data sample analyzed, being higher for multijet final states such us this WH sample.

Figure 4.10 shows that the primary vertex resolution, computed as the difference between reconstructed and generated vertex, is of the order of $15\,\mu m$ in the transverse plane, and $30\,\mu m$ in the longitudinal plane.

Shown in Figure 4.11 are the pull vertex distributions, computed as the difference between reconstructed and generated vertex divided by the reconstructed vertex error. These distributions were fitted with a double Gaussian function. The central Gaussian accounts for the vertex pull resolution and contains information about the proper error calculation. The second Gaussian accounts for the tails originated

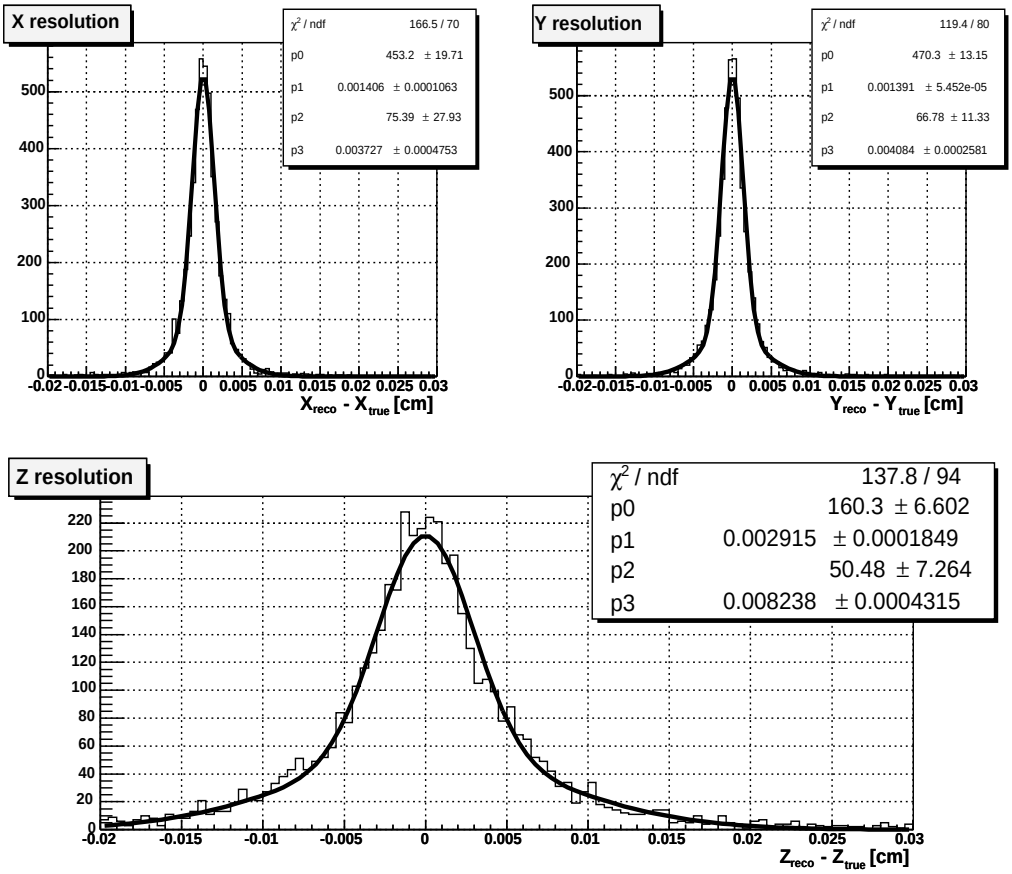

Figure 4.10: Primary vertex resolution in the simulation

by mis-reconstructed vertices. There are many sources for the tails in the pull distribution: badly reconstructed tracks in the vertex, mis-identified vertices due to a minimum bias interaction very close to the hard vertex, misalignment, etc. Ideally, the central Gaussian resolution should be 1, whereas it is ~ 1.1. The 10% discrepancy is mostly due to the fact that the input curvature ($1/p_T$) track parameter pull distribution is different from 1.

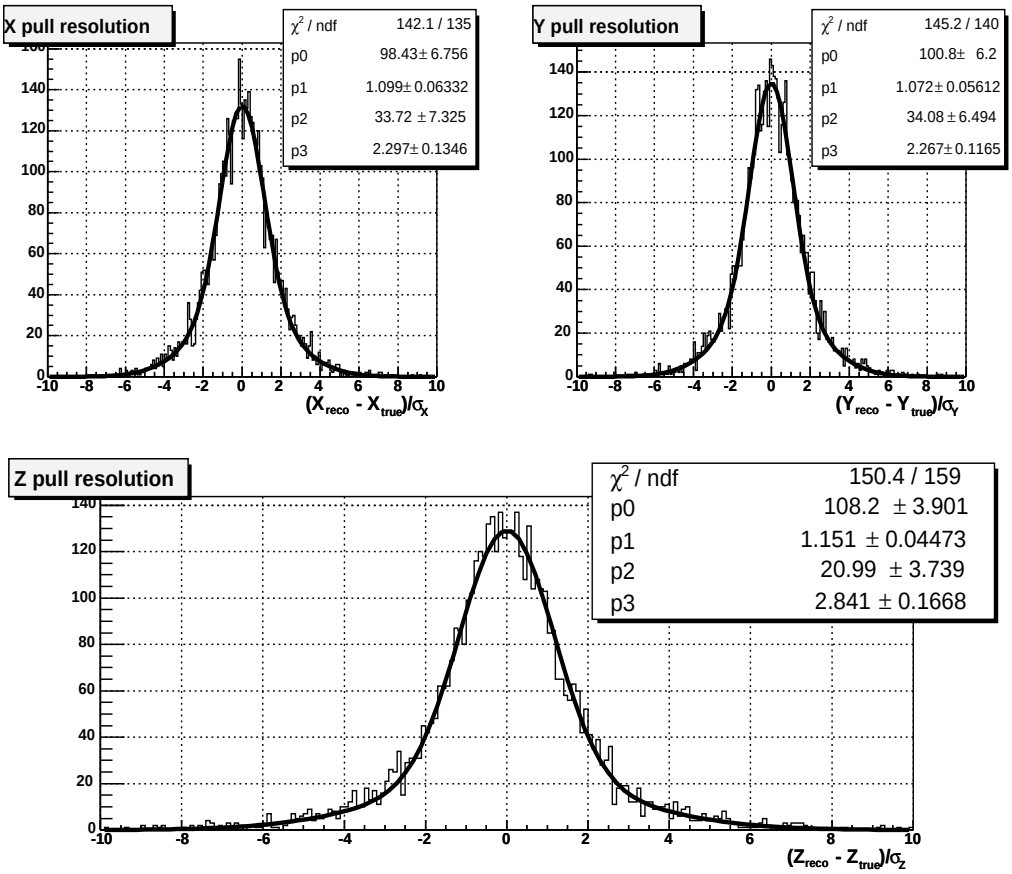

Figure 4.11: Primary vertex pull distributions in the simulation

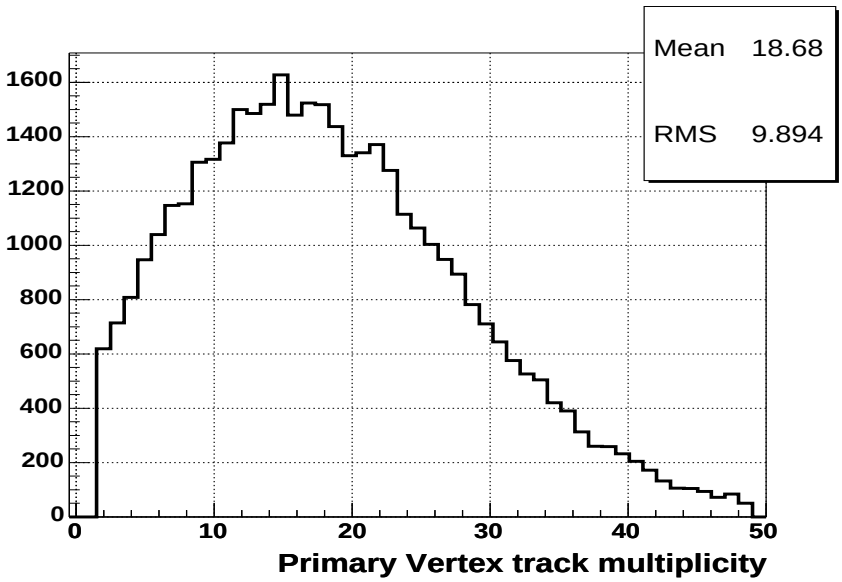

Figure 4.12: Track multiplicity distribution of primary vertices in the data.

4.4.2 Primary Vertex Performance in Data

The primary vertex performace in the data was studied in a subsample of the run 157708, selected by events where any of the hadronic jet triggers were fired. Figure 4.12 shows the track multiplicity distribution of the reconstructed primary vertices. The mean value and width of this distribution depends on the trigger used to select the sample. Jet triggers give rise to higher track multiplicities than low p_T muon triggers.

Figure 4.13 shows the x, y, and z distributions for vertices with 15 or more attached tracks. This high track multiplicity requirement is to ensure that the dominant contribution to these distributions is the actual beam size rather than the intrinsic vertex resolution. These distributions indicate that the beam spot position, for this run, is centered at $(x, y) \sim (0, 0.052)\, cm$, and the z distribution has a width very close to the expected $25\, cm$ for RunII.

Figures 4.14 and 4.15 show the primary vertex width as a function of the number of attached tracks to the vertex. We see that for tracks multiplicities below 10, the

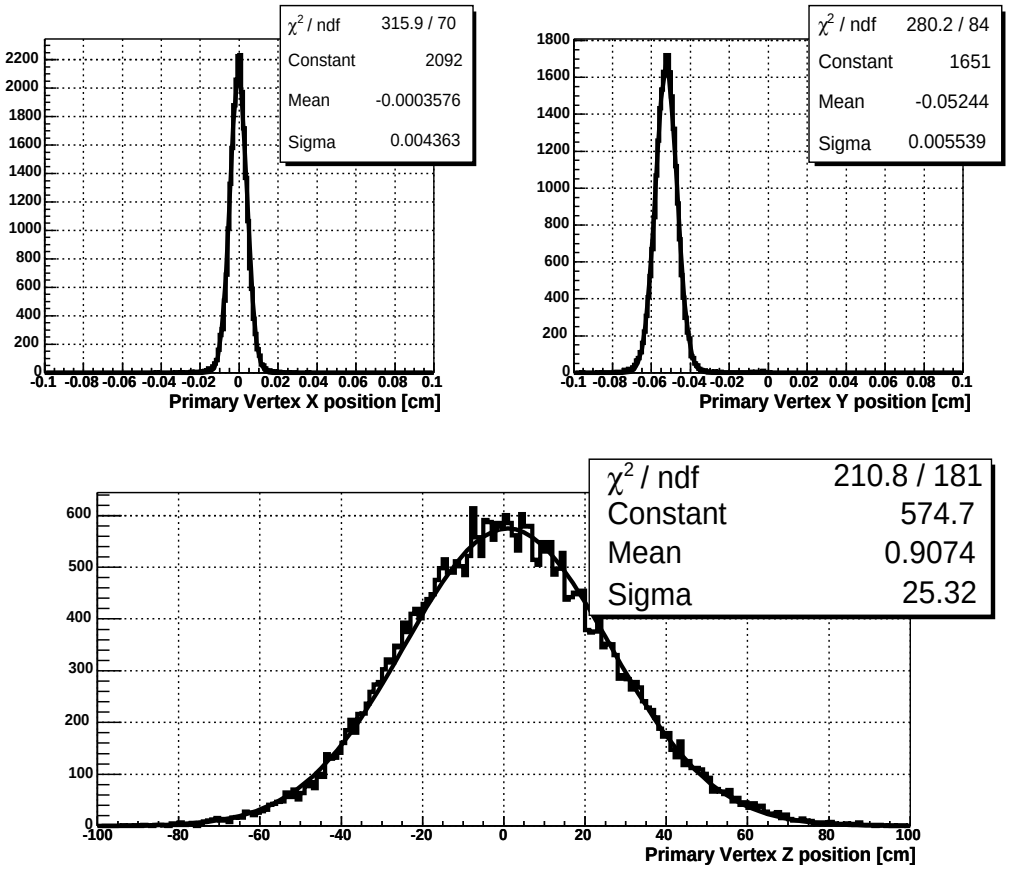

Figure 4.13: Primary vertex distributions in the data.

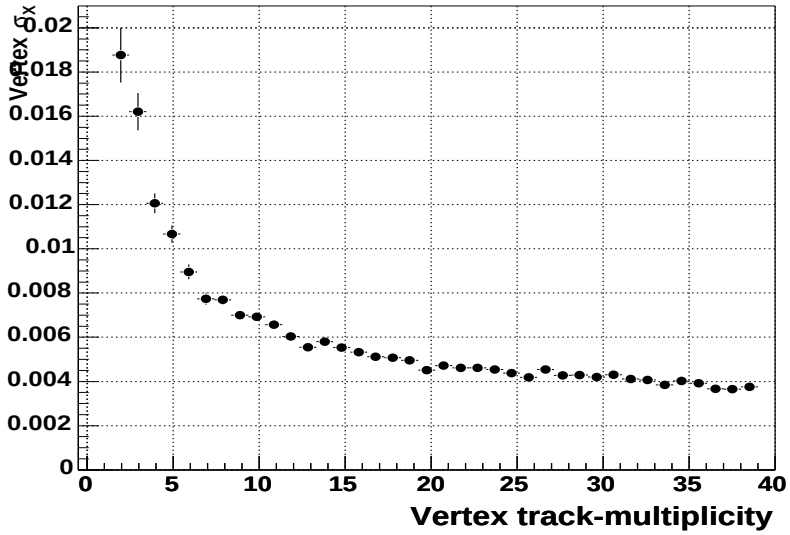

Figure 4.14: Primary vertex x-width as a function of the number of attached tracks in the data.

width is dominated by the vertex resolution, while at high multiplicities it is governed by the width of the beam spot.

The variation of the x and y position of the primary vertex as a function of the z position of the interaction is shown in Figures 4.16 and 4.17. The width of the distribution in x and y as a function of z is shown in Figures 4.18 and 4.19. Only vertices with 10 or more tracks were used in these plots.

We observe that the beam spot position varies by approximately $150\,\mu m$ over the length of the SMT and its σ changes by approximately 25% of its central value of $40\,\mu m$. The beam spot position is rather stable within a run, or for consecutive ones. However, we have observed large variations (of the order of the $100\,\mu m$) after accelerator shutdown periods.

The shape of the primary vertex width is due to two main effects: the beam spot size delivered by the accelerator increases as function of Z and the vertex resolution decreases beyond de geometric acceptance of the silicon vertex detector.

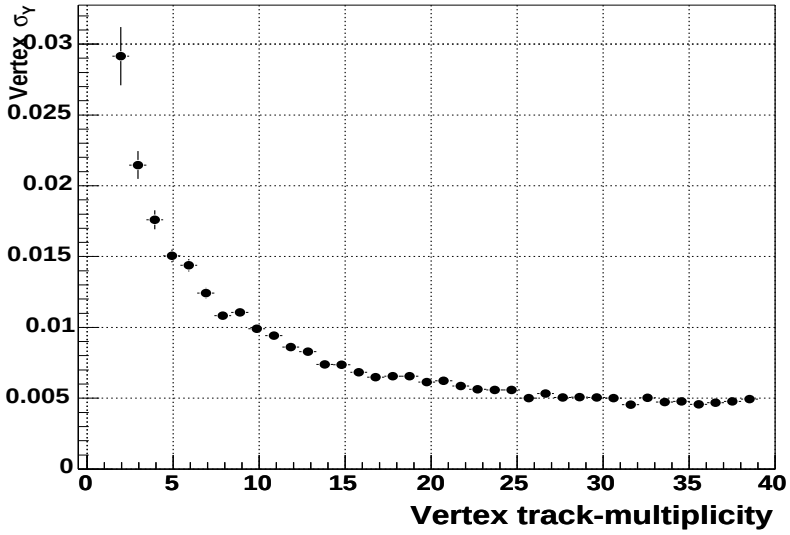

Figure 4.15: Primary vertex y-width as a function of the number of attached tracks in the data.

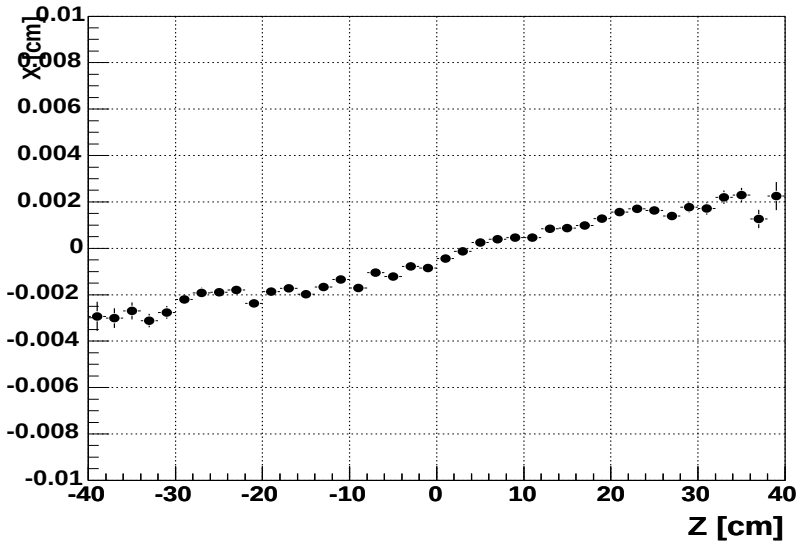

Figure 4.16: Variation of the x position of the primary vertex as a function of z in the data.

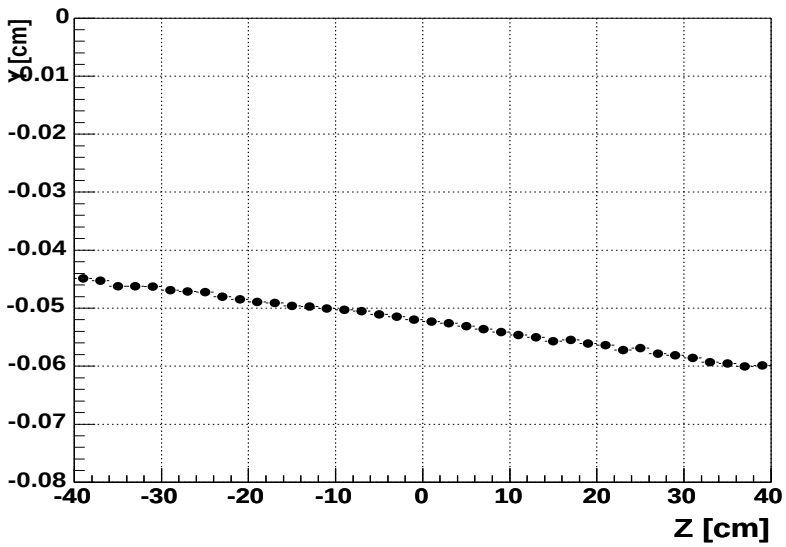

Figure 4.17: Variation of the y position of the primary vertex as a function of z in the data.

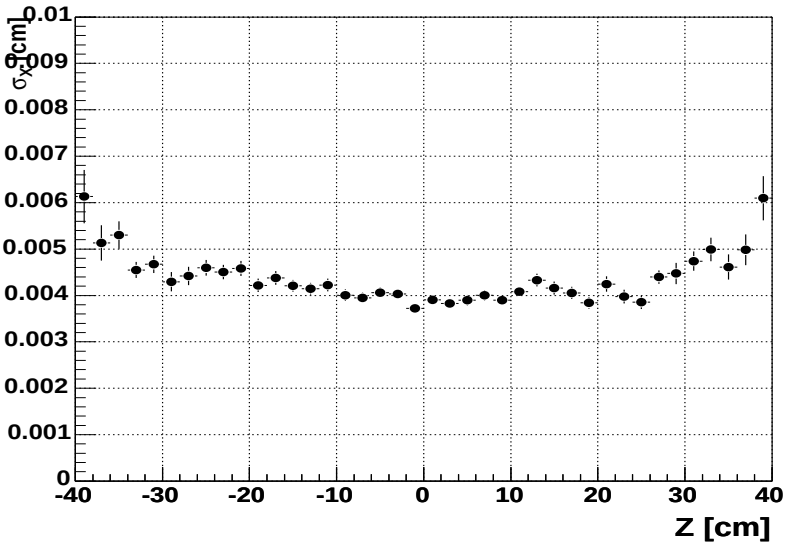

Figure 4.18: Width of the primary vertex in x as a function of z in the data.

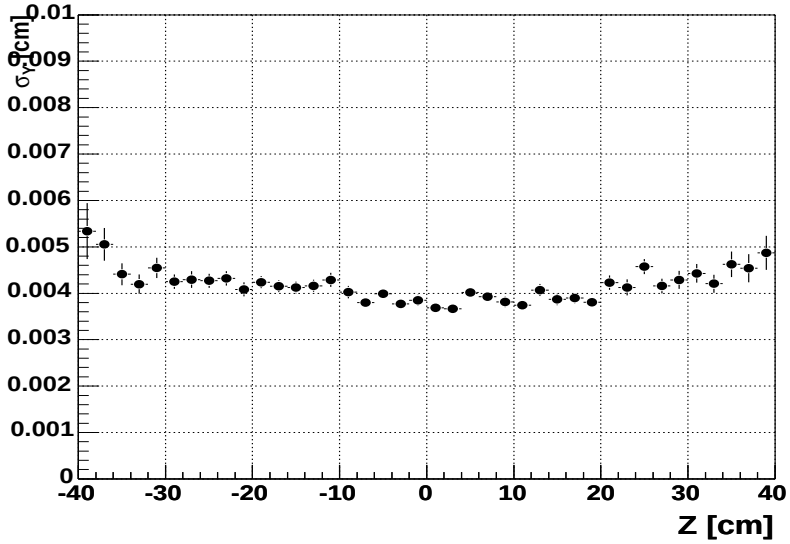

Figure 4.19: Width of the primary vertex in y as a function of z in the data.

4.5 Primary Vertex Selection

The last step of the primary vertex reconstruction is the identification of the hard scatter and additional minimum bias vertices of the event from the list of all primary vertices found. The selected primary vertex is used to reconstruct jets, b-jets, electrons and $\not\!\!E_T$. Thus, it is important to optimize its performance to be able to efficiently reconstruct physics objects in the detector.

4.5.1 Minimum Bias Vertex Probability

Our goal is to assign to each vertex, a probability that it comes from a minimum bias interaction.

We could use a multivariate technique to assign a probability to each vertex, for instance, training a neural network with kinematic variables associated to hard and MB vertices. This, however, requires a model for the hard process which is physics dependent leading to an approach that will be very different for each single physics

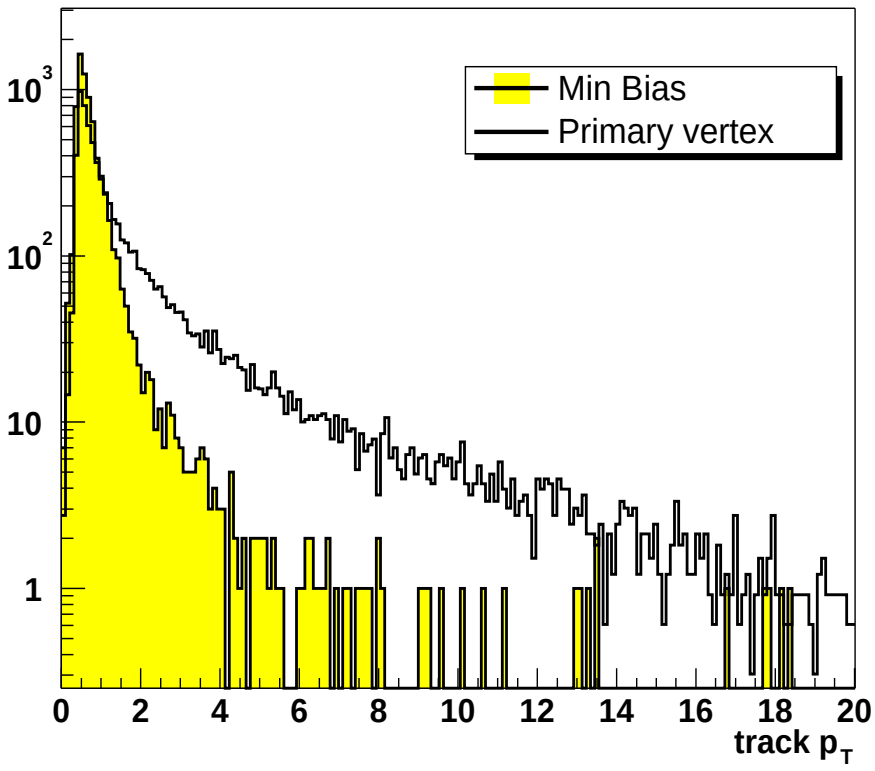

Figure 4.20: p_T spectrum of minimum bias and primary interactions tracks in a Monte Carlo sample of light quark jets.

process, and would require defining separate probability density functions for every one.

Instead, the primary selection algorithm is based only on the properties of MB vertices and quantifies how similar the selected vertices are to the MB kinematics. The unique assumption made is that tracks from hard interactions have higher p_T than tracks from MB interactions, as it is shown in Figure 4.20.

The method consists in comparing the p_T of particles associated to each interaction, with the p_T spectrum of minimum bias particles in order to calculate, for every vertex, the probability that there are no hard interaction tracks on them.

The $\log_{10}(p_T)$ distribution is used to define the probability $P(p_T)$ that the observed p_T of a given track is compatible with coming from a MB interaction:

$$P(p_T) = \frac{\int_{log_{10}(pt)}^{\infty} F(p_T)dp_T}{\int_{log_{10}(0.5)}^{\infty} F(p_T)dp_T} \tag{4.56}$$

where $F(p_T)$ is the minimum bias track $\log_{10}(p_T)$ spectrum distribution obtained from the Monte Carlo simulation. The track p_T cut off of $0.5\,GeV/c$ is to avoid including poorly or mis-reconstructed tracks in the probability calculation.

The probability that a vertex is consistent with a minimum bias interaction is given by

$$P_{MB} = \Pi \sum_{k=0}^{N-1} \frac{(-\ln \Pi)^k}{k!} \tag{4.57}$$

where Π is the product of the individual probabilities of the $N > 0$ tracks associated to the vertex:

$$\Pi = \prod_{i=1}^{N} P(p_T) \tag{4.58}$$

Only tracks with $p_T > 0.5$ are used for the calculation. We use the above definition instead of the simple product of track probabilities Π since it is independent of the number of tracks used in the calculation.

Figures 4.21 and 4.22 show the MB track probability distribution for minimum bias and hard scatter tracks in the simulation. The track probability for MB vertices is quite flat, as expected, indicating that the $F(p_T)$ distribution used correctly describes the MB characteristics. Any discrepancy between the $F(p_T)$ distribution used in the calculation and the actual distribution from the simulation would be seen as peaks at $P(p_T) = 0$ (if the discrepancy is at high p_T) or $P(p_T) = 1$ (if the differences are at low p_T).

The MB track probability for primary vertex interaction tracks peaks at 0, as expected, showing the incompatibility of primary vertex tracks with minimum bias tracks at high p_T.

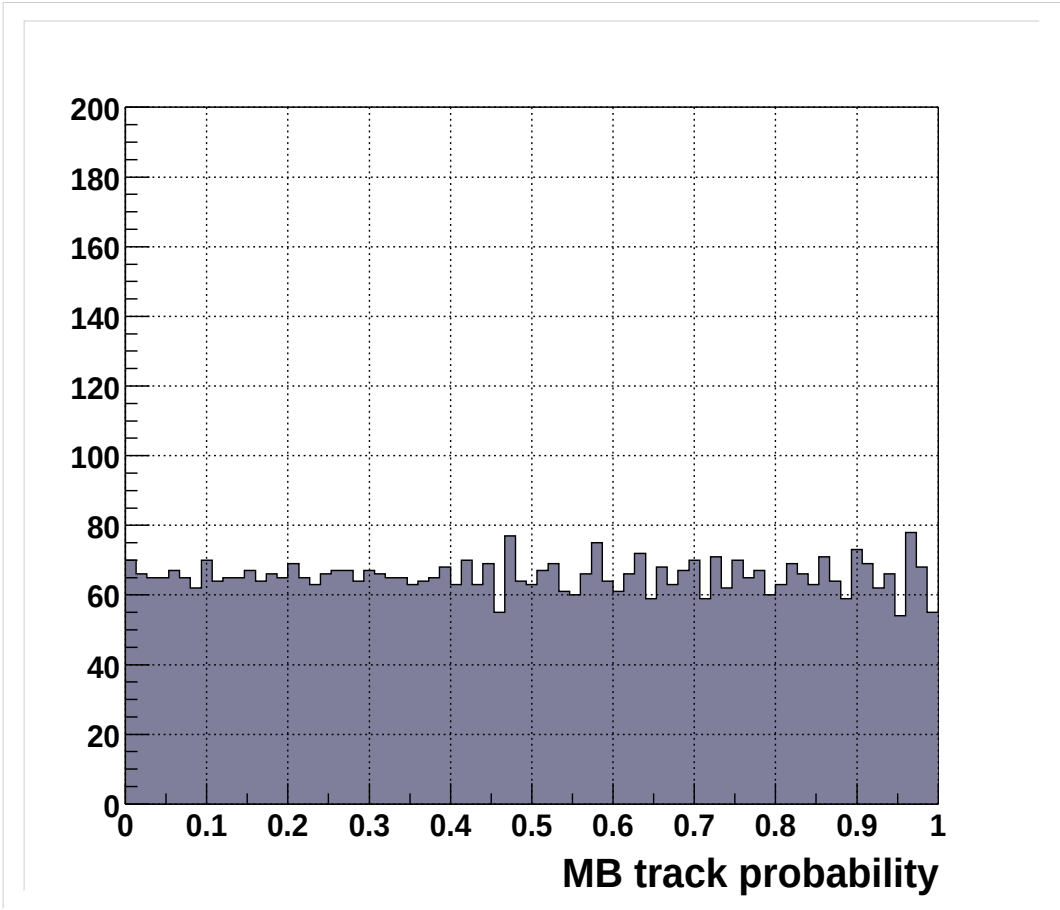

Figure 4.21: Track probability distribution for minimum bias tracks in the simulation.

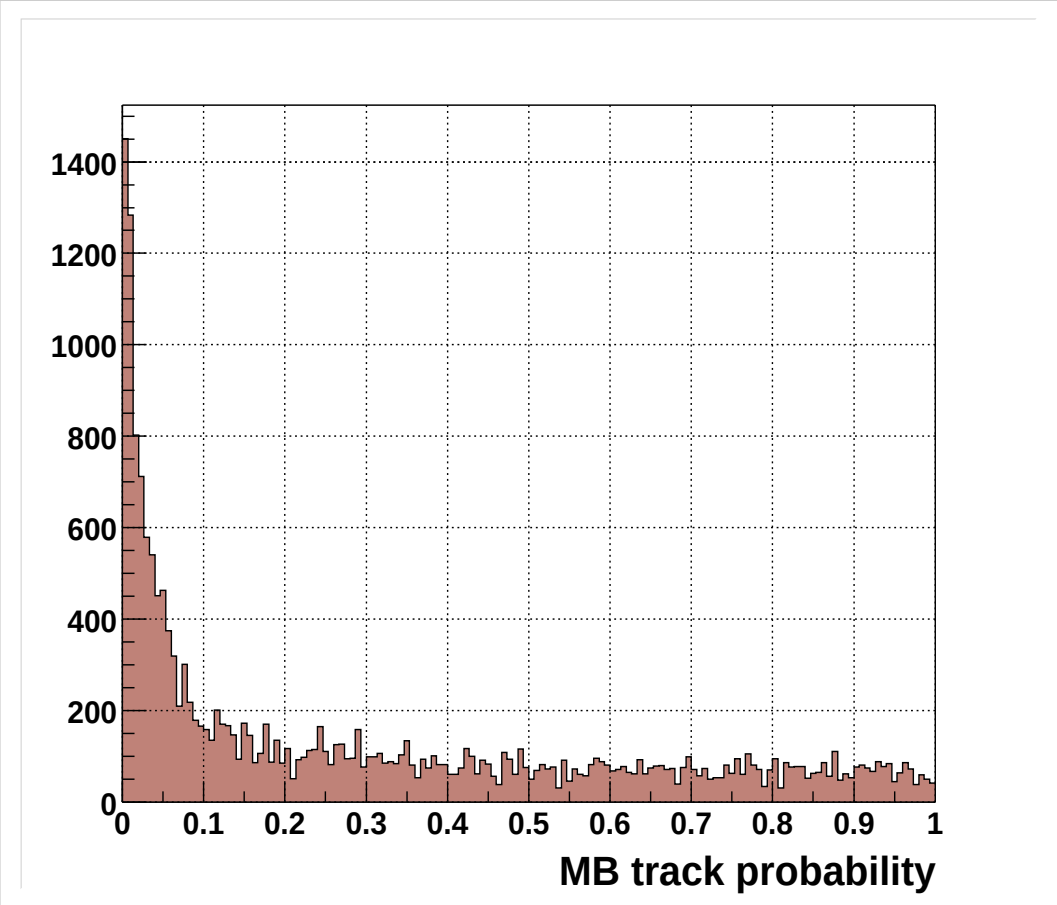

Figure 4.22: Track probability distribution for primary vertex tracks in the simulation.

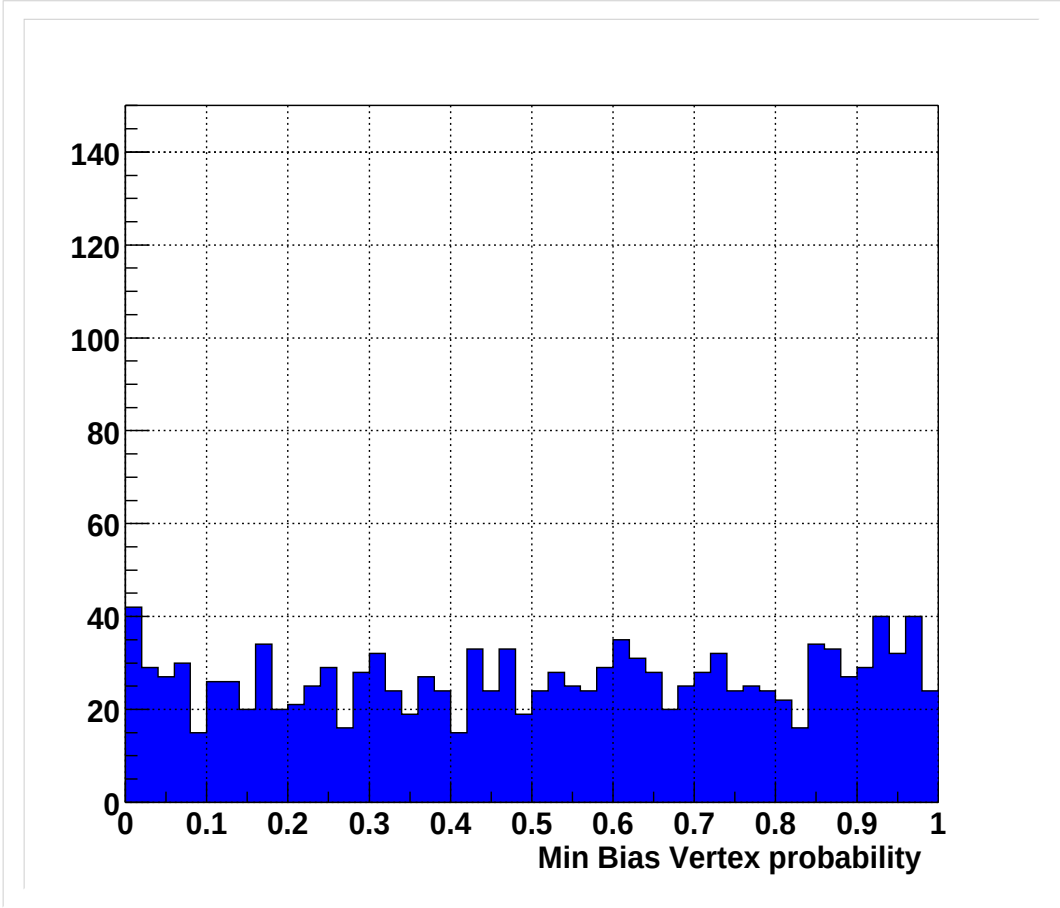

Figure 4.23: Vertex probability distribution for minimum bias vertices in the simulation.

Figure 4.23 and 4.24 show the combined P_{MB} vertex probability for minimum bias and hard scatter vertices in the simulation. The peak at zero for primary vertices is much more marked than for single tracks (Fig. 4.22). This is reasonable, because a test based on several tracks is expected to be more sensitive than one based on an individual one.

It must be noted that all tracks selected in each z-cluster are used for the probability calculation, rather than only the tracks associated to each vertex. The reason for this is motivated by the fact that low p_T primary vertices (such as in a $b\bar{b}$ process) have associated high p_T displaced tracks from the decay of long lived hadrons which

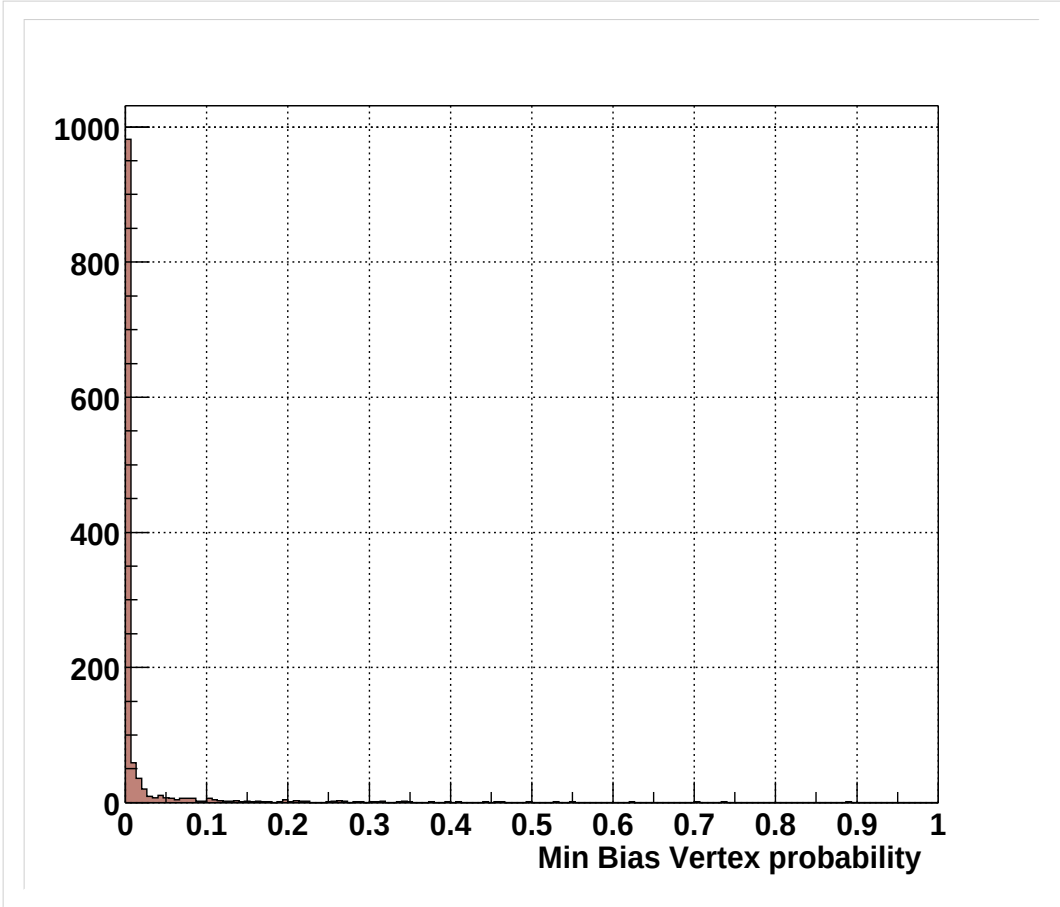

Figure 4.24: Vertex probability distribution for primary vertices in the simulation.

are most likely not attached to the primary vertex. The use of these tracks provides additional information to the probability discriminator.

4.5.2 Primary Vertex Selection Performance in the Data

In order to study the efficiency of the primary vertex selection in the data, we need to be able to identify hard scatter and min bias vertices in an unbiased way. For this purpose we selected di-muon events ($p_T > 2\,GeV/c$) where both muons were matched to global tracks and the z distance of closest approach between the 2 tracks was smaller than $500\,\mu m$. The p_T-weighted average z position of the di-muon object (mostly J/ψs) was identified as the hard scatter vertex z position. We then study the primary vertex selection efficiency in events with at least 2 reconstructed vertices separated by more than 2 cm. Figure 4.25 shows that, in average, there are 1.2 vertices in this data sample.

Figure 4.26 shows the distribution of $\log_{10}(p_T)$ for minimum bias interactions in the data and the simulation. Note that the track p_T turn-on is for $p_T > 0.5\,GeV$ or $\log_{10}(p_T) > -3$.

We could define the $F(p_T)$ distribution separately for data and Monte Carlo in order to account for the differences between simulated and real MB events, but since the agreement is reasonably good, we used the Monte Carlo $F(p_T)$ distribution also for the data.

The primary vertex selection efficiency, defined as the number of correctly identified hard scatter vertices divided by the total number of events, is $\epsilon_{|z|<40cm} = 0.97$.

4.6 Secondary Vertex Reconstruction

The track selection procedure described in Section 4.4 allows to pick tracks that are consistent with being produced in the $p\overline{p}$ collision. Secondary particles produced in

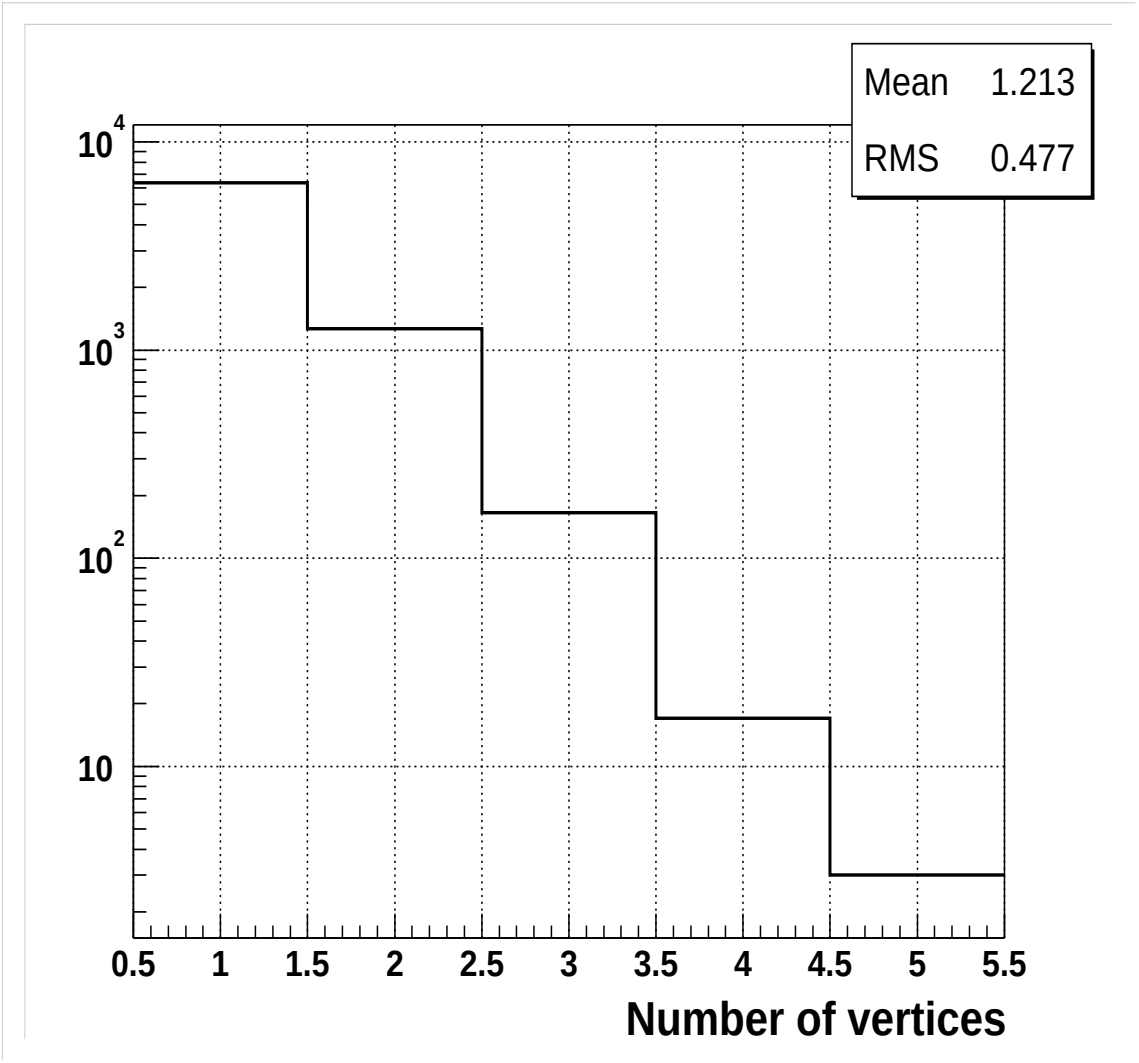

Figure 4.25: Vertex multiplicity distribution in di-muon data.

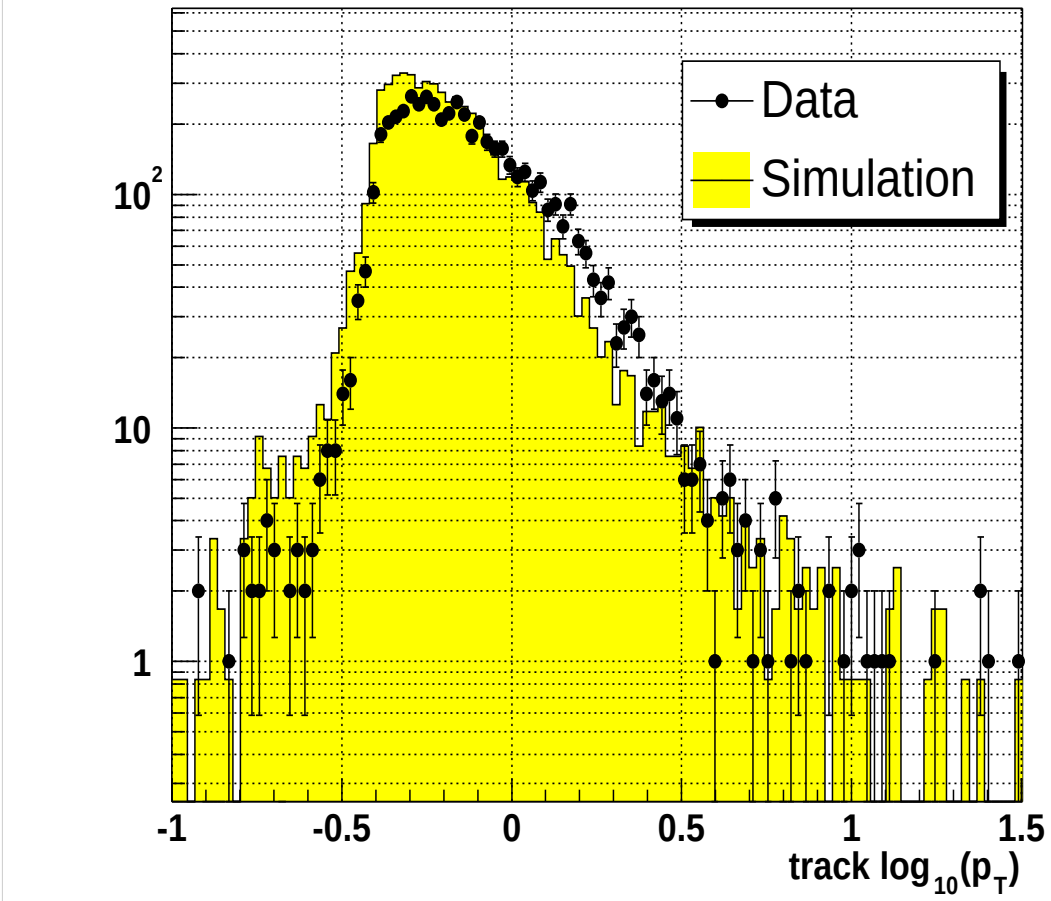

Figure 4.26: Distribution of minimum bias track $\log_{10}(p_T)$ for data (points) and the simulation (histogram).

the decay of long lived hadrons, tend to have large impact parameters. Therefore, secondary vertex tracks are most likely not attached to the primary or minimum bias vertices. The purpose of secondary vertex reconstruction is to be able to identify the decay of a B hadron from the signature of several tracks emanating from a common point displaced from the primary interaction.

As a first approach, we tried to use all remaining tracks unassociated to the primary and minimum bias vertices, produce all 2-track combinations seed vertices and attach additional tracks to seeds when the distance between them were small enough. This *build-up* method did not sucessfully work because the number of seed vertices formed was too large resulting in an enormous number of fake secondary vertices.

We finally decided to follow a more physics-motivated approach where we search for vertices combining the simple build-up technique with a requirement of a given physics content or topology of the vertices. The reconstruction of secondary vertices in jets for b-quark identification and exclusive $B^{\pm}$ mesons for lifetime measurements are the subject of the next two chapters. In this section we will describe the reconstruction of K^0_S and Λ (usually called *V0*s) secondary vertices which illustrate the ability to find real vertices in the data.

4.6.1 *V0* Vertex Reconstruction

The reconstruction of *V0* secondary vertices starts by fitting all pair of opposite charged tracks in the event. The identification of K^0_S and Λ vertices is done as a second step by considering their physics characteristics.

For the $K^0_S \rightarrow \pi^+\pi^-$ search, both tracks are assumed to be charged pions, whereas for the $\Lambda \rightarrow p^{\pm}\pi^{\mp}$, the highest p_T track is assumed to be the proton and the lowest p_T track the pion. These mass assignments are used in the calculation of the vertex invariant mass. The additional physics requirements are:

- Quality of the vertex fit: The vertex χ^2 probability ($prob(\chi^2)$) is required to be greater than 1%.

- Pointing to the primary vertex (collinearity): The momentum of the secondary vertex is required to point back towards the primary vertex where it is assumed to come from[1]. The vertex collinearity is defined as

$$\cos(\vec{L_{xy}}, \vec{p}_T) \tag{4.59}$$

  where L_{xy} is the transverse vertex decay length ($L_{xy} = \vec{r}_{SV} - \vec{r}_{PV}$) and $\vec{p}_T$ is the vertex total transverse momentum defined as $\vec{p}_T = (\sum_{j=1}^{N} p_j)\sin(\theta)$.

  The collinearity is required to be greater than 0.9999. Collinearity 1 means a perfect pointing towards the primary vertex. Collinearity 0 occurs when the momentum of the secondary vertex is orthogonal to its decay length. Collinearity -1 means that the secondary vertex originated before than the primary interaction, indicative of a fake vertex.

- Impact Parameter Significance ($|IP|/\sigma$): Since $V0$ vertices are displaced from the primary vertex, the track impact parameter significance is required to be greater than 3. Note that primary vertex reconstructions requires $|IP|/\sigma < 3$

Figure 4.27 shows the invariant mass distribution of K^0_S secondary vertex candidates before the quality cuts. A small K^0_S mass peak can be observed over a huge background.

Figures 4.28, 4.29, and 4.30 show the kinematic distributions of the three quality variables used for the K^0_S vertex selection.

The K^0_S invariant mass after the χ^2 and impact parameter significance cuts is shown in Figure 4.31. We can observe a significant improvement on the signal over the background.

[1]In the case of $B^0 \to K^0 + X$, the pointing is towards the B^0 vertex instead of towards the primary vertex.

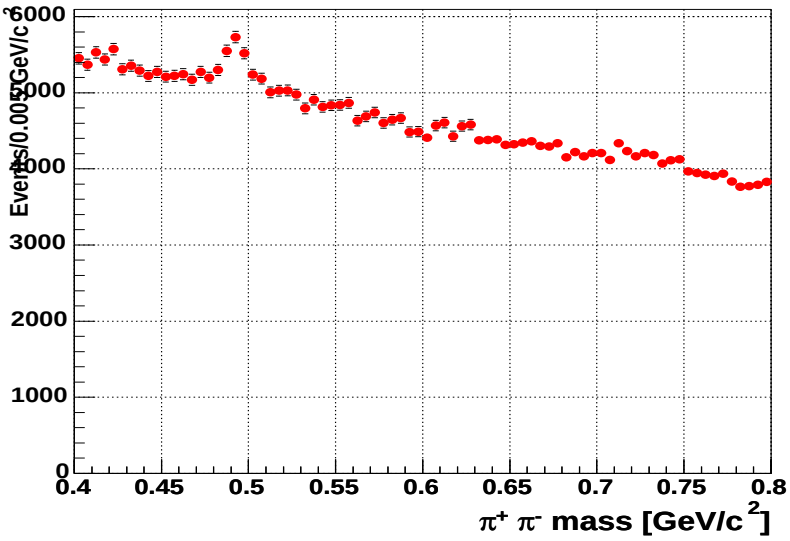

Figure 4.27: Invariant mass of K^0_S secondary vertex candidates before selection cuts.

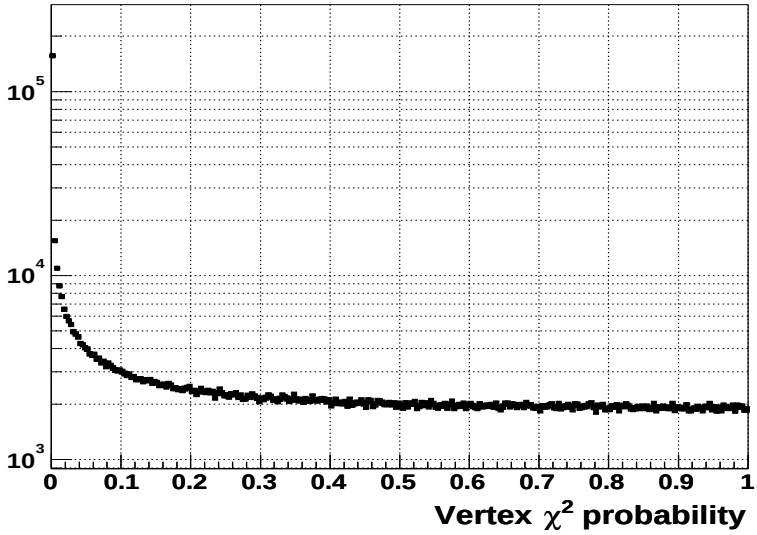

Figure 4.28: χ^2 probability distribution of secondary vertices.

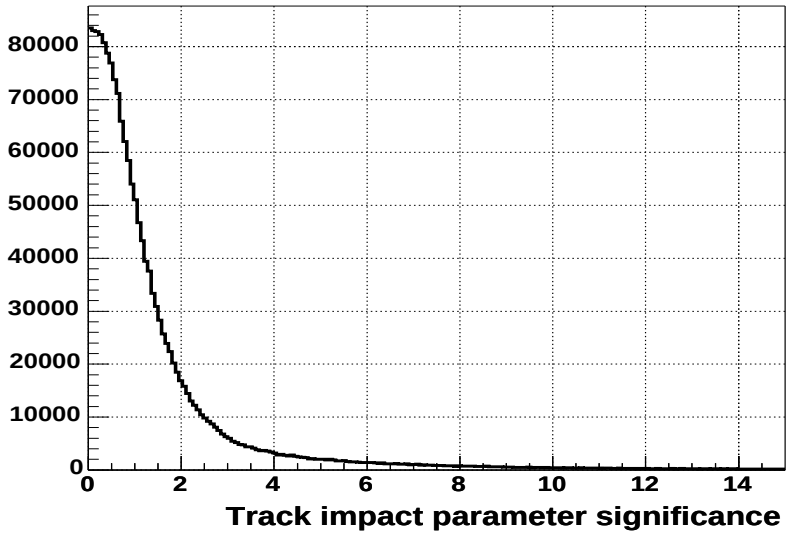

Figure 4.29: Impact parameter significance of tracks attached to secondary vertices.

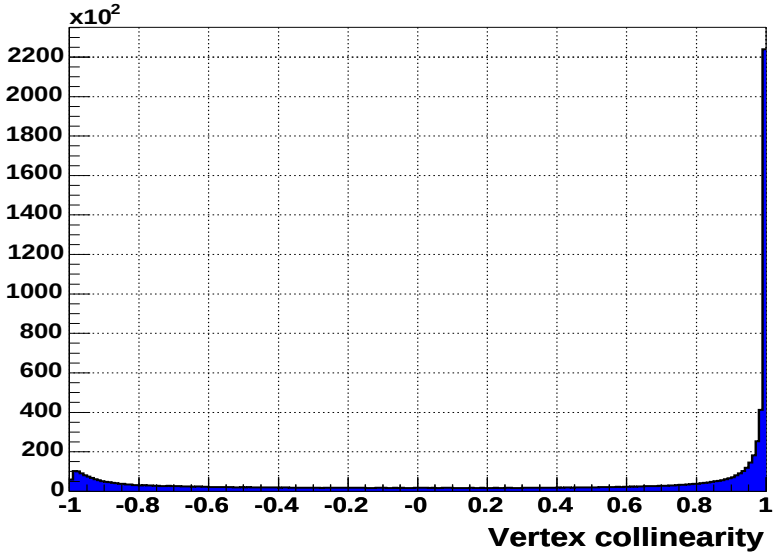

Figure 4.30: Collinearity distribution of secondary vertex candidates.

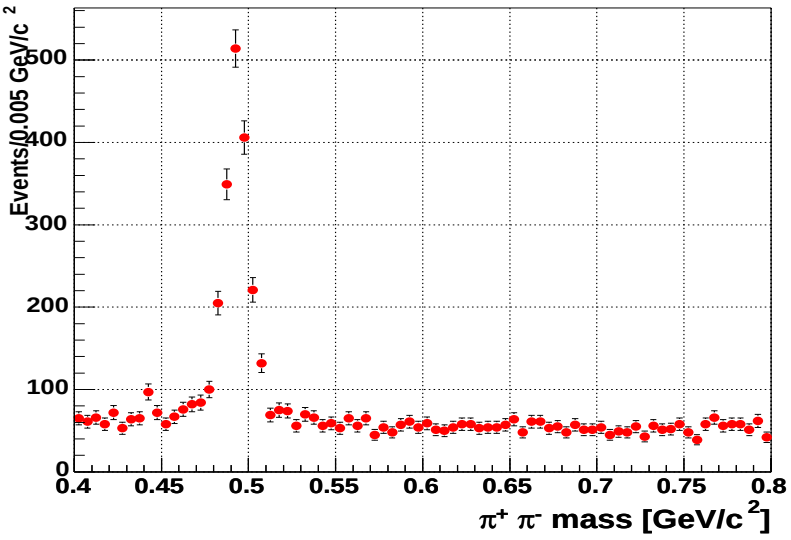

Figure 4.31: Invariant mass of K^0_S secondary vertex candidates for $prob(\chi^2) > 0.01$ and $|IP/\sigma| > 3$.

The vertex collinearity distribution after the preliminary quality cuts is shown in Figure 4.32, and its effect on the invariant mass distribution is shown in Figure 4.33.

Since the vertex Kalman Filter algorithm uses the re-fitted track momenta to compute the invariant mass distribution, its width is improved with respect to the same distribution based on the original track parameters. Thus, vertex reconstruction contributes in two aspects to the identification of *V0* secondary vertices: on the one hand, the vertex requirement allows to reduce background events, on the other hand, the vertex constraint fit of the track momenta, improves the mass resolution. For comparison, Figure 4.34 shows the same invariant mass distribution shown in Figure 4.33, using the original track parameters. The mass resolution is improved by a factor of 2.

The same quality cuts are applied in the identification of Λ and $\bar{\Lambda}$ secondary vertices, with the exception of the track mass assignment as it was already explained.

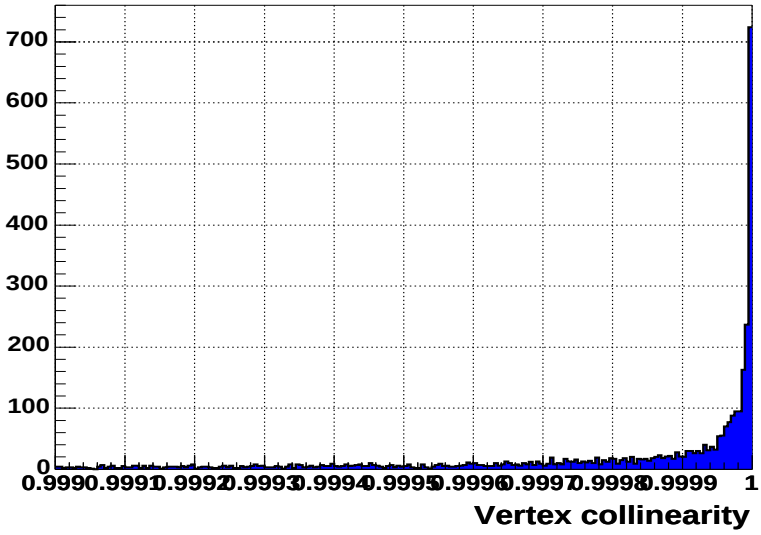

Figure 4.32: Collinearity distribution of secondary vertex candidates for $prob(\chi^2) > 0.01$ and $|IP/\sigma| > 3$.

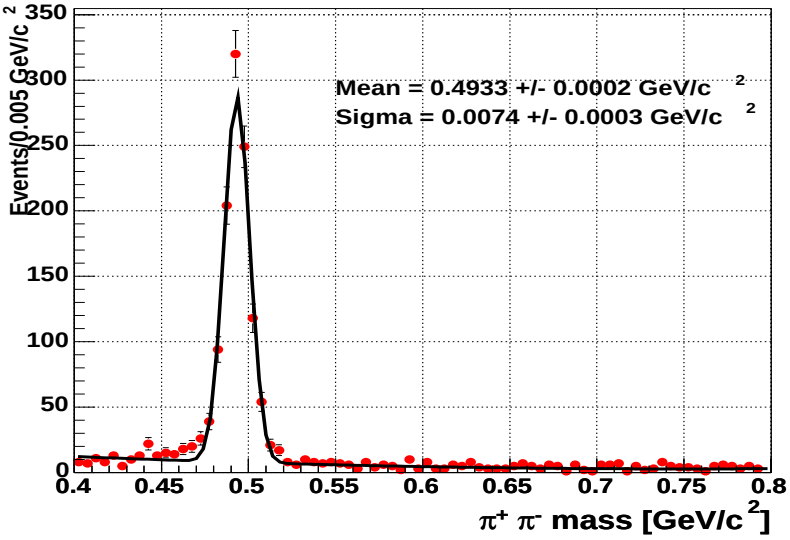

Figure 4.33: Invariant mass of K^0_S secondary vertex candidates for $prob(\chi^2) > 0.01$, $|IP/\sigma| > 3$, and collinearity> 0.9999.

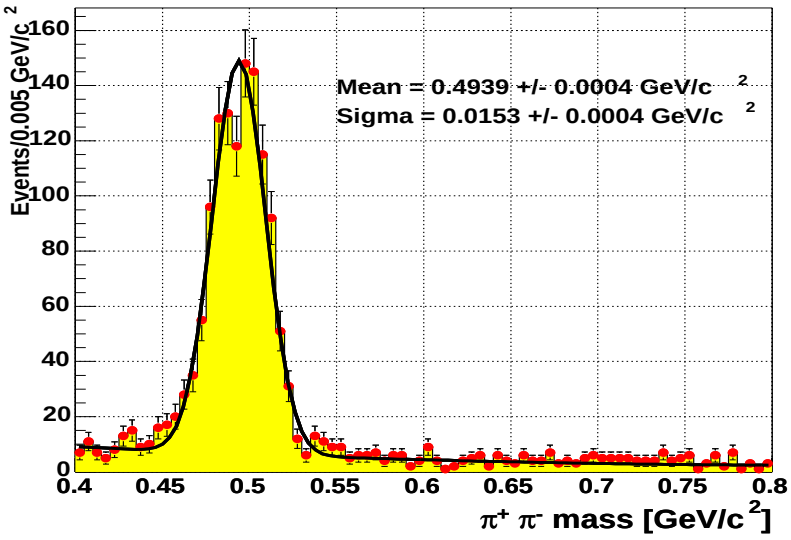

Figure 4.34: Invariant mass of K^0_S secondary vertex candidates for $prob(\chi^2) > 0.01$, $|IP/\sigma| > 3$, and collinearity> 0.9999 using the unconstrained vertex track parameters.

The invariant mass of the reconstructed candidates is shown in Figure 4.35.

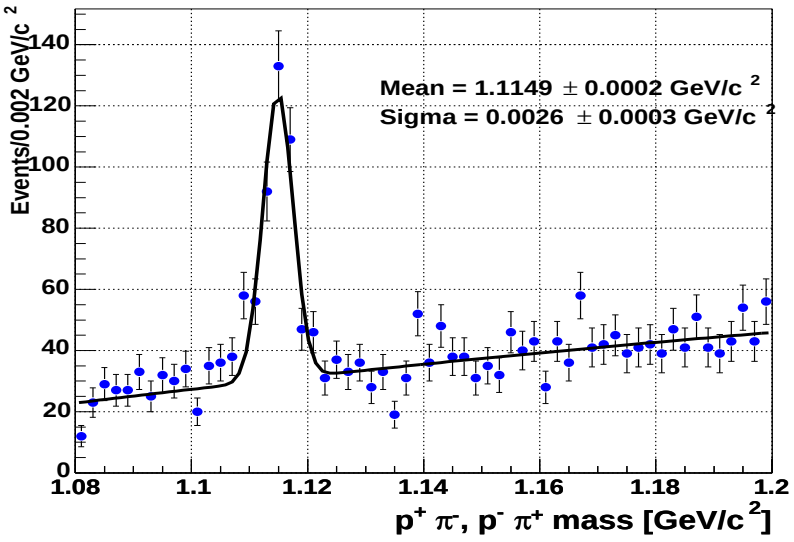

Figure 4.35: Invariant mass of Λ and $\bar{\Lambda}$ secondary vertex candidates for $prob(\chi^2) > 0.01$, $|IP/\sigma| > 3$, and collinearity> 0.9999.

Chapter 5

Secondary Vertex *b*-tagging

This chapter describes the development and optimization of the secondary vertex b-tagger algorithm (SVT) at DØ and its performance in simulated $t\bar{t}$ events and Run II data. Identification of b-quark jets is a crucial ingredient for many forefront physics analyses which will be done during Run II: top quark production, search for the Higgs Boson and search for exotic particles (SUSY and Technicolor), they all predict b-quark in the final states. As it was outlined in Chapter 4, we use a physics-oriented strategy for the search of secondary vertices in high p_T events, different from the method used for exclusive B meson reconstruction.

This chapter is organized as follows. Section 5.1 describes the main characteristics of B hadrons in top decays which will guide us in the development of the SVT algorithm. Section 5.2 describes the secondary vertex b-tagger algorithm. Its performance in Monte Carlo simulations and its optimization with Run II data are analyzed in Sections 5.3 and 5.4. In Section 5.5 we present the measurement of the efficiency for tagging b-hadron jets via secondary vertex reconstruction in the muon+jet data sample. We also derive the rate for mistagging a generic light quark jet as a heavy flavor jet using a multijet data sample. Finally, Section 5.6 shows a method to identify the b-jet flavor based on the charge of its associated tracks.

5.1 Kinematics of B Hadrons in Top Quark Decays

In this section we study the properties of B hadrons in top quark decays using a full Monte Carlo simulation of $t\bar{t}$ events in the $t \to Wb \to l\nu b$ and $\bar{t} \to Wb \to qqb$ channels. The goal is to guide the development and optimization of the secondary vertex b-tag algorithm to maximize the efficiency for identifying b-jets while minimizing the fake tag rate.

Figure 5.1 shows several kinematic distributions for B hadrons from top decays. The average p_T is $50\,GeV/c$ and almost all of them are within $|\eta| < 2$. The average number of charged particles with $p_T > 0.5\,GeV/c$ is 5 and the mean transverse decay length from the primary vertex is $\langle L_{xy} \rangle = 3\,mm$. 75 percent of the decay vertices have $L_{xy} > 1\,mm$.

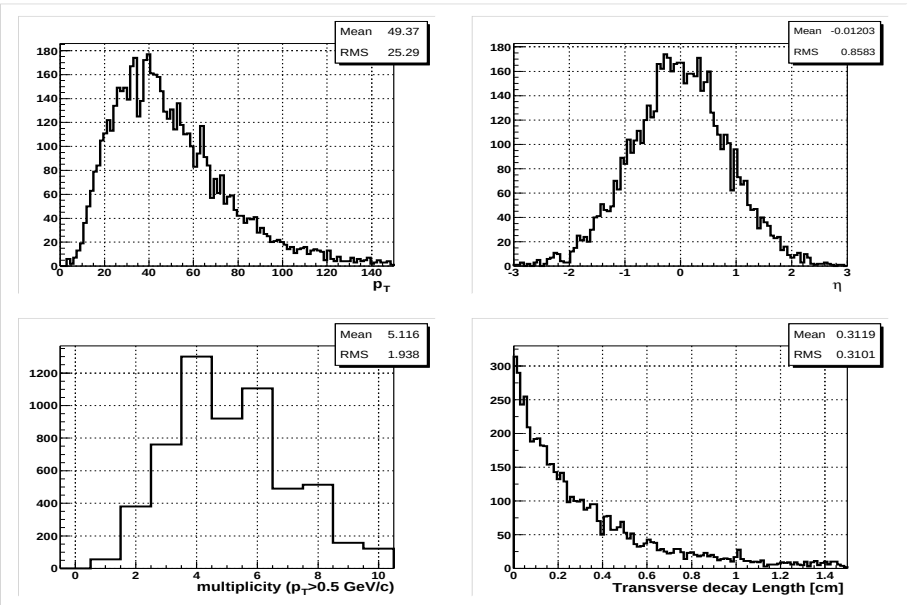

Figure 5.1: Properties of B hadrons in top quark decays.

Figure 5.2 shows the same kinematic variables for the sequentially decaying charmed D hadron. The mean transverse decay length from the B decay vertex

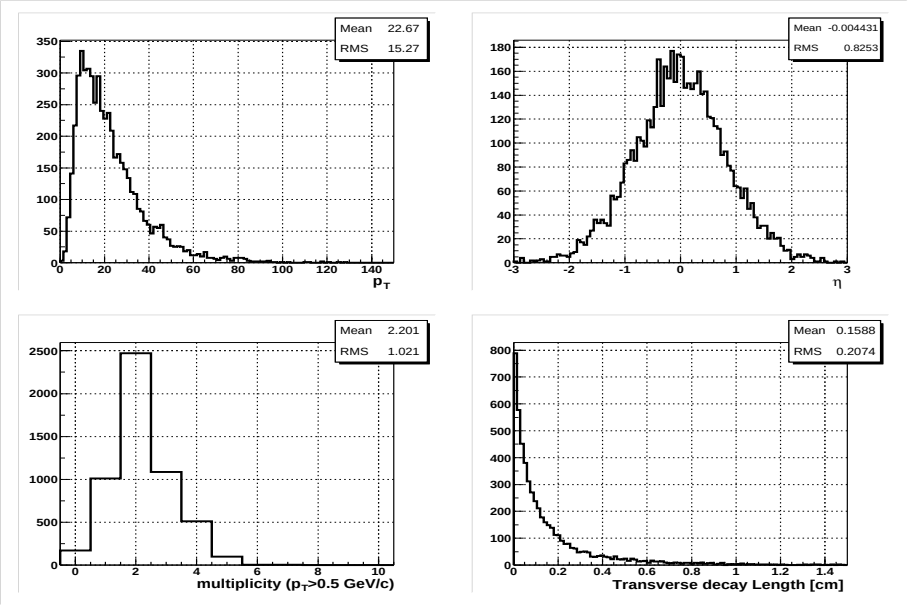

Figure 5.2: Properties of D hadrons in top quark decays.

is $1.6\,mm$ and its mean charged multiplicity is 2.2.

Figure 5.3 shows the $\Delta R = \sqrt{(\Delta\eta)^2 + (\Delta\phi)^2}$ distance between the B hadron direction and its decay charged descendants. Almost 99 percent of the B decay particles are within a $\Delta R = 0.5$ cone size around the B axis. The distance between the B and the sequential D hadron directions is shown in figure 5.4. D decay particles form a "sub-jet" not always pointing in the same direction of the B hadron.

Figures 5.5 and 5.6 show the transverse (dca) and longitudinal ($zdca$) impact parameter of B/D hadron decay particles. A cut of $|dca| < 0.15\,cm$ and $|zdca| < 0.4\,cm$ retains 99% of them. This cut is useful to remove charged tracks from long lived particle decays, such as K^0_S and Λ, which have very large impact parameters due to their $2.5\,cm$ and $7\,cm$ mean decay lengths.

Figure 5.7 shows the number of charged particles within a 0.5 cone around the B direction with impact parameter significance $S = dca/\sigma(dca)$ greater than 3 and for different B decay lengths. When $L_{xy} > 1\,mm$, more than 70% of the jets have at least 2 displaced charged particles with $|dca|/\sigma(dca) > 3$. The fraction of b-jets with at

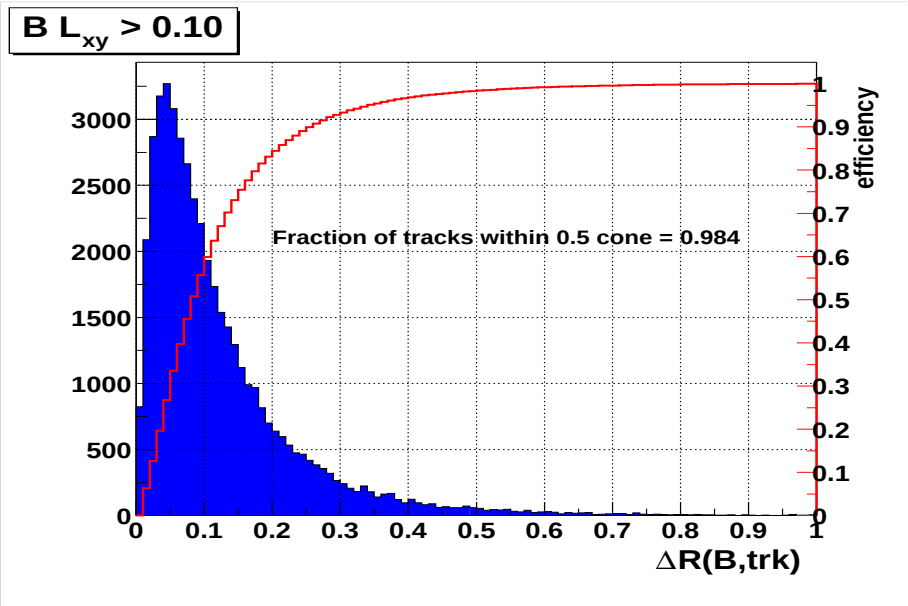

Figure 5.3: Distance between the B hadron direction and its decay charged daughters in $\eta - \phi$ space, when $L_{xy} > 1\,mm$

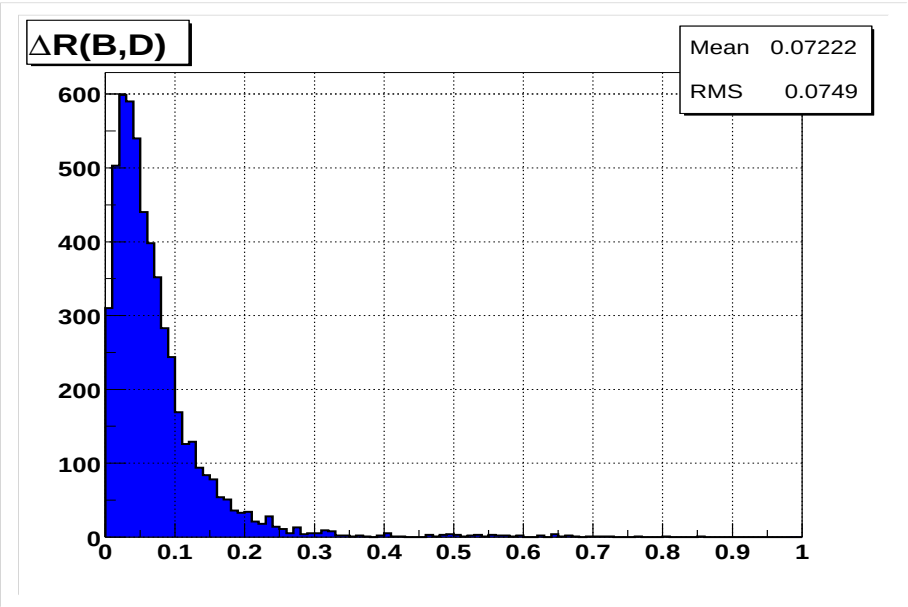

Figure 5.4: Distance between the B and the sequential D hadron directions in $\eta - \phi$ space.

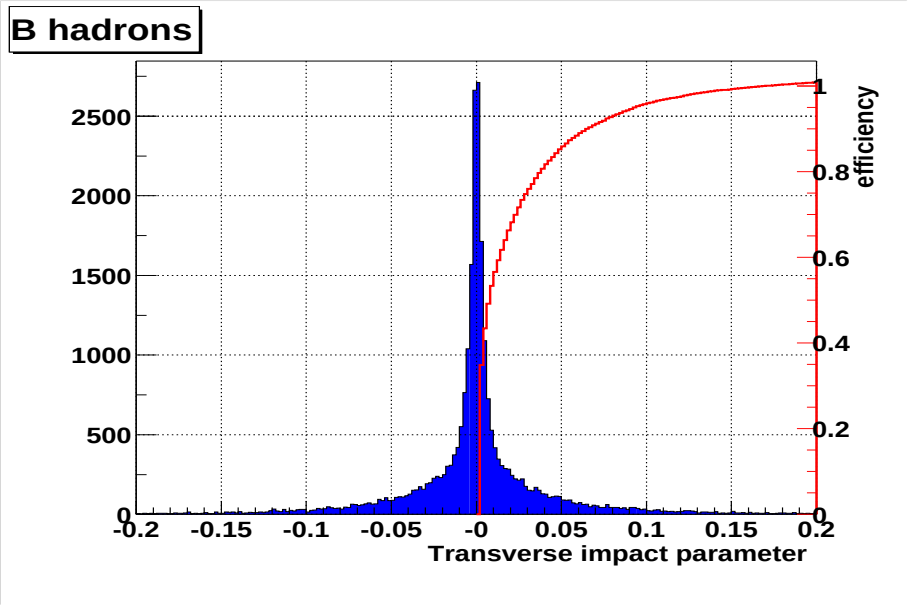

Figure 5.5: Transverse impact parameter of B and D hadron decay particles.

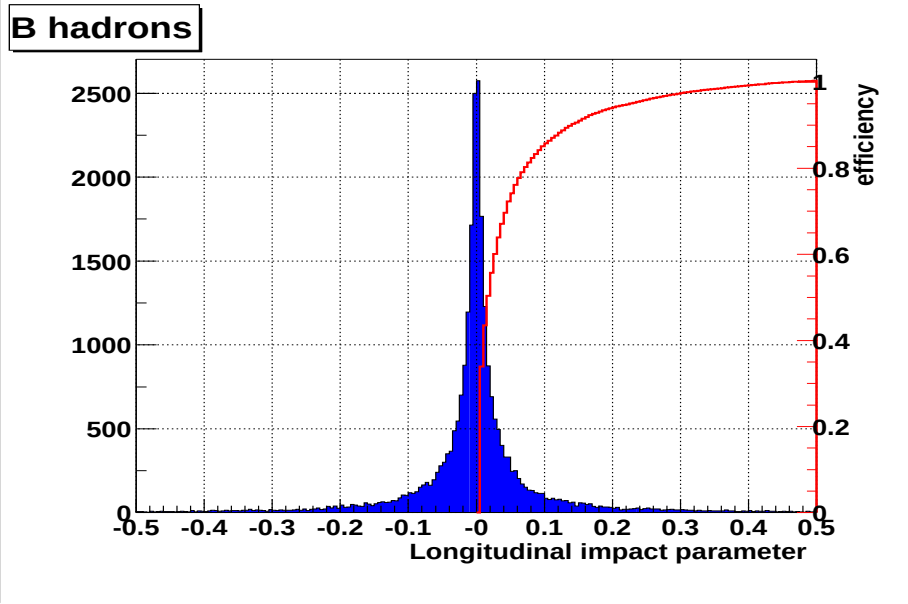

Figure 5.6: Longitudinal impact parameter of B and D hadron decay particles.

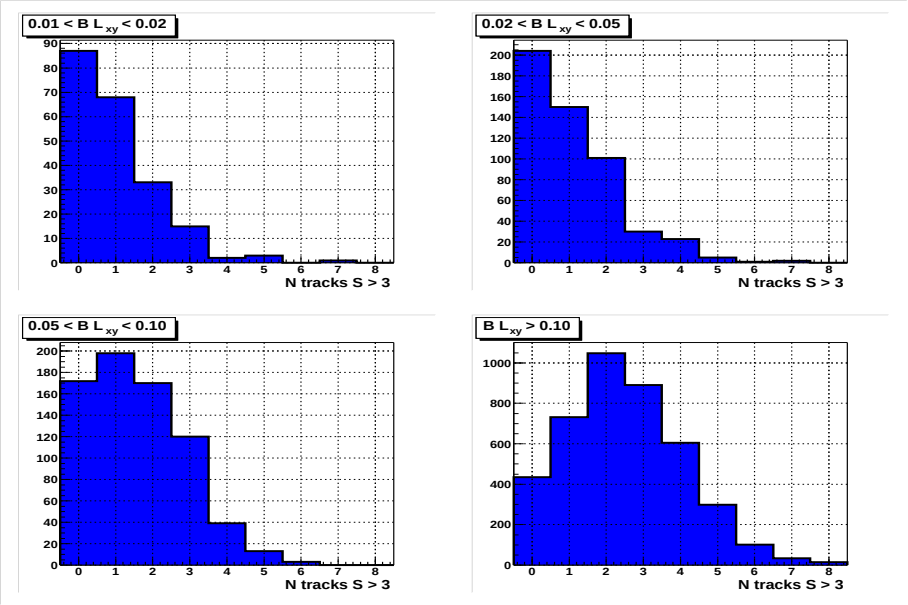

Figure 5.7: Number of charged particles within a 0.5 cone around the B direction with impact parameter significance greater than 3.

least two displaced charged tracks is shown in figure 5.8 as a function of the B hadron decay length and for different significance values. These plots are important for they give us an idea of what level of efficiency we can expect in b-tagging. For short transverse decay lengths L_{xy}, the efficiency will be low because charged decay tracks can't acquire a large impact parameter and will therefore be mistaken as originating from the primary vertex. Only for $L_{xy} \gtrsim 1\,cm$ do we attain enough resolving power. Fig. 5.8 indicates that this could be increased by lowering the significance cut, S. But this is a compromise solution which increases the background, because at low S we start picking up tracks coming the primary interaction, unrelated to the B decay chain.

It was shown that the charmed D hadron mean decay length from the B vertex is $0.16\,cm$, so it is expected that a significant fraction of the time, both vertices will not be resolved by the vertex reconstruction. This means that very often, the secondary vertex algorithm will *merge* B and D particles into a common vertex. The

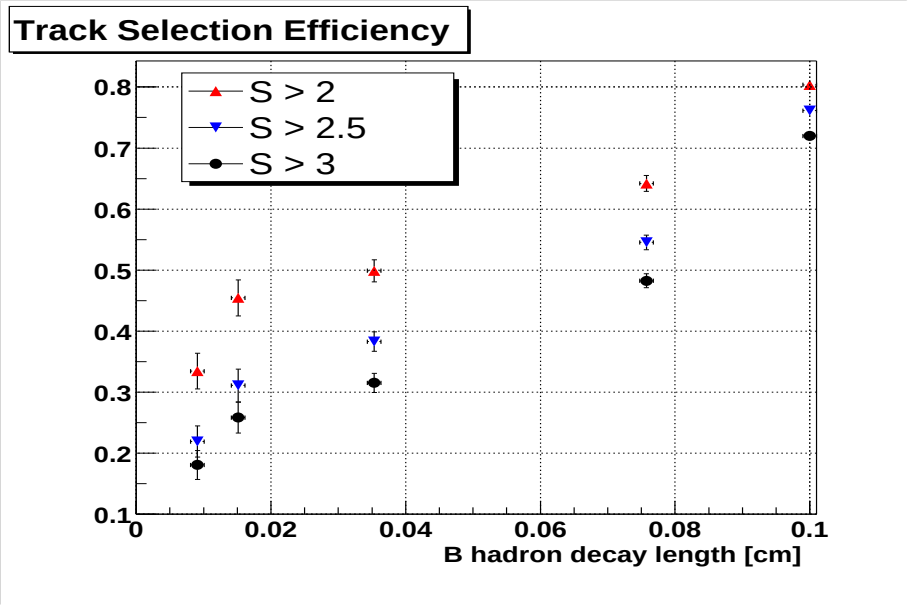

Figure 5.8: Fraction of b-jets with at least two displaced charged tracks as a function of the B hadron decay length. Different symbols correspond to different impact parameter significance values.

influence of D hadron particles to the reconstruction of b-jets was studied by finding a secondary vertex from all tracks with $dca/\sigma(dca) > 3$ within b-jets and comparing the reconstructed vertex decay length with the B hadron true decay length. The results are summarized in figures 5.9 and 5.10

The negative tail in figure 5.9 shows that most of the time, tracks from the tertiary D vertex are included in the fit, either by combining D with B tracks or by reconstructing both decay vertices. This is confirmed in figure 5.10 which shows that the negative tail almost disappears when we plot the decay length difference between the reconstructed vertex and the closest Monte Carlo vertex (B or D).

These studies indicates that D particles are important for b-jet secondary vertex tagging since they can often be associated to the reconstructed displaced vertex from a b-jet.

As a summary, we have seen that we can identify b-quark jets from top decays by

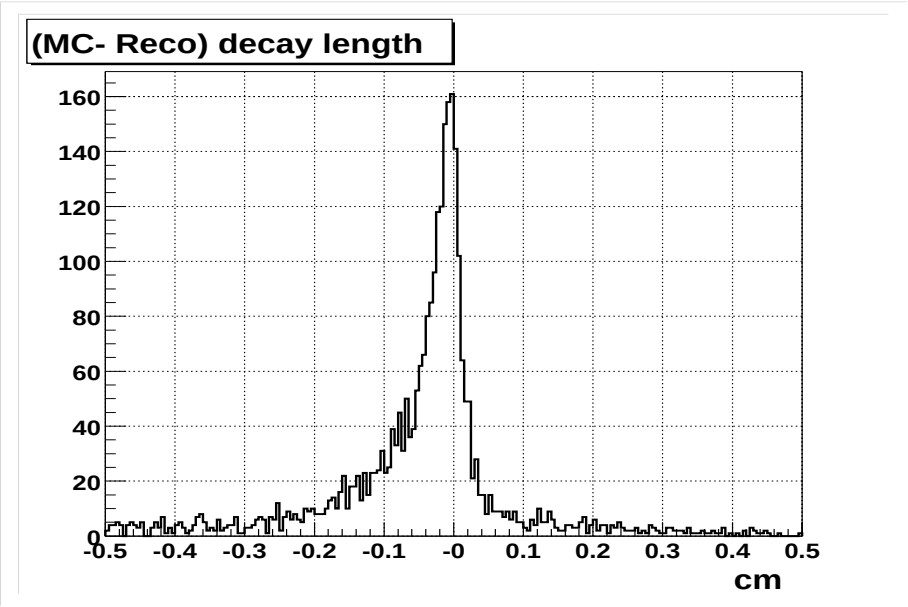

Figure 5.9: Decay length difference between the Monte Carlo generated B hadron and the reconstructed vertex. The negative tail indicates that tracks from the tertiary D vertex are included in the fit

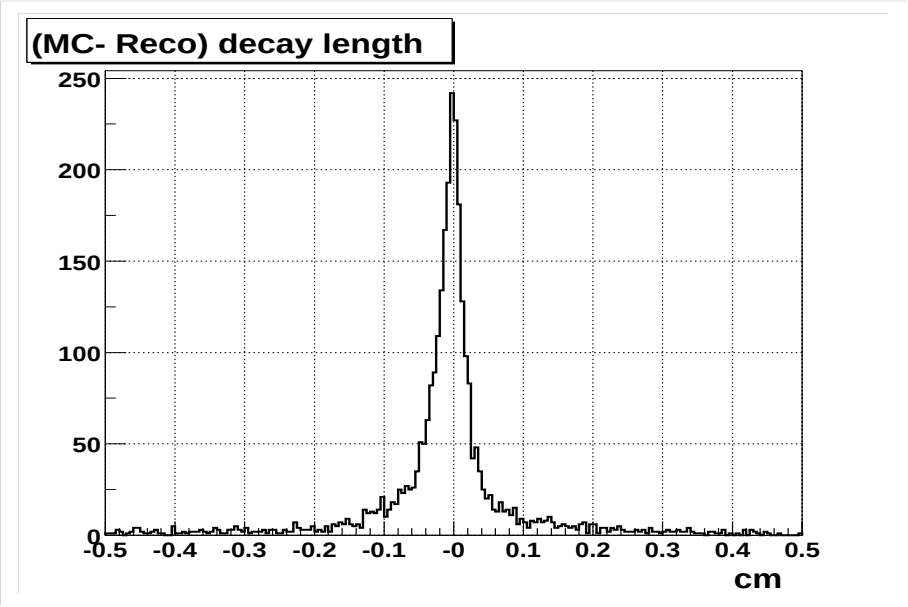

Figure 5.10: Decay length difference between the closest Monte Carlo generated B/D hadron and the reconstructed vertex.

tagging long lived hadron decay vertices within jets. The decay of B and D hadrons consists of several charged particles emanating from a displaced vertex, with large impact parameter significance. Note that our goal is to *tag* jets from b-quark decays without the exclusive vertex reconstruction of the B/D hadron decays. With this in mind, we have seen that it is important to make use of the charmed tracks to increase the b-jet reconstruction efficiency.

In the next sections we describe the development and optimization of the secondary vertex algorithm guided by these Monte Carlo studies.

5.2 The Secondary Vertex b-tagging Algorithm

The secondary vertex b-tag algorithm consist of three main steps: the identification of the primary interaction vertex, the reconstruction of displaced secondary vertices, and the association of secondary vertices with calorimeter jets. The first two steps are independent from the last one since vertex reconstruction relies on tracking information only.

In this section we first review the primary interaction vertex reconstruction and then discuss the four steps composing the search for secondary vertices: track-jet reconstruction, track selection, vertex finding and vertex selection.

5.2.1 Primary Vertex Determination

The reconstruction and selection of the event primary vertex was already discussed in detail in Chapter 4. Here a brief outline is presented.

The primary vertex identification consists of 2 steps: first, the reconstruction of all interactions in a given event, and second, the selection of the hard scatter primary vertex.

Primary vertices are found using a *Tear-down* finding approach: First, tracks are

clustered along the z axis by means of a cone algorithm and tracks with small impact parameter significance with respect to $(0,0)$ are selected. All selected tracks are fitted together to a common point and the χ^2 contribution of each individual track to the vertex is computed. The track with the highest χ^2 contribution is excluded and the vertex is re-fitted. This process is iterated until the vertex $\chi^2/ndof$ is smaller than 10. After a vertex is found, the whole procedure is repeated using the remaining tracks in the event until no more tracks can be vertexed.

The selection of the hard scatter vertex is based on a probabilistic algorithm described in more detail in Section 4.5. Based on the different p_T spectrum between tracks from minimum bias and hard interactions, a track minimum-bias probability (MB-probability) is built integrating the distribution of track $\log_{10} p_T$ -obtained in minimum bias events- from a given track p_T to infinity (i.e. the MB-probability is the probability that a track from a minimum bias interaction can be reconstructed with momentum p_T or higher). For each vertex, the individual track MB-probabilities are combined to define a *vertex* MB-probability. The vertex with the smallest MB-probability is selected as the hard scatter primary vertex of the event. Figure 5.11 shows the vertex and track multiplicities, and the z distribution of the selected hard scatter vertex in the qcd_em data sample.

5.2.2 Track-Jet Reconstruction

Motivated by the kinematic characteristics of B hadron decays in Top events, the search for displaced secondary vertices can be greatly simplified if we first pre-cluster tracks within cone jets. As it was shown in 5.1, more than 98% of the B decay particles are within a 0.5 cone around the B direction.

There are a number of advantages in using track-based jets instead of calorimeter jets (or a combination of both). Track-based jets are not correlated with noisy jets and are not affected by the tracker-calorimeter alignment. In addition, track-jets

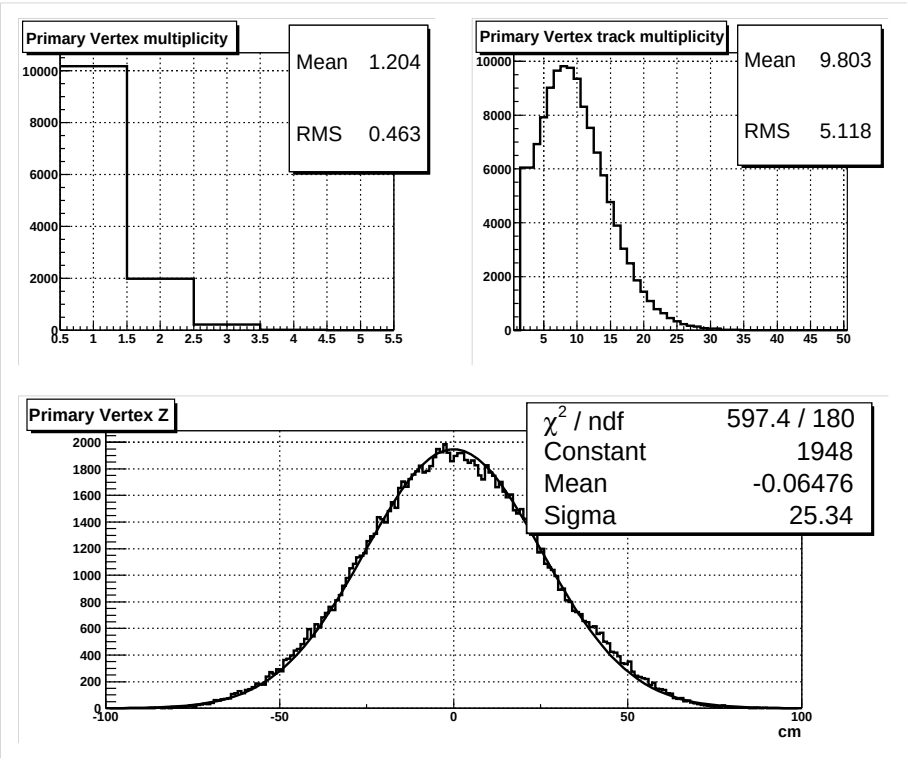

Figure 5.11: (a) Number of reconstructed primary vertices, (b) selected primary vertex track multiplicity, (c) selected primary vertex z position.

make use of the 3-Dimensional capabilities of the tracker detector allowing to build 3-Dimensional objects. This represents an advantage over the more common 2-Dim association of tracks around calorimeter-based jets, because 3D track-jets are not sensitive to minimum bias interactions. Furthermore, tracking information allows to reconstruct low p_T jets, whereas calorimeter jets have an energy threshold of $8\,GeV/c$.

There are many other advantages by using a track-jet clustering algorithm to preselect tracks prior to secondary vertex reconstruction: the number of tracks input to the vertex fitting algorithm is significatly reduced, the influence of fake or unrelated tracks is minimized with no loss of efficiency, and the vertex reconstruction becomes independent from calorimeter information since only tracking information is used.

The track-jet reconstruction consists of three main steps: Z pre-clustering, track selection and jet-clustering:

1. **Z pre-clustering**: cluster tracks according to their z of closest approach with respect to $z = 0$.

   - Order tracks by p_T
   - Looping in descendent order of track p_T, tracks are added to the Z pre-cluster if $\Delta z < 2\,cm$, where Δz is the difference between the z of closest approach of the track to the origin and the pre-cluster z-average position.

2. **Track Selection**: For every pre-cluster, identify its reconstructed vertex by choosing the primary vertex with the highest multiplicity within 2 cm of the center of the pre-cluster. Then select tracks with the following criteria:

   - $Nsmt \geq 3$.
   - $p_T > 0.5\,GeV/c$.

- $|dca| < 0.15\,cm.$
- $|zdca| < 0.4\,cm.$

These cuts are motivated by the kinematics of B hadrons in $t\bar{t}$ Monte Carlo, and by the track quality studies in data (section 5.4). The impact parameters, $|dca|$ and $|zdca|$, are calculated with respect to the previously associated primary vertex.

3. **Jet-Clustering**: For every pre-cluster of selected tracks, cluster tracks in the (η, ϕ) plane using a jet algorithm. We have implemented two different jet-clustering algorithms, as discussed below.

The Simple Cone Algorithm

The cone algorithm basically combines in a jet all tracks lying within a πR^2 area in $\eta - \phi$ space. Its steps are:

- Starting with the highest $p_T > p_T^{seed}$ track, η and ϕ are calculated.
- Looping in descending order of track p_T, tracks are added to the jet cone if

$$\Delta R = \sqrt{(\Delta\phi)^2 + (\Delta\eta)^2} < R \tag{5.1}$$

  where R is the cone size.
- Once a track has been added to the jet, the jet variables are re-computed by adding the track 4-momentum.
- The process is repeated until no more seed tracks are left.

The k_T algorithm

The k_T algorithm attemts to reconstruct back the decay chain leading to the final jet. It clusters tracks recursively, by merging them either when they are close in $\eta - \phi$ space, or when one of them is very soft:

1. For every pair of tracks, compute

$$d_{ij} = \min(p_{Ti}^2, p_{Tj}^2) \left(\frac{\Delta R_{ij}}{D} \right)^2 \qquad i \neq j \tag{5.2}$$

$$d_{ii} = d_i = p_{Ti}^2 \qquad i = j \tag{5.3}$$

2. Find the minimum of all d_{ij} and d_i.

3. If the minimum is a d_{ij} ($i \neq j$), combine tracks i and j into a composite object k by adding their 3-momenta, and remove i and j from the list.

4. If the minimum is a d_i, then store the list of tracks associated to object i as a jet if it contains 2 or more tracks, at least one with $p_T > 1\,GeV/c$.

5. Iterate until all tracks are clustered.

The parameter D ensures that objects cannot be clustered if their separation is greater than D. However, since an object here is a combination of one or more tracks, tracks with $\Delta R > D$ can end up associated to the same track-jet.

The motivation for introducing the k_T algorithm, a successive recombination scheme which is not limited to a given cone size, is that it might provide better performance than a fixed cone algorithm to identify all the final particles from a b-jet, specially those from the tertiary D decay vertex.

In the following sections we describe the track jet reconstruction process, both for the cone and the k_T algorithms, and discuss the optimization of the parameters involved in track preselection and jet +reconstruction. We then measure (a) the efficiency to find track jets, showing that it is basically governed by the track reconstruction efficiency, and (b) its angular resolution, which turns out to be similar to the calorimeter resolution even though track jets are not sensitive to neutral particles. We study in detail the case when two track jets correspond to the same calorimeter jet, and analyze its dependence on the algorithm and jet size.

Track-Jet Parameter Optimization

In order to discriminate track-jets made of particles from the underlying event, we studied the properties of track-jets associated to the primary interaction and track jets from the additional minimum bias interactions in the data.

We use the same event selection described in the previous section and we identify as hard interaction track-jets all those associated to the vertex with the smallest minimum bias probability of the event. All remaining track-jets were identified as minimum bias jets. We required minimum bias vertices to be more displaced than 10 centimeters from the primary vertex.

Figure 5.12 compares the distance between track-jets and the closest calorimeter jet for primary and minimum bias track-jets. We see how min bias track-jets do not show any correlation with calorimeter jets. Primary track-jets show on the contrary a strong correlation with calorimeter jets, over a constant background arising from difference sources such us underlying event jets, wider jets reconstructed as 2 jets, fakes, etc.

Figures 5.13 and 5.14 show the number of track-jets and the number of attached tracks to them for primary and minimum bias jets. We observe a much smaller number of track-jets associated to minimum bias interactions, most of them being composed of only 2 tracks. These result is intuitively consistent with the picture of the primary interaction as the one giving rise to a high p_T high multiplicity inelastic $p\bar{p}$ collision. Remark also that it serves as a consistency check, for the primary vertex identification was not based on track-jets nor multiplicities, but only on the p_T spectrum of the intervening tracks.

Figures 5.15 and 5.16 show the total track-jet p_T and the seed p_T (highest p_T track) for primary and minimum bias jets. As expected, we observe that minimum bias jets are made of softer tracks than primary jets. Based on Figure 5.16, we will select track-jets requiring a seed $p_T > 1\,GeV/c$, which keeps 99% of the primary

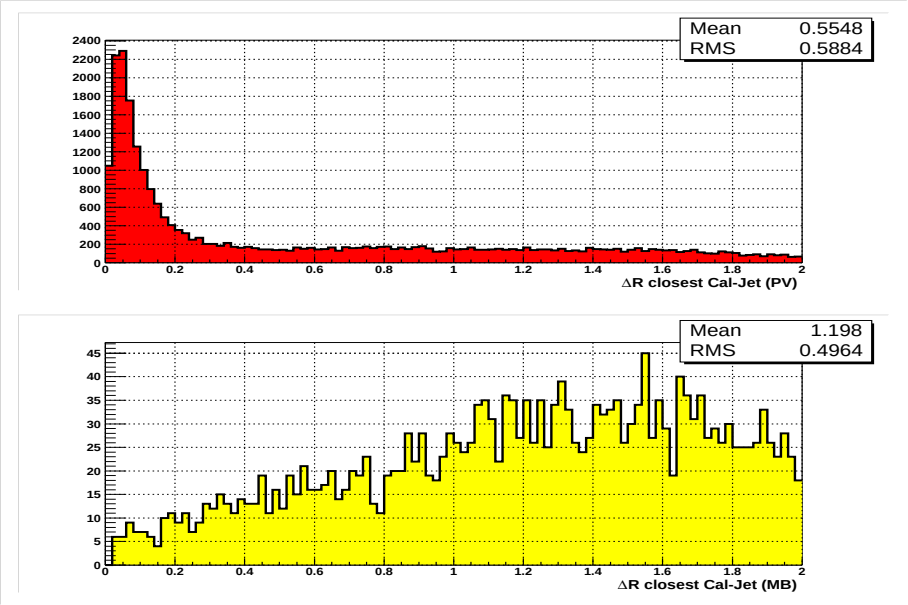

Figure 5.12: Distribution of the ΔR distance between track-jets and calorimeter-jets in primary and minimum bias interactions

track-jets and rejects 40 percent of the underlying event jets.

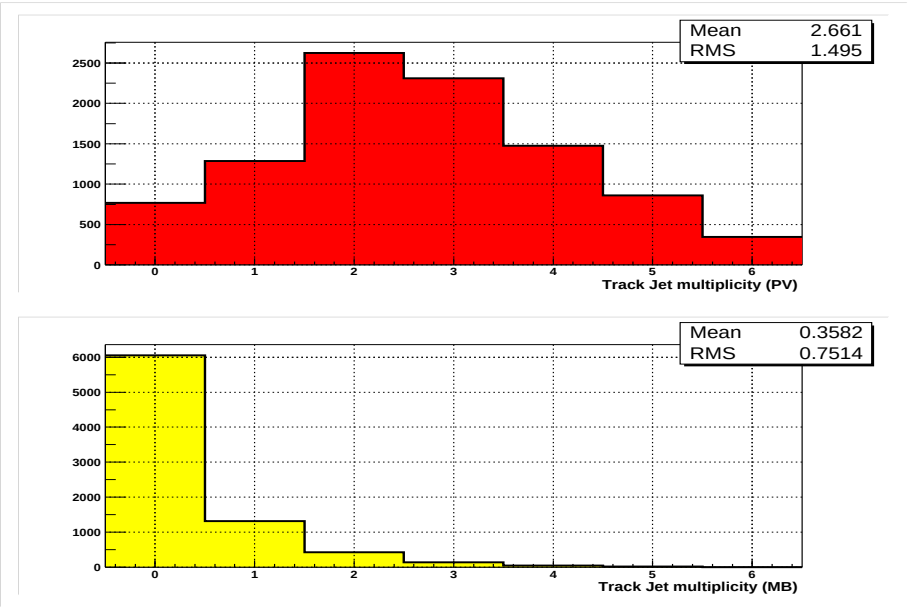

Figure 5.13: Number of track-jets in primary and minimum bias interactions

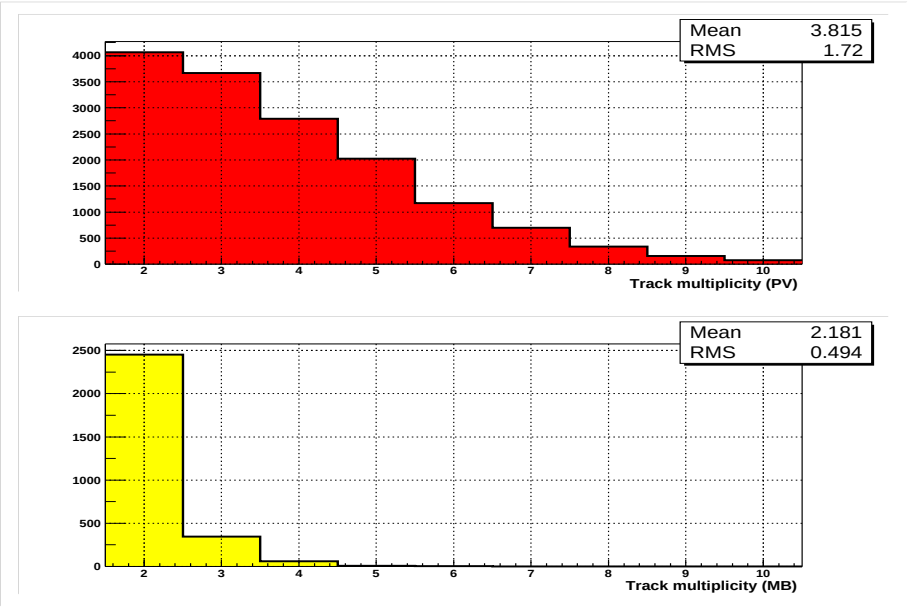

Figure 5.14: Track multiplicity for primary and minimum bias track-jets

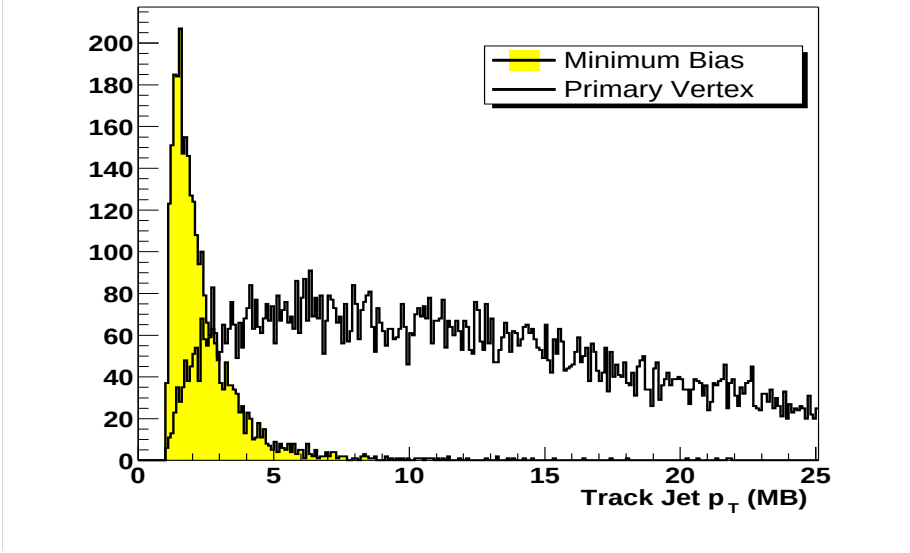

Figure 5.15: Total track-jet p_T for primary and minimum bias jets

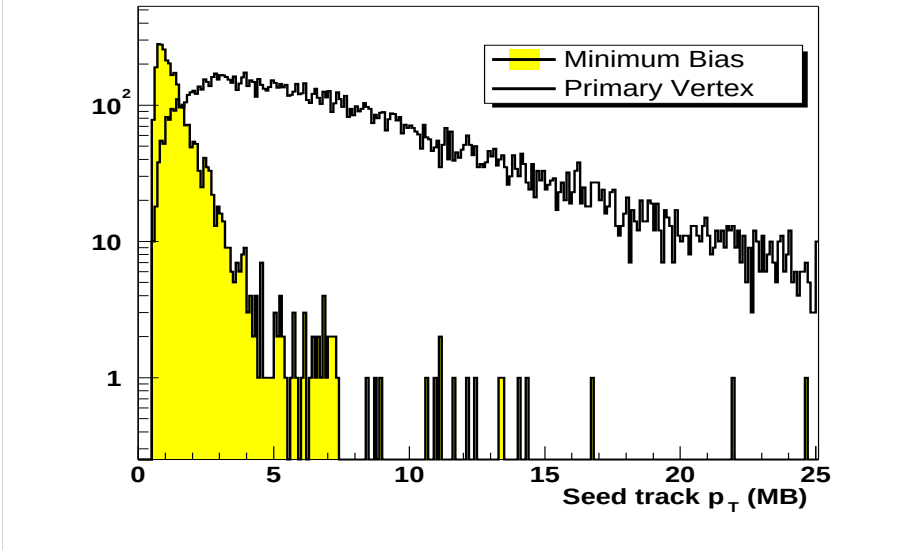

Figure 5.16: Track-jet seed p_T for primary and minimum bias jets

Track-Jet Clustering Performance in Data and Monte Carlo

In this section we study the performance of the track-jet algorithms in di-jet data and $t\bar{t}$ simulated events. We will focus on efficiency, angular resolution and the presence of extra jets due to the lack of the splitting and merging scheme, like the one used for calorimeter jets.

Efficiency

We define the efficiency to reconstruct track-jets in data, as the fraction of calorimeter jets ($p_T > 20\,GeV/c$, $|\eta| < 2.0$) matched to a track-jet within $\Delta R < 0.5$. We also define the double jet efficiency as the fraction of di-jet events with both calorimeter jets matched to track-jets.

Single and double efficiencies are shown in figures 5.17 and 5.18 for the cone algorithm, and in figures 5.19 and 5.20 for the k_T case. The efficieny is not symmetric along z due to hardware ineficiencies in the south SMT detector.

The main source of inefficiency is the tracking efficiency, that is, the absence of 2 or more good tracks pointing to the calorimeter jet axis. In effect, the fraction of calorimeter jets with 2 good tracks within $\Delta R < 0.5$, that are matched to a track-jet, is 98% for R=0.5 cone jets, 99% for k_T D=0.5, and 100% for R=0.7 cone and D=0.7 k_T jets. Here good track means that it passes the quality requirements used to build track-jets.

Angular Resolution

The angular resolution is measured by comparing $\Delta\phi$ between calorimeter jets and their closest track-jets.

Figure 5.21 shows the $\Delta\phi$ resolution in the data and the simulation for 0.5 cone track-jets with four or more attached tracks. The fraction of events in the tails in the simulation and the data are 0.10 and 0.14 respectively.

Figures 5.22 and 5.23 compare the $\Delta\phi$ resolution in the data for cone and k_T jet algorithms as a function of the number of tracks in the jet. The resolution was

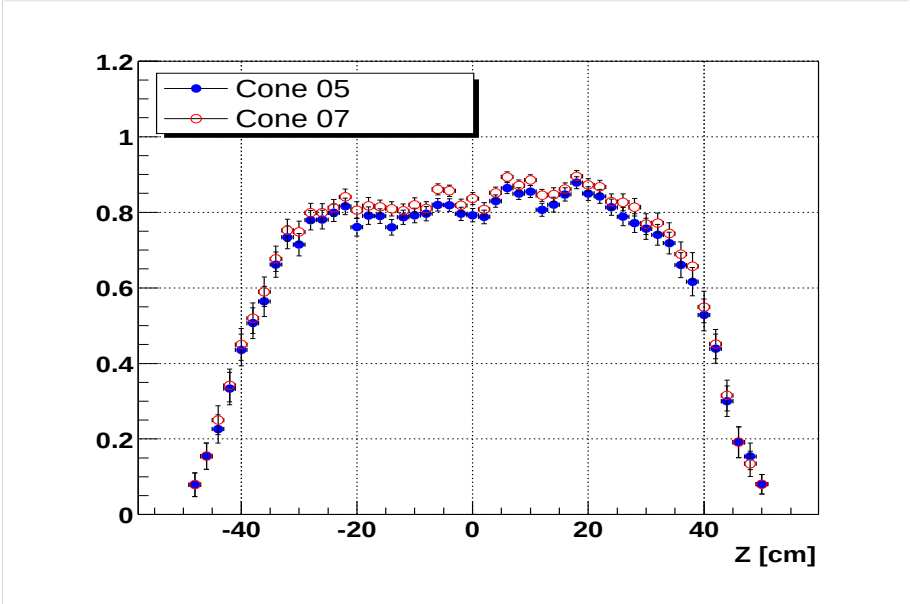

Figure 5.17: Single track-jet efficiency for the cone algorithm: fraction of calorimeter jets matched to track-jets in the data.

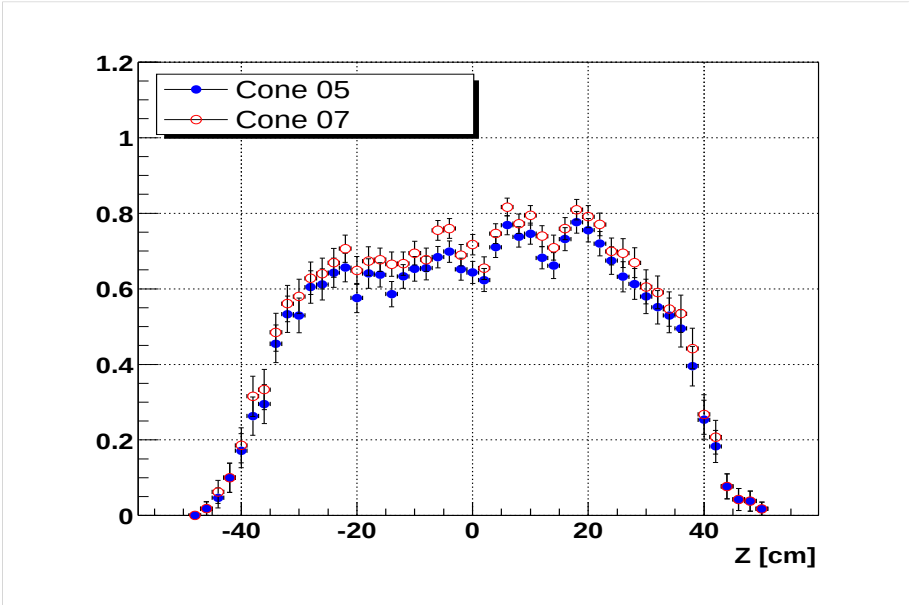

Figure 5.18: Double track-jet efficiency for the cone algorithm: fraction of back-to-back di-jet events with both calorimeter jets matched to track-jets.

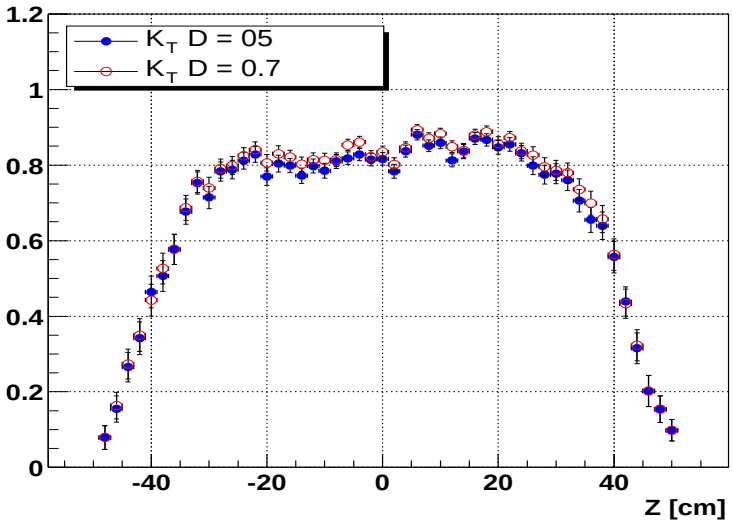

Figure 5.19: Single track-jet efficiency for the k_T algorithm.

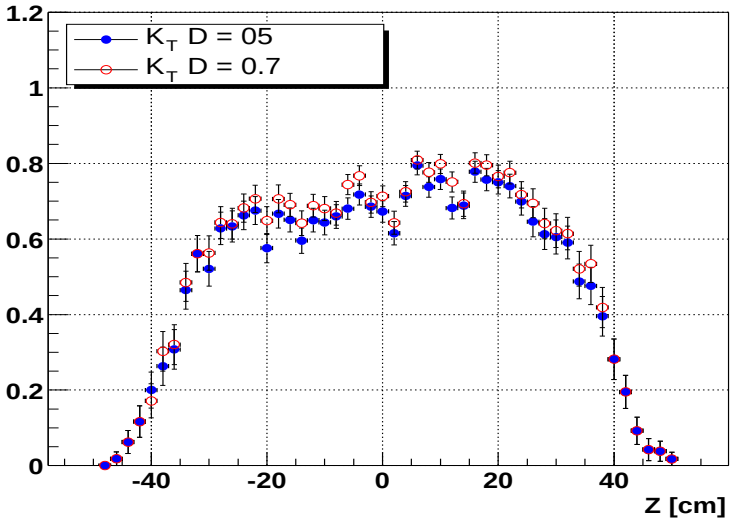

Figure 5.20: Double track-jet efficiency for the k_T algorithm.

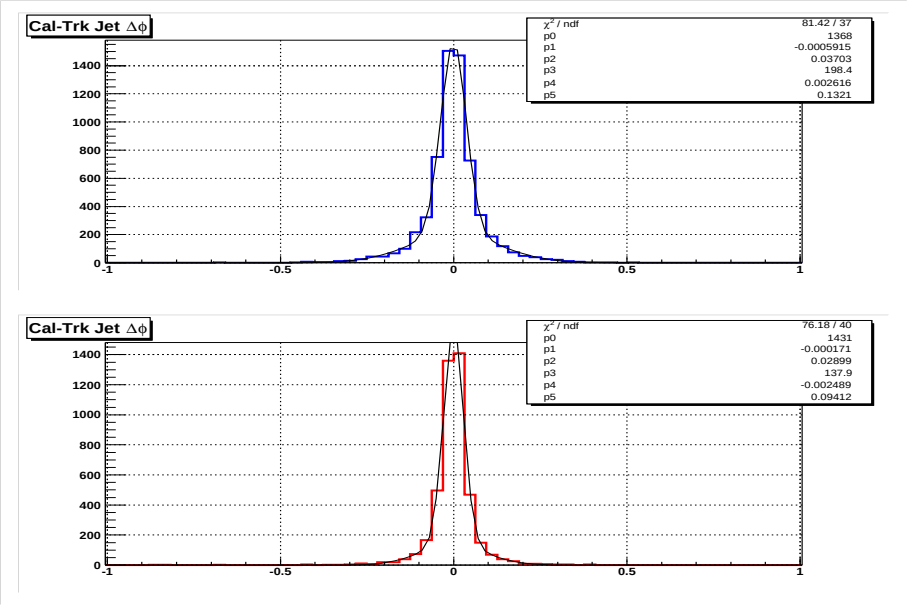

Figure 5.21: $\Delta\phi$ resolution in the data (above) and in the simulation (below) for R=0.5 cone track-jets with 4 or more attached tracks.

obtained with a single Gaussian fit. We observe that increasing the size of the clustering algorithm degrades the angular resolution. On the other hand, this one improves, as expected, when the number of tracks is larger.

The track-jet multiplicity distribution in the data and the simulation is shown in Figure 5.24 for the 0.5 cone algorithm. There is an average of one additional track in the simulation than in the data, and an excess of 2- and 3-track jets in the latter.

Extra Jets

If the ΔR distance between tracks from jet hadronization is wider than the size used in the jet clustering algorithm, instead of finding a single track-jet pointing in the direction of the calorimeter jet, we could find one or more additional low multiplicity track-jets also pointing in the same direction but with larger ΔR with respect to the calorimeter jet. These extra jets can be identified by looking at the second best calorimeter/track-jet match. A peak around $\Delta R \lesssim R_0$ would be indicative of the presence of extra-jets, where R_0 is the either the cone size R or the

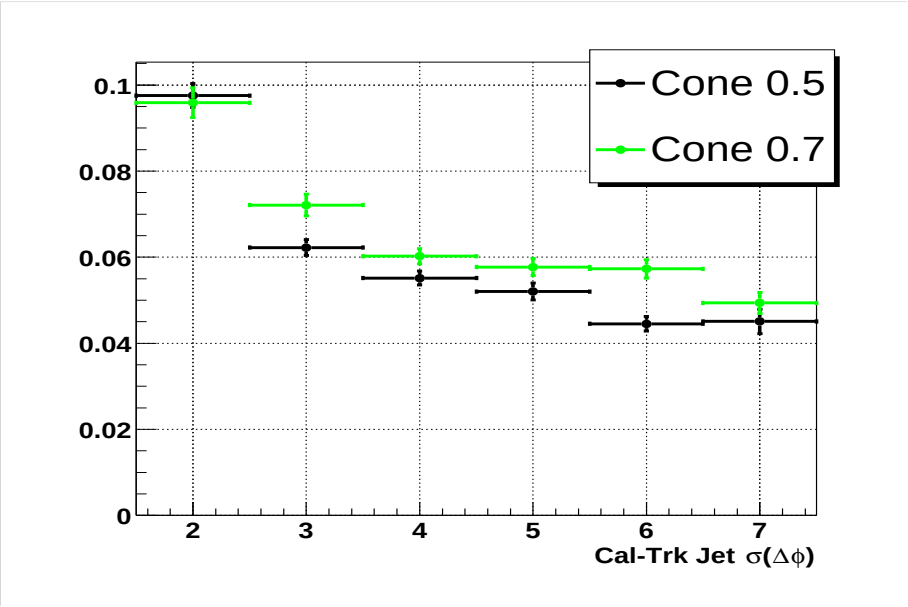

Figure 5.22: Track jet $\Delta\phi$ resolution in the data for the cone algorithm as a function of the number of tracks

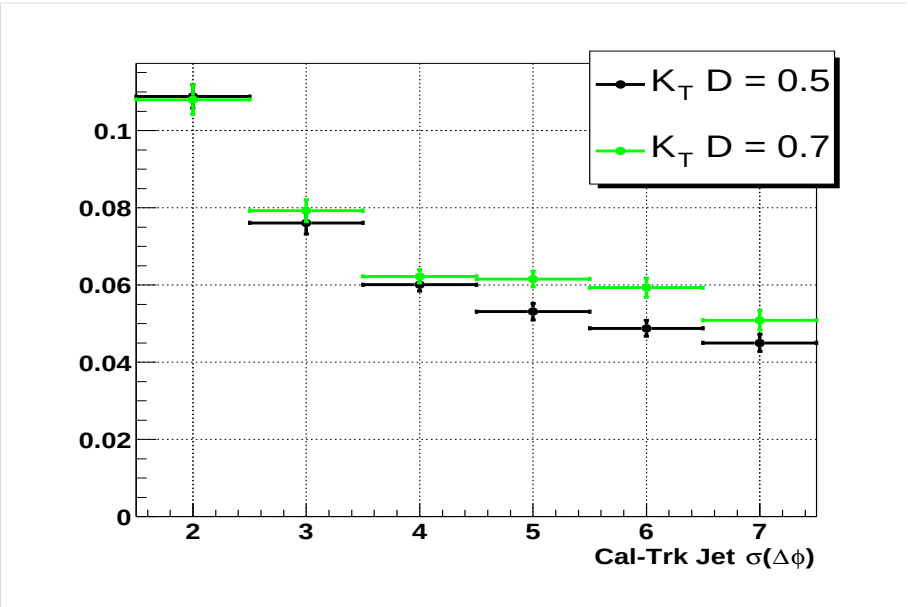

Figure 5.23: Track jet $\Delta\phi$ resolution in the data for the k_T algorithm as a function of the number of tracks

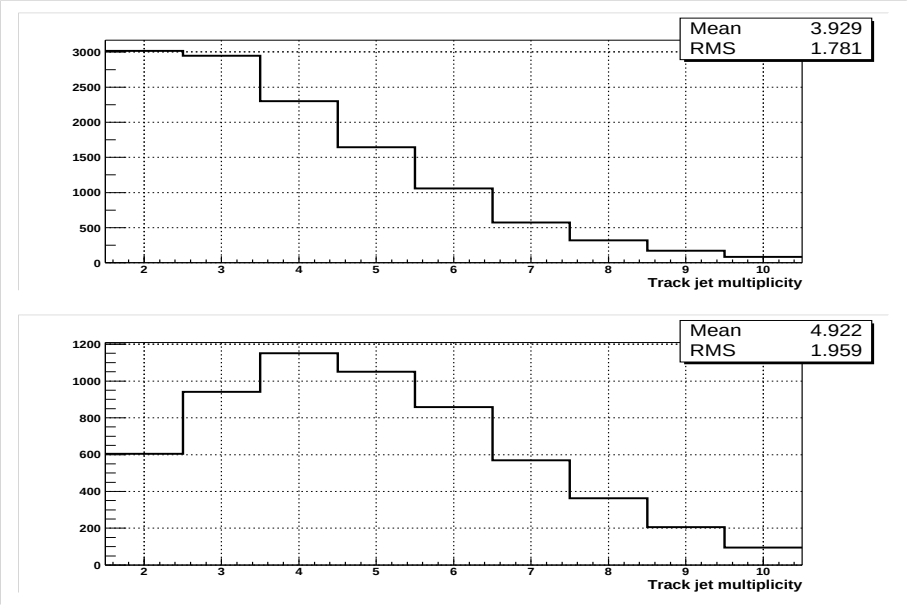

Figure 5.24: Distribution of the track-jet multiplicity in the data and the simulation.

k_T D parameter. Extra jets can also be reconstructed from the underlying event or from soft radiation jets so we expect in addition a flat ΔR distribution for the second best matched jet.

Figures 5.27 and 5.28 show the $\Delta\phi$, $\Delta\eta$ and ΔR distributions of the best and second best calorimeter/track-jet match for 0.5 k_T jets. Similar plots are obtained for 0.7 k_T and 0.5/0.7 cone jets. The small peaks at $|\phi| = \pi$ of Figure 5.27 corresponds to events where one of the track-jets was not reconstructed. Figure 5.28 show that, in addition to the expected flat background from the underlying event and soft radiation and the large peak at $\Delta\phi = \pi$, a small mound is visible at $\Delta R \approx 0.5$, a clear indication of the presence of extra-jets.

Figures 5.29 and 5.30 present the track multiplicity and highest p_T track of the best and second best match (if $\Delta R < 1.0$) for 0.5 k_T track-jets. We see that the second best match track jet is made of fewer and softer tracks than the best match. Again, similar plots hold for 0.7 k_T and 0.5/0.7 cone jets.

Tables 5.1 and 5.2 summarize the average multiplicity and average highest p_T

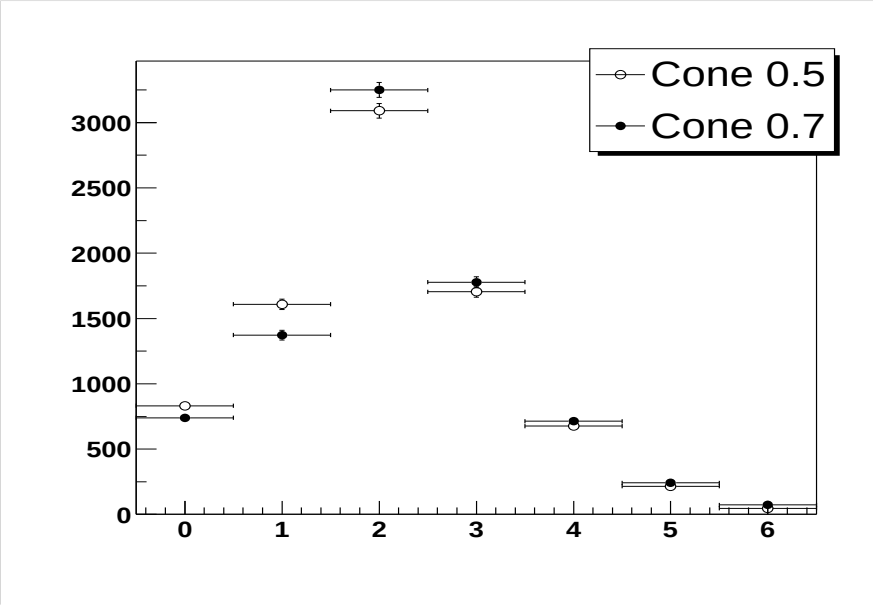

Figure 5.25: Cone track-jet multiplicity in di-jet data events.

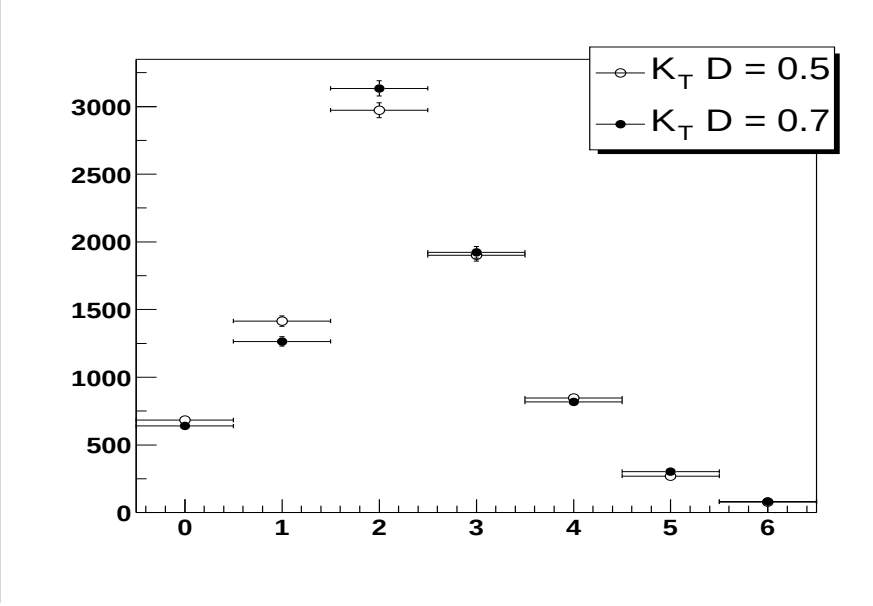

Figure 5.26: k_T track-jet multiplicity in di-jet data events.

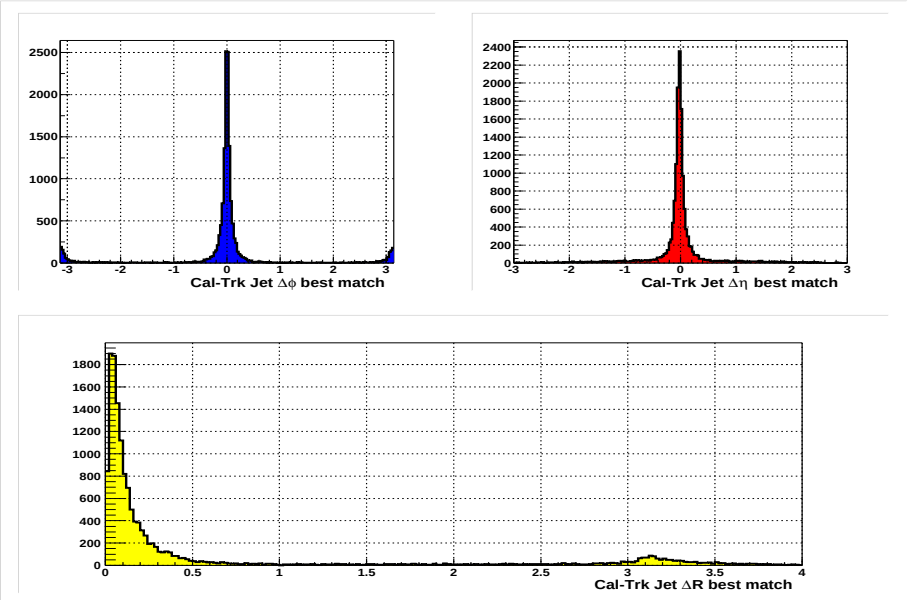

Figure 5.27: Distribution of $\Delta\phi$, $\Delta\eta$ and ΔR between calorimeter jets and the closest track-jet reconstructed with the 0.5 k_T algorithm.

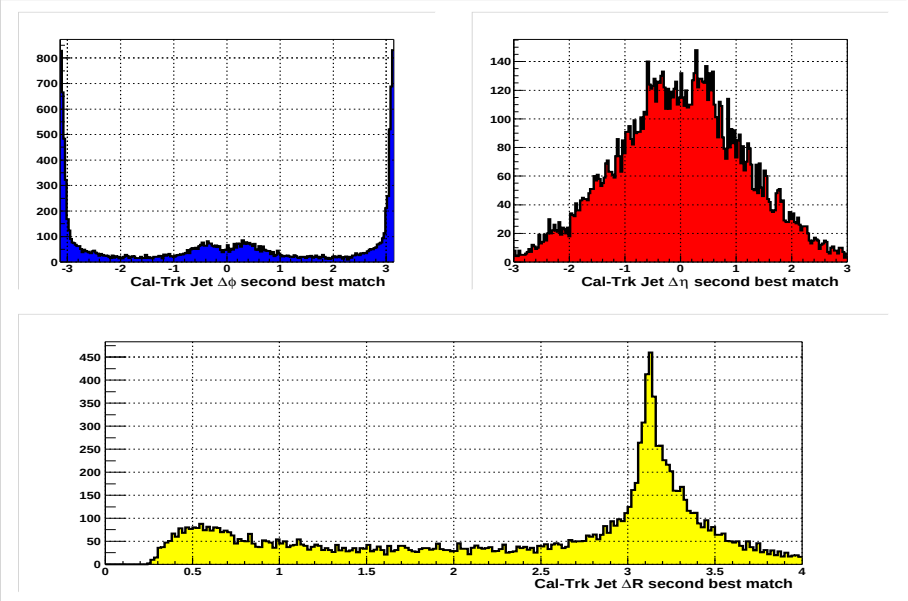

Figure 5.28: Distribution of $\Delta\phi$, $\Delta\eta$ and ΔR between calorimeter jets and the second closest track-jet reconstructed with the 0.5 k_T algorithm.

for the best and second best matched track-jet for the different jet algorithms. We observe that k_T algorithm always clusters more tracks than the cone algorithm for the same parameter size.

The fact that the k_T jet algorithm finds jets with larger multiplicity than the cone algorithm is due to the fact that it can cluster tracks which are separated by more than its D size parameter, as it was explained in the introduction. This can be observed in Figures 5.31 and 5.32 which show the width distribution for the best and second best match for the cone and k_T algorithms. The jet width is defined as a momentum weighted sum of the ΔR between the tracks belonging to the jet and its direction.

$$\sigma = \frac{\sum p_{Tj} \Delta R(j, \vec{a})}{\sum p_{Tj}} \tag{5.4}$$

where p_{Tj} is the transverse momentum of the track j and $\vec{a}$ is the track jet axis. These figures illustrate that the second best matched jet tends to be wider, and that cone and k_T jet width distributions are similar, except for a slowly dying tail in the second case.

	$\langle$ **multiplicity** $\rangle$	
	best match	*2nd best match*
Cone 0.5	3.93	2.42
k_T 0.5	4.11	2.53
Cone 0.7	4.35	2.47
k_T 0.7	4.48	2.56

Table 5.1: Average multiplicity for the best and second best matched track jet for the different jet algorithms.

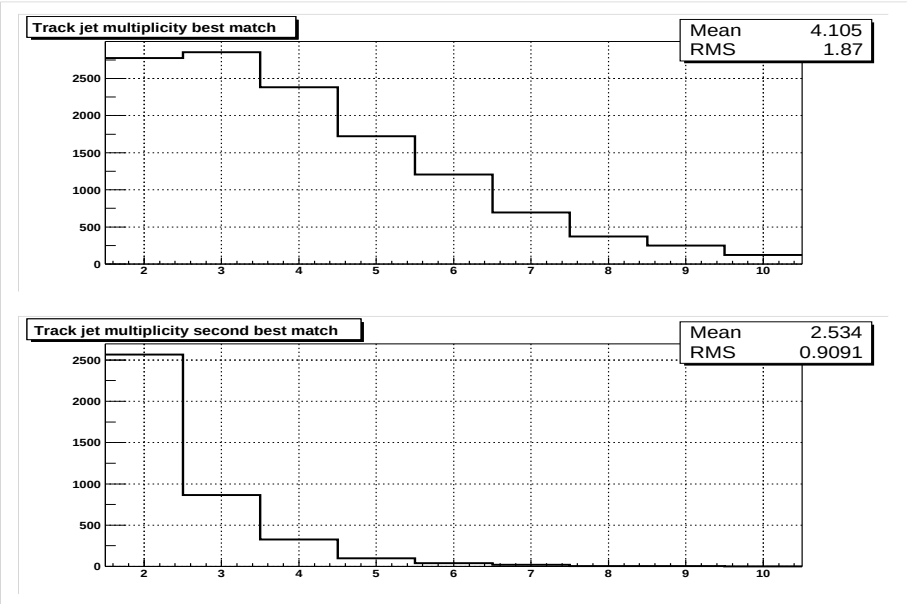

Figure 5.29: Track multiplicity of the best and second best track-jet cal-jet match (if ΔR (track-jet, cal-jet) < 1.0) for 0.5 k_T track-jets.

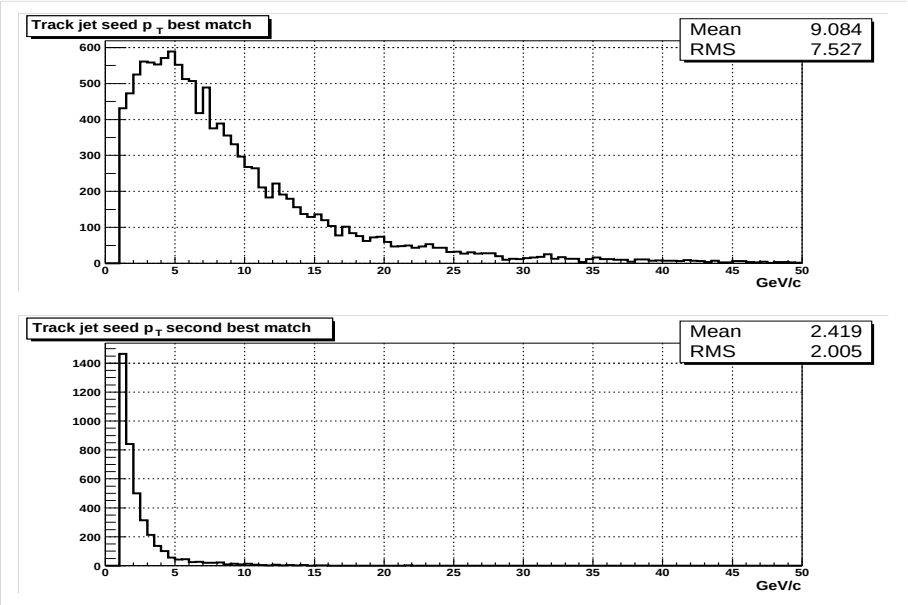

Figure 5.30: Highest p_T track of the best and second best track-jet cal-jet match (if ΔR (track-jet, cal-jet) < 1.0) for 0.5 k_T track-jets.

	$\langle$ **seed** $\boldsymbol{p_T}$ $\rangle$	
	best match	*2nd best match*
Cone 0.5	9.18	2.39
k_T 0.5	9.09	2.42
Cone 0.7	9.13	1.95
k_T 0.7	9.09	1.98

Table 5.2: Average highest p_T for the best and second best matched track jet for the different jet algorithms.

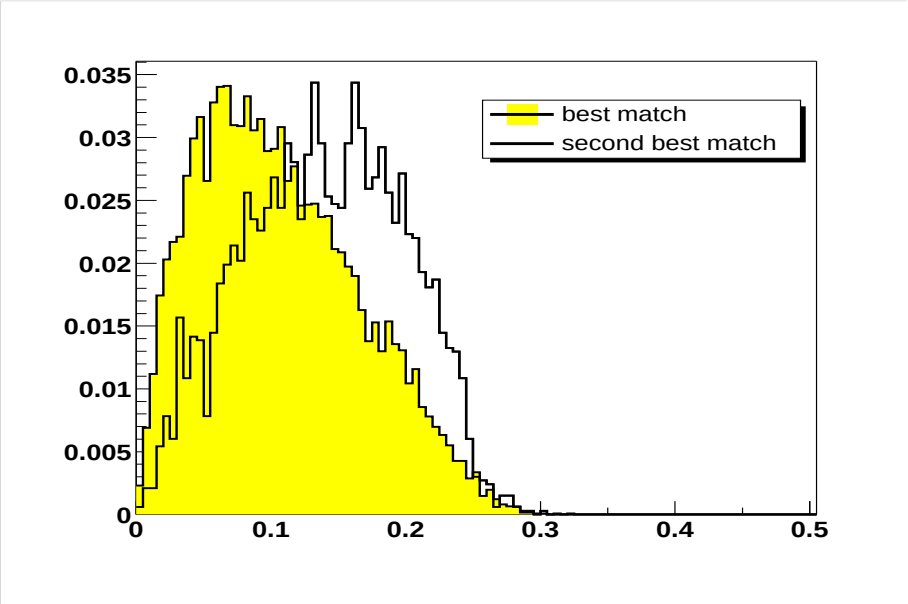

Figure 5.31: Distribution of jet width of the best and second best matches for the 0.5 cone algorithm.

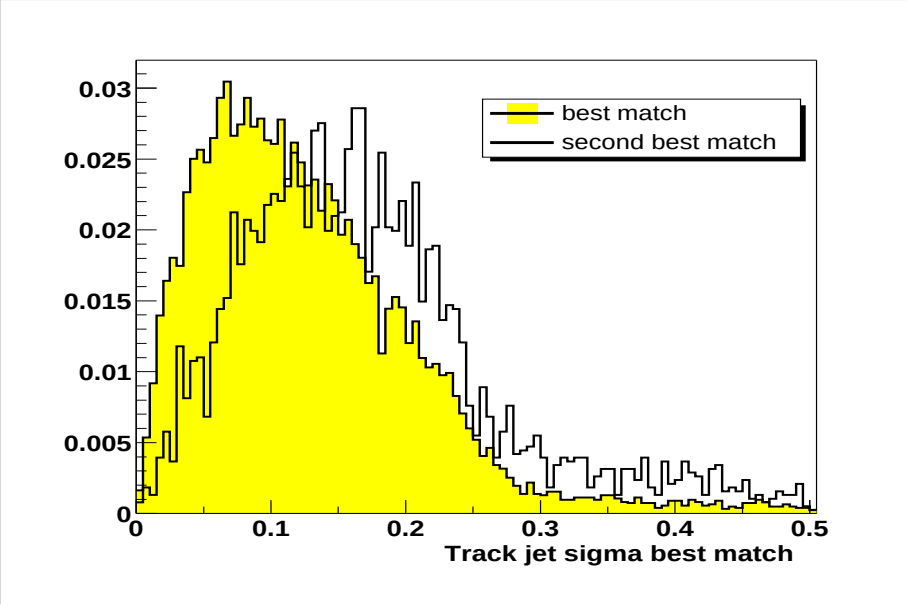

Figure 5.32: Distribution of jet width of the best and second best matches for the 0.5 k_T algorithm.

5.2.3 Track Selection

For every track-jet, we select displaced tracks based on the impact parameter significance $S = dca/\sigma(dca)$, with respect to the primary vertex. Motivated by Figure 5.7, we impose a $S > 3$ requirement on eligible tracks. The impact parameter significance can be calculated in the transverse or longitudinal plane or both. We have not yet attempted to combine transverse and logitudinal impact parameter information.

Table 5.3 summarizes the b-tag track selection criteria.

Variable	Cut
Number of SMT hits	≥ 3
Transverse impact parameter ($\|dca\|$)	$< 0.15\,cm$
Longitudinal impact parameter ($\|zdca\|$)	$< 0.40\,cm$
Transverse momentum (p_T)	$\geq 0.5\,GeV/c$
Impact Parameter significance (S)	> 3

Table 5.3: Selection criteria for tracks used in the b-tag algorithm.

5.2.4 Vertex Finding and Fitting

In every track-jet with at least two selected tracks, we attempt to find a secondary vertex. We implemented two different methods: the *Tear-down* and the *Build-Up* algorithms, which tend to be complementary to each other. In the first case, all selected tracks within jets are fitted to a common vertex. The track with the largest χ^2 contribution to the fit is removed and a new vertex is found. This process is repeated until the total vertex χ^2 is smaller than a threshold χ^2_0. The Build-Up algorithm starts finding *seed* 2-track vertices, by fitting all combination of pairs of selected tracks in jets. Then, it attempts to attach additional tracks pointing to the seeds according to the resulting χ^2 contribution to the vertex. All tracks considered

are required to satisfy the track selection criteria. The process is repeated until no more tracks can be associated to seeds. This procedure is such that the resulting vertices might share tracks.

There are qualitative differences among these two methods: the Tear-Down vertex finder tends to find less vertices with more attached tracks than the Build-Up algorithm, which usually finds more than one vertex per jet, with shared tracks. The Tear-Down approach is expected to have higher purity and lower efficiency than the Build-Up method.

The implementation of secondary vertex b-tag algorithm in the DØ software, provides the option to use any of these two finding algorithms, so that every particular physics analysis can determine the most appropriate one.

5.2.5 Vertex Selection

If at least one vertex was found in a jet, we apply the vertex selection criteria shown in Table 5.4.

Variable	Cut
Decay length, $\|\vec{L}_{xy}\|$	$< 2.6\,cm$
Decay length significance, $\|L_{xy}/\sigma(L_{xy})\|$	> 5
Collinearity, $\vec{L}_{xy} \cdot \vec{p}_T / \|\vec{L}_{xy}\|\,\|\vec{p}_T\|$	> 0.9
Multiplicity, N	≥ 2
K^0_S rejection	see text

Table 5.4: Selection criteria for secondary vertices

The transverse vertex decay length is defined as

$$|\vec{L}_{xy}| = |\vec{r}_{SV} - \vec{r}_{PV}| \tag{5.5}$$

The first requirement attempts to reject vertices found inside the SMT detector to reduce the number of secondary vertices produced by conversions due to the interaction between primary particles and the SMT mechanical structure. It also helps to reduce long lived neutral particle decays (*V0*s), such as K^0 and Λ.

The collinearity angle is defined as the inner product of $\vec{L}_{xy}$ and the total vertex transverse momentum computed as the sum of the momenta of all attached tracks after the constrained fit. It is defined in the range $(-1, 1)$ and it measures how well the secondary vertex points back to the primary. Negative collinearity angles have two different sources:

- Misreconstruction.

- Resolution.

The former is the reconstruction of a fake vertex from tracks originating from different decays, and is due to algorithm inefficiencies. The latter happens when, due to tracking resolution fluctuations, tracks from a real displaced vertex are reconstructed as coming from behind the primary vertex.

K^0_S vertices are identified as 2-track vertices of total charge $Q = 0$, with their invariant mass within a window around the K^0_S mass ($N = 2$, $Q = 0$, $0.483 < M_{\pi\pi} < 0.503$).

A jet is considered *b-tagged* if it contains at least one vertex with decay length significance $|L_{xy}/\sigma(L_{xy})| > 5$. Tags with $L_{xy} < 0$ are called *negative* tags whereas tags with $L_{xy} > 0$ are called *positive*. The sign of the decay length is given by the sign of the vertex collinearity angle.

5.3 Algorithm Optimization and Performance in the Simulation

In this section we study the effect of different parameters and selections of the b-tag algorithm on the overall performance in the $t\bar{t}$ Monte Carlo sample. We compare the use of several track-jet algorithms and the two vertex finder strategies. Since the vertex decay length significance L_{xy} is the most powerful discriminating variable of the algorithm, we leave this variable as a tunable parameter.

5.3.1 Effect of Track-Jet Reconstruction

Figure 5.33 shows the number of tracks clustered by the Cone and k_T track-jet algorithms for track-jets matched to b-jets. We observe that increasing the jet width (cone size for cone algorithm or D parameter for K_T) from 0.5 to 0.7 results in an increase of 11% in the number of attached tracks. We don't observe significant differences on the average number of tracks associated by both jet algorithms.

Even if the average properties of track-jet algorithms are similar, both algorithms might impact differently on the b-tag algorithm since what really matters for secondary vertex b-tagging is the ability to cluster the right tracks coming from B and D decays and cone/k_T track-jets are not identical event by event. An example of the different track assignment is shown in Figure 5.34. The plots correspond to the same event reconstructed by cone and k_T algorithms of size 0.5. One of the jets found by the cone algorithm is reconstructed as two different jets by k_T. Figures 5.35 and 5.36 show the number of attached tracks in secondary vertices reconstructed using different jet algorithms. We don't observe significant differences among the algorithms used. This suggests that the 11% of extra tracks clustered by the 0.7 track-jet algorithms do not contain significant number of displaced vertexable tracks.

The algorithm performance is evaluated by two-dimensional plots of b-tagging

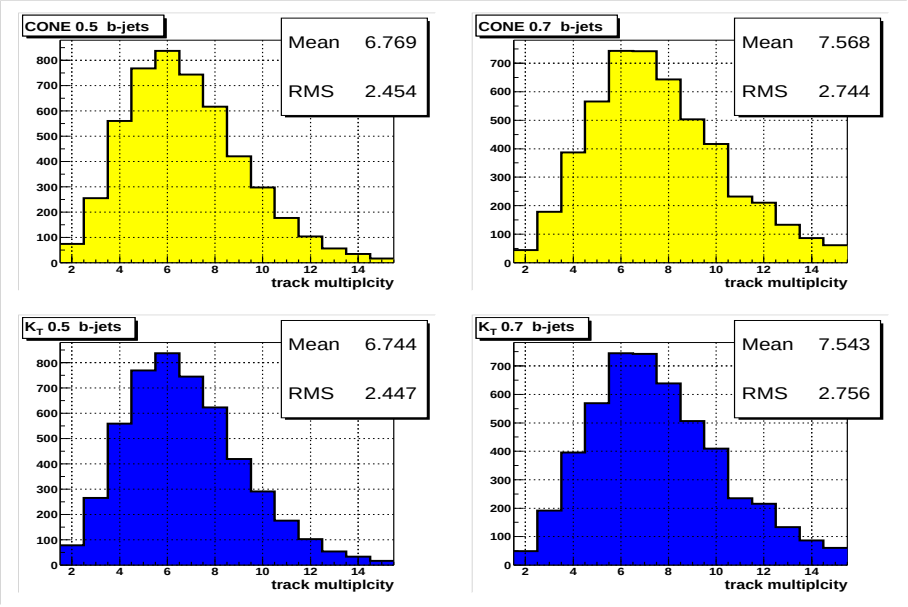

Figure 5.33: Number of tracks clustered by the cone and k_T track-jet algorithms for track-jets matched to b-jets

efficiency versus light-quark-tagging efficiency. The light-quark-tagging efficieny is measured as the fraction of light-quark taggable jets -in the $t\bar{t}$ Monte Carlo sample- tagged as b-jets.

The overall tagging performance for different track-jet algorithms is shown as a function of the decay length significance cut in figure 5.37. No significant differences are observed. We thus choose the 0.5 Simple Cone as the track clustering algorithm due to its simplicity over k_T, and its similar performance.

5.3.2 Effect of Vertex Finding

In this section we compare the properties of the secondary vertices obtained with the *Build-Up* (BU) and *Tear-Down* (TD) vertex finding methods and their performance to tag b-jets.

Figure 5.38 compares the number of tracks attached to secondary vertices reconstructed with the BU and TD algorithms from b and light quark jets. As expected,

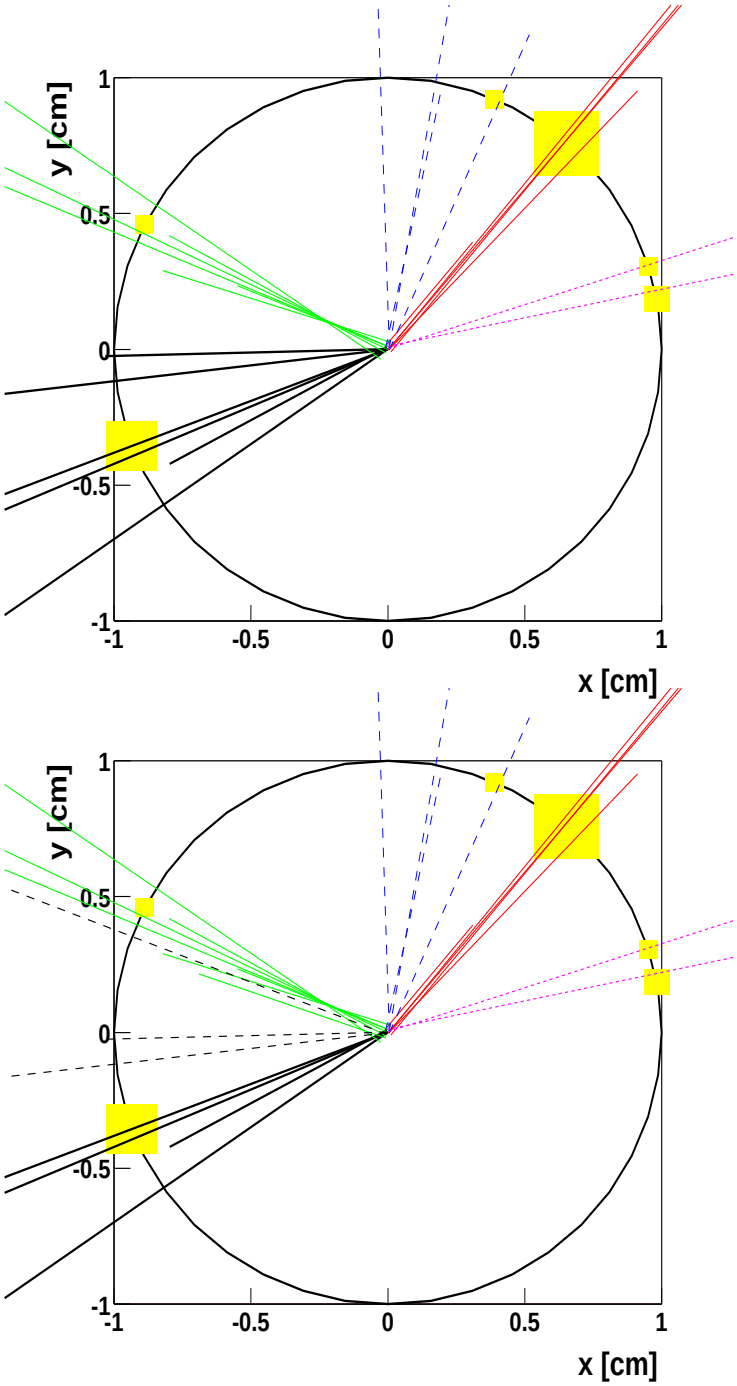

Figure 5.34: The same event reconstructed with the R=0.5 Simple Cone (*top*) and D=0.5 k_T (*bottom*) algorithms. Tracks from separate track-jets are shown with different line types, and calorimeter jets as grey boxes. One of the jets found by the cone algorithm is reconstructed as two different k_T jets.

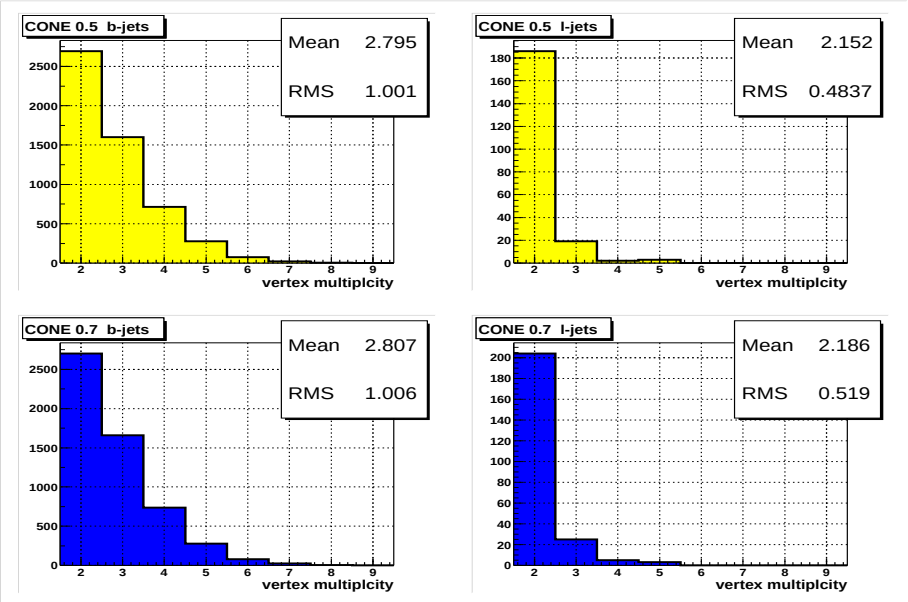

Figure 5.35: Number of attached tracks in secondary vertices reconstructed using different sizes for the cone track-jet algorithm

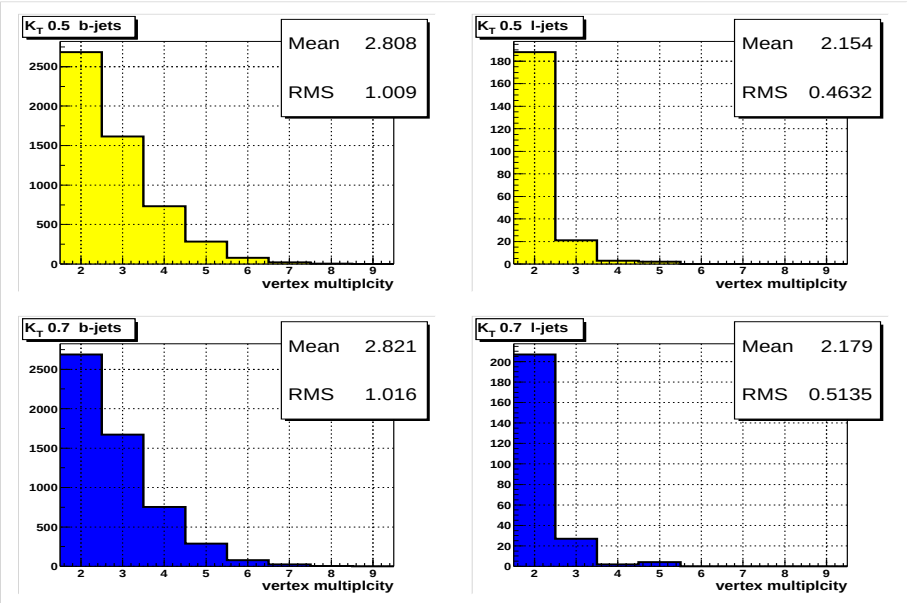

Figure 5.36: Number of attached tracks in secondary vertices reconstructed using different sizes for the k_T track-jet algorithm

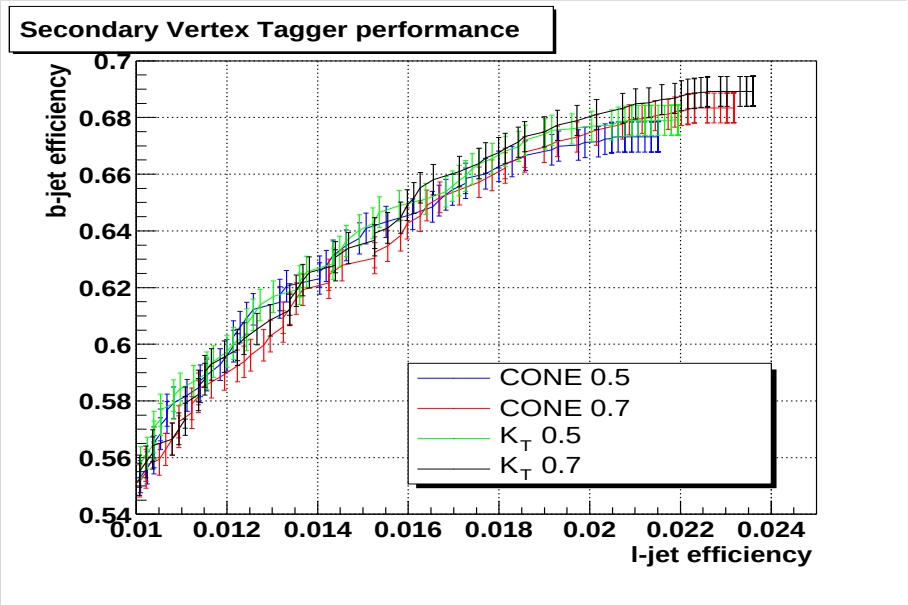

Figure 5.37: Overall tagging performance for different track-jet algorithms as a function of the decay length significance cut.

the TD algorithm attaches more tracks to secondary vertices than BU, but the difference is small. It is not straightforward to estimate how the larger multiplicity of tags will impact the overall b-tagging efficiency; the measurement of the vertex decay length will be improved by the presence of more (real) tracks, but, on the other hand, the increase in the number of attached tracks to mis-reconstructed vertices in light jets might dilute the discrimination power against them.

The overall b-taggging efficiency for both vertex finder algorithms is shown in figure 5.39. We also compare the algorithm performance using the second pass method (allowing looser requirement on the significance of selected tracks but tightening the vertex multiplicity). No significant differences are observed among the vertex finder algorithms. BU method can achieve slightly higher efficiencies but at a higher mistag rate.

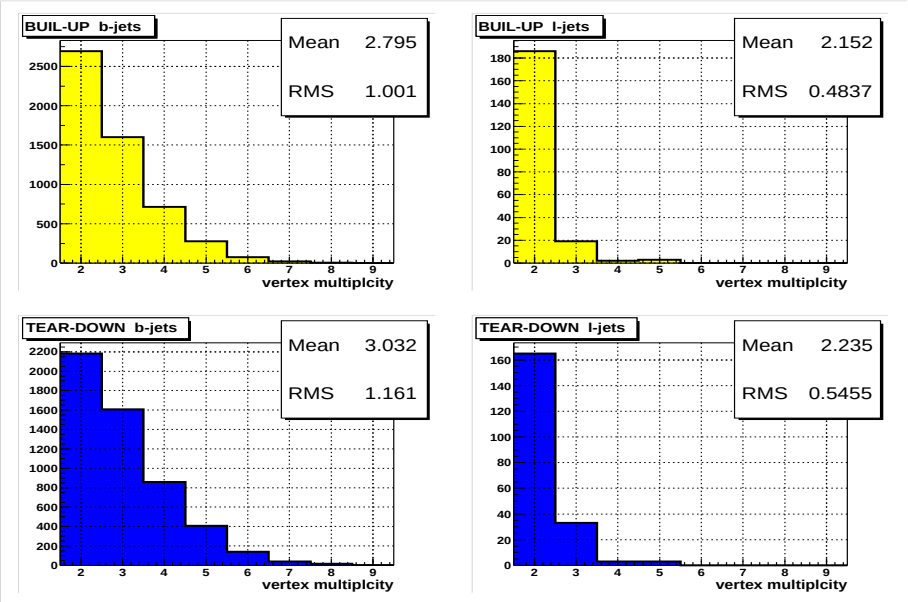

Figure 5.38: Number of tracks attached to secondary vertices reconstructed with the BU and TD algorithms from b and light quark jets.

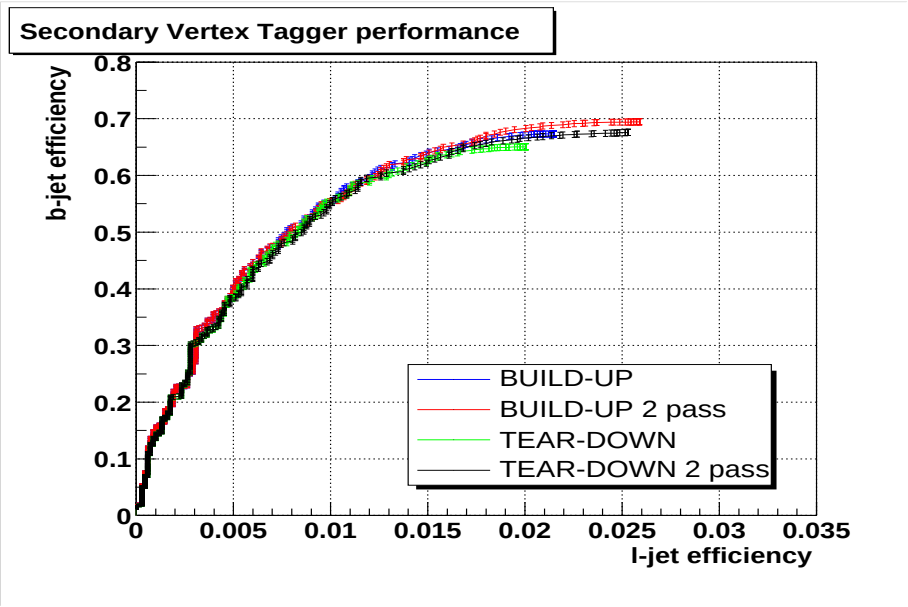

Figure 5.39: Overall b-tagging efficiency for Tear-Down and Buil-Up vertex finder algorithms.

5.3.3 Effect of Track and Vertex Selection

The pre-selection of displaced tracks based on its impact parameter significance can be done in the transverse plane as well as in the longitudinal plane. The 3-dimensional track selection can request tracks having $S_{r\phi} > 3$ *or* $S_z > 3$, where $S_{r\phi}$ and S_z are the transverse and the longitudinal impact parameters with respect to the primary vertex.

Figure 5.40 shows the tagging performance for BU and TD algorithms using 2 and 3-Dimensional (3D) track selection. The 3D track-selection allows to achieve higher b-tagging efficiencies at higher mistag rates.

Figure 5.41 shows the overall performance for the Build-Up vertex algorithm, after removing K_S^0 displaced vertices. K_S^0 are identified as 2 opposite charged track vertices with $0.483\,GeV/c^2 < M_{vtx} < 0.503\,GeV/c^2$. The rejection of K_S^0 vertices has a significant effect in reducing the mistag rate and keeping a high b-tagging efficiency.

5.3.4 Performance

The performance of the secondary vertex b-tag algorithm was evaluated with the following final set of parameters:

- 0.5 Simple Cone Track-Jet.
- 2D track-selection.
- Build-Up vertex finding.
- K_S^0 rejection.
- $L_{xy}/\sigma(L_{xy}) > 5$

The primary vertex interaction was required to be within $40\,cm$ of the center of the SMT detector. Only jets with $p_T > 10\,GeV/c$ and $|\eta| < 2$ were considered.

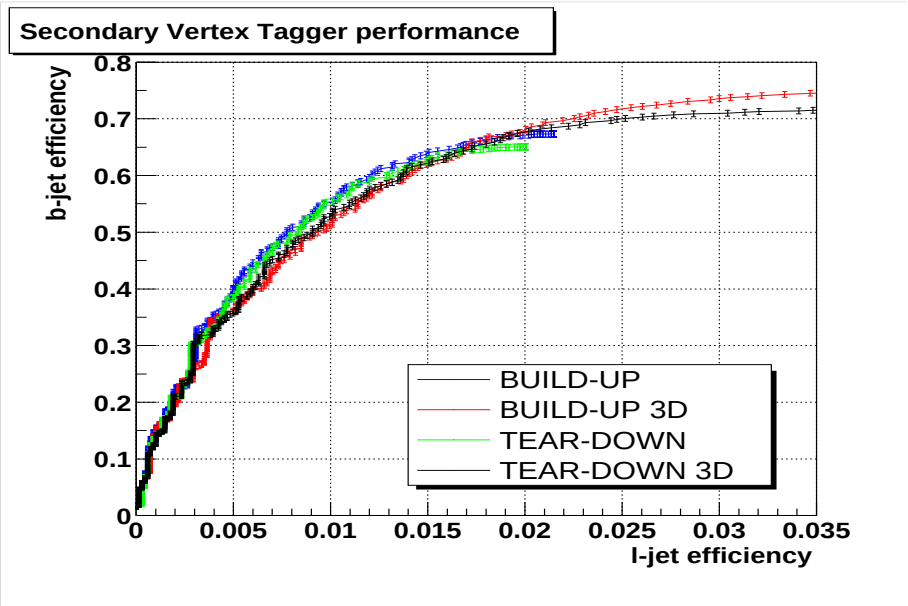

Figure 5.40: Tagging performance for Buil-Up and Tear-Down algorithms using 2 and 3-Dimensional (3D) track selection.

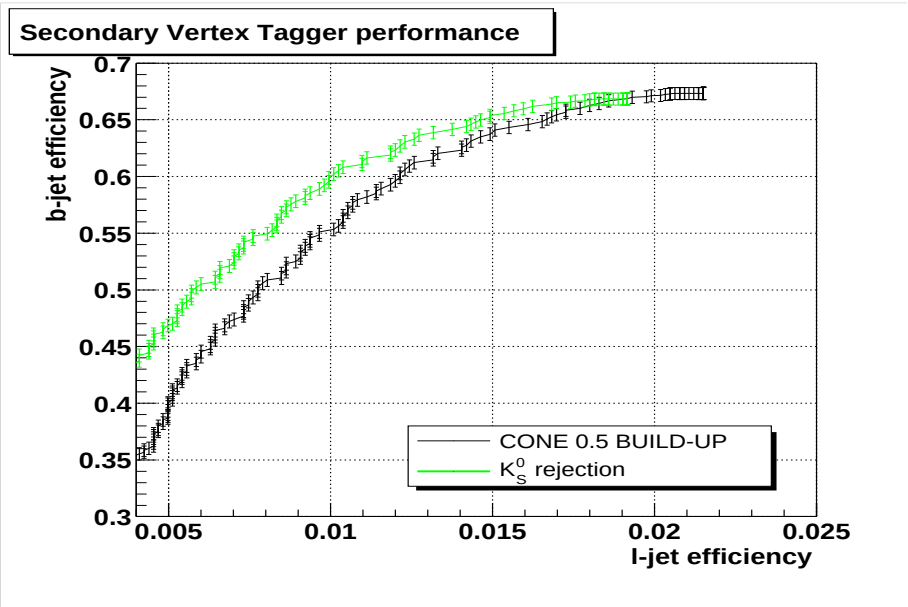

Figure 5.41: Overall performance for the Build-Up vertex algorithm after removing identified K^0_S displaced vertices.

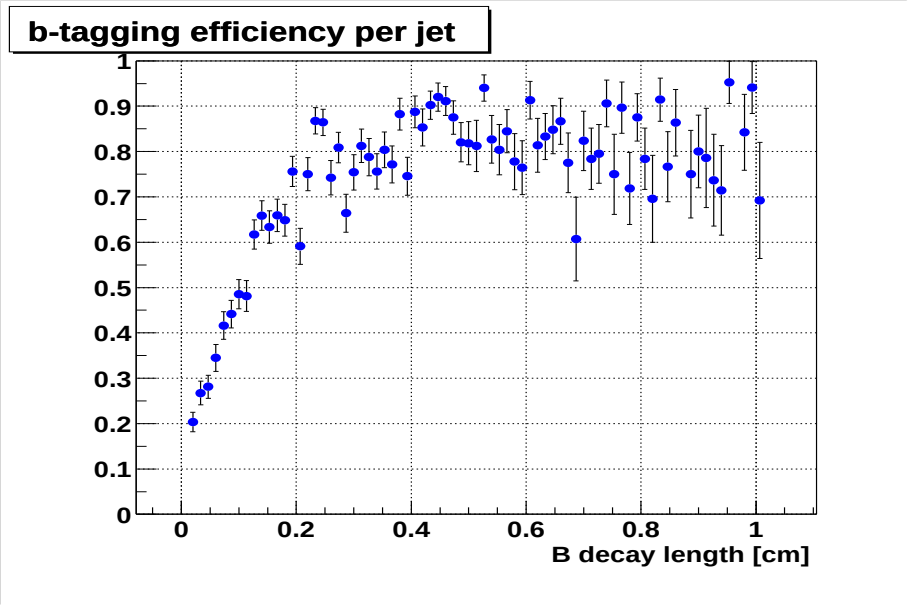

Figure 5.42: b-tagging efficiency as a function of the B hadron decay length.

The efficiency is defined with respect to track-jets matched to calorimeter jets ($\Delta R(trk, cal) < 0.5$). We will refer to them as *taggable jets*.

We consider a jet *tagged* if there is at least one secondary vertex within $\Delta R(vtx, jet) < 0.3$.

Figures 5.42 and 5.43 show the b-tagging efficiency as a function of the B hadron decay length and b-jet multiplicity. The single and double event tagging efficiencies are shown in figures 5.44 and 5.45 as a function of the total number of jets in the event. We observe no significant dependence of the tagging efficiency on jet activity.

Table 5.5 summarizes the algorithm performance in $t\bar{t}$ events.

5.4 Algorithm Optimization in the Data

In this section we concentrate on understanding the quality of global tracks in order to discriminate good tracks from poorly measured ones. The selection of tracks is one of the key points in the development of the secondary vertex b-tag algorithm,

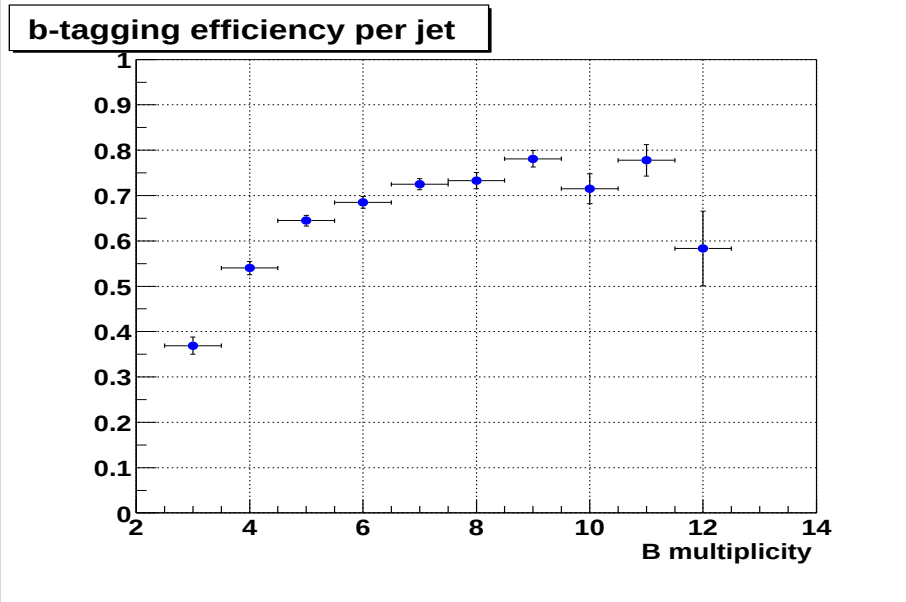

Figure 5.43: b-tagging efficiency as a function of the B hadron jet multiplicity.

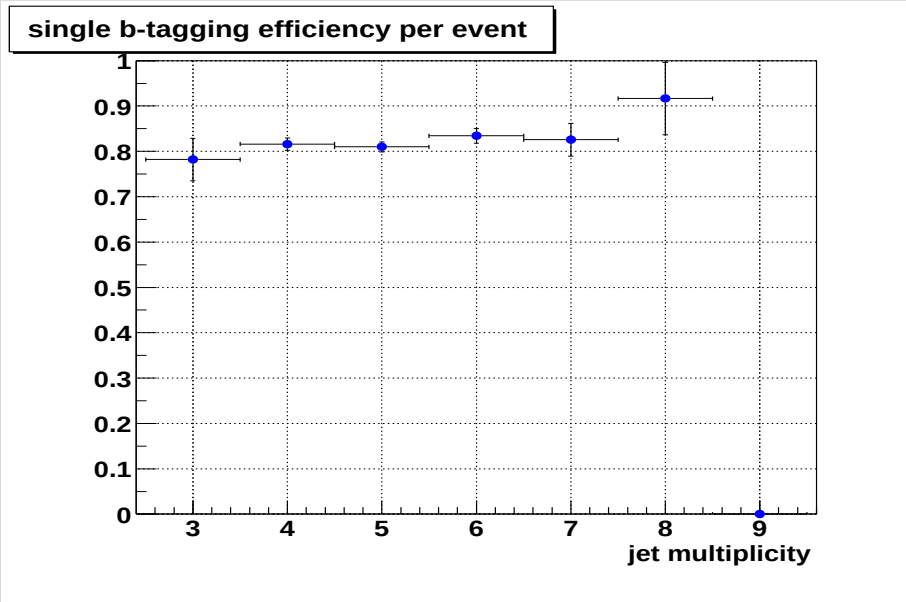

Figure 5.44: Event single b-tagging efficiency as a function of the inclusive number of jets.

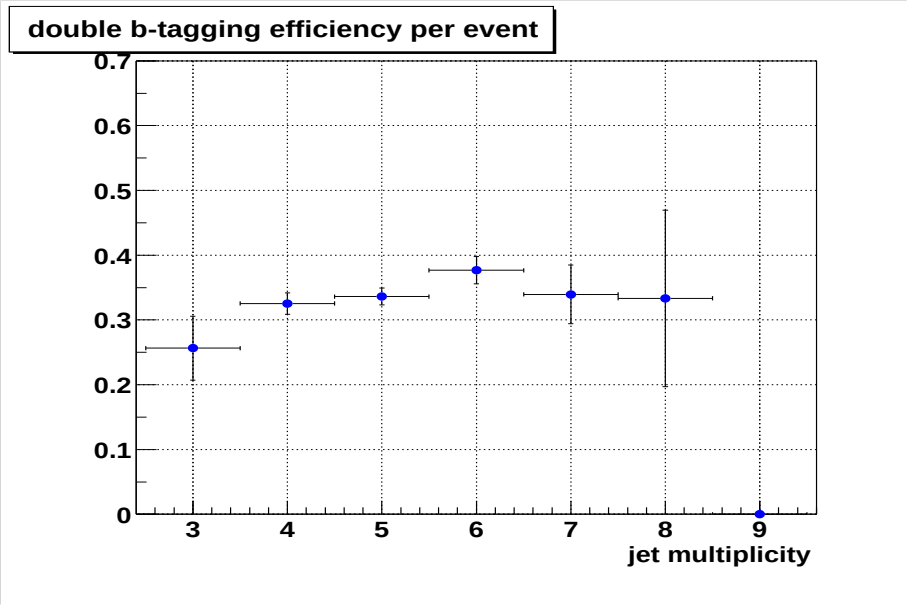

Figure 5.45: Event double b-tagging efficiency as a function of the inclusive number of jets.

since poorly measured tracks, in combination with any other one, will give rise to fake secondary vertices.

We study the quality of reconstructed tracks in a multi-jet data sample with the following requirements: requirements, designed to select clean di-jet events:

1. Any Jet trigger.

2. 2 or more jets with $p_T > 20\,GeV/c$ and $|\eta| < 2.0$.

3. $\Delta\phi > 175^\circ$ between the 2 leading jets.

4. Veto events with at least 1 jet not satisfying the above criteria.

5. Primary vertex $|z| < 40\,cm$ and 4 or more attached tracks .

By requiring $\Delta\phi > 175^\circ$ between the 2 leading jets, we make sure to select clean jets for optimization studies. Gluon splitted jets will be most likely be rejected by

Jet b-tag efficiency	0.648 ± 0.006
Jet uds-tag efficiency	0.017 ± 0.002
Event single-tag efficiency	0.82 ± 0.01
Event double-tag efficiency	0.35 ± 0.01

Table 5.5: Performance of the b-tag algorithm in simulated $t\bar{t}$ events.

this criteria. The last requirement enables the selection of tracks with full SMT information.

For every calorimeter jet, we match tracks with $p_T > 0.5\,GeV/c$ and $|zdca| < 0.5\,cm$ within $\Delta R < 0.5$ around the calorimeter jet axis and measure its signed transverse impact parameter, IP.Figure 5.46 shows the IP distribution of tracks with different number of SMT hits and $\geq$7 CFT hits. The small excess at positive IP's is due to the presence of long lived particles and heavy flavor jets, whereas negative impact parameters are mostly due to track resolution.

We quantify the quality of tracks with different number of SMT hits as the fraction with negative IP significance within 3 sigma of the primary vertex $N(S > -3)/N(S < 0)$. Since the majority of negative IP tracks are due to tracking resolution, the track quality will be proportional to $N(S > -3)/N(S < 0)$. Table 5.6 shows the fraction of tracks and the fraction of negative impact parameter tracks within 3 sigma of the primary vertex.

Figure 5.47 shows the distribution of number of SMT hits per track in the data and the Monte Carlo simulation. We observe a large discrepancy. In the simulation, 92% percent of the tracks has 3 or more hits, whereas in data this fraction is 78%.

Based on the results shown in Table 5.6 and Figure 5.46, we selected tracks with 3 or more SMT hits, in order to keep to less than 10% the number of tracks populating the tails of the transverse impact parameter distribution.

We will see that the performance of the secondary vertex b-tagging algorithm

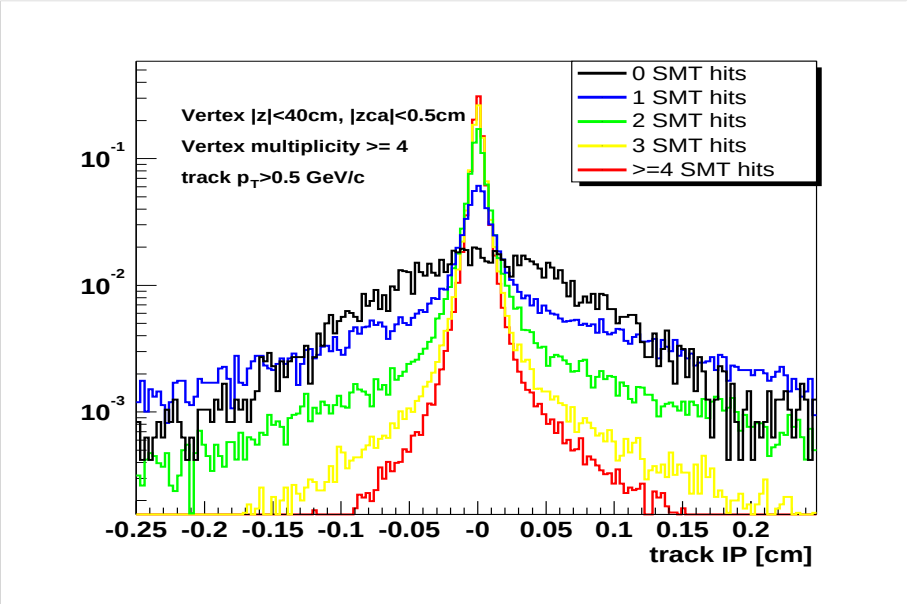

Figure 5.46: Transverse signed impact parameter distribution in the data for tracks with different number of SMT hits and $\geq$7 CFT hits.

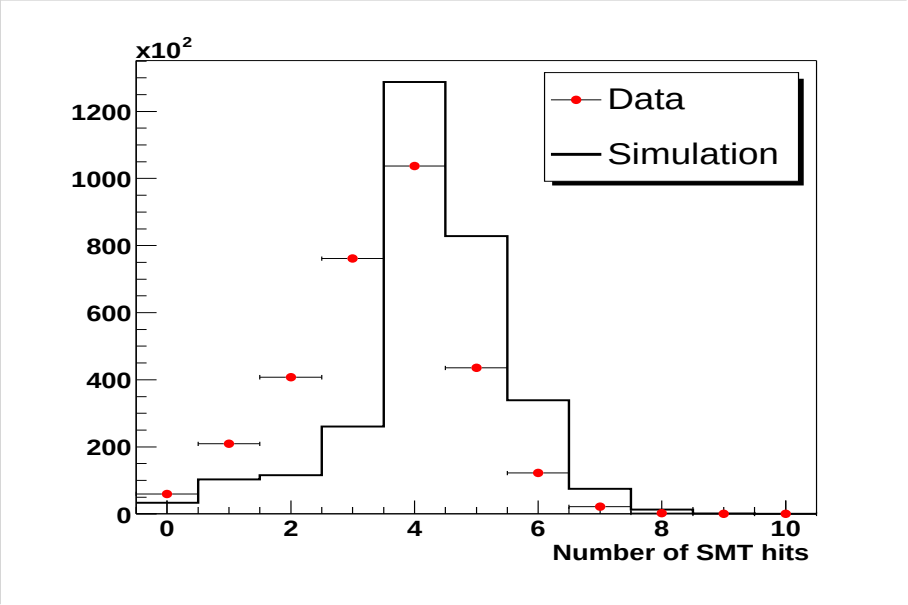

Figure 5.47: Distribution of the number of SMT hits in the data (dots) and the corresponding simulation (histogram).

No. of SMT hits	Fraction	$N(S > -3)/N(S < 0)$
1	0.069	0.439
2	0.133	0.761
3	0.249	0.893
4 or more	0.530	0.933

Table 5.6: Total fraction of tracks and fraction of negative impact parameter tracks within 3 sigma of the primary vertex in the data.

strongly depends on the number of selected tracks. As the alignment and tracking reconstruction algorithms continue to improve with the better understanding of the detector, the number of selected good tracks will increase, resulting in an enhanced overall b-tagging performance.

5.5 Algorithm Performance in the Data

In this section we study the performance of the secondary vertex tagger algorithm in inclusive jet and inclusive muon-jet samples. The goal is to understand how often we mistakenly tag jets without heavy flavor and also how efficiently the jets from b quark decays are identified. We also want to estimate how well we can predict the expected number of tags from QCD production in different data samples.

The performance is evaluated by searching for secondary vertices within *taggable* jets and measuring the rate of positive and negative tags in different data samples. A taggable jet is defined as a calorimeter jet matched to a track-jet with at least 2 tracks passing the track quality selection of Table 5.3.

We "tag" a jet according to the largest transverse decay length significance (L_{xy}) vertex found, around $\Delta R < 0.5$ of the jet axis. If $L_{xy} > 5$, we call the jet a *positive tag* whereas a *negative tag* is a jet with $L_{xy} < -5$. We apply the same vertex quality

cuts defined in Section 5.3.4.

5.5.1 Data Samples

We use the following data samples to evaluate the performance of the b-tag algorithm.

- Inclusive muon-jet sample (**μ+jet**)

  This sample is selected by requiring a $p_T > 3\,GeV/c$ global muon track, and one or more calorimeter jets. We require the muon to be in the vecinity of one of the jets: $\Delta R(\mu, jet) < 0.7$.

- Jet-trigger sample (**qcd_jet**)

  This sample was selected by requiring any jet trigger and at least one calorimeter jet. We divided this sample into a subsample with exactly 2 jets (**qcd2_jet**) and another subsample with two or more jets (**qcdINCL_jet**).

- EM-trigger sample (**qcd_em**)

  This sample requires a single EM trigger (EM_HI, EM_HI_TR, EM_HI, SH, EM_HI_SH_TR), at least one electron with $p_T > 20.0\,GeV/c$, $\not\!\!E_T < 10\,GeV$ and one or more calorimeter jets. We subdivided this sample in a subsample with exactly 2 jets (**qcd2_em**) and another subsample with two or more jets (**qcdINCL_em**).

- Inclusive electron sample (**e+jets**)

  This sample requires the EM15_2JT15 trigger which consist of at least one electromagnetic trigger tower in excess of $15\,GeV$ and two additional hadronic trigger towers with energy above $15\,GeV$, one electron, one or more jets and

$\not\!\!E_T < 15\,GeV$. This sample is very close to the the sample used for top-quark identification with the exception of the $\not\!\!E_T$ cut. This cut removes events containing real electrons from W leptonic decays.

5.5.2 Mistags

Tags in jets due to light quarks (u, d, s) are called mistags and they are most probably caused by tracking errors and resolution effects. These effects cause that tracks originating at the primary vertex appear as displaced. Mistagged secondary vertices are expected to be distributed symmetrically about $L_{xy} = 0$. We measure the mistag rate in the data as the fraction of jets with a negative tag. We also measure the mistage rate as a function of the track-jet track multiplicity in inclusive jet samples.

Positive tags from heavy flavor in inclusive jet samples are expected from the three different sources already discussed in Section 5.1: direct production, gluon splitting and flavor excitation. Direct production is responsible for ~20% of heavy flavor jets with energy above $20\,GeV$ [37], about 35% are produced by flavor excitation and 45% by gluon splitting. The relative contribution of different process changes after b-tagging is applied. Secondary vertex tagging is expected to be more efficient for directly produced b-jets which tend to be back-to-back. b-jets which are due to gluon splitting are not well separated and are often assigned to the same jet. In the case of flavor excitation, one of the b-jets does not participate in the hard process and is often outside the detector acceptance.

The study of positive and negative tags in inclusive jet events was performed in the **qcd_em** and **qcd_jet** samples described in section 5.4.

Figures 5.48 and 5.49 show the secondary vertex decay length and decay length significance distributions in the **qcd_em** sample. The excess of positive decay lengths is mostly from heavy flavor jets since we explicitly reject remaining K_S^0

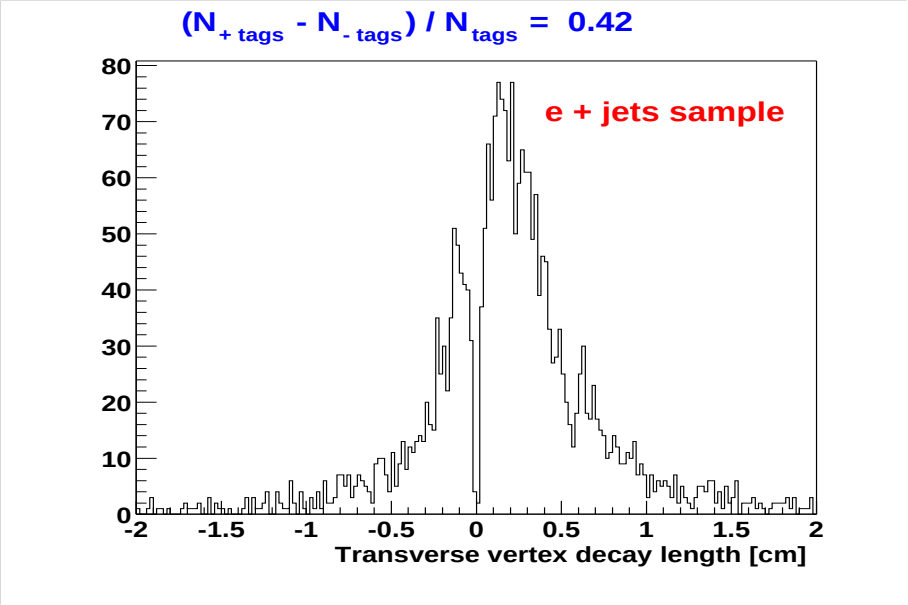

Figure 5.48: Secondary vertex decay length distribution in the **qcd_em** data sample. The excess of events with positive tags is mostly from heavy flavor.

vertices which pass the track selection criteria.

The positive (negative) tag rate is determined as the number of taggable jets with a positive (negative) secondary vertex tag. A taggable jets is defined as a jet with at least 2 tracks passing the track quality selection (3 or more SMT hits, $|dca| < 0.15\,cm$, $|zdca| < 0.4\,cm$, $p_T > 0.5\,GeV/c$).

We parametrize the positive and negative tag rate as a function of the number of tracks in jets and η. This parametrization is called Tag Rate Function (TRF) and it gives the probability that a jet with a given track multiplicity, will be tagged. Due to the limited statistics, we only considered 2 η bins in the parameterization: $|\eta| < 1.0$ and $|\eta| > 1.0$

Figure 5.50 shows the TRF parametrization for positive and negative tags in the **qcd_jet** data sample, requiring 2 inclusive jets in the central η region. Similar plots are obtained for inclusive and exclusive jets, in the central and forward regions, for the **qcd_em** and **qcd_jet** data samples. Figure 5.51 compares the TRFs derived in

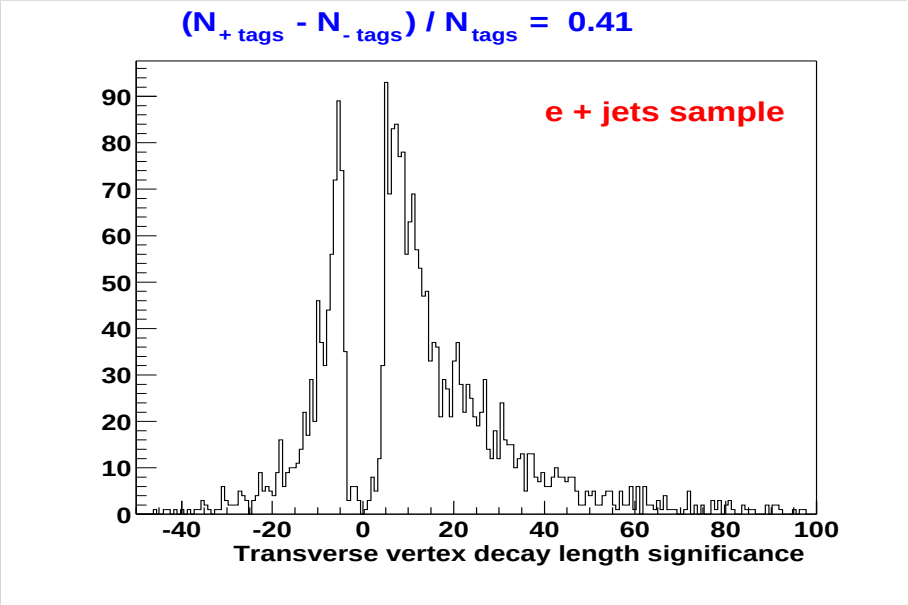

Figure 5.49: Secondary vertex decay length significance distribution in the **qcd_em** data sample.

the 4 different samples in the central region.

We check that the parametrization chosen accurately predicts the positive and negative tag rates by applying them to different data samples and examining various kinematic variables which characterize the events and were not used in the process of parametrizing the mistag rate function. Any discrepancy in the distributions of predicted and observed tags will indicate that a single variable is not sufficient to correctly describe the tag rate.

We compare predicted and observed jet and event distributions. The predicted tagged jets are estimated by weighting the particular distribution with the TRF of every jet obtained from the inclusive *qcdINCL_em* sample.

$$X_{pred} = \sum_{jets} X \,.\, \mathrm{TRF} \tag{5.6}$$

The distribution of expected single tagged events (i.e. events with at least one b-tagged jet), is obtained by combining the individual TRFs for jets in a given event.

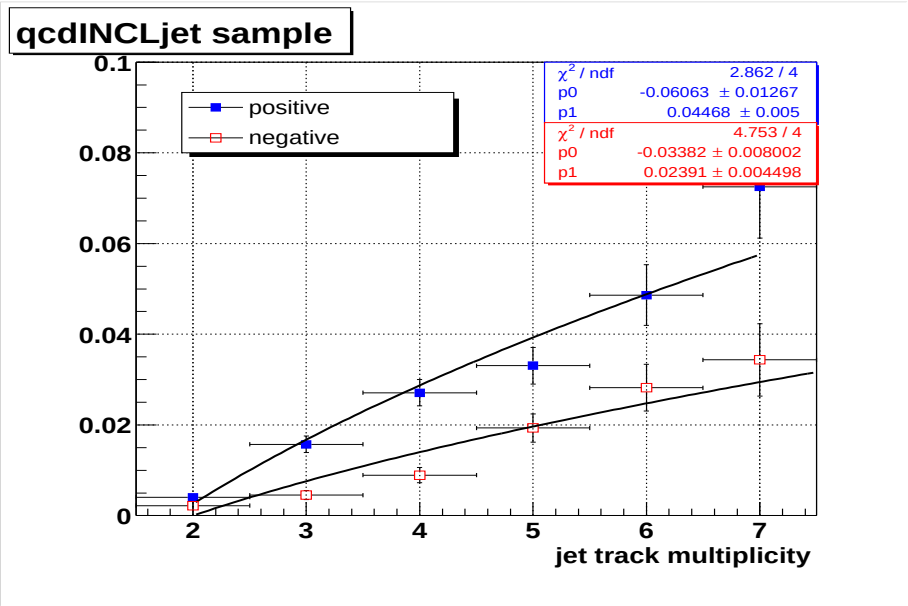

Figure 5.50: Tag rate function parametrization in the qcdINCL_jet sample for jet $|\eta| < 1.0$.

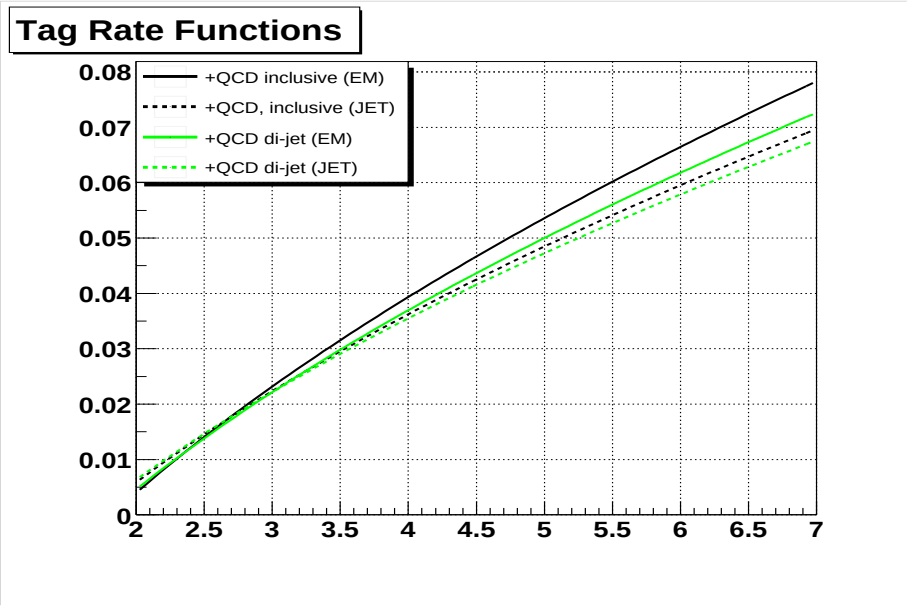

Figure 5.51: Tag rate function parametrizations in the 4 qcd data samples for jet $|\eta| < 1.0$.

For instance, in a n-jet event with tag rate probabilities per jet TRF_i, the single event tag probability will be

$$P(\text{event}) = 1 - \prod_{i=1}^{n} (1 - \mathrm{TRF}_i)$$

which corresponds to the probability to tag at least one jet in the event.

Figures 5.52 and 5.53 compare the predicted and observed positively tagged distributions in the inclusive *qcd_em* sample for jet η and p_T.

Figures 5.54 and 5.55 compare the predicted and observed positively tagged distributions in the inclusive *qcd_em* sample for the event scalar E_T and number of jets.

The good agreement between prediction and observation in figures 5.52 to 5.55 indicates that the η and track multiplicity dependent TRF parameterizations correctly describes the data. The same distributions for the inclusive *qcd_jet* sample are shown in figures 5.56 to 5.59.

Figure 5.60 summarizes the relative difference between predicted and observed tags in all different samples.

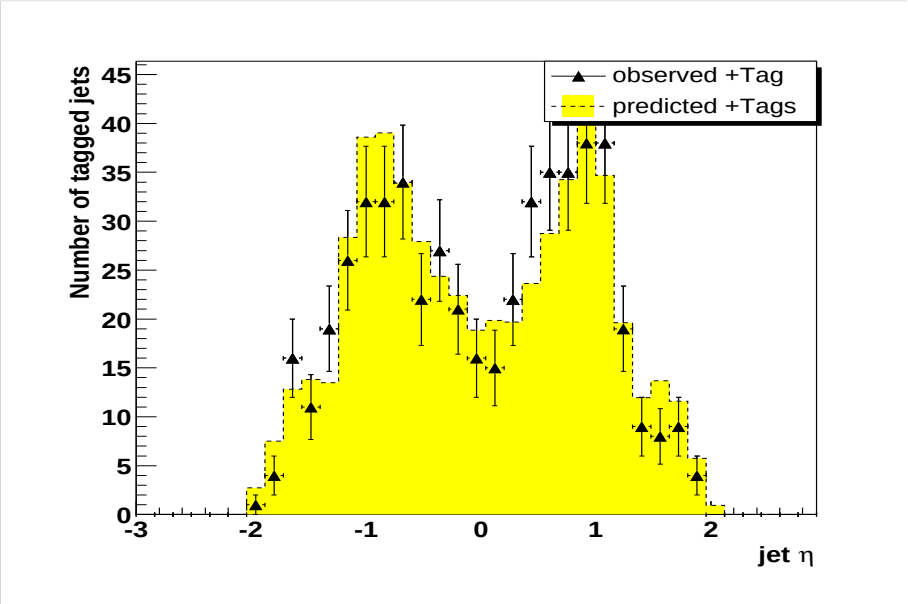

Figure 5.52: η distribution of predicted and observed positive tags in the inclusive qcd_em sample.

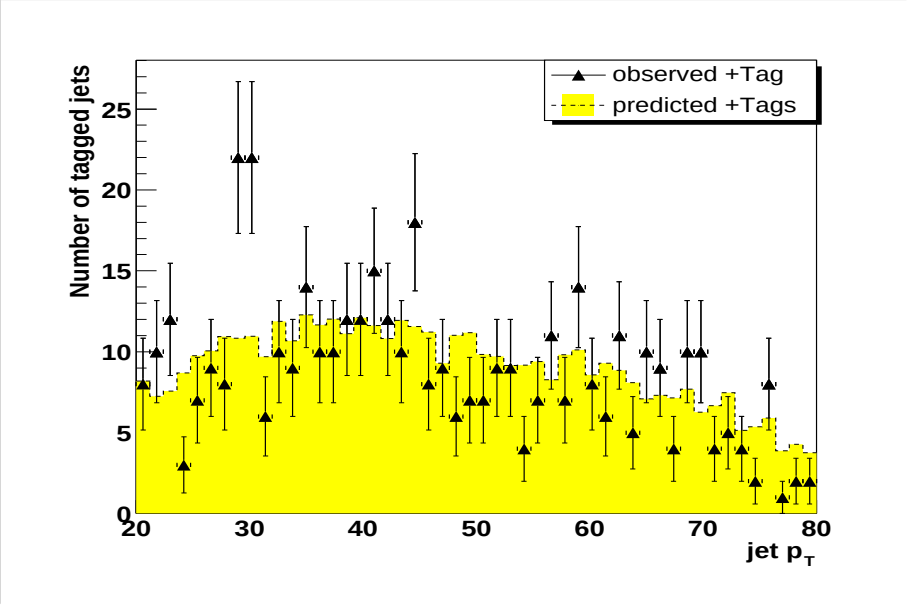

Figure 5.53: p_T distribution of predicted and observed positive tags in the inclusive qcd_em sample.

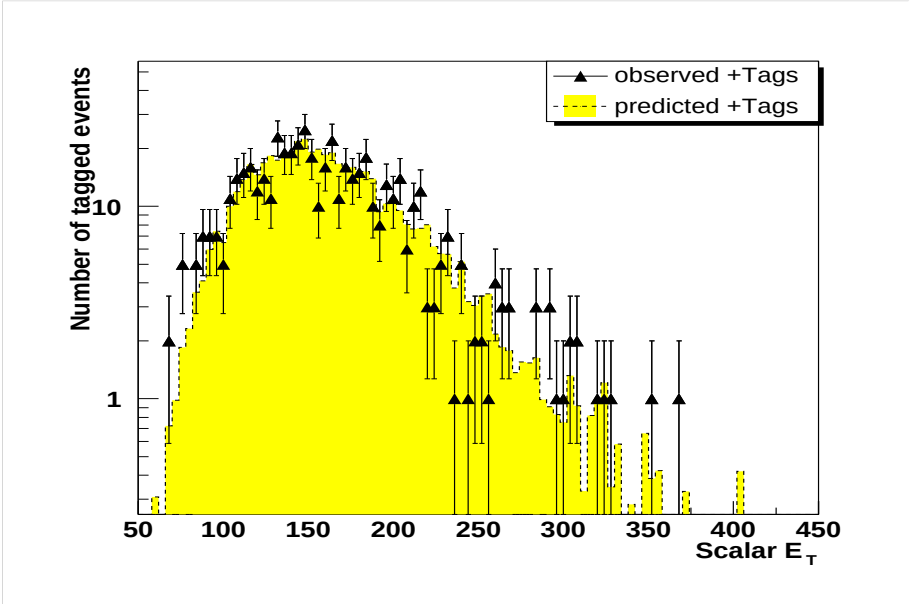

Figure 5.54: Scalar E_T distribution of predicted and observed positive tags in the inclusive qcd_em sample.

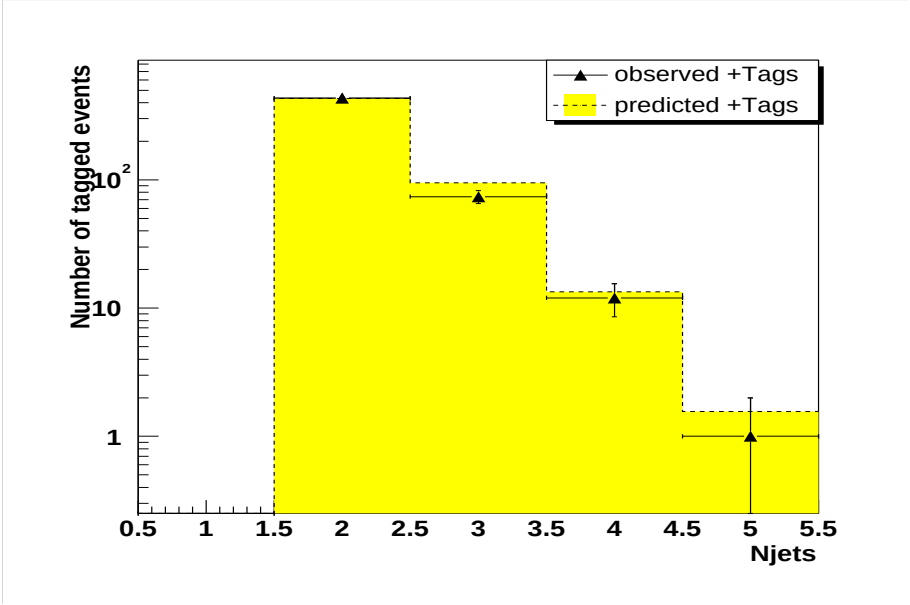

Figure 5.55: Jet multiplicity distribution of predicted and observed positive tags in the inclusive qcd_em sample.

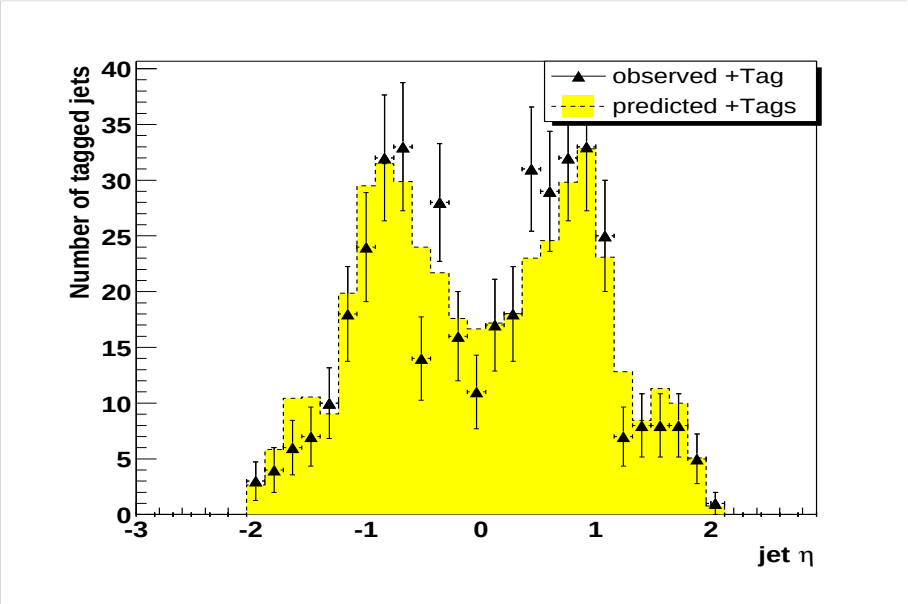

Figure 5.56: η distribution of predicted and observed positive tags in the inclusive qcd_jet sample.

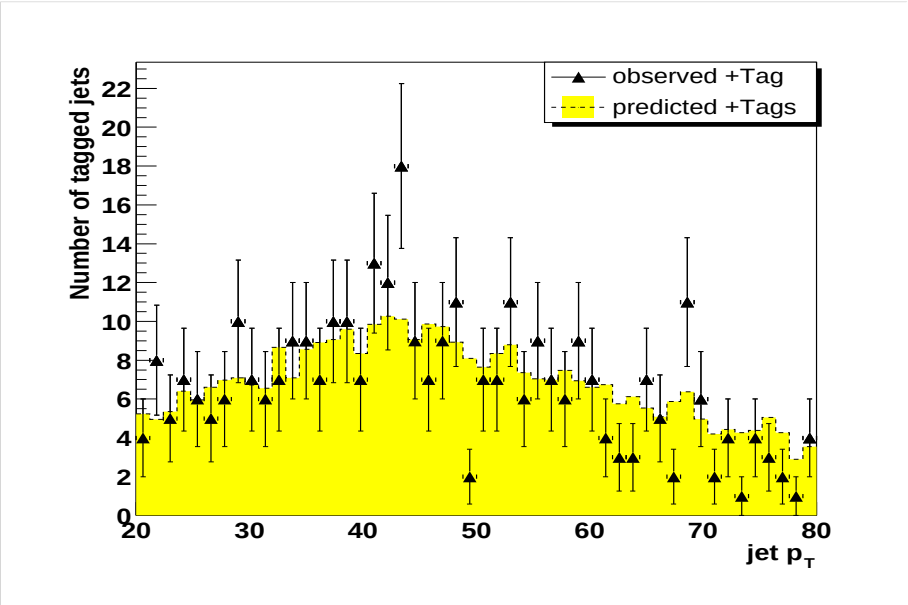

Figure 5.57: p_T distribution of predicted and observed positive tags in the inclusive qcd_jet sample.

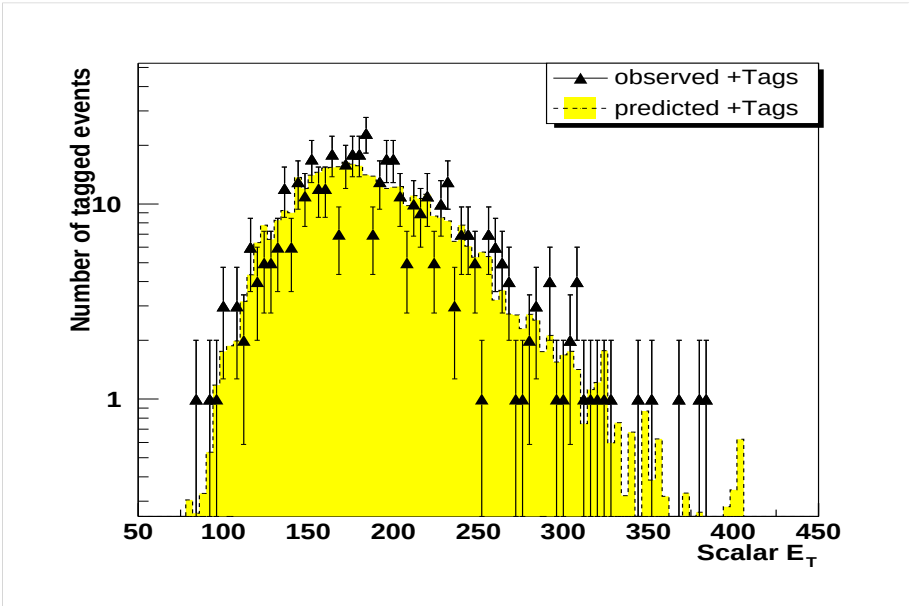

Figure 5.58: Scalar E_T distribution of predicted and observed positive tags in the inclusive qcd_jet sample.

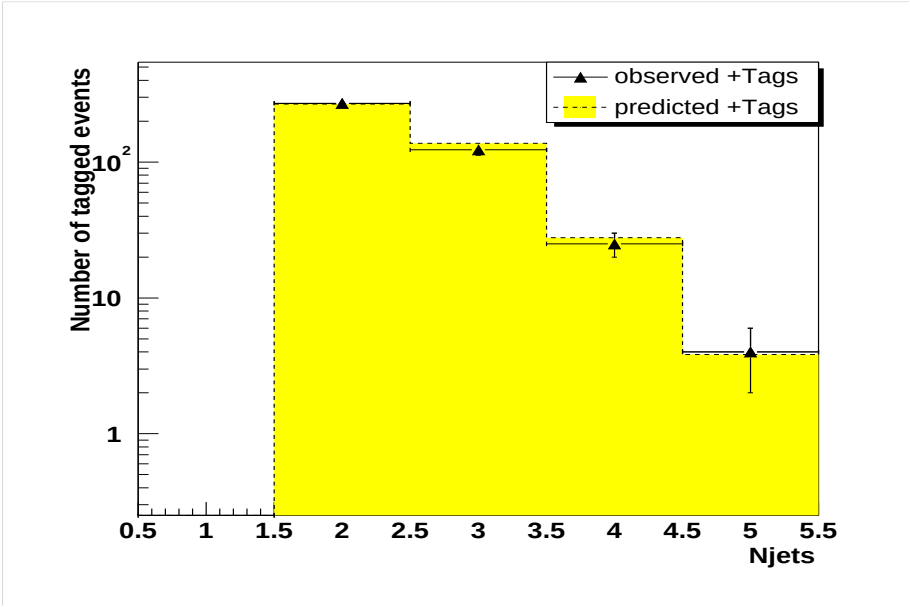

Figure 5.59: Jet multiplicity distribution of predicted and observed positive tags in the inclusive qcd_jet sample.

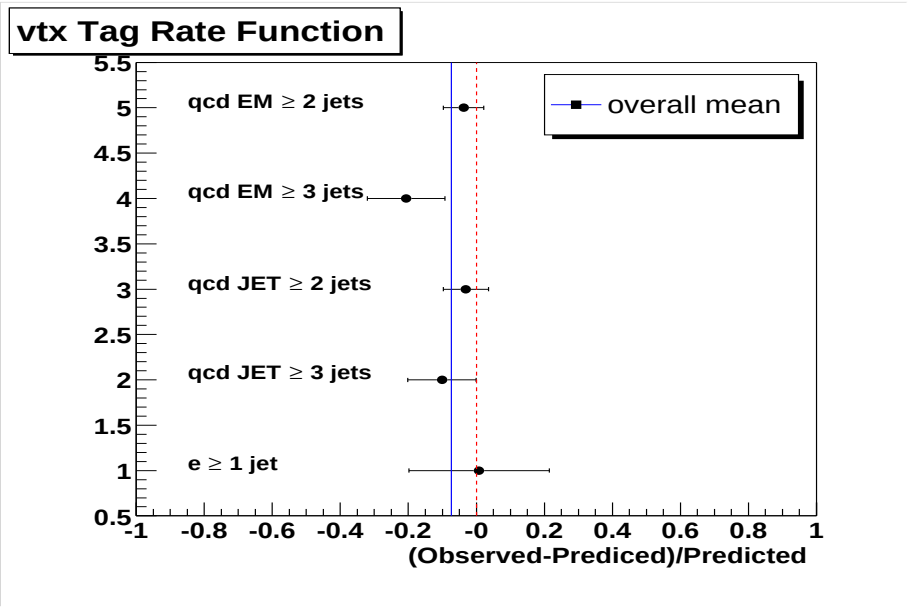

Figure 5.60: Relative difference between predicted and observed tags in all different samples.

5.5.3 *b*-tagging Efficiency

We measured the efficiency to tag real b-jets in the b enriched inclusive muon-jet sample. A large fraction of the events in this sample is expected to originate from $b\bar{b}$ production in which the decay of one of the b quarks produces the muon trigger and the other a hadronic jet. The muon is not isolated but produced in the vicinity of a jet. We identify the muon and its associated calorimeter jet as the *muon-jet* in which we look for secondary displaced vertices. The hadronic jet is referred to as the *away-jet*. We require a muon with $p_T > 2\,GeV/c$ and a matched central track within $\Delta R < 0.7$ of a calorimeter jet with $p_T > 10\,GeV/c$ and $|\eta| < 3$. The calorimeter jet is required to be matched $\Delta R < 0.5$ to a track-jet with at least 2 tracks satisfying the track selection criteria.

Figures 5.61 and 5.62 show the secondary vertex transverse decay length distribution in muon-jet and away-jet tags. These distributions show a larger positive excess than in inclusive jet events, due to their larger heavy flavor content. The smaller positive excess in the away jet is expected due to the presence of gluon splitting and flavor excitation processes in the sample. In these cases, when one of the b-jets is not reconstructed, the away jet is not a heavy flavor jet. A detailed study of the away hadronic jet requires the generation of special Monte Carlo samples unavailable at the time of writing this Thesis.

The b content of the muon-jet sample is obtained by using the fit templates of the transverse momentum of the muon relative to the calorimeter jet axis (p_T^{rel}) [38]. Figure 5.63 shows the distribution of p_T^{rel} in the data and in the simulation, for different Monte Carlo samples: $b\bar{b}$, $c\bar{c}$ and *QCD*. The $b\bar{b}$ template includes the sequential decay $b \to c \to \mu$ which is indistinguishable from the direct $b \to \mu$ decay. These fit template functions are used to predict the b, c and *light* quark content probabilities of muon-jets on an event-by-event basis.

The discrimination power of the p_T^{rel} variable is illustrated in figure 5.64, showing

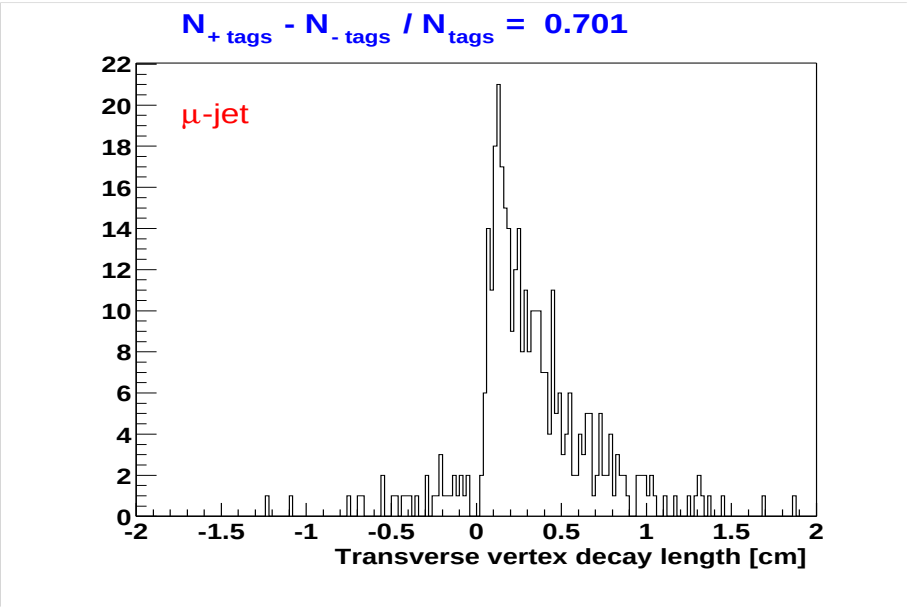

Figure 5.61: Secondary vertex decay length distribution in muon-jets

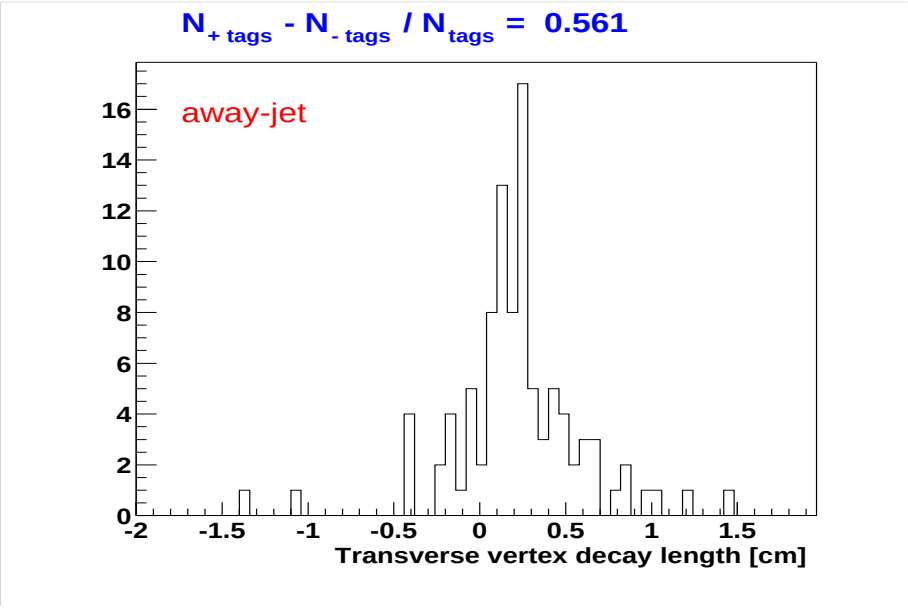

Figure 5.62: Secondary vertex decay length distribution in away-jets

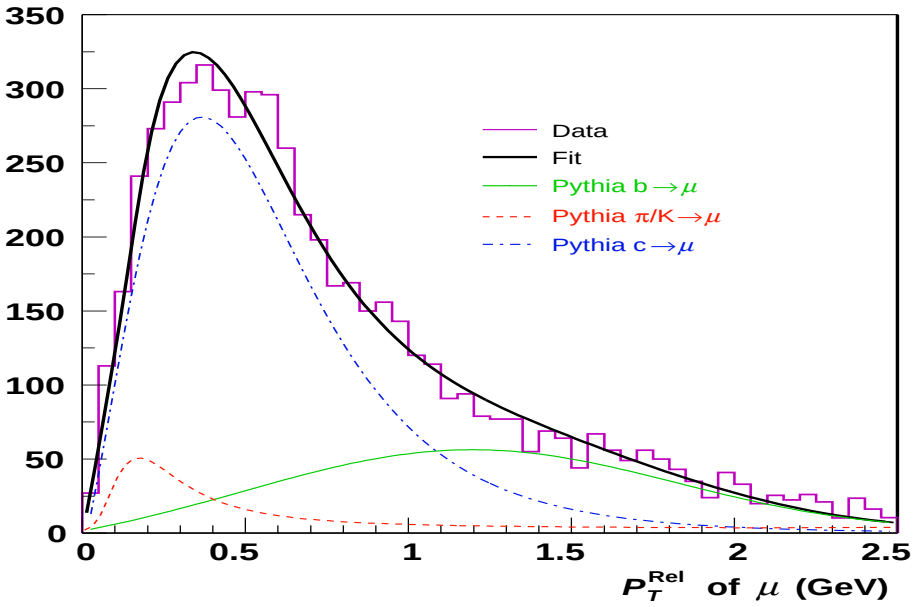

Figure 5.63: Distribution of muon p_T^{rel} in the data and simulation.

efficiency and purity as a function of the minimum p_T^{rel} cut. We require $p_T^{rel} > 1.0\,GeV$ to enhance the b content of the sample.

The secondary vertex jet tagging efficiency, in semileptonic b decays, is obtained by counting the number of positive tags in the muon-jet sample and subtracting out the number of expected c-jets and positive mistags from QCD, as explained below. The heavy flavor content is obtained from the p_T^{rel} template fits. Let ϵ_b, ϵ_c, and ϵ_{qcd} be the efficiencies, and N_b, N_c, and N_{qcd} the number, of b, c and *light* quark jets, respectively. The total number of positive tags can be expressed as

$$+Tags = N_b\epsilon_b + N_c\epsilon_c + N_{qcd}\epsilon_{qcd} \tag{5.7}$$

The total number of jets of a particular flavor $f = b, c, uds$ is obtained from the p_T^{rel} template fits applied to the muon-jets:

$$N_f = \sum_{\mu-jets} F_f \tag{5.8}$$

where F_f is the f-flavor content of the muon-jet.

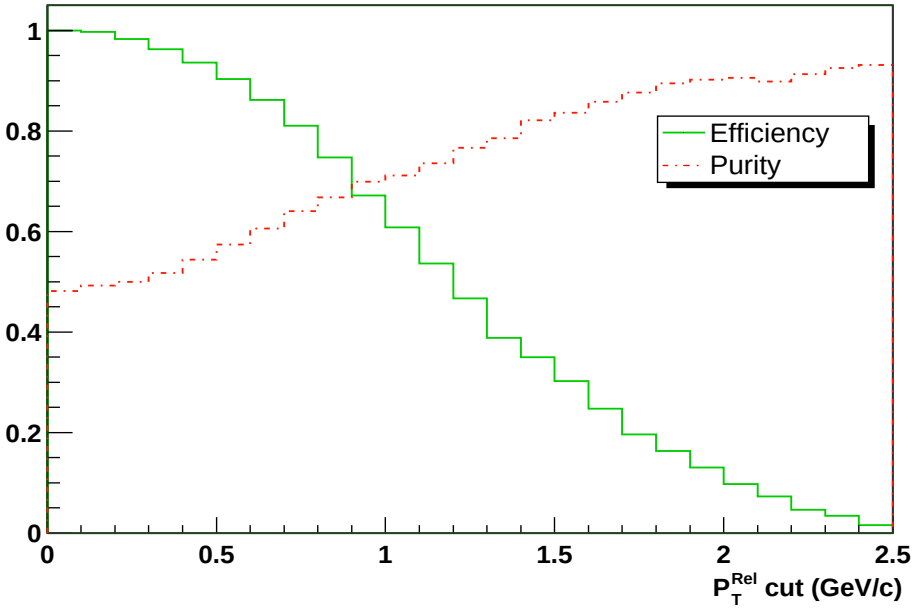

Figure 5.64: b-jet efficiency versus purity as a function of muon p_T^{rel}.

Given that the secondary vertex tagger algorithm does not discriminate b from c vertices, we use the ratio of b- and c-jet tagging efficiencies in the simulation to eliminate the ϵ_c unknown in equation (5.7). We assume $\epsilon_c = R\epsilon_b$, with $R = \epsilon_c^{MC}/\epsilon_b^{MC}$.

The last term in equation (5.7) is obtained from the parametrization of the positive tag rate in the inclusive QCD data sample. The total number of positive tags expected from QCD is obtained by multiplying the positive tag rate function, evaluated at the track-jet multiplicity, by the qcd fraction F_{qcd}.

Thus, equation 5.7 can be solved for ϵ_b:

$$\epsilon_b = \frac{+Tags - N_{qcd}\,\epsilon_{qcd}}{N_b + R\,N_c} \tag{5.9}$$

Figure 5.65 shows the muon-jet p_T distribution in the data for all jets (points), b-jets (grey), $+Tags$ (solid black) and qcd (black line). The b-jet p_T distribution is obtained by weighting every p_T bin of the histogram by F_b.

Figure 5.66 shows the b-tagging efficiency as a function of jet p_T obtained from

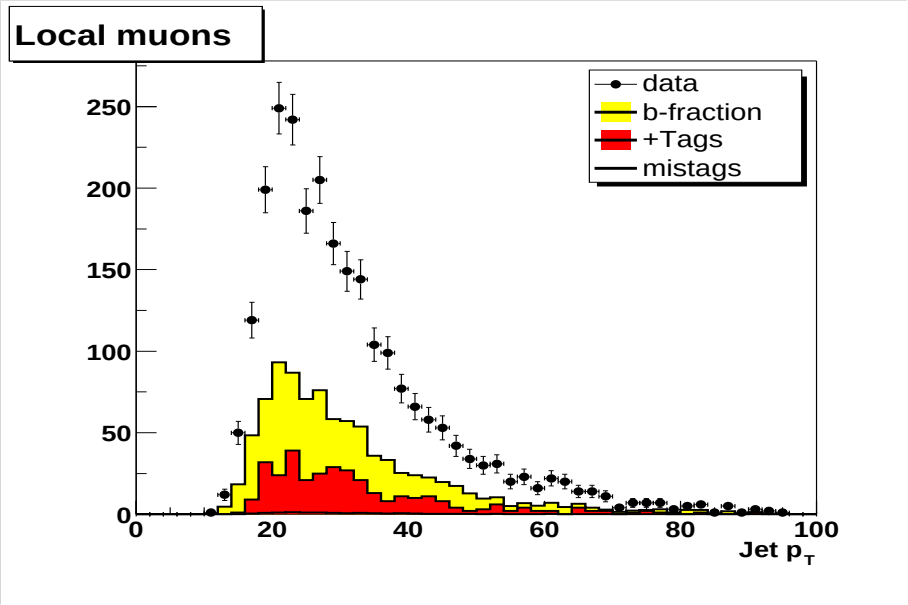

Figure 5.65: Jet p_T spectrum in the data for all jets (dots) and jets weighted with the b-jet content from the p_T^{rel} template fits.

equation (5.9). The overall efficiency is $\epsilon_b = 0.29 \pm 0.02$.

The primary reason for the different efficiencies obtained in the data and the simulation is the lower number of good quality reconstructed tracks in jets, in the former case. This is demonstrated in Figure 5.67, where the b-tagging efficiency in muon-jets is plotted as a function of the track-jet multiplicity. We observe that we can achieve more than 40% efficiency when the jet has four or more tracks. Note that the b-tagging efficiency definition (5.9) subtracts the mistag background contribution, This indicates that the increase in efficiency is not a consequence of increasing the mistag rate.

It is not possible to measure the b-tagging efficiency in hadronic jets with our current *muon*-jet sample, due to the smaller number of *away*-jets and the lack of Monte Carlo sample containing all three $b\bar{b}$ heavy flavor processes. This measurement will be done for data reconstructed with further DØreco versions.

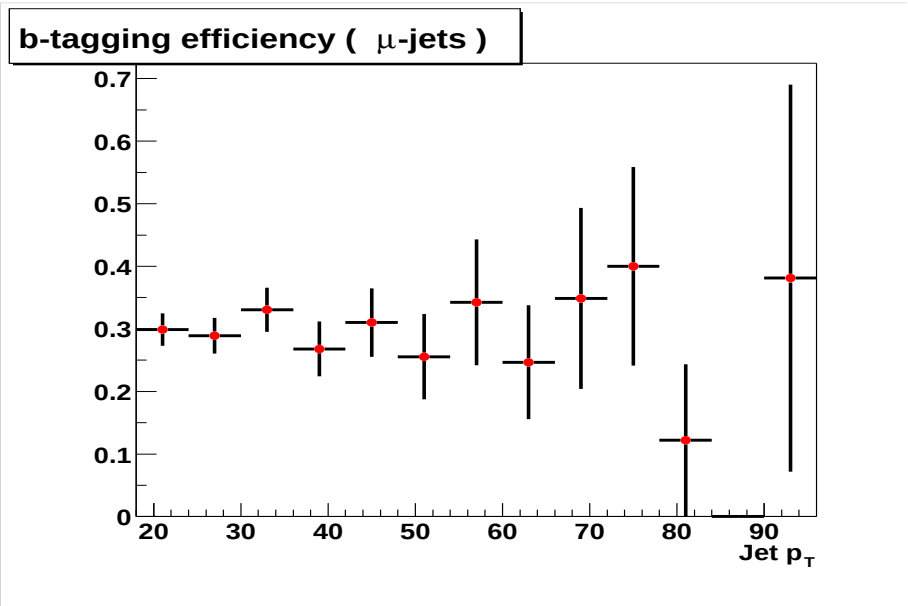

Figure 5.66: b-jet tagging efficiency in semileptonic mu-jet events as function of jet p_T. The overall efficiency, obtained from a linear fit, is $\epsilon_b = 0.29 \pm 0.02$.

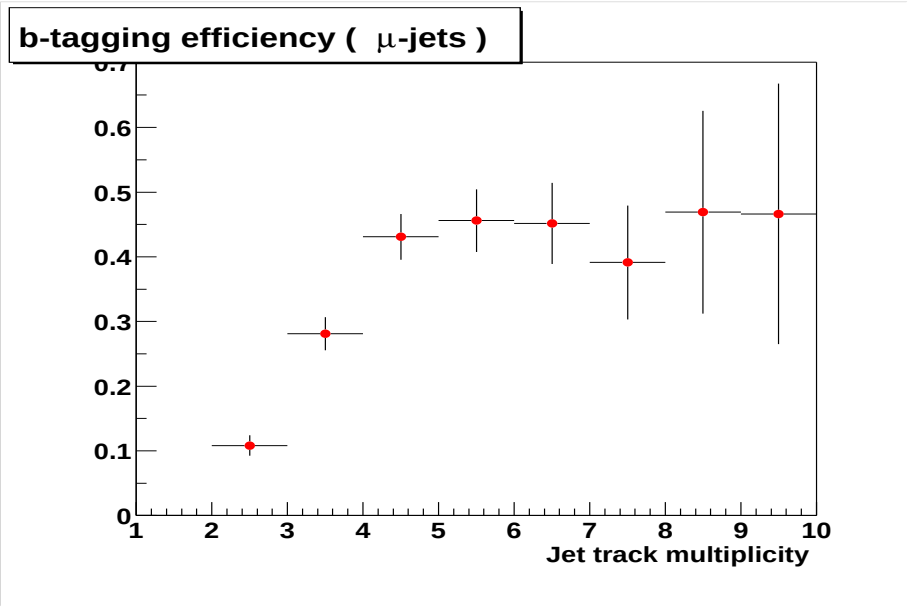

Figure 5.67: b-jet tagging efficiency in semileptonic mu-jet events as function of the number of tracks in the jet.

5.6 Flavor Tagging

In addition to the the identification of b-quark jets, it is possible to discriminate between b- and $\bar{b}$-jets using the charge information of the tracks associated to jets.

The charge of a jet can be determined by computing a weighted sum of the charge of tracks associated to a track-jet. The charge of a heavy quark is correlated with the jet charge: If the heavy quark decays semileptonically, the lepton, which has the same charge sign than the quark, will strongly contribute to the charge average. When the heavy quark decays into a neutral meson, particles produced in the fragmentation together with the neutral meson will also bear a memory of the heavy quark charge sign.

We define the jet charge as a momentum weighted charge average of the tracks in the track-jet [39]

$$Q = \frac{\sum_{j=1}^{N} q_j \, (\hat{p}_j \cdot \hat{a})^{\kappa}}{\sum (\hat{p}_j \cdot \hat{a})^{\kappa}} \tag{5.10}$$

where q_j and $\hat{p}_j$ are the charge and momentum of the track j, $\hat{a}$ is the jet direction and κ is a parameter that weights tracks according to their momentum. If $\kappa \to 0$, all tracks are equally weighted. If $\kappa \to \infty$, only the highest p_T track will contribute to the jet charge.

Figures 5.68 and 5.69 show the jet charge distribution for b and $\bar{b}$ jets in a $t\bar{t}$ Monte Carlo sample for $\kappa = 0.5$ and $\kappa = 1.0$. The spikes at $|Q| = 1$ are produced when all tracks in the jet have the same charge.

In order to quantify the performance of flavor quark identification we define the efficiency ϵ, purity P and dilution D, as a function of the cut value Q of the jet charge as follows:

- ϵ = (Number of correctly tagged jets) / (all jets)
- P = (Number of correctly tagged jets) / (all tagged jets)
- D = (Number of correct tags - Number of mistags) / (all tagged jets)

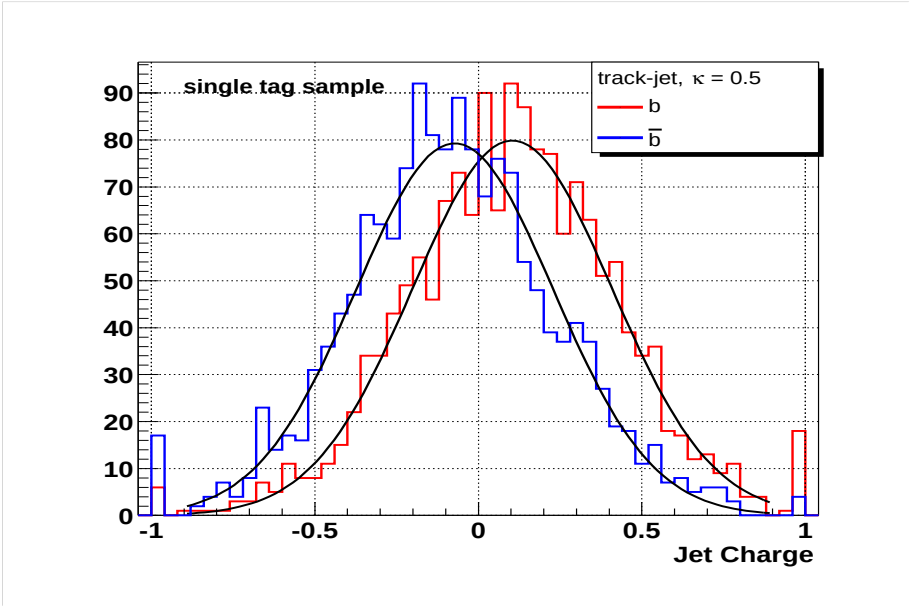

Figure 5.68: Distribution of jet charge in b and $\bar{b}$ jets in a $t\bar{t}$ Monte Carlo sample for $\kappa = 0.5$.

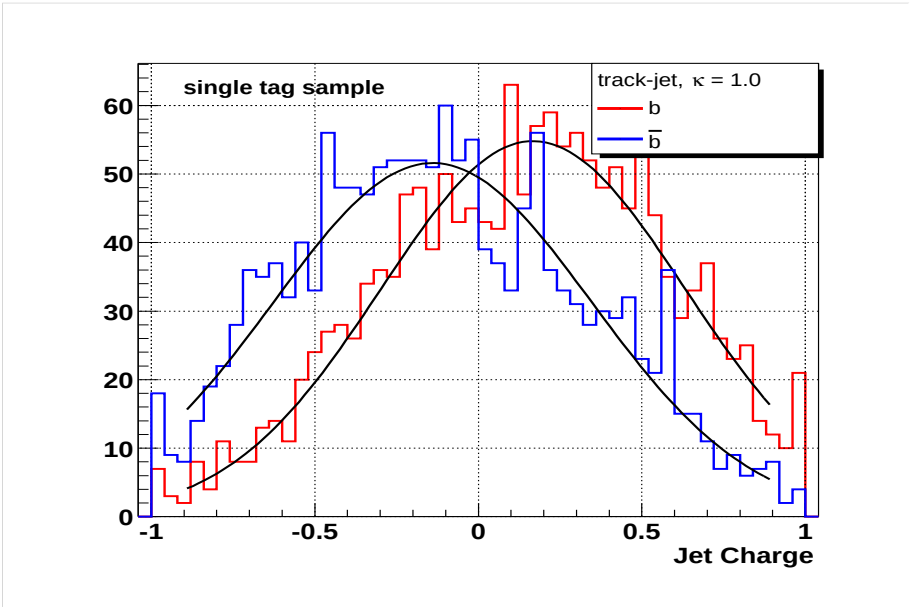

Figure 5.69: Distribution of jet charge in b and $\bar{b}$ jets in a $t\bar{t}$ Monte Carlo sample for $\kappa = 1.0$.

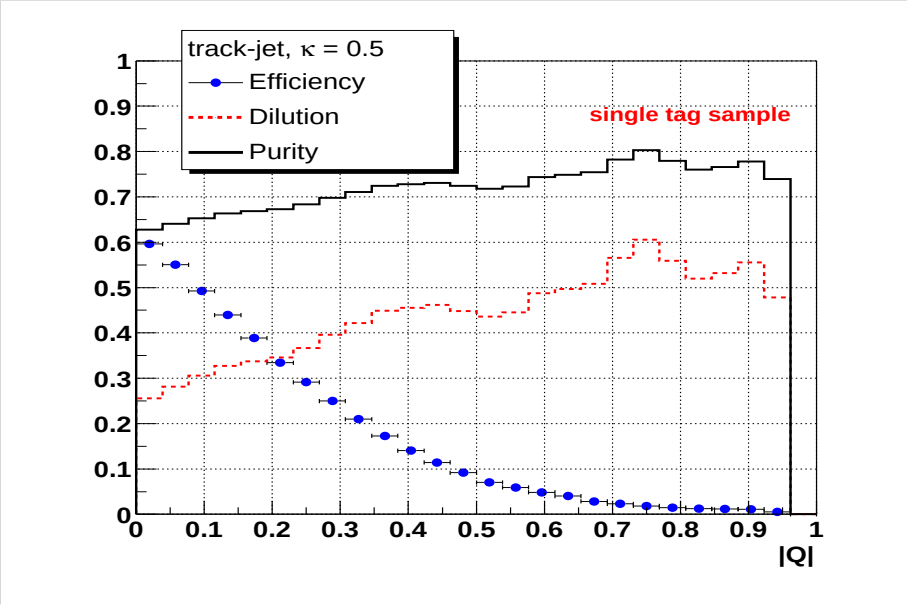

Figure 5.70: Performance of the jet flavor tagging as a function of the jet charge cut Q for $\kappa = 0.5$.

A zero value for the dilution means that the jet charge gives a random answer (half of the time it is right, half of the time it is wrong) whereas $D = 1$ corresponds to a perfect algorithm.

Figures 5.70 and 5.71 show ϵ, P and D for jet flavor identification as a function of the jet charge Q when $\kappa = 0.5$ and $\kappa = 1.0$. For instance, if we tag b-jets when $Q > 0.1$, using $\kappa = 1.0$, it is possible achieve an efficiency $\epsilon = 0.54$ and a purity $P = 0.62$.

The jet charge distribution in the data was studied in the subset of di-muon events containing a displaced $B^{\pm}$ secondary vertex ($K^{\pm}$ with $p_T > 1.5$, SMThits ≥ 3, collinearity > 0.9, $\chi^2_K < 10$, $\chi^2_B < 20$, lifetime $> 0.02\,cm$). Once a B displaced vertex was identified, we divide the event in two hemispheres considering the opposite hemisphere as containing an unbiased b-jet. Thus, we loop over track-jets on the opposite hemisphere and select the highest multiplicity jet with $\Delta R(B, jet) > 2.8$ and $p_T > 4\,GeV$. Figure 5.72 shows the jet charge distribution in the unbiased

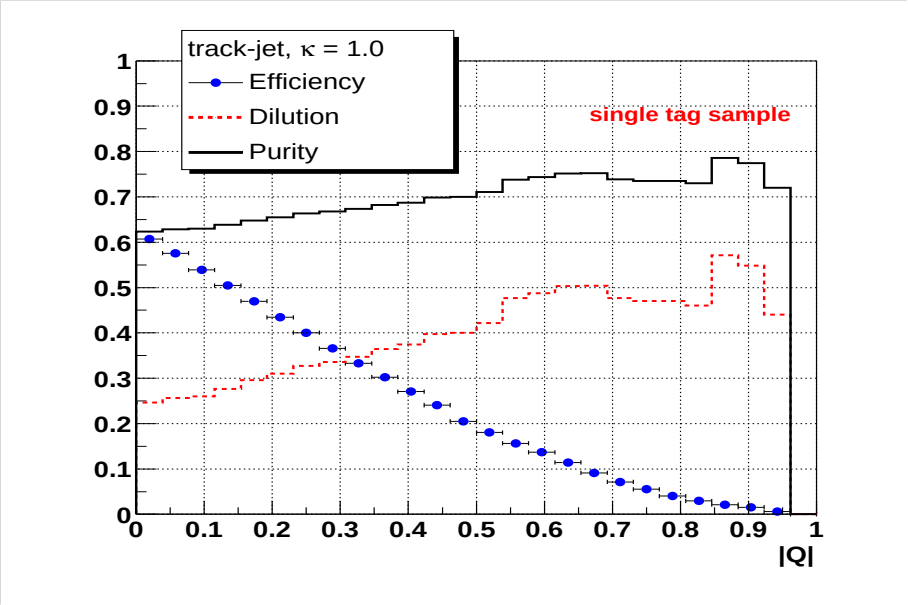

Figure 5.71: Performance of the jet flavor tagging as a function of the jet charge cut Q for $\kappa = 1.0$.

opposite track-jet. This plot shows a negative correlation between the B vertex charge (given by the K charge) and the opposite-jet charge. The final tuning of the Jet-Charge algorithm will be done in a larger sample of dimuon events.

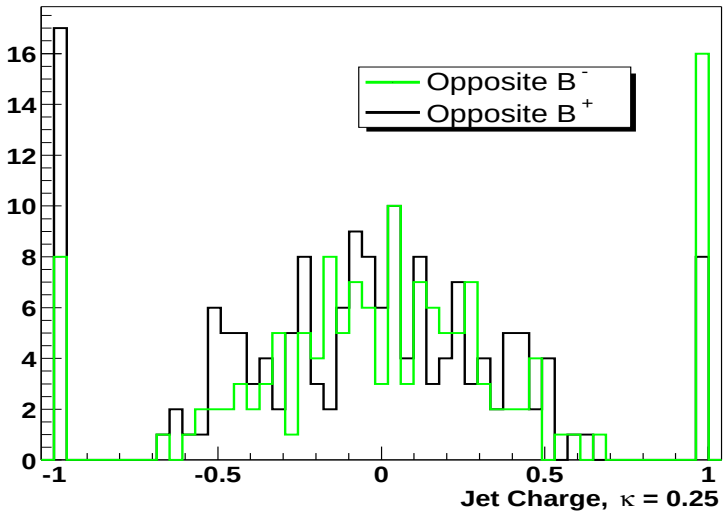

Figure 5.72: Distribution of jet charge in the $B^{\pm}$ data sample for $\kappa = 0.5$.

Chapter 6

$\not\!\!E_T$ Significance

This Chapter is devoted to the implementation of a probabilistic technique for the identification of events with significant $\not\!\!E_T$. There are many physics analyses that can benefit from such a tool, like new phenomena searches with neutralino particles in the final state, Higgs searches, top quark identification in the lepton channels, etc.

The $\not\!\!E_T$ Significance (METsig) algorithm was originally developed during Run I [40] and, as part of this Thesis, I have adapted, optimized and implemented it for Run II.

This chapter describes the METsig algorithm, its definition, optimization with Run II data, and it analyses its performance for discriminating events with real $\not\!\!E_T$ from events with fake or mis-measured $\not\!\!E_T$.

6.1 The $\not\!\!E_T$ Significance Algorithm

6.1.1 Introduction

The missing transverse energy of an event is defined as the vector that needs to be added to the transverse energy of all cells in the calorimeter in order to achieve a

perfect balance in the transverse plane. In an ideal detector, a non-zero $\not\!\!E_T$ value is the signal of the presence of non-interacting particles, like high-p_T muons, neutrinos or other beyond the Standard Model particles. However, experimental effects can mimic a large $\not\!\!E_T$ measurement in an event that has none, due to its finite resolution.

The missing transverse energy resolution is governed by many effects: mis-identification of the primary vertex, energy resolution of jets, electrons, muons and unclustered energy, hot cells, etc. Given a particular event with some measured missing transverse energy $\not\!\!E_T$, we may ask how likely it could be due to a resolution fluctuation, taking into account the particular topology and measured physics objects in the event. In other words, which is the *significance* of the measured $\not\!\!E_T$ for that particular event. Based on the knowledge of the energy resolution of the different physics objects, the METsig algorithm computes the probability distribution for the $\not\!\!E_T$, and it evaluates how likely the measured $\not\!\!E_T$ value is consistent with a resolution fluctuation in the direction of the observed $\not\!\!E_T$ ($\vec{a}$), on an event-by-event basis. This is illustrated in Figure 6.1, where an hypothetical transverse view of an event is shown. The dark lines represent the transverse energy of two jets, the light line the energy of an electron, the arrow the measured $\not\!\!E_T$, and the point on the arrow the magnitude of the $\not\!\!E_T$. The METsig algorithm, by fluctuating the jet and electron energies according to their resolutions, computes the expected $\not\!\!E_T$ distribution along the $\vec{a}$ direction. The width of this probability distribution is used to build a likelihood variable to quantify the number of standard deviations by which the $\not\!\!E_T$ probability, in the direction of the measured $\not\!\!E_T$, is different from 0.

The METsig algorithm was developed to discriminate events with real $\not\!\!E_T$ from those with fake or mis-measured $\not\!\!E_T$. Traditionally, this is performed through a $\not\!\!E_T$ cut off above a certain value, such as $\not\!\!E_T > 25\,GeV/c$. This approach has the disadvantage that it depends on the event topology. Since events with several high p_T jets are more likely to give rise to a mismeasured large value of $\not\!\!E_T$ than events

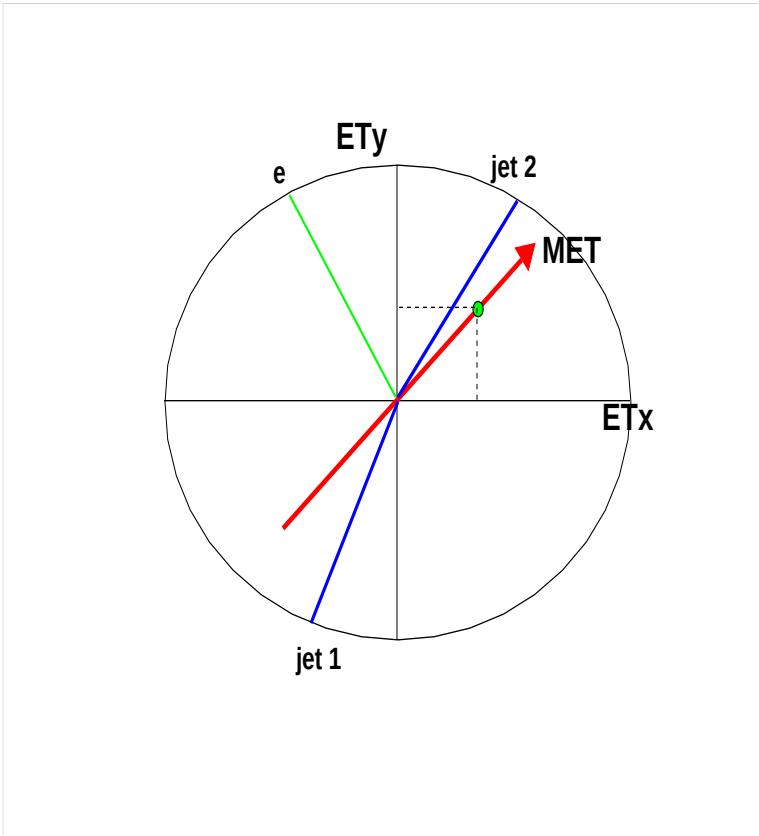

Figure 6.1: Example of an event in the transverse energy plane. The METsig algorithm computes the probability distribution for the $\not\!\!E_T$, in the direction of the measured $\not\!\!E_T$, and it evaluates the number of standard deviations by which the $\not\!\!E_T$ probability, in the direction of the measured $\not\!\!E_T$, is different from 0.

with lower jet multiplicity, any event selection based on a constant $\not\!\!E_T$ cut off will perform differently depending on the p_T spectrum and jet multiplicity. A cut on $\not\!\!E_T$ significance, on the other hand, will retain events where the observed $\not\!\!E_T$ cannot be explained by resolution effects, *independently* of the event topology. This technique has shown to be very effective in Run I analyses, outperforming other topological methods developed to isolate events with large true $\not\!\!E_T$.

6.1.2 Algorithm Definition

We are interested in the probability distribution for the $\not\!\!E_T$, due to the resolution fluctuations of the N objects present in a particular event, each with respective transverse energies $\vec{E}_T^{\,j}$ $(j = 1, N)$.

Let us denote by $\vec{a}$ the actual measured transverse missing energy in the event, $\vec{a} = (\not\!\!E_X^{\,m}, \not\!\!E_Y^{\,m})$, $\not\!\!E_T^{\,m} = |\vec{a}|$, and consider that the module of the transverse energy of physics object j fluctuates from E_T^j to $E_T^{j\,\prime}$. The resulting event $\not\!\!E_T$ would then change to

$$\not\!\!E_T = \left| \vec{a} - \sum_{j=1}^{N} (E_T^{j\,\prime} - E_T^j)\, \vec{j} \right| = \left| \vec{a} - \sum_{j=1}^{N} (\Delta E_T^j)\, \vec{j} \right| \tag{6.1}$$

where $\vec{j}$ is the direction of object j in the transverse plane.

The projection of $\not\!\!E_T$ in the direction of the measured $\not\!\!E_T^{\,m}$, we called this direction $\vec{a}$, will be denoted $\not\!\!E_T^{\,a}$ and is given by

$$\not\!\!E_T^{\,a} = \not\!\!E_T^{\,m} - \sum_{j} (\Delta E_T^j)\, \cos(\vec{j}, \vec{a}) \tag{6.2}$$

The probability distributions for the transverse energy fluctuations of the physics objects, ΔE_T^j, are experimentally found to be well described by gaussians, as discussed in detail in the following section. Thus

$$p(\Delta E_T^j) = N(0\,, \sigma^j) \tag{6.3}$$

where $\sigma_j = \sigma(E_T^j, \eta^j)$ is the j^{th} object transverse resolution and $N(\mu, \sigma)$ represents a Gaussian distribution of mean value μ and width σ. Actually, the resolutions are parameterized as a function of E_T^j for jets and E^j for electromagnetic objects, but the conversion is readily done by knowing the respective rapidities η^j.

Since a linear combination of gaussian distributions is itself a gaussian distribution, the probability distribution for the $\not\!\!E_T^{\,a}$ turns out to be

$$p\left(\not\!\!E_T^{\,a}\right) = N\left(\not\!\!E_T^{\,m}, \sqrt{\sum_j^N \sigma_j^2 \cos^2(\vec{j}, \vec{a})}\right) \tag{6.4}$$

The unclustered energy object requires special consideration since we assume it can fluctuate in any direction. Its contribution to the resolution, $\sigma_{U.E}^2$, is therefore not multiplied by a cosine, yielding as a final result for the probability distribution of $\not\!\!E_T$ projected along the direction of the measured transverse missing energy

$$p\left(\not\!\!E_T^{\,a}\right) = N\left(\not\!\!E_T^{\,m}, \sqrt{\sum_j^{N-1} \sigma_j^2 \cos^2(\vec{j}, \vec{a}) + \sigma_{U.E}^2}\right) \tag{6.5}$$

Based on this probability density, we can define a pseudo likelihood

$$L \equiv \log \frac{p\left(\not\!\!E_T^{\,a} = \not\!\!E_T^{\,m}\right)}{p\left(\not\!\!E_T^{\,a} = 0\right)} = 2 \log \frac{\not\!\!E_T^{\,m}}{\sqrt{2}\,\sigma} \tag{6.6}$$

where σ is the variance of the $p(\not\!\!E_T^{\,a})$ probability distribution. This likelihood is higher, the larger the probability that the $\not\!\!E_T^{\,m}$ of the event differs from zero due to a statistical fluctuation. The likelihood as defined ranges between 0 and infinity, but we set $p\left(\not\!\!E_T^{\,a} = 0\right) = e^{-4}$ when $p\left(\not\!\!E_T^{\,a} = 0\right) < e^{-4}$ in order to constrain L to values smaller than 10.0.

Figure 6.2 shows two examples of $p(\not\!\!E_T^{\,a})$ corresponding to events with large $\not\!\!E_T$. In the first event (left plot), the $\not\!\!E_T$ is due to an energy imbalance from jet resolution fluctuations. The width of $p(\not\!\!E_T^{\,a})$ is wide enough to have a significant contribution at $\not\!\!E_T^{\,a} = 0$. In the second event (right plot), the $\not\!\!E_T$ is genuine, due to the presence

of a neutrino. The $p(\not\!\!E_T^{\,a})$ distribution, even though it peaks at a lower value than in the previous case, is very narrow, with almost no contribution at $p(\not\!\!E_T^{\,a} = 0)$. As a consecuence, both events with $\not\!\!E_T \sim 50\,GeV/c$, will have small and large $\not\!\!E_T$ significances due to their particular topology.

6.2 Probability Density Functions

In this section we will review how the energy resolutions are determined from the data. We consider three different physics objects: jets, electromagnetic objects (electrons and photons) and unclustered energy. We define the probability density functions, $p(E_i)$, such that the probability that the i^{th} physics object has an energy between E_i and $E_i + \delta E_i$, is given by $p(E_i)\delta E_i$. These functions are well described by gaussians.

6.2.1 Jets

The jet energy resolution is obtained from the p_T momentum imbalance in dijet back-to-back events using the same method as in RunI [41]. The method begins by measuring the asymmetry variable A,

$$A = (E_T^1 - E_T^2)/(E_T^1 + E_T^2) \tag{6.7}$$

as a function of the average di-jet p_T, $\langle E_T \rangle = (E_T^1 + E_T^2)/2$. In the ideal case of E_T-balanced jets at particle level, the jet resolution σ_{E_T} is related to the width of the asymmetry distribution by the equation

$$\frac{\sigma_{E_T}}{E_T} = \sqrt{2}\sigma_A \tag{6.8}$$

Formula 6.8 must be corrected for the fact that, in higher orders of the perturbative expansion, or after hadronization, the presence of additional soft jets might

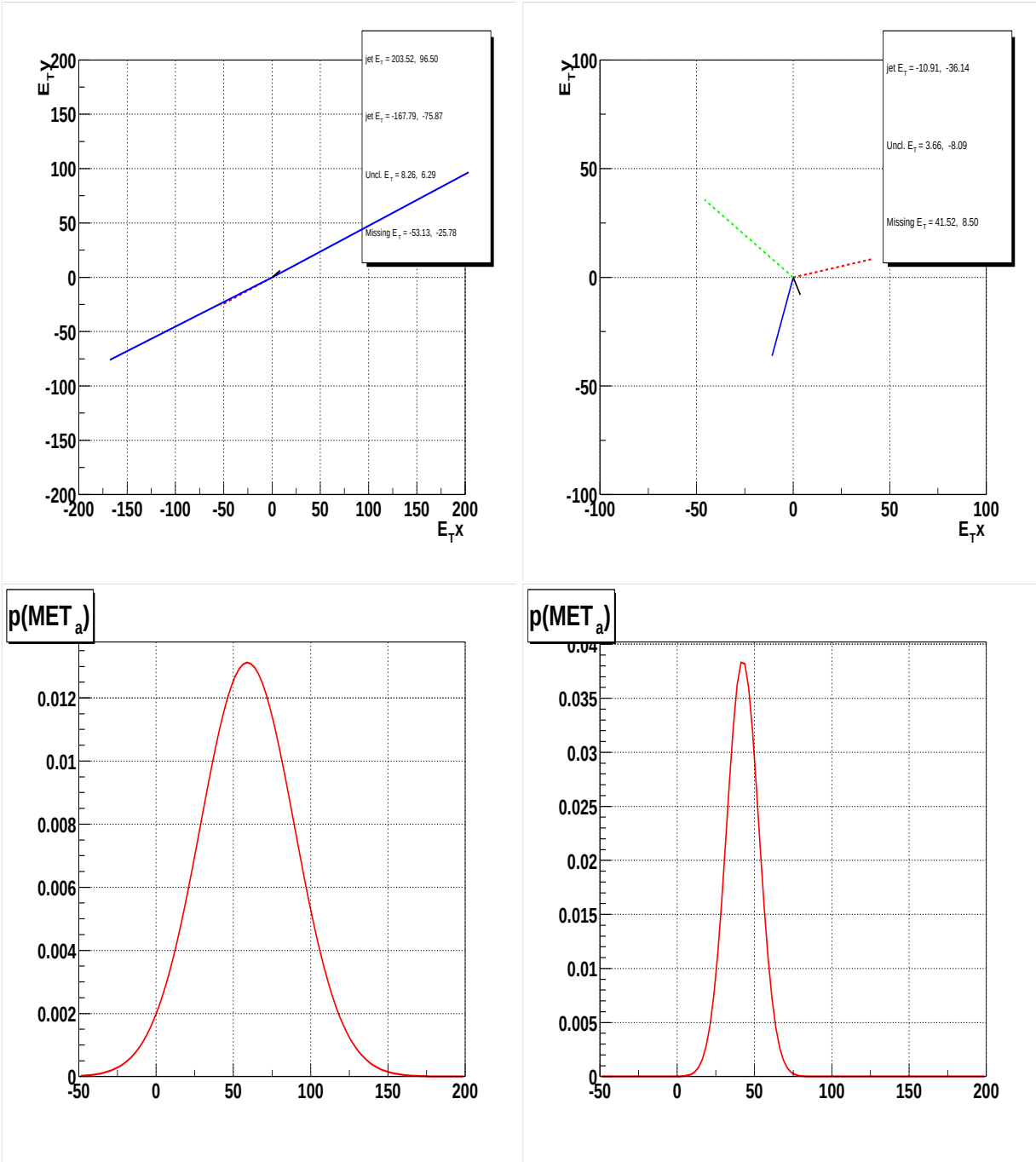

Figure 6.2: Example of $p(\not\!\!E_T^{\,a})$ in two events with large $\not\!\!E_T$.

	$\lvert\eta\rvert < 0.5$	$0.5 < \lvert\eta\rvert < 1.0$	$1.0 < \lvert\eta\rvert < 1.5$	$1.5 < \lvert\eta\rvert$
N	0.0 ± 3.0	7.9 ± 1.7	0.0 ± 33	9.0 ± 7.0
S	0.98 ± 0.01	1.0 ± 0.2	1.8 ± 0.8	0.7 ± 1.5
C	0.08 ± 0.01	0.2 ± 0.1	0.0 ± 0.1	0.0 ± 0.7

Table 6.1: Jet energy resolution parametrisation fits.

introduce some imbalance in the transverse momentum of the two leading jets. Moreover, soft jets are usually not reconstructed due to the $8\,GeV/c$ cut off on jet p_T. After these effects are taken into account, the jet energy resolution is parametrised with the formula

$$\frac{\sigma_{E_T}}{E_T} = \sqrt{\frac{N^2}{E_T^2} + \frac{S^2}{E_T} + C^2} \tag{6.9}$$

in four calorimeter detector-η regions: $|\eta| < 0.5$, $0.5 < |\eta| < 1.0$, $1.0 < |\eta| < 1.5$ and $1.5 < |\eta|$.

In formula 6.9, the sampling term, S describes sampling and showering fluctuation of the incident particles, the limit on resolution at high energies is described by the constant term C and noise fluctuations that affect the low energy range are given by the noise term, N.

The values of the fit parameters are summarized in table 6.1.

Thus, the probability density for jets is given by

$$p(E_{T_i}) = N(E_{T_i}, \sigma_i(E_T, \eta)) \tag{6.10}$$

6.2.2 Unclustered Energy

The unclustered energy in an event corresponds to the calorimeter energy unassociated with jets. There are many sources for unclustered energy:

- **Soft jets** Due to the $8\,GeV/c$ cut of jet p_T, the energy from soft jets remains unassociated to physics objects and adds to the unclustered energy of the event.

- **Out-of-cone energy** In the case of the fixed size 0.5 Cone jet algorithm used in this analysis, energy outside a 0.5 radius around the jet axis will not be associated to the reconstructed jet, contributing to the unclustered energy of the event.

- **Warm regions** Noisy calorimeter regions, usually called warm regions, might contribute with calorimeter energy unassociated to jet objects.

- **Underlying event** The energy distribution from parton remnants from the hard interaction and additional minimum bias interactions also contribute with energy unassociated to calorimeter jets.

In addition, the amount of unclustered energy in an event depends on the physics process and its topology.

Figure 6.3 shows the distribution of scalar transverse unclustered energy in triggered-jet events as a function of the number of jets in the event. Since the original data sample was selected by requiring at least one jet, the scalar unclustered energy for 0-jet events is zero. We observe how the mean value increases as more jets contribute with more out-of-cone unclustered energy. Figure 6.4 shows the ratio between scalar transverse unclustered energy and scalar total transverse energy in the event. The fraction of unassociated energy to jets is of the order of 25%.

We parametrised the x and y components of the unclustered energy resolution as a function of the scalar unclustered energy in the event, by a linear relationship:

$$\sigma_{E_T} = a + b \cdot USE_T \tag{6.11}$$

We plan to extend this parametrisation considering the event jet multiplicity, as a future improvement.

Figures 6.5 and 6.6 show the distribution of transverse x and y components of the unclustered energy vector, in bins of scalar unclustered energy. The linear fits

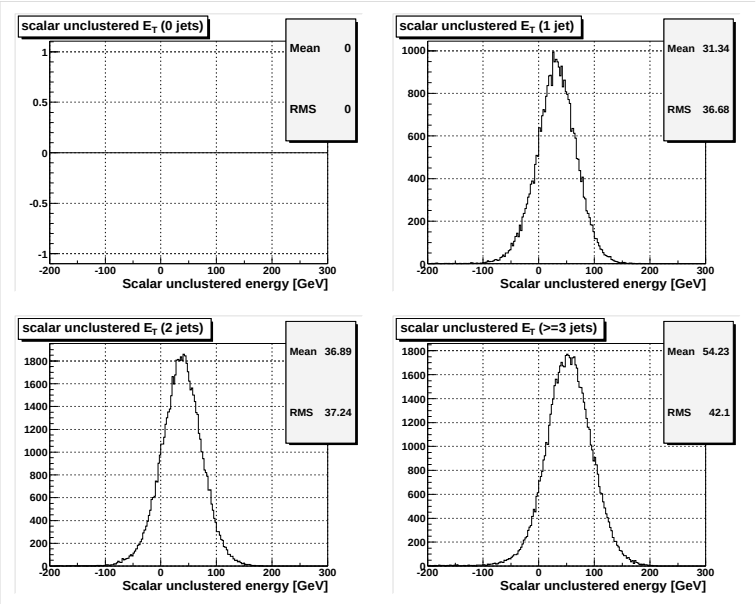

Figure 6.3: Distribution of scalar unclustered energy as a function of jet multiplicity

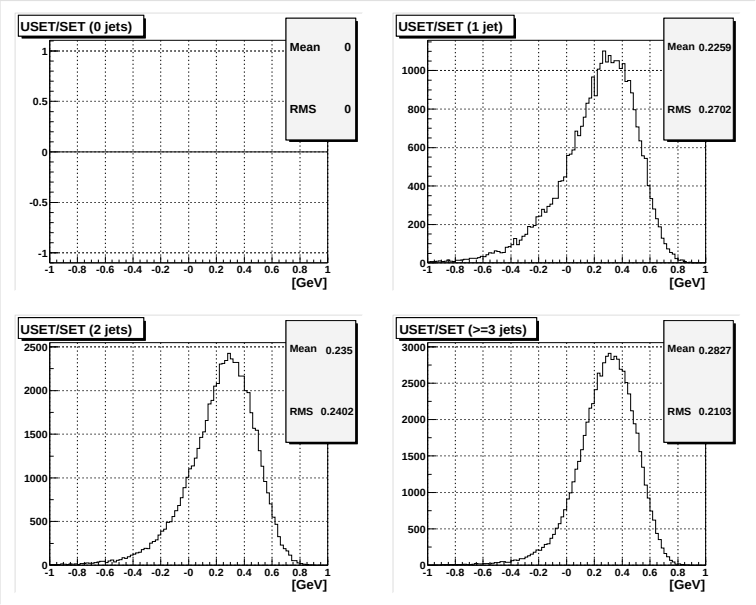

Figure 6.4: Fraction of the total transverse energy unassociated to jets as a function of jet multiplicity.

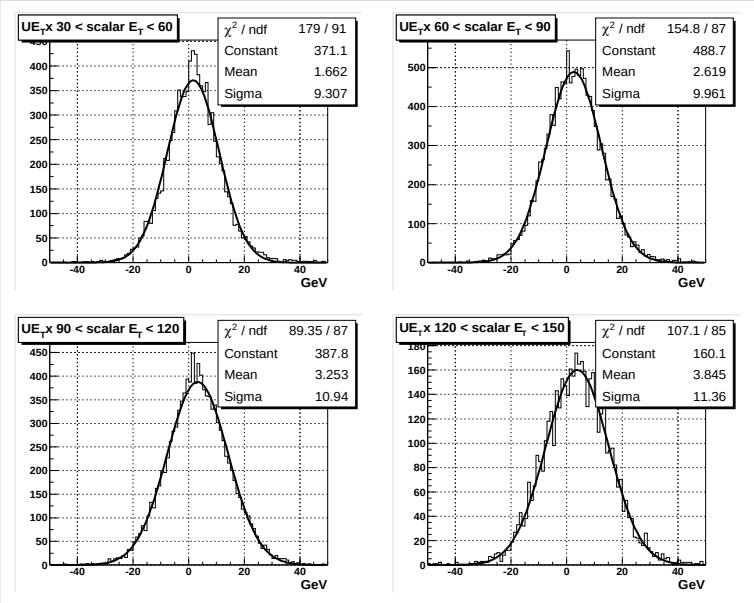

Figure 6.5: Distribution of the x component of the unclustered transverse energy vector in bins of scalar transverse unclustered energy.

to these distributions, are shown in Figures 6.7 and 6.8.

The probability density for the transverse unclustered energy is assumed to be Normally and randomly distributed in the transverse plane, since it can fluctuate in any direction:

$$p(E_T) = N(0, \sigma_{U.E}) \tag{6.12}$$

6.2.3 Electrons and Photons

The probability density for electromagnetic objects is given by

$$p(E_i) = N(E_i, \sigma_i) \tag{6.13}$$

where E_i is is the energy of the electromagnetic object and σ_i is its resolution, derived from the Monte Carlo simulation [28]:

$$\sigma_i = 0.202 + 0.004E_i + 0.23\sqrt{E_i}; \tag{6.14}$$

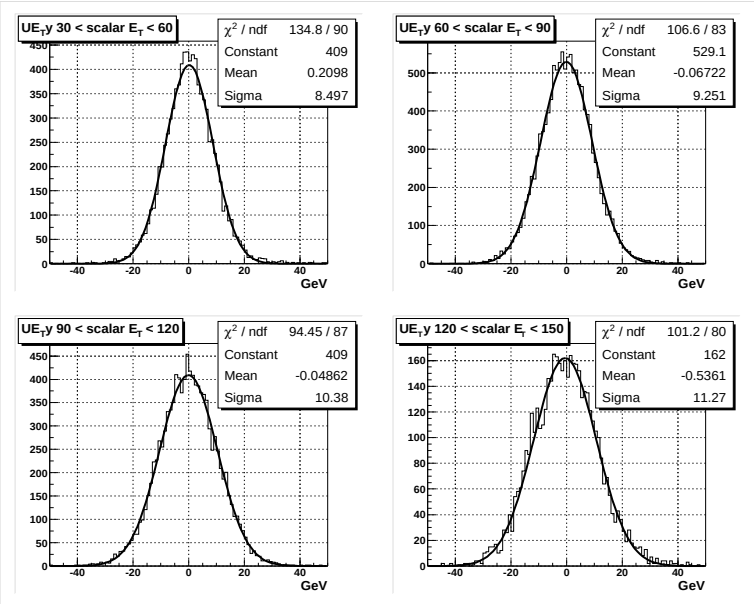

Figure 6.6: Distribution of the y components of the unclustered energy vector in bins of scalar unclustered energy.

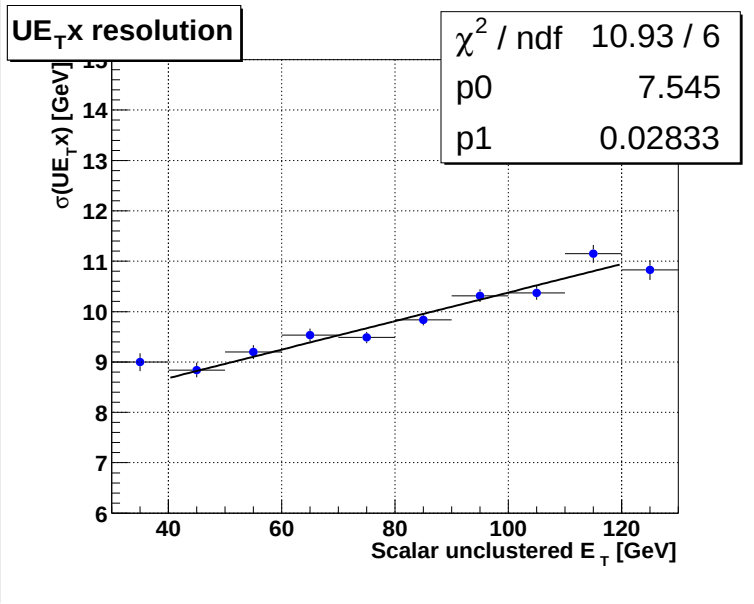

Figure 6.7: Unclustered energy resolution in the x component.

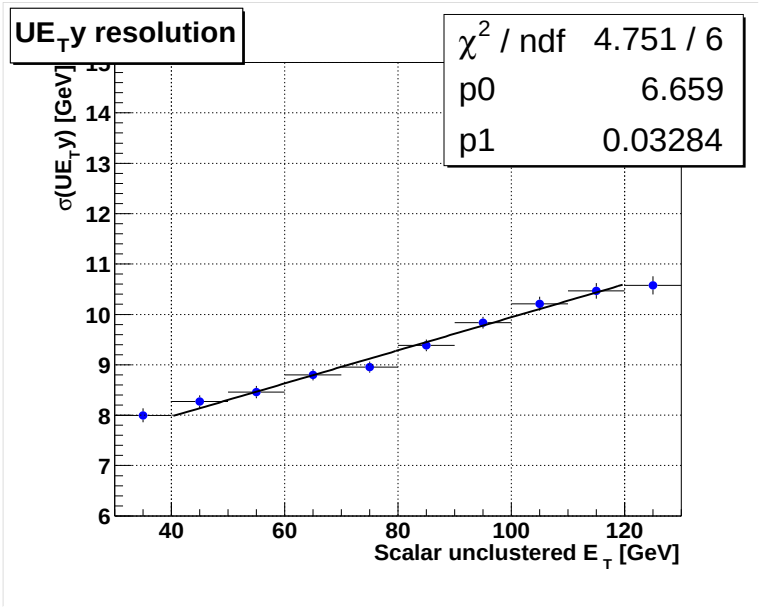

Figure 6.8: Unclustered energy resolution in the y component.

6.3 Test of Probability Density Functions

We tested the energy resolution parametrisations by comparing the *predicted* $\not\!\!E_T$ distribution with the *observed* $\not\!\!E_T$ in different control samples with no real $\not\!\!E_T$. The distribution of predicted $\not\!\!E_T$ is obtained by assuming that the event has no real $\not\!\!E_T$. It is generated by resolution fluctuations of all measured physics objects according to their PDF distributions:

$$\not\!\!E_{T\,pred} = 0 - \sum_{jets} \delta E_i - \sum_{EMs} \delta E_i - \delta UE \tag{6.15}$$

Each δE_i term is obtained by fluctuating the actual object energy at random, according to its respective resolution distribution.

The tests were performed in two different control samples:

- *QCD inclusive*: any jet trigger and two or more jets
- *Zee*: di-EM trigger, 2 tight EM objects and 0 jets

These samples were chosen since they have many physics differences: jet multiplicity, energy resolutions, color flow, etc.

Since Z events have a different color flow than multijet events, it is expected than the unclustered energy resolution, derived from multijet samples, is an over-estimation for Z events. Thus, we derived two different unclustered energy resolutions: a *minimum bias* (mb) unclustered energy resolution, from minimum bias triggered events, and a qcd unclustered energy resolution, from multijet events. The constant term a for the minimum bias resolution is $2\,GeV/c$ smaller than the qcd resolution.

6.3.1 QCD inclusive sample, $H_T > 100\,GeV/c$

Figure 6.9 shows the comparison between predicted and observed $\not\!\!E_T$ distributions in linear and log scales. The first two distributions were obtained using the qcd unclustered energy resolution, whereas the last two, with the mb resolution. We applied a cut of $H_T > 100$ to select a sample of high E_T jets, where their resolutions are know more accurately. The observed $\not\!\!E_T$ is shown in black dots. The dark grey histogram corresponds to the predicted $\not\!\!E_T$ from unclustered energy resolution effects only. The light grey histogram is the resulting $\not\!\!E_T$ distribution from jet energy fluctuations only. The black histogram is the sum of unclustered and jet energy resolutions, corresponding to the final predicted $\not\!\!E_T$. We observe a very good agreement between predicted and observed $\not\!\!E_T$ distributions for both unclustered energy resolution parametrisations. The reason for this is that the main contribution to the $\not\!\!E_T$ comes from jet energy fluctuations, being the unclustered energy a second order effect.

6.3.2 QCD inclusive sample, 2 or more jets

In this sub-sample with larger jet multiplicity, the unclustered energy contribution is larger than before, due to a larger out-of-cone unassociated energy. Figure 6.10 shows the same four predicted-observed comparison distributions. We note a better

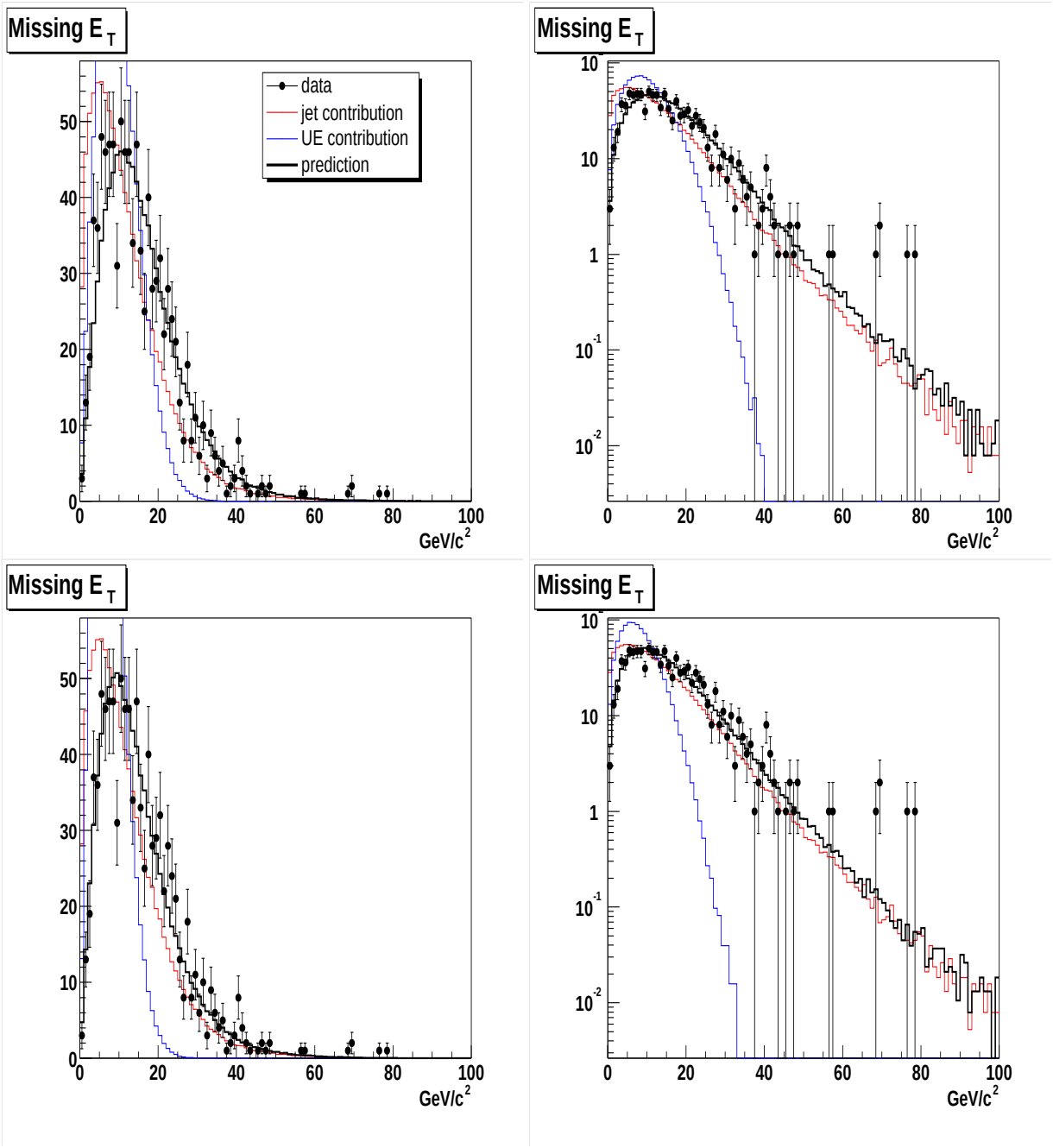

Figure 6.9: Comparison between predicted (black histogram) and observed (dots) $\not\!\!E_T$ distributions in the $QCD\, H_T > 100\, GeV/c$ sample. The dark (light) grey histograms show the unclustered (jet) energy resolution contributions to the predicted $\not\!\!E_T$. In the top (bottom) plots the qcd (mb) unclustered energy parametrisation was used.

agreement between predicted and observed $\not\!\!E_T$ distributions when we use the *qcd* unclustered energy resolution, as expected.

6.3.3 *di–EM* sample, 0 jets

Figure 6.11 shows the comparison between predicted and observed $\not\!\!E_T$ distributions in the *Zee* sample. In this sample, which was selected by requiring to have no reconstructed jets, the unclustered energy resolution is the leading contribution to the $\not\!\!E_T$ distribution. Thus, a better agreement, as expected, is observed for the case where the *mb* unclustered energy is used.

These studies suggest that two (or many) unclustered energy resolution parametrisations might be used for different physics process. However, it must be noted that the aim of the $\not\!\!E_T$ significance algorithm, is to discriminate events with large mis-measured $\not\!\!E_T$ from events with real $\not\!\!E_T$. Since the largest source of mis-measured $\not\!\!E_T$ comes from multijet events, where, as it was shown, the $\not\!\!E_T$ is dominated by jet energy fluctuations, the unclustered energy resolution parametrisation is not expected to play a significant role in the discrimination power of the method. This hypothesis is in fact verified in the next Section.

6.4 $\not\!\!E_T$ Significance Performance

In order to understand whether the $\not\!\!E_T$ significance algorithm can be used to discriminate between signal events, with large true $\not\!\!E_T$, and background events, with zero true $\not\!\!E_T$ but large mis-measured $\not\!\!E_T$, we considered two samples, one with true missing transverse energy, and another without. The first is a sample of $W+ \geq 1$ jets data events, and the second is a sample of QCD multijet data events containing two or more jets, in which any missing transverse energy is most likely to arise from detector effects.

For a particular cut on the $\not\!\!E_T$ significance likelihood, and $\not\!\!E_T$ variable, Fig-

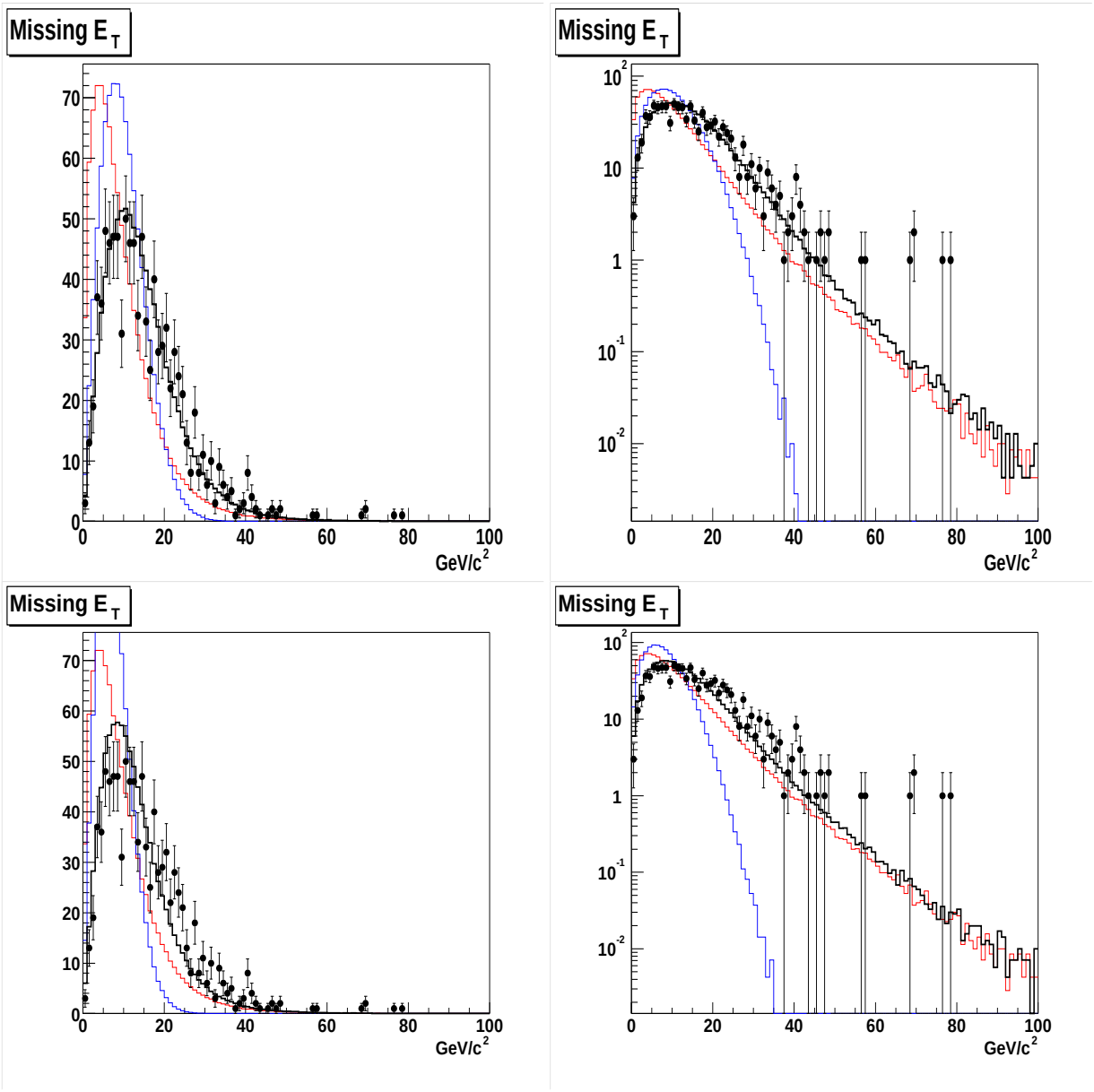

Figure 6.10: Comparison between predicted (black histogram) and observed (dots) $\not\!\!E_T$ distributions in the $QCD \geq 2$ jet sample. The dark (light) grey histograms show the unclustered (jet) energy resolution contributions to the predicted $\not\!\!E_T$. In the top (bottom) plots the qcd (mb) unclustered energy parametrisation was used.

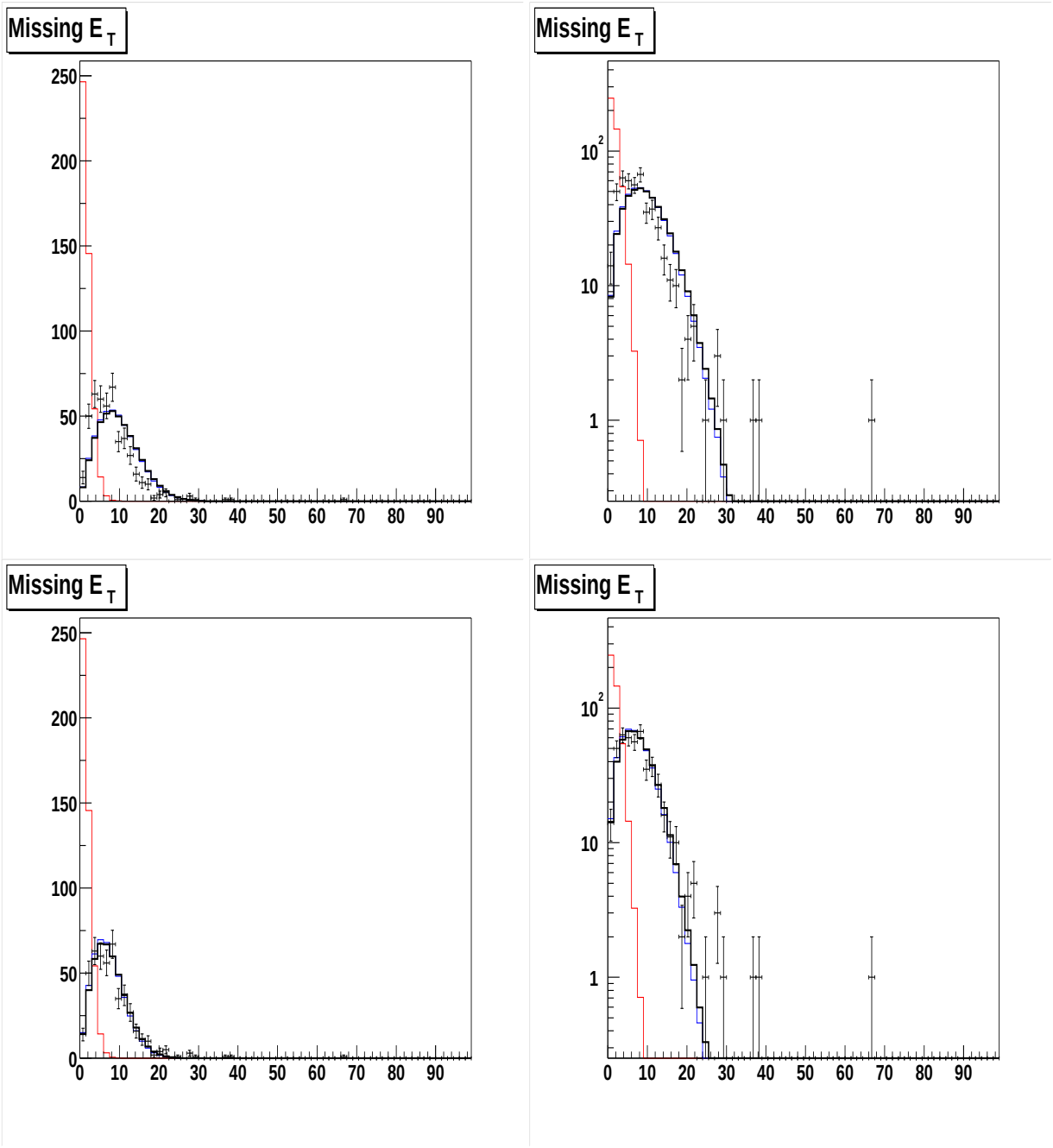

Figure 6.11: Comparison between predicted (black histogram) and observed (dots) $\not\!\!E_T$ distributions in the $Zee\ 0jet$ sample. The dark (light) grey histograms show the unclustered (jet) energy resolution contributions to the predicted $\not\!\!E_T$. In the top (bottom) plots the qcd (mb) unclustered energy parametrisation was used.

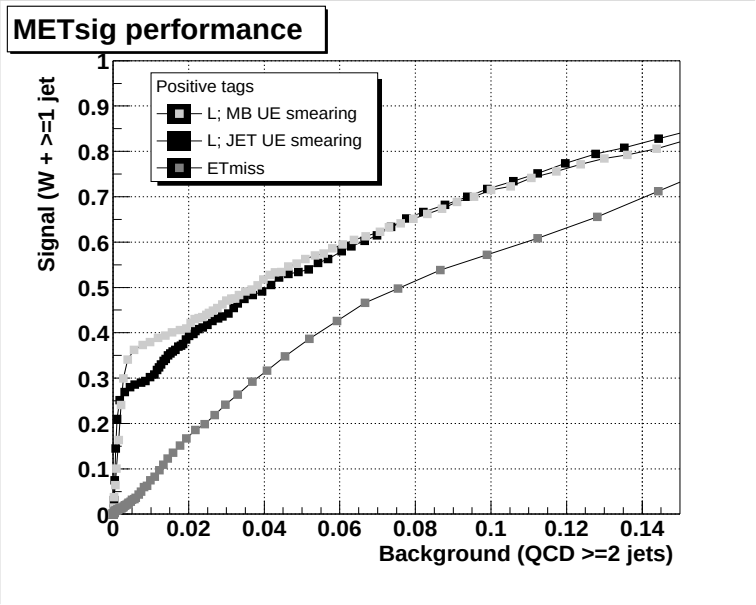

Figure 6.12: Signal vs. background efficiencies for the $\not\!\!E_T$ *qcd* likelihood (black), $\not\!\!E_T$ *mb* likelihood (light grey) and standard $\not\!\!E_T$ cut (dark grey).

ure 6.12 shows the number of signal versus background events left. We used two different likelihood definitions, corresponding to *qcd* (black) and *mb* (grey) unclustered energy resolutions. We find that a cut on the $\not\!\!E_T$ significance likelihood that keeps 80% of the signal events, retains 13% of background. If we want to achieve the same background rejection, using a standard cut on $\not\!\!E_T$, only 65% of the signal is kept. Thus, the $\not\!\!E_T$ significance likelihood outperforms the standard selection based on a $\not\!\!E_T$ cut off.

For very high background rejection (below 2%), we observed that the *mb* resolution likelihood allows to keep more signal than the *qcd* likelihood. This is due to the fact that the *qcd* unclustered energy resolution overestimates its contribution in $W \to e\nu$ events, resulting in lower $\not\!\!E_T$ significance. On the other hand, for high signal efficiency, the QCD background dominates, and the *qcd* unclustered resolution gives an overall better performance.

Using the *qcd* likelihood definition, Figure 6.13 shows a comparison between the $\not\!\!E_T$ and the $\not\!\!E_T$ significance variable L for the $W+ \geq 1$ jets and $QCD+ \geq 2$ jets

samples. The likelihood cut was chosen such that it keeps the same amount of signal events as a $\not\!\!E_T > 20\,GeV/c$ cut. We observed that the standard $\not\!\!E_T$ cut retains 30% more background events than a $\not\!\!E_T$ significance cut of $L > 2$.

The same comparison is shown in Figure 6.14 for a $W+ \geq 2$ jets and $QCD+ \geq 3$ jets samples. We find that the standard $\not\!\!E_T > 20\,GeV/c$ cut retains 26% more background than $L > 2$.

The improved signal over background performance of the $\not\!\!E_T$ significance algorithm can be better understood from the correlation between $\not\!\!E_T$ significance and $\not\!\!E_T$. Figure 6.15 shows such correlation in a sample containing two electromagnetic objects without track-match requirement (i.e. consistent with being photons) where any $\not\!\!E_T$ is probably due to resolution fluctuations of the photons and unclustered energy. We note a large number of events with $\not\!\!E_T > 15\,GeV/c$ but $L < 2$ which are tagged, and can be rejected, as mis-measured $\not\!\!E_T$ events by the METsig algorithm.

Finally, Figure 6.16 shows the likelihood distribution for $\gamma\gamma\not\!\!E_T$ and W events in a same plot to make it more evident the discrimination power of the method.

6.5 Conclusions

This Chapter has detailed the current implementation and performance of the $\not\!\!E_T$ significance algorithm for Run II. We have shown that a cut on the $\not\!\!E_T$ likelihood variable is more powerful than a cut on the standard $\not\!\!E_T$ variable in terms of keeping signal W+jets and rejecting QCD multijets events. The next step is to study the application of the $\not\!\!E_T$ significance algorithm for the selection of the $W+ \geq 3$ jets sample for *top* quark identification. In addition, further improvements are expected as the mis-vertexing and muon PDF distributions are incorporated to this method.

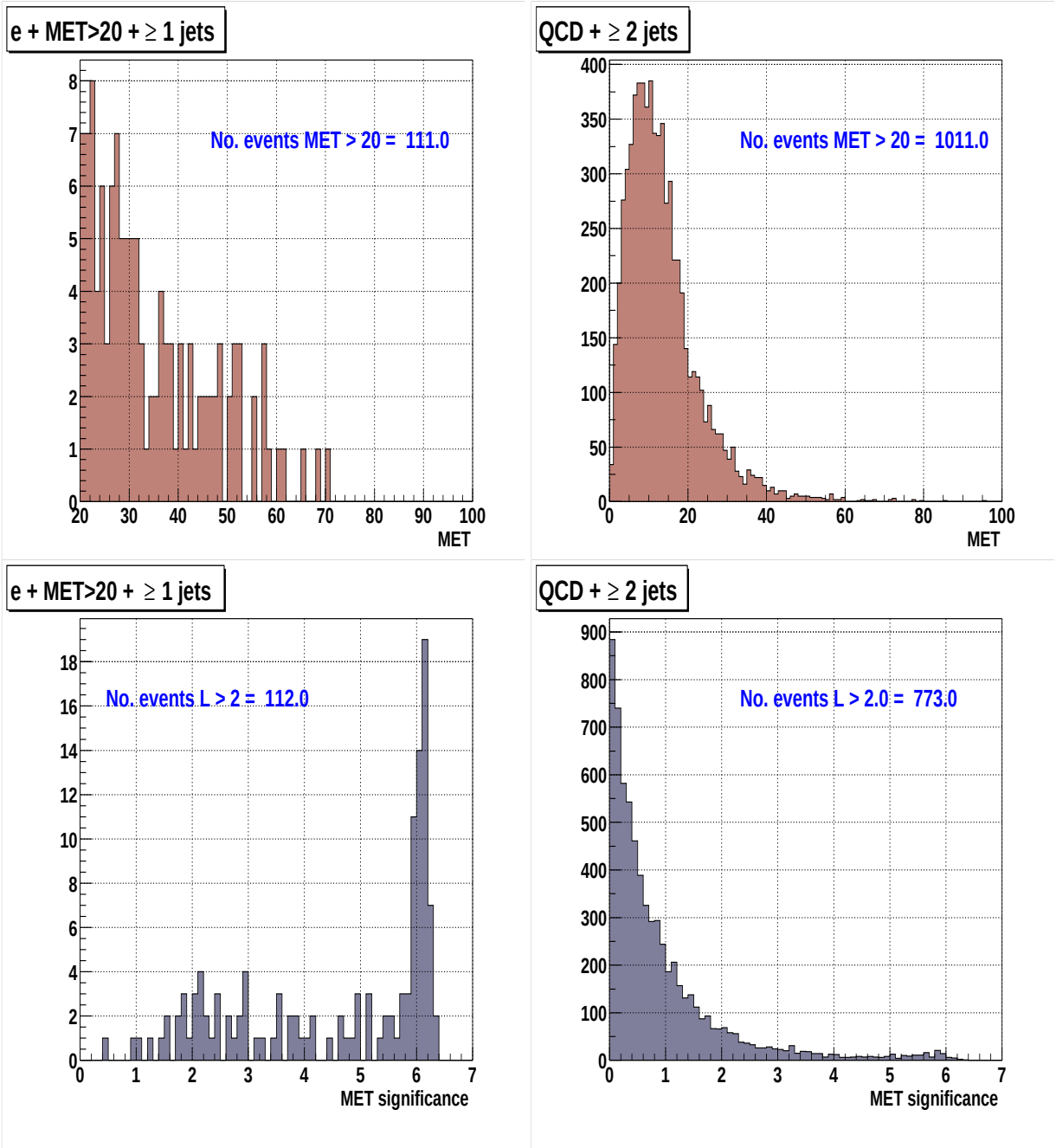

Figure 6.13: $\not\!\!E_T$ and $\not\!\!E_T$ significance likelihood distributions in $W+ \geq 1$ jets and $QCD+ \geq 2$ jets samples.

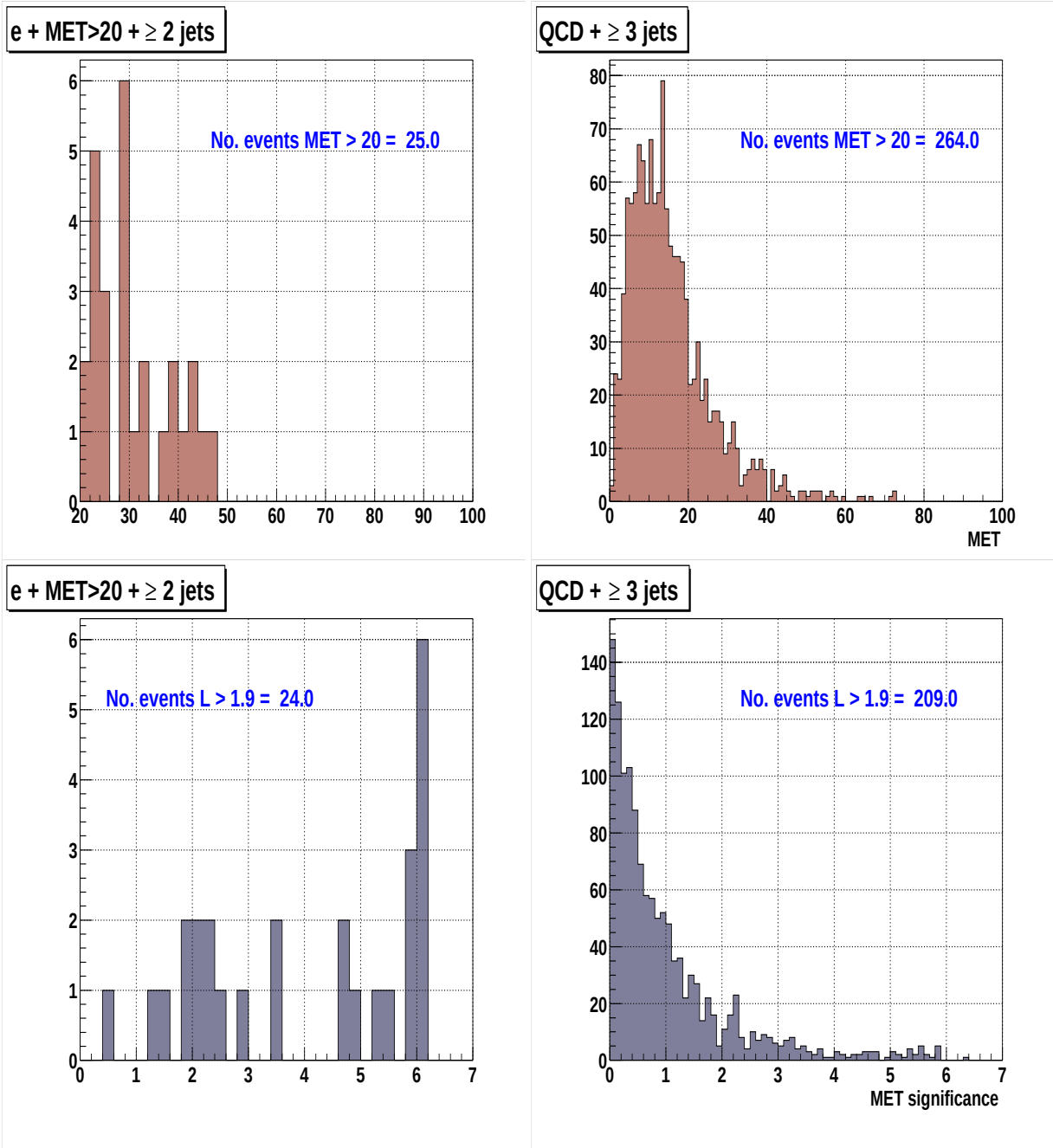

Figure 6.14: $\not\!\!E_T$ and $\not\!\!E_T$ significance likelihood distributions in $W+ \geq 2$ jets and $QCD+ \geq 3$ jets samples

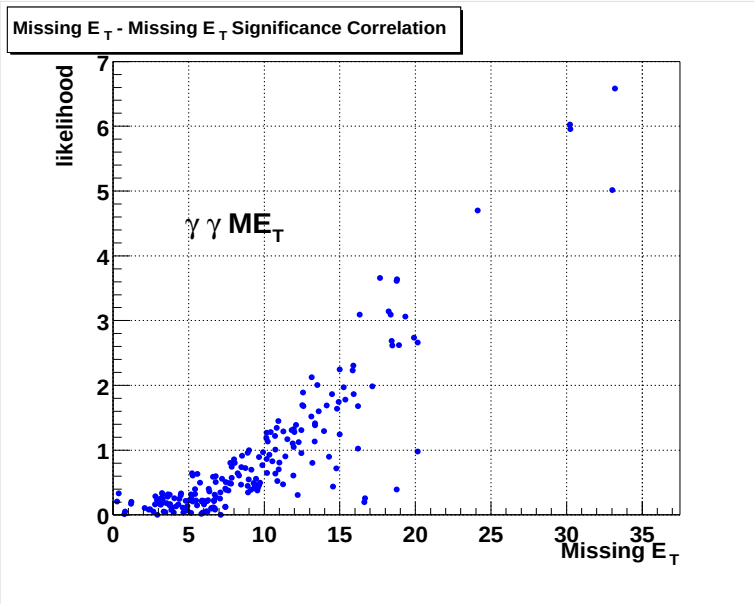

Figure 6.15: Correlation between between $\not\!\!E_T$ significance and $\not\!\!E_T$ in a $\gamma\gamma\not\!\!E_T$ event sample.

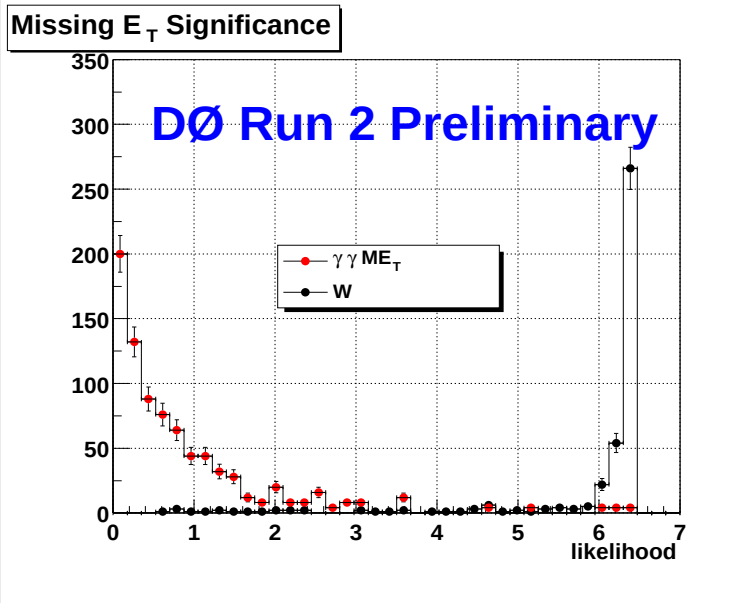

Figure 6.16: $\not\!\!E_T$ significance likelihood distribution for $\gamma\gamma\not\!\!E_T$ and W events.

Chapter 7

Measurement of the Exclusive $B^{\pm}$ Lifetime

In this chapter we present a preliminary measurement of the $B^{\pm}$ meson lifetime using the exclusive decay mode $B^{\pm} \to J/\psi\, K^{\pm}$ with $J/\psi \to \mu^{+}\mu^{-}$. The data sample corresponds to an integrated luminosity of $47\, pb^{-1}$, collected during the July-December 2002 period.

This chapter is organized as follows: Section 7.1 briefly summarizes basic kinematic characteristics of the $B^{\pm}$ meson decays to guide the reconstruction and selection of the $B^{\pm}$ vertices used in this analysis. Section 7.2 describes the method used to identify secondary B vertices in the decay mode $B^{\pm} \to J/\psi(\mu^{+}\mu^{-})\, K^{\pm}$, and the determination of the kinematic variables used to measure the lifetime. Finally, section 7.3 describes the fitting technique used to extract the $B^{\pm}$ meson lifetime.

7.1 Kinematics of $B^{\pm}$ Meson Decays

In this section we study the kinematics of the $B^{\pm} \to J/\psi\, K^{\pm}$ decays with the MC simulation. Our goal is to guide the reconstruction and selection of exclusive $B^{\pm}$

meson decays in this mode. The simulated sample requires that each muon from the J/ψ has $p_T > 1.5\,GeV/c$, so that they go through the toroid magnet of the muon system, and $|\eta| < 2.4$, in order for them to be within the muon trigger acceptance.

The $B^{\pm}$ is produced at the primary interaction vertex, it travels a small distance, and decays (via the weak interaction) to $J/\psi\,K^{\pm}$. The J/ψ decays immediately, via the electromagnetic interaction, to $\mu^+\mu^-$. Thus, the vertex decay topology consists of two muons and a charged kaon emanating from a secondary displaced vertex, as shown in Figure 7.1.

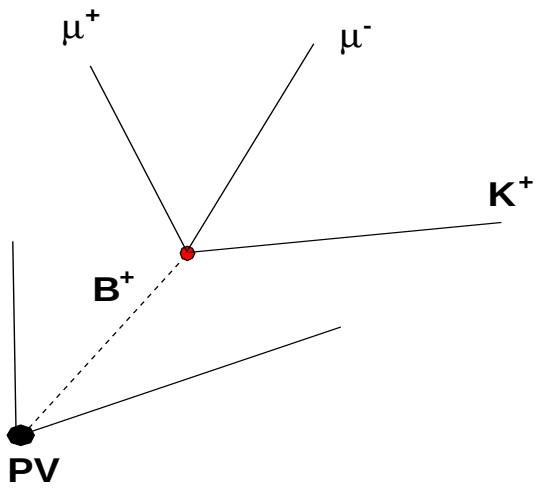

Figure 7.1: $B^+ \rightarrow J/\psi\,K^+$ vertex decay topology. The B^+ meson is produced together with other fragmentation particles from the parent b-quark.

Figure 7.2 shows the transverse and longitudinal momentum and η distribution of the produced $B^{\pm}$ vertices.

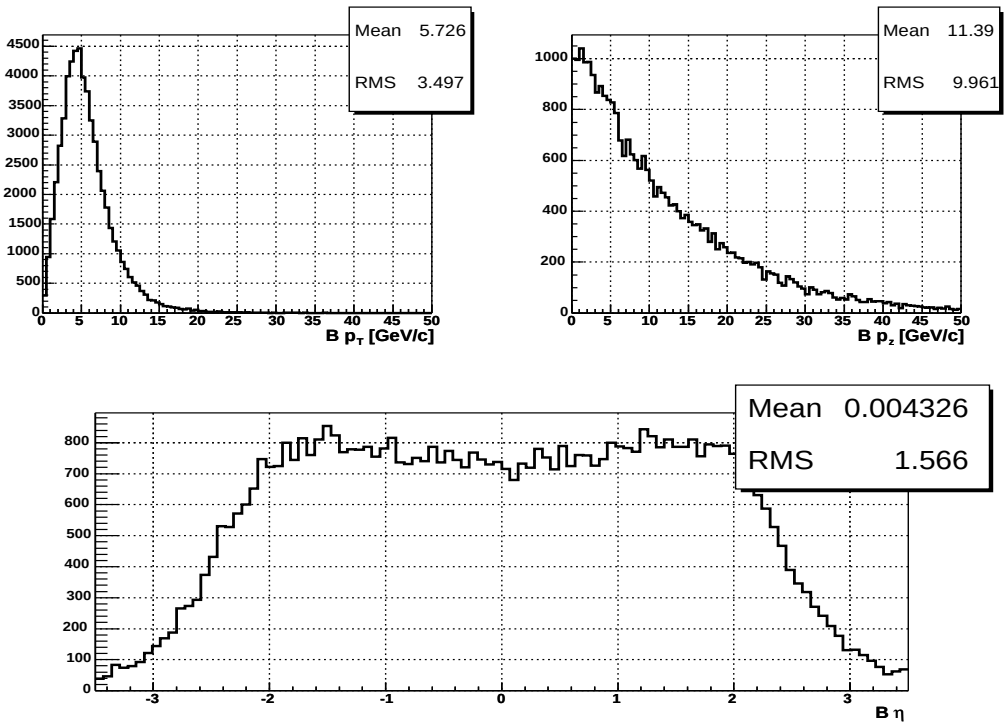

Figure 7.2: Properties of $B^{\pm}$ mesons in $B^{\pm} \to J/\psi K^{\pm}$ decays

The longitudinal momentum, p_Z, depends of the event-by-event boost and is greater, on average, than the transverse momentum. The combination of transverse and longitudinal momentum give rise to the observed η distribution.

The transverse momentum and η distributions for the final state particles are shown in Figure 7.3. We observe how the transverse momentum of the kaon is much softer than the muon's. This can be inferred from Figure 7.4, where the ratios $p_{T\mu}/p_{TB}$, p_{TK}/p_{TB}, and $p_{TJ/\psi}/p_{TB}$ are shown. Most of the transverse momentum of the B meson is carried by the J/ψ, which in turn is divided symmetrically between the two muons. Figure 7.5 shows that, on average, 70% of the B meson energy is carried by the J/ψ, whereas 30% is carried by the kaon.

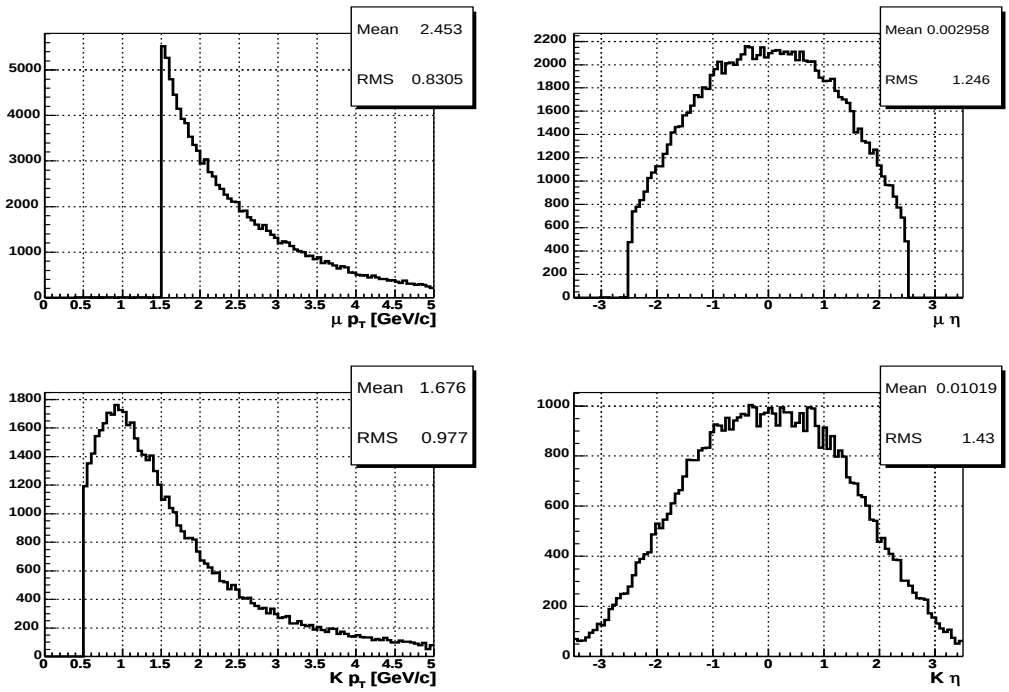

Figure 7.3: Properties of the final state particles in $B^{\pm} \to J/\psi K^{\pm}$ decays. The minimum track p_T is $0.5\,GeV/c$ for the kaon and $1.5\,GeV/c$ for the muon.

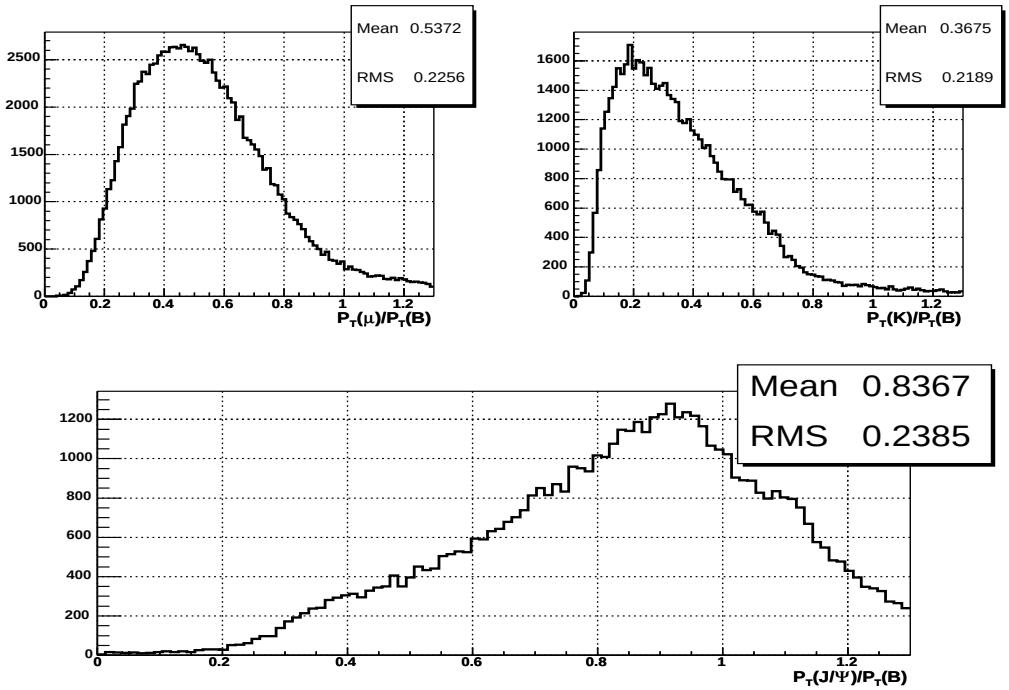

Figure 7.4: Fraction of the B transverse momentum carried by its daughters.

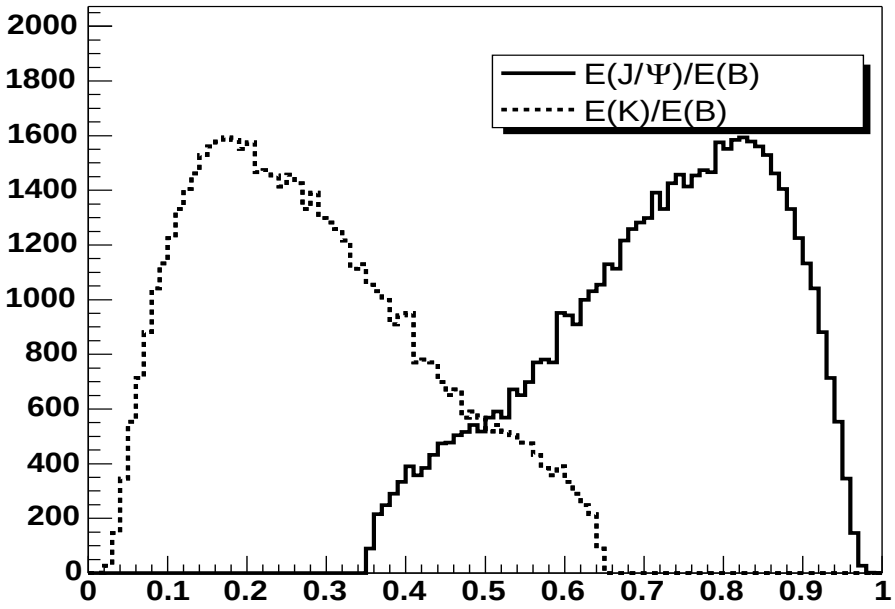

Figure 7.5: Fraction of the B meson energy carried by the J/ψ and K decay particles. The mean values are 70% and 30%, respectively.

The topology of the $B^{\pm}$ vertex decay can be understood from Figure 7.6, where $\Delta R = \sqrt{(\Delta\phi)^2 + (\Delta\eta)^2}$ is plotted for different pairs of particles. Muons are produced with a very large angle among each other. The mean value of $\Delta R(\mu, \mu)$ is approximately 80°. The J/ψ is produced more collinear with the B momentum than the kaon. The distributions of ΔR between the B and the muon and kaon momenta indicate that the topology of the decay consists of a 3 charged tracks very spread in space.

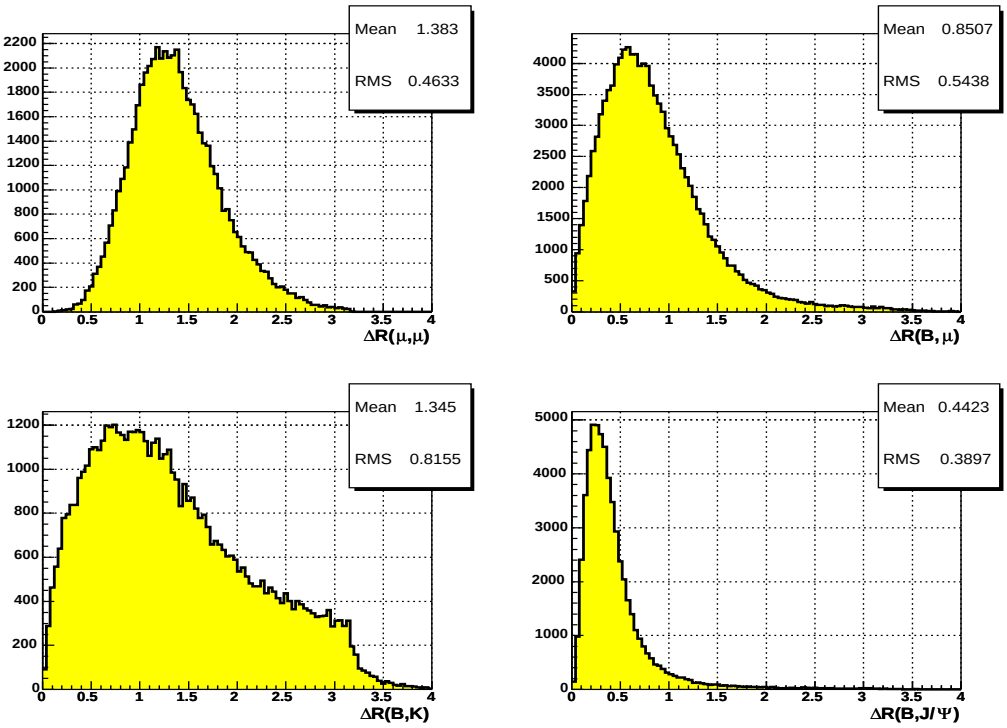

Figure 7.6: Topology of the $B^{\pm} \to J/\psi K^{\pm}$ decay vertex.

7.2 Exclusive $B^{\pm}$ Vertex Reconstruction

As it was discussed in Section 4.6, the algorithm for the identification of $B^{\pm}$ secondary vertices is based on the particular kinematic characteristics of this decay. It consists of four main steps: the reconstruction and selection of the primary vertex, the selection of the decay particles, the reconstruction of J/ψ vertices, and the identification of $J/\psi\, K^{\pm}$ decays, by combining the J/ψ vertices with $K^{\pm}$ track candidates.

7.2.1 Primary Vertex Identification

Primary vertices were reconstructed using the Kalman Filter technique described in Chapter 4. For the selection of the hard scatter vertex, we did not use the probabilistic algorithm but a different method based on the particular characteristics of the di-muon data sample. Since the 2 muon tracks are originated from the hard scatter vertex, we select the primary vertex as the closest one, in z, to the p_T-average z position of the 2 muon tracks[1], $Z_{\mu\mu} = (\sum_{i=1,2} p_{Ti}\, Zdca_i \,/\, \sum_{i=1,2} p_{Ti})$, if $\Delta Z = |Z_{\mu\mu} - Z_{PV}| < 3\, cm$.

7.2.2 μ and $K^{\pm}$ Selection

The $B^{\pm}$ reconstruction starts by preselecting the final state particles. Both muons are required to be reconstructed as a segment in at least one layer of the muon system, and matched to a central track containing at least 3 SMT hits and transverse momentum greater than $1.5\, GeV/c$. All remaining tracks, containing at least 3 SMT hits and transverse momentum greater than $1.5\, GeV/c$, are considered Kaon candidate tracks. The SMT hit requirement assures the track momentum is measured

[1]This was, in fact, the unbiased method used to derive the minimum bias probability method in Section 4.5.2.

accurately. The p_T requirement reduces the number of background candidate events, resulting from vertices with similar characteristics to the $B^{\pm} \rightarrow J/\psi K^{\pm}$ decay, but which are due to accidental combinations of real or fake muons and tracks. Since background events tend to have less energy than the signal events, a minimum p_T requirement for the final state particles increases the signal over background ratio.

In addition to the kinematic track selection, events were preselected by requiring that any dimuon trigger has fired.

7.2.3 J/ψ Reconstruction and Selection

$J/\psi \rightarrow \mu^+\mu^-$ vertex decays were reconstructed by a Kalman Filter vertex constrained fit of the two opposite charge muon tracks in the event. If there were more than two muons in the event, all charged allowed pair combinations were considered at a first stage. The vertex χ^2 was required to be less than 10 to assure that the two muons are consistent with originating from a same common spatial point. The vertex constrained fit allows to improve the vertex mass resolution as μ track momenta are refitted with the constraint that they come from the same vertex. In addition, the uncertainty in the transverse vertex decay length is required to be less than $0.02\,cm$ to reject poorly measured vertices. Figure 7.7 shows the decay length error distribution of J/ψ vertex candidates.

Figure 7.8 shows the invariant mass distribution for J/ψ candidates. The distribution was fitted with a signal function consisting of 2 Gaussian, and a linear background function. We observe $64974.2 \pm XXXX$ signal J/ψ events after background subtraction. A smaller mass peak for the $\psi(2S)$ resonance at $\sim$3.6 GeV/c^2 can also be observed. Figure 7.9 shows the $\psi(2S)$ mass range in more detail. We select J/ψ vertex candidates if their invariant mass is in the range $2.9 - 3.3\,GeV/c^2$.

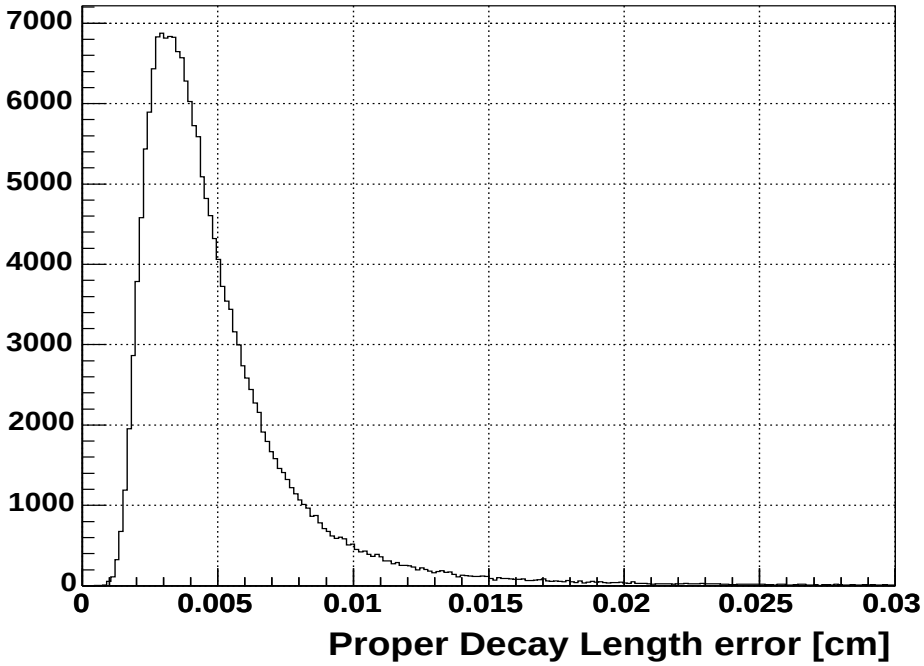

Figure 7.7: Uncertainty in the transverse proper decay length $\sigma_{L_{xy}}$ for J/ψ vertex candidates. We require $\sigma_{L_{xy}} < 0.02\,cm$

.

7.2.4 $J/\psi\, K^{\pm}$ Reconstruction and Selection

After a J/ψ candidate vertex was found, the algorithm attempts to attach to it an additional kaon track, which passes the selection criteria described in Section 7.2.2. A three track constrained vertex fit is performed with each kaon candidate. The χ^2 contribution of the kaon track to the $J/\psi\, K^{\pm}$ vertex (χ^2_K), as well as the total vertex χ^2 (χ^2_{vtx}) is a measure of how well the additional track is consistent with the hypothesis of originating from the J/ψ vertex. We require $\chi^2_K < 10$ and $\chi^2_{vtx} < 20$. The loose χ^2_{vtx} requirement was chosen to increase the number of signal events. When calculating the $J/\psi\, K^{\pm}$ vertex invariant mass, the kaon track is assigned the tabulated kaon mass [1], and the J/ψ vertex is constrained to the world average

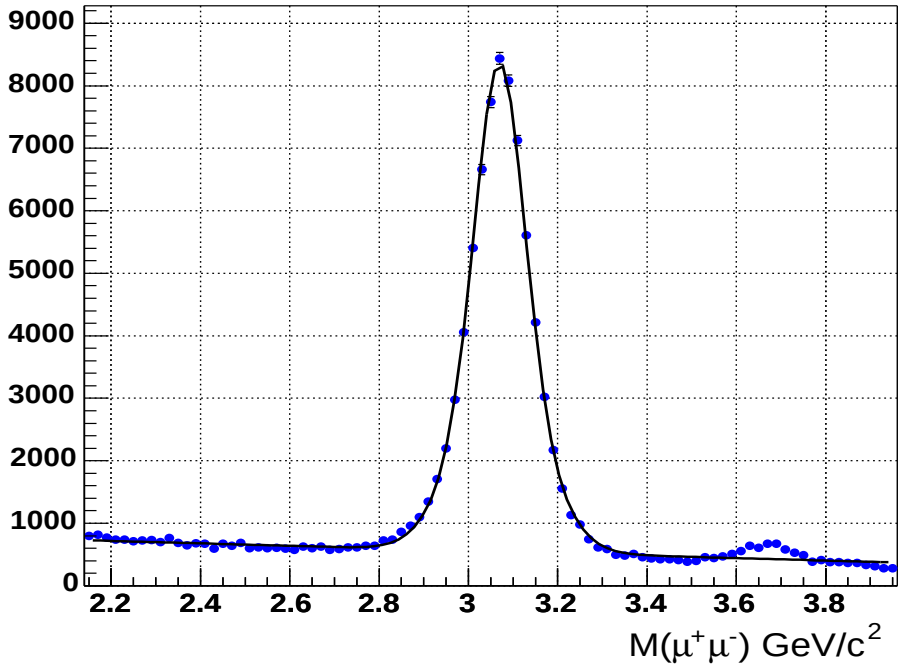

Figure 7.8: Invariant mass distribution of opposite charged muon tracks after vertex selection cuts. The mean value of the central Gaussian fit function is $3.0751 \pm 0.0007\, GeV/c^2$ and $\sigma = 0.054 \pm 0.001$.

J/ψ mass [1]. If there are more than one $B^{\pm}$ vertex candidate in an event, we consider them all for the rest of the analysis. Figure 7.10 shows the invariant mass distribution of the $B^{\pm}$ vertex candidates. We observe a signal over background ratio of 0.11. The same invariant mass plot, requiring a decay length greater than $200\,\mu m$, is shown in Figure 7.11, where the signal over background ratio is enhanced to 2.6.

Figures 7.10 and 7.11 were obtained with the additional requirement that the $J/\psi\, K^{\pm}$ candidate vertex points back to the primary interaction vertex with a collinearity angle larger than 0.9, where the collinearity angle is defined in Section 5.2. This requirement is very effective in removing background events, but due to the fact that collinearity is a function of decay length, it cannot be applied for

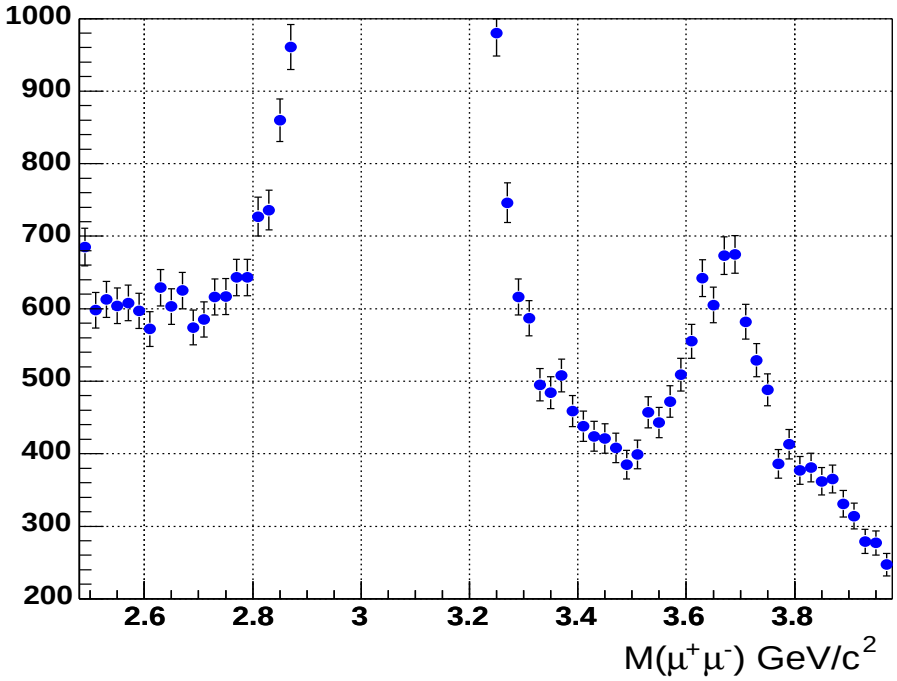

Figure 7.9: Invariant mass distribution of $\psi(2S)$ vertex candidates.

the lifetime measurement.

Table 7.1 summarizes the selection criteria used for $J/\psi\, K^{\pm}$ identification.

7.3 $B^{\pm}$ Lifetime Measurement

In this section we describe the fitting technique and the quantities used to measure the $B^{\pm}$ lifetime.

The signed transverse decay length is defined as the projection, along the B meson transverse momentum direction, of the vector pointing from the primary to the secondary $B^{\pm}$ vertex:

$$L_{xy}^{B} = (\vec{x}_B - \vec{x}_{PV}) \cdot \frac{\vec{p}_T}{|\vec{p}_T|} \tag{7.1}$$

where $\vec{p}_T$ is the B transverse momentum vector.

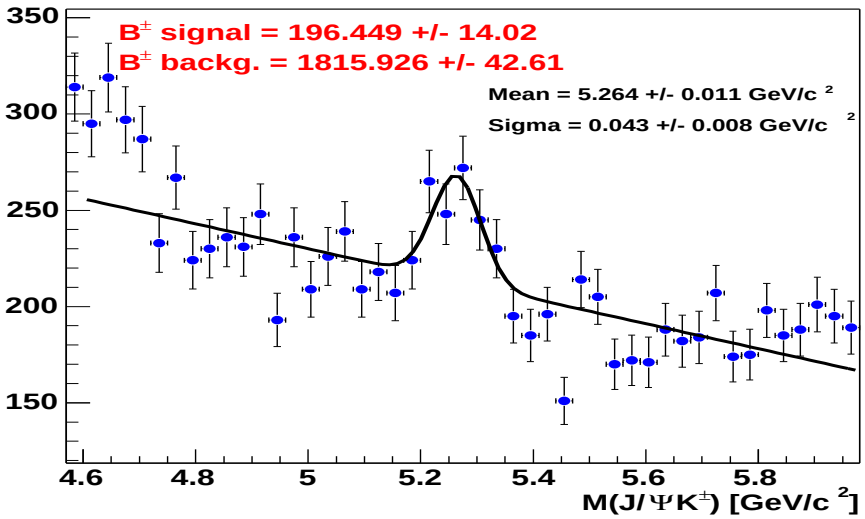

Figure 7.10: Invariant mass distribution of $B^{\pm}$ candidate vertices.

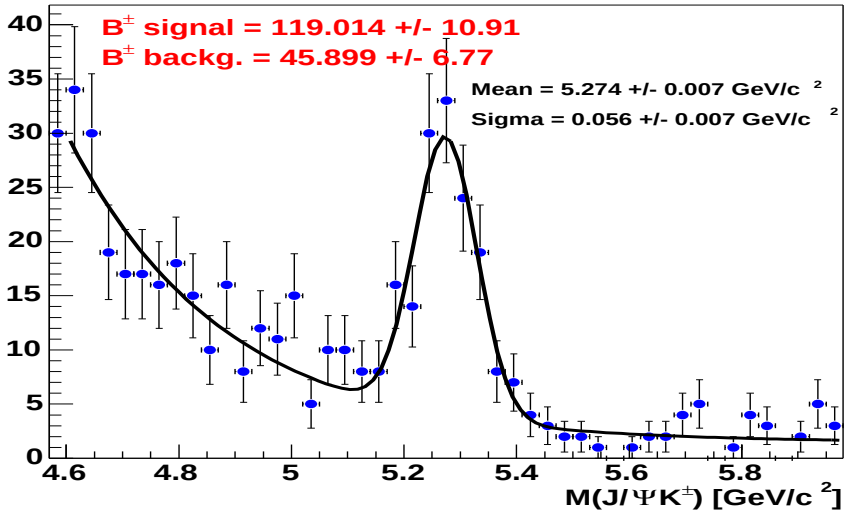

Figure 7.11: Invariant mass distribution of $B^{\pm}$ candidate vertices, but including a $L_{xy} > 200\,\mu m$ requirement.

$\mu\ p_T$	$> 1.5\,GeV/c$
μ SMT hits	> 2
$K\ p_T$	$> 1.5\,GeV/c$
K SMT hits	> 2
$J/\psi\ \chi^2_{vtx}$	< 10
$J/\psi\ \sigma_{Lxy}$	$< 0.02\,cm$
χ^2_K	< 10
χ^2_{vtx}	< 20

Table 7.1: Summary of $B^{\pm} \to J/\psi\, K^{\pm}$ vertex reconstruction and selection criteria.

L^B_{xy} is negative when the reconstructed B meson seems to decay before the point it was produced. For a zero-lifetime sample, a Gaussian distribution with mean value $L^B_{xy} = 0$ is expected, with a width governed by the tracking resolution.

The proper decay length, $c\tau$, is calculated for each event as

$$c\tau = L^B_{xy}\ M_{B^{\pm}}\ /\ |\vec{p}_T| \tag{7.2}$$

where $M_{B^{\pm}}$ is the world average mass of the B^+ meson and $\vec{p}_T$ is the measured transverse momentum of the B hadron. Equation 7.2 is obtained from the following relation:

$$c\tau = L^B_{xyz}\ /\ \beta\gamma = L^B_{xyz}\ M_{B^{\pm}}\ /\ |\vec{p}| \tag{7.3}$$

where L^B_{xyz} is the three-dimensional decay length and $\vec{p}$ the total B hadron momentum.

7.3.1 $B^{\pm}$ Proper Lifetime Fitting

We divide the $B^{\pm}$ mass range in three regions: left side-band (4.6<M(B)<4.9), signal (5.1<M(B)<5.4), and right side-band (5.6<M(B)<6.0), where all mass units are implicitly in GeV/c^2. The left and right side-band regions were chosen so that they have similar number of events. The signal region contains a mixture of approximately 10% real $B^{\pm}$ vertices plus background events. The proper lifetime

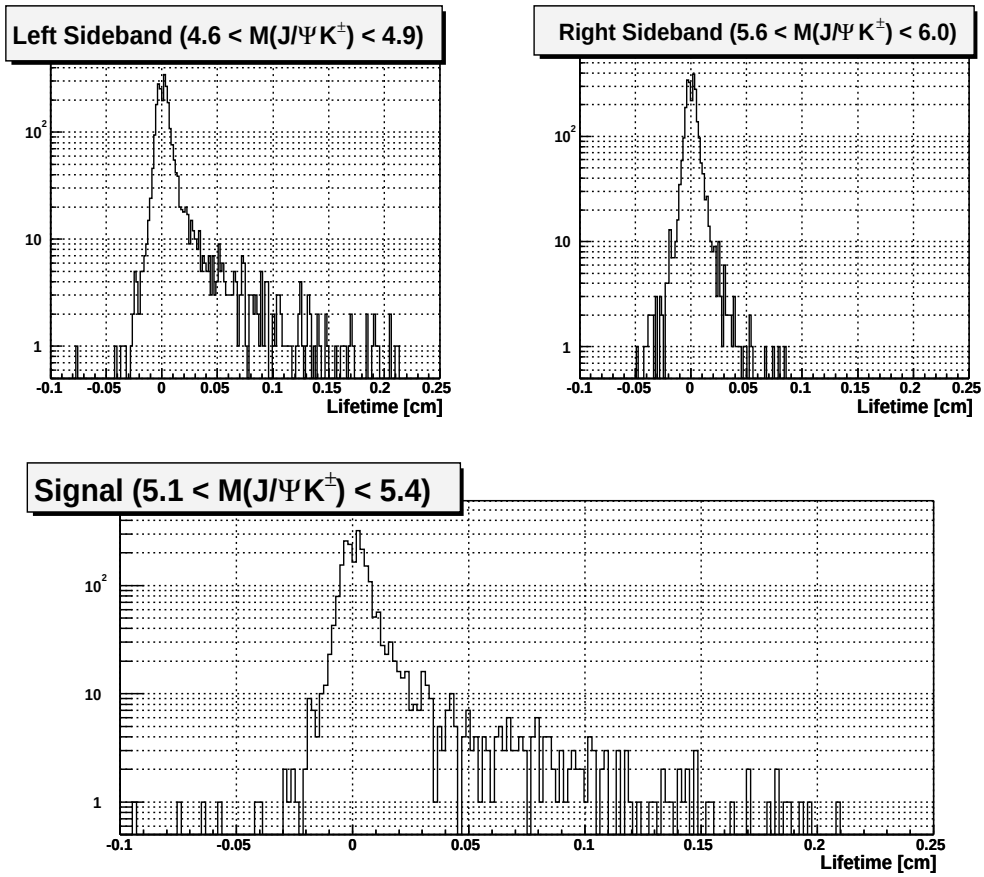

Figure 7.12: Proper lifetime distribution in the left side-band, right side-band and signal regions.

distributions of all $B^{\pm}$ candidates in these three regions are shown in Figure 7.12. Since we are interested in a lifetime measurement, we did not apply the collinearity cut for the selection of $B^{\pm}$ events.

We note that the proper lifetime distributions for the left side-band is very similar to the same distribution in the signal region. This is due to the fact that real B mesons, where one particle hasn't been reconstructed, will appear to have a smaller invariant mass. For instance, $B \to J/\psi K^{*+} \to \mu\mu K^0_S \pi^+$, where the K^0_S is not reconstructed and the pion is misidentified as the kaon track. Thus, we assume that the left side-band region, as the signal region, is composed of a combination of real

$B^{\pm}$ and background decays.

The fit to the lifetime distribution was done using an unbinned maximum log-likelihood method [36]. The likelihood function was defined as:

$$L = \prod_{i=1}^{N} [F g^i_{sig} + (1 - F)\, g^i_{bck}\,] \tag{7.4}$$

where $N = 4031$ is the number of events in the signal region, F is the fraction of signal events, and g^i_{sig} and g^i_{bck} are the proper decay length probability density functions for the signal and background respectively.

The lifetime distribution of background events, g^i_{bck}, was parametrized as a Gaussian for zero-lifetime events (i.e. vertices with zero lifetime that appear displaced due to resolution effects), one exponential for the negative lifetime background and one exponential for the positive lifetime background. The two exponentials account for non-Gaussian tails and we assume they can have different slopes, as we expect some enhancement of events with positive lifetime due to the presence of sequential semileptonic B decays in the di-muon sample. The width of the Gaussian is the lifetime uncertainty of each event, multiplied by a scale factor ϵ, to account for the possibility that it is systematically underestimated.

The background distribution function was defined as:

$$g^i_{bck} = \begin{cases} (1 - f_+ - f_-)\, \frac{e^{-\lambda_i^2/2(\epsilon\sigma_i)^2}}{\sqrt{2\pi}\,\epsilon\sigma_i} + \frac{f_+}{\lambda_+}\, e^{-\lambda_i/\lambda_+} & \lambda_i \leq 0 \\ (1 - f_+ - f_-)\, \frac{e^{-\lambda_i^2/2(\epsilon\sigma_i)^2}}{\sqrt{2\pi}\,\epsilon\sigma_i} + \frac{f_-}{\lambda_-}\, e^{+\lambda_i/\lambda_-} & \lambda_i > 0 \end{cases} \tag{7.5}$$

where ϵ is the error scale factor, f_+ and f_- the fractions of right and left side exponentials, λ_+ and λ_- the respective coefficients for the positive and negative background exponential tails, and λ_i and σ_i are the lifetime and its uncertainty for the i^{th} event.

The proper lifetime distribution for signal events, g^i_{sig}, was parametrized as an

Exponential convoluted with a Gaussian resolution function:

$$g^i_{sig} = \frac{1}{\sqrt{2\pi}\,\epsilon\sigma_i\lambda_B}\int_0^\infty e^{-\frac{(c\tau-\lambda_i)^2}{2(\epsilon\sigma_i)^2}} e^{-\frac{c\tau}{\lambda_B}}\; d(c\tau) \tag{7.6}$$

where λ_B is the mean $B^\pm$ proper decay length.

The fit results are listed in Table 7.2 and the proper decay length distributions with the fits superimposed are shown in Figure 7.13. We obtain

$$c\tau(B^+) = 471 \pm 53\,(stat)\,\mu m \tag{7.7}$$

$$\tau(B^+) = 1.57 \pm 0.18\,(stat)\,ps \tag{7.8}$$

which is consistent with other $B^\pm$ lifetime measurements [1]. The current world average $B^\pm$ lifetime is $1.674 \pm 0.018\,ps$.

Parameter	Value
ϵ	1.176 ± 0.035
F	$9.2 \pm 1.3\%$
λ_B	$0.0471 \pm 0.0053\,cm$
λ_-	$0.0077 \pm 0.0018\,cm$
λ_+	$0.0079 \pm 0.0012\,cm$
f_-	$5.2 \pm 1.7\%$
f_+	$15.4 \pm 2.0\%$

Table 7.2: Fit parameters for the $B^\pm$ lifetime measurement

Table 7.2 shows that the fraction of signal $B^\pm \to \mu\mu K^\pm$ events is 9.2%. We note that the errors in the lifetime are underestimated by 17.6%. There are several hypothesis that may lead to a misestimation of the lifetime error. Some examples are:

- underestimation of track parameter errors is translated in a underestimation of vertex errors.

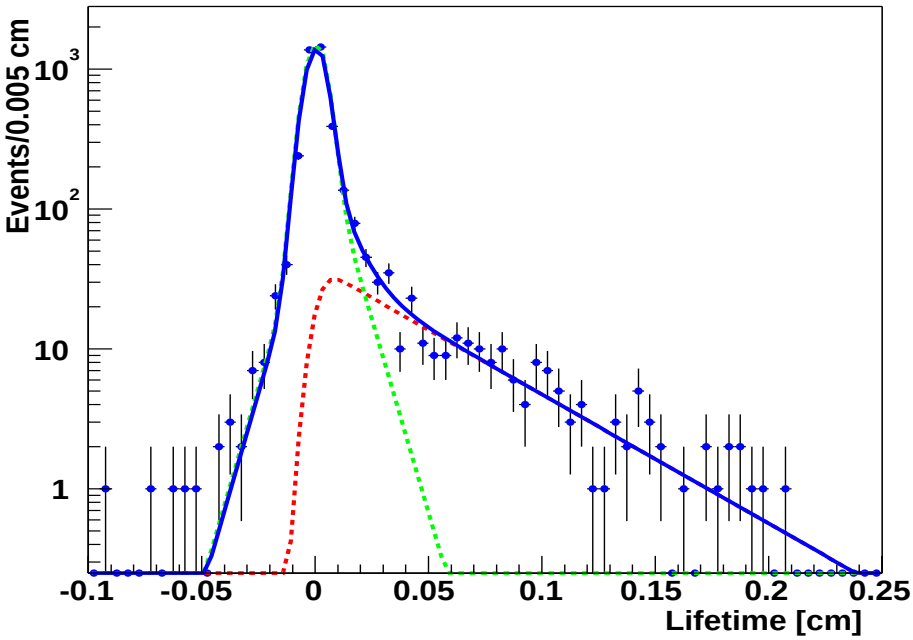

Figure 7.13: Proper decay length $c\tau$ of $B^{\pm}$ candidates. The background (signal) contribution is shown in light (dark) dashed lines. The sum of background and signal contribution is shown with the solid line.

- non-Gaussian tails in the distribution of track parameters bias the vertex estimation which assumes Gaussian errors.
- the primary vertex is affected by the presence of small-lifetime B vertex tracks.

Given the small number of events collected so far, statistical errors dominate over systematic errors. Some sources of systematic errors and how they can be estimated are listed bellow:

- Primary and secondary vertex determination: the effect of primary vertex reconstruction can be determined by using a different algorithm to find and select the primary vertex, such us using the probabilistic selection method.

Secondary vertex systematics can be evaluated by measuring the lifetime at the J/ψ decay vertex rather than at the $B^{\pm}$ vertex. Both vertices are physically identical, but experimentally they differ due to track and vertex resolution.

- p_T cuts: the effect of the kaon and J/ψ p_T, can be studied by estimating the lifetime with different transverse momentum cuts.

- Background parametrization: the systematic uncertainty on the background estimation can determined by varying the the fraction and slopes of the exponential functions by $\pm 1\sigma$ of the fit values and fixed them in the fit.

7.4 Conclusions

This chapter described the application of the Kalman Filter vertex techniques developed to the measurement of the $B^{\pm}$ hadron lifetime in the exclusive decay channel $B^{\pm} \rightarrow J/\psi K^{\pm}$. This is a very first measurement using RunII data which will be significantly improved within the next years, by using a much larger data sample. The main motivation for this analysis was to prove that the Kalman Filter algorithm can be used to carry out B-physics measurements with the DØ detector.

An accurate measurement of B meson lifetimes are crucial for the measurement of $B - \bar{B}$ oscilations and other Standar Model parameters such us the the CKM parameter V_{cb}.

Chapter 8

Top Quark Identification Using Secondary Vertex b-tagging

In this Chapter we discuss the application of the secondary vertex b-tagger algorithm to the identification of top quark events in the electron plus jets channel.

As mentioned in Chapter 1, 30% of $t\bar{t}$ events decay in the lepton+jets channel, where one W decays leptonically, $\ell\nu_\ell$, and the other one hadronically into two quarks, giving rise to jets. The signature for this channel is thus a lepton, $\not\!\!E_T$ from the neutrino, and four jets, not necesarilly all reconstructed, but two of which originating from b quark fragmentation. The major background source for this channel is W+jets production, which gives rise to basically the same final state signature, with the important difference that in general no b quarks are present in this case.

Although several techniques have been devised to isolate the $t\bar{t}$ signal, like exploiting its particular kinematics in a topologically based analysis, the most successful methods rely on b-tagging, that is, identifying the presence of b-jets. There are three main b-tagging methods: the *soft lepton* [42, 43], which searches for a jet embedded low p_T lepton from B decay; the *impact parameter* [44, 45], exploiting that particles from B decay should have in general large impact parameters with

respect to the primary vertex; and the most sensitive one, the *secondary vertex*, which attempts to reconstruct the displaced B hadron decay vertex, as explained in Chapter 5. During Run I, DØ did not have precision vertex tracking, and could thus only implement this last method. This thesis has discussed in detail the development, implementation and optimization of the secondary vertex b-tagging for DØ, exploiting the newly installed microstrip silicon vertex detector. In this Chapter we present its preliminary application for top quark identification.

Since $t\bar{t}$ events have two b-quarks in their final state, while no b quarks are present in the majority of the W+jets background, the method consists in selecting e+jets events with at least one b-tagged jet, and subtracting the tagged background in the e+jets data sample. This Chapter is organized as follows: Section 8.1 describes the selection of the e+jets data sample. Section 8.2 details the sources of background tagged events and Section 8.3 compares the background estimation to the observed number of tagged events. The excess of tagged events over background is associated to $t\bar{t}$.

8.1 Selection of the e+jets Sample

The e+jets sample, which contains the $t\bar{t}$ signal, is pre-selected by requiring a high p_T electron, large $\not\!\!E_T$, and at least one jet with transverse momentum $p_T > 15\,GeV/c$. Primary vertices were reconstructed with the Tear-down Kalman Filter vertex finder described in Section 4.4 and selected using the minimum bias probability technique detailed in Section 4.5. The two main backgrounds are W multi-jet production and QCD events with a misidentified electron and mismeasured $\not\!\!E_T$.

A summary of the pre-selection cuts for the $e + jets$ sample is given in Table 8.1

Electrons were required to have $E_T > 20\,GeV/c$ and be associated with a track match in order to reduce the QCD background contaminating the electron sample. One example of this background is a jet fragmenting into a leading π^0, which decays

EM particle, $E_T > 20\,GeV/c$, $\|\eta\| < 1.1$
Electron track match
Second electron veto
$\not\!\!E_T > 20\,GeV$
$\Delta\phi(\not\!\!E_T, e) > 0.5$
At least 1 jet with $E_T > 15\,GeV/c$
Trigger "EM15_2JT15"

Table 8.1: Summary of the pre-selection cuts for the $e + jets$ sample.

with 98.8% branching ratio to a pair of collimated photons, thus producing basically the same the signature as an isolated electron. Figure 8.1 shows the E_T distribution for electrons from a data sample containing a single EM trigger and an electron with $E_T > 20\,GeV/c$ and simulated $t\bar{t}$ events in the single electron channel. Most of the data events in this sample consist of false electrons. Only electrons in the central calorimeter were considered for this analysis. This was motivated from the fact that all decay products in $t\bar{t}$ events tend to be more centrally produced than jets from QCD processes. In addition, it is more difficult experimentally to discriminate between true and false electrons in the forward region. Figure 8.2 shows the η distribution of electrons in the data and the simulation.

Events with two high p_T isolated electrons were rejected in order to reduce some of the Z+jets events in which the second electron falls into the detector acceptance. Since W+jets and Z+jets events have similar production mechanisms, there is a significant fraction of Z+jets events in the e+jets sample.

Since the electron from the W is produced with a neutrino, a cut of $\not\!\!E_T > 20\,GeV$ was applied in order to increase the purity for W events. The $\not\!\!E_T$ distribution for simulated $t\bar{t}$ and data is shown in Figure 8.3. The missing E_T significance was not used in this analysis, as it was not yet approved by the collaboration at the time of writing. Instead, topological cuts were required in order to eliminate events with

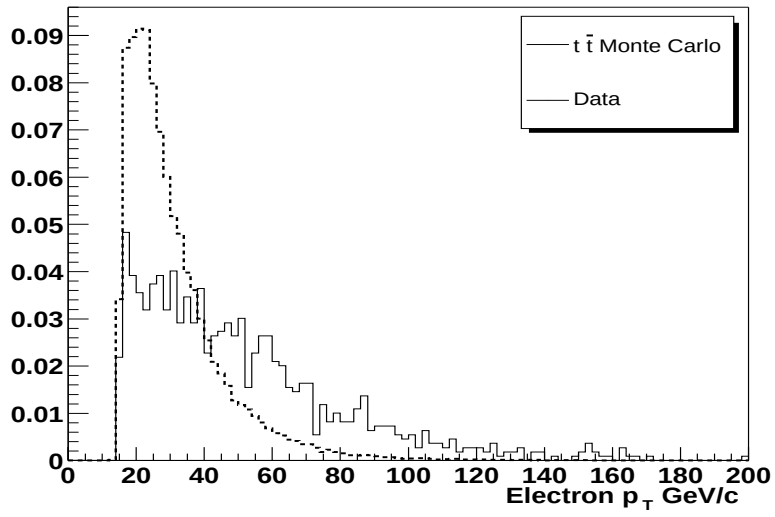

Figure 8.1: Electron p_T distribution for data (dashed) and simulated $t\bar{t}$ events (solid). Both histograms are normalized to unit area.

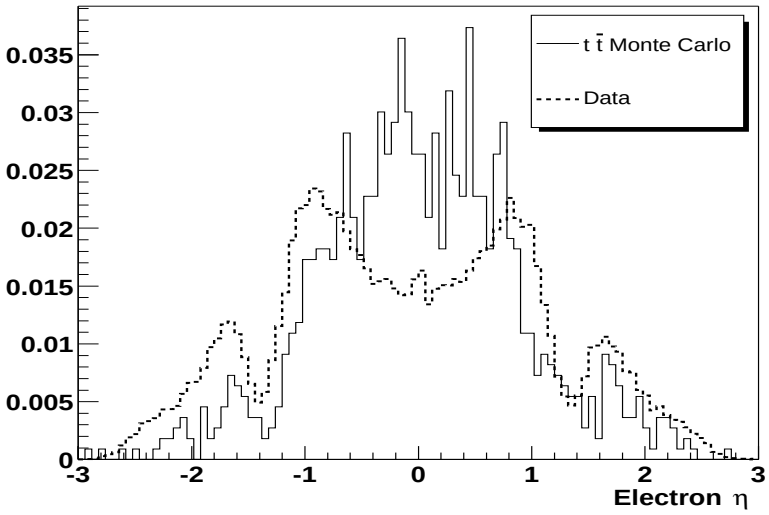

Figure 8.2: Electron η distribution for data (dashed) and simulated $t\bar{t}$ events (solid). Both histograms are normalized to unit area.

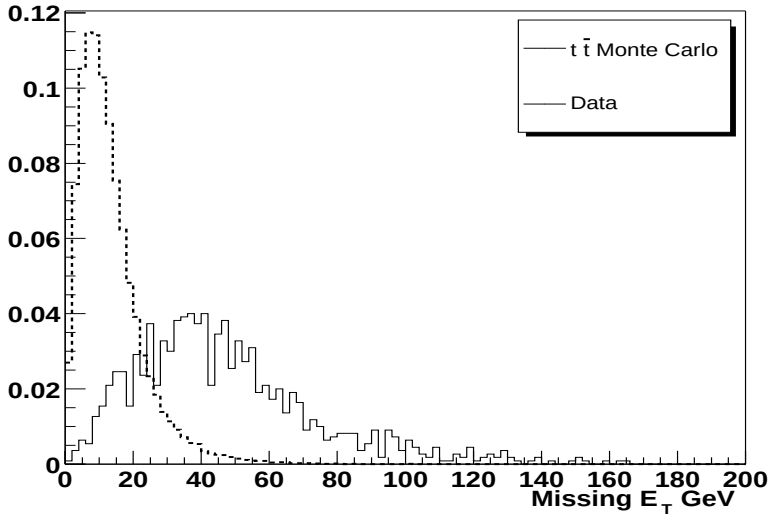

Figure 8.3: $\not\!\!E_T$ distribution for events containing an electron candidate in data (dashed) and simulated $t\bar{t}$ events (solid). Both histograms are normalized to unit area.

fake high transverse missing energy due to energy resolution fluctuations. The main contribution to fake $\not\!\!E_T$ originates due to the different resolution between hadronic and electromagnetic jets. In multi-jet data, the distribution of the ϕ angle between the $\not\!\!E_T$ and the electron, $\Delta\phi(\not\!\!E_T, e)$ peaks at 0 and 180 degrees, whereas for $t\bar{t}$ events it rises monotonically as shown in Figure 8.4. Thus, we require the minimum opening angle between the electron and the $\not\!\!E_T$ to be greater than 0.5.

The trigger requirement was specifically designed for the $e + jets$ channel and studied in detail in [29]. The *EM15_2JT15* trigger fires when the event consists of at least one electromagnetic trigger tower in excess of $15\,GeV$ and two additional hadronic trigger towers with energy above $15\,GeV$.

Secondary vertices were reconstructed using the b-tagging algorithm described in Section 5.2. A brief summary of the method is given below:

- Identification of the primary interaction vertex.

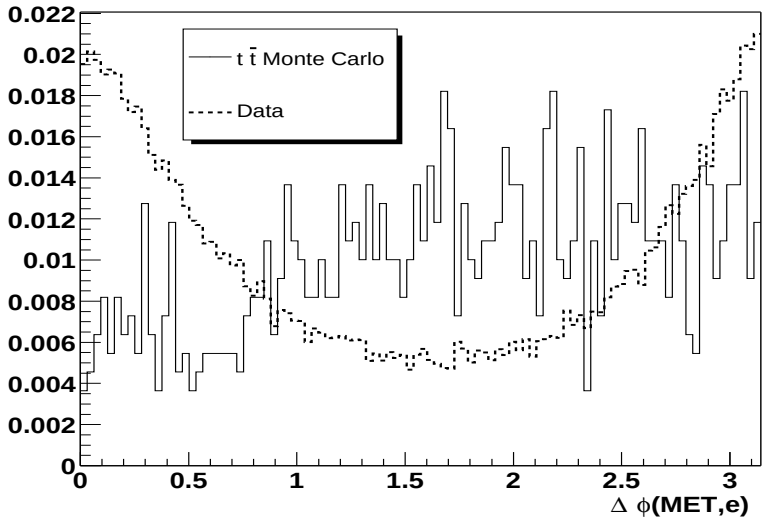

Figure 8.4: $\Delta\phi(\not\!\!E_T, e)$ distribution for data (dashed) and simulated $t\bar{t}$ events (solid). Both histograms are normalized to unit area.

- Reconstruction of secondary displaced vertices.
  - Find track-based jets using a 3-dimensional cone algorithm of size 0.5. Tracks are required to have at least 2 SMT hits, $p_T > 0.5\,GeV$, $|dca| <$ 0.15 cm and $|zdca|$ <0.4 cm.
  - Select tracks with large transverse impact parameter within track-jets and find all possible 2-track seed vertices with them.
  - Select vertices based on their decay length, collinearity angle and vertex χ^2. Reject identified *V0* vertices and associate secondary vertices with calorimeter jets if $\Delta R(vtx, jet) < 0.5$.
- A calorimeter jet is tagged as a b-jet if it has at least one secondary vertex with decay length significance $L_{xy} > 5$. The decay length significance of a jet is defined as the signed decay length divided by its error. This quantity is signed positive if the secondary vertex is displaced from the primary vertex in

the same direction as the jet momentum and negative otherwise.

Figure 8.5 shows the distribution of the secondary vertex decay length and significance in the selected e+jets sample. There is a 30% excess of positive tags, indicating the presence of heavy flavor in the sample.

8.2 Tagged Background in the e+jets Sample

In order to understand whether the tagged events we observed in the e+jets sample are from $t\bar{t}$ events, we need to calculate how many tags we would expect from background sources. There are several sources: mistag jets, heavy flavor production in W+jets events, Wc production, direct $b\bar{b}$ production, WW, WZ, and $Z \to \tau\tau$ events. The largest backgrounds are heavy flavor processes in association with W bosons ($Wb\bar{b}$, $Wc\bar{c}$) where the $b\bar{b}$ and $c\bar{c}$ pairs are produced from gluon spitting, and Wc production ($gs \to Wc$). Diboson production may produce tags through the decay $W \to c\bar{s}$ and $Z \to b\bar{b}$. Tags in $Z \to \tau\tau$ processes arise from tagging multi-prong hadronic decays of long-lived taus.

Table 8.2 summarizes the contribution of the main tagged background sources obtained from ALPGEN Monte Carlo simulations [47].

An accurate background estimate would require to calculate the fraction of tagged events in Monte Carlo simulated background events, to scale it with a data-Monte Carlo scale factor, and to normalize it to the number of observed W+jets events in bins of jet multiplicity. This approach could not be followed given the absence of large Monte Carlo background samples at the time this analysis was performed.

Instead of an explicit calculation of the Wbb, Wcc and Wc backgrounds from Monte Carlo, we use the positive tag rate parametrization $+L_{xy}$ obtained from $EMqcd$ sample (See Section 5.5.2) which accounts for all sources of heavy flavor

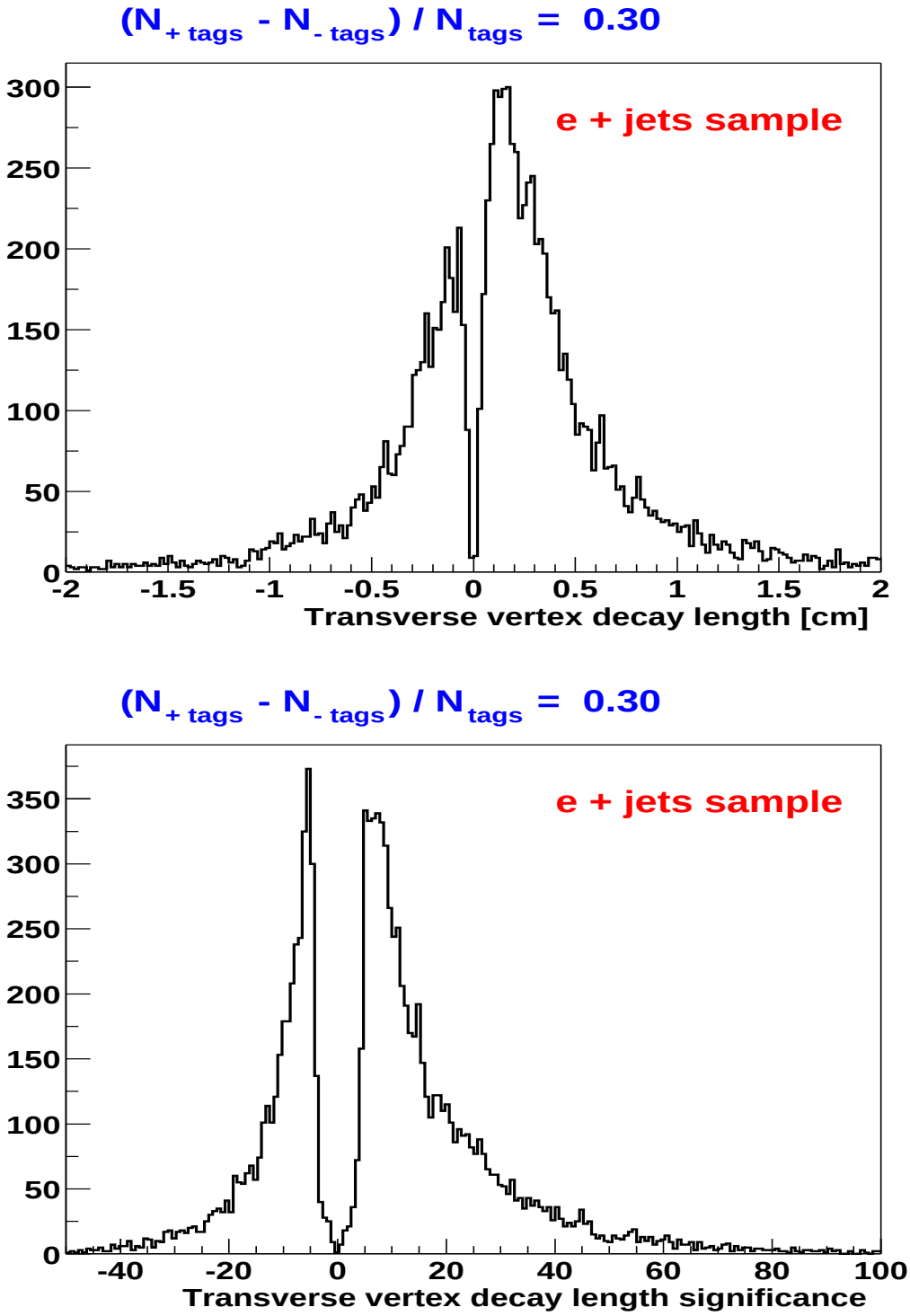

Figure 8.5: Transverse vertex decay length and significance in the e+jets sample.

Source	$W+1$ jet	$W+2$ jets	$W+3$ jets	$W+4$ jets
$Wb\bar{b}$		$(0.88 \pm 0.04)\%$	$(1.57 \pm 0.09)\%$	$(3.17\pm)\%$
$Wc\bar{c}$		$(1.25 \pm 0.13)\%$	$(2.33 \pm 0.26)\%$	$(3.34 \pm 0.88)\%$
$W(b\bar{b})$	$(0.50 \pm 0.11)\%$	$(1.70 \pm 0.48)\%$	$(1.40 \pm 0.44)\%$	$(0.92 \pm 0.83)\%$
$W(c\bar{c})$	$(1.21 \pm 0.16)\%$	$(2.16 \pm 0.55)\%$	$(5.52 \pm 0.88)\%$	$(9.28 \pm 2.66)\%$
Wc	$(2.96 \pm 0.07)\%$	$(6.51 \pm 0.69)\%$	$(3.84 \pm 0.83)\%$	$(3.86 \pm 1.69)\%$

Table 8.2: Summary of the fraction of different W+jets flavor processes as a function of exclusive jet multiplicity obtained from ALPGEN simulation. We distinguish cases in which the two heavy flavor jets are resolved ($Wb\bar{b}$) from the cases where both heavy flavor jets are reconstructed as a single jet ($W(b\bar{b})$) The remaining background corresponds to mistags.

production in multi-jet events in addition to mistags. This method is known to be an overestimation of heavy flavor in W+jets events [46] because

- heavy flavor production in W+jets events is through gluon splitting whereas in multi-jet events it can also proceed through direct and flavor excitation process.

- a higher fraction of gluon jets (in which heavy flavor is suppressed) is present in W+jets events than in multi-jet events.

This calculation of background cannot be used for a cross-section measurement, but it constitutes a simple method to observe a $t\bar{t}$ signal in the W+jets sample that can be used as a cross-check to a full MC background calculation [46].

The idea is to estimate the number of tagged background events as a function of inclusive jet multiplicity. If we call $f(\eta, ntrk)$ the positive jet tag probability parametrization, the probability to tag an event is given by

$$P(n \geq 1\, tags; N\, jets) = 1 - \prod_{i=1}^{N} (1 - f_i(\eta, ntrk)) \tag{8.1}$$

where "tagged event" means that it has at least one tagged jet. We then compare it with the observed number in each inclusive jet multiplicity bin. The presence of a $t\bar{t}$ signal should be observed as an excess of tagged events in the $N_{jets} \geq 3$ and $N_{jets} \geq 4$ bins.

8.3 Application to the Data

Figures 8.6 to 8.9 show the comparison of the kinematic distributions between observed and predicted tagged events, and the distribution of transverse vertex decay length of the tagged jets as a function of jet multiplicity. Figure 8.10 and Table 8.3 summarize the observed number of tagged events and the expected background for different jet multiplicities. We note that the observed number of tags exceeds the background expectation for e + 3jets and e + 4jets events, as we expect from a $t\bar{t}$ contribution. This is the first evidence of top production in Run II data, and the first application ever in DØ of the secondary vertex b-tagging technique. It is expected to become the major tool for top identification in the near future. The observed excesses can be transformed into a cross section measurement upon a more detailed background estimation based on Monte Carlo simulations [47], and the inclusion of the tagging efficiency and the luminosity.

Figure 8.11 shows one $t\bar{t}$ candidate event with one tagged jet (single tagged event) in which two secondary vertices were found. This vertex topology is consistent with a decay chain of $b \to B \to D$.

With this first evidence of $t\bar{t}$ production using the displaced vertex b-tagging method, this Thesis concludes. Its main purpose has been to develop the new tools and analysis schemes that are necessary to harness the enormous physics potential unleashed by the recent DØ upgrade effort, and the starting of the high luminosity Run II. The new state-of-the-art DØ tracking system, and in particular the silicon microstrip detector, has opened a myriad of possibilities not available during the

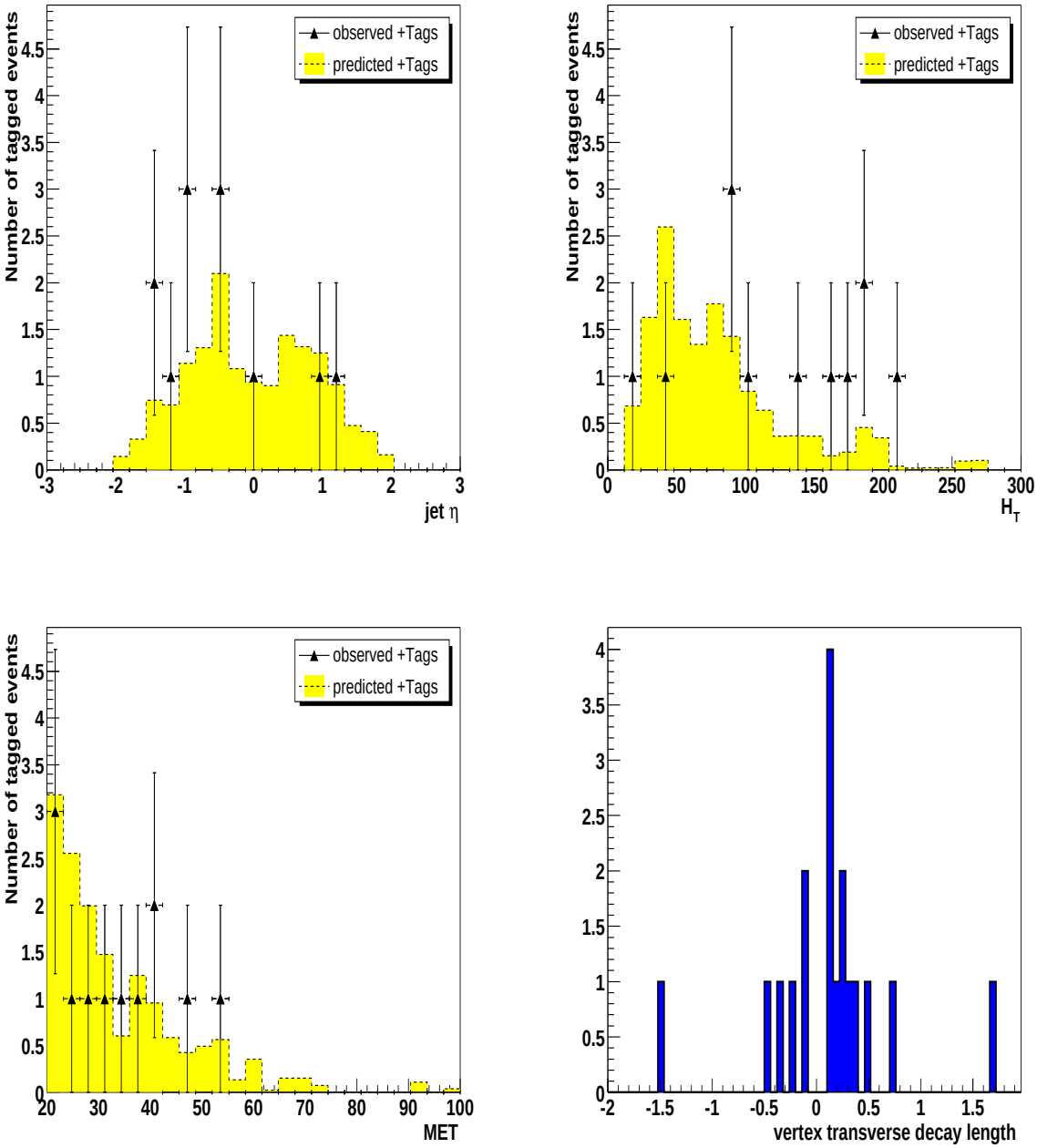

Figure 8.6: Kinematics of the tagged W plus ≥ 1 jet sample. Comparison between distribution of η, H_T and $\not\!\!E_T$ for predicted background and observed tagged events and decay length of distribution of the tagged jets.

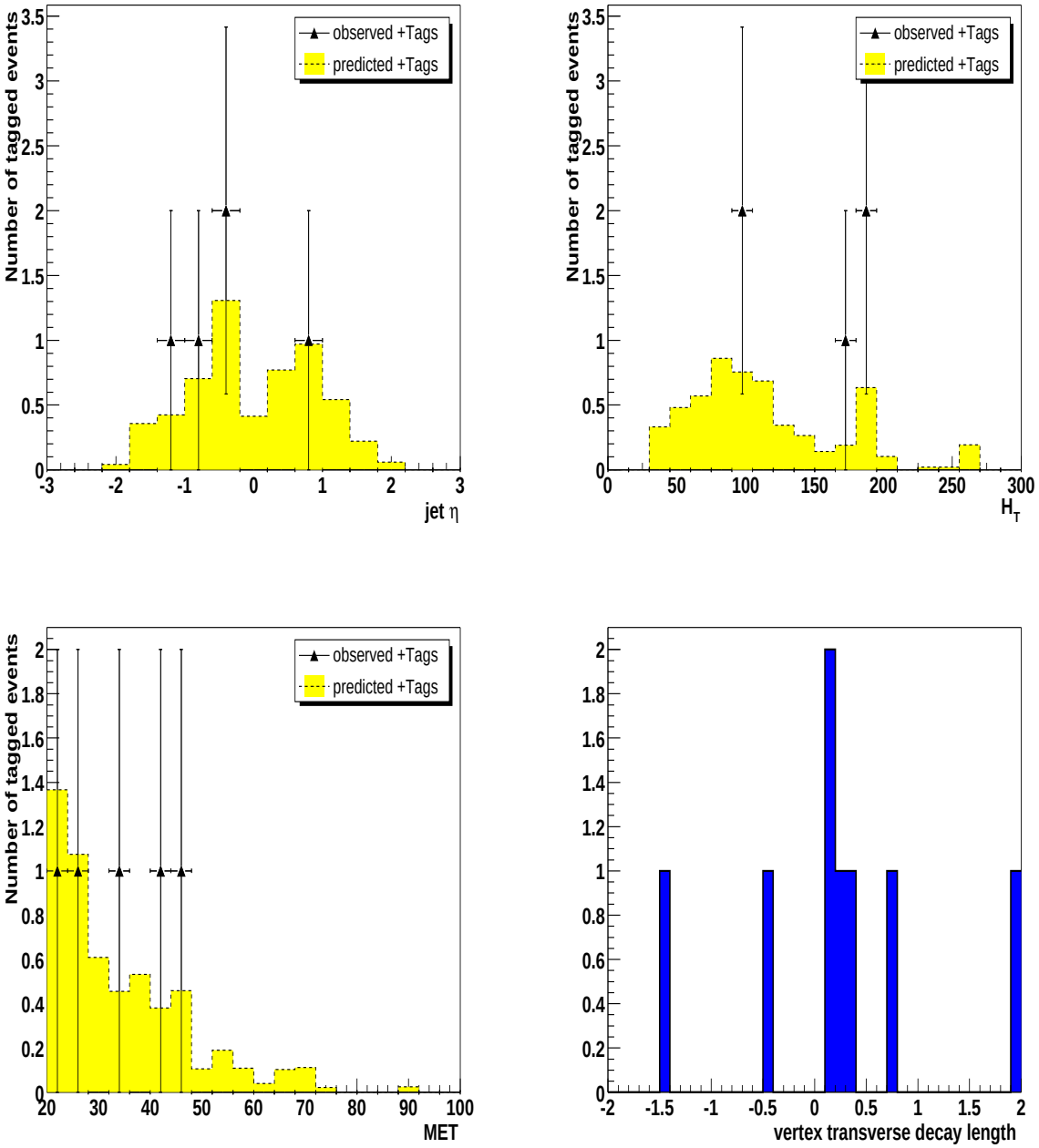

Figure 8.7: Kinematics of the tagged $W+ \geq$ 2jets sample. Comparison between distribution of η, H_T and $\not\!\!E_T$ for predicted background and observed tagged events and decay length of distribution of the tagged jets.

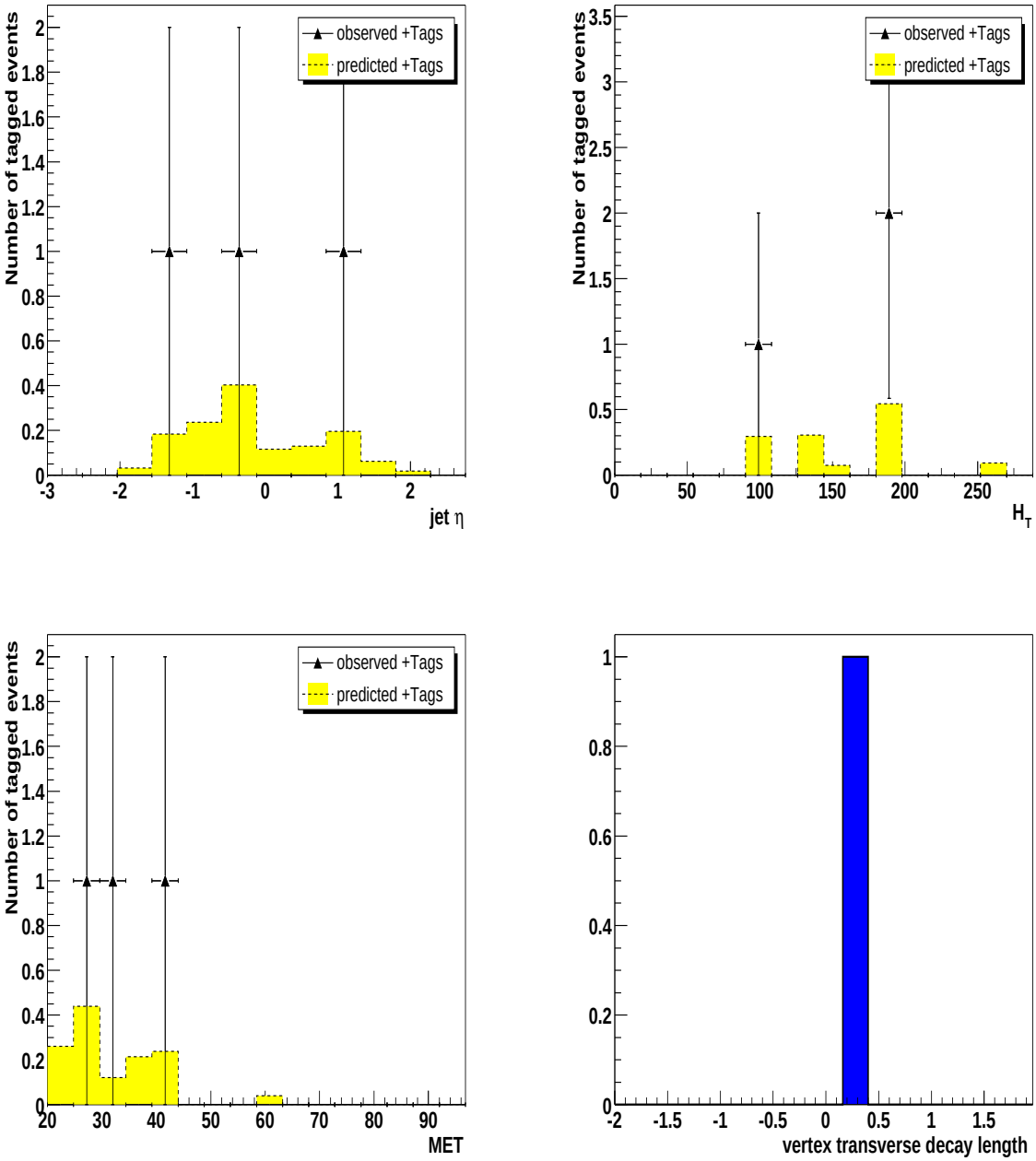

Figure 8.8: Kinematics of the tagged $W+ \geq$ 3jets sample. Comparison between distribution of η, H_T and $\not\!\!E_T$ for predicted background and observed tagged events and decay length of distribution of the tagged jets.

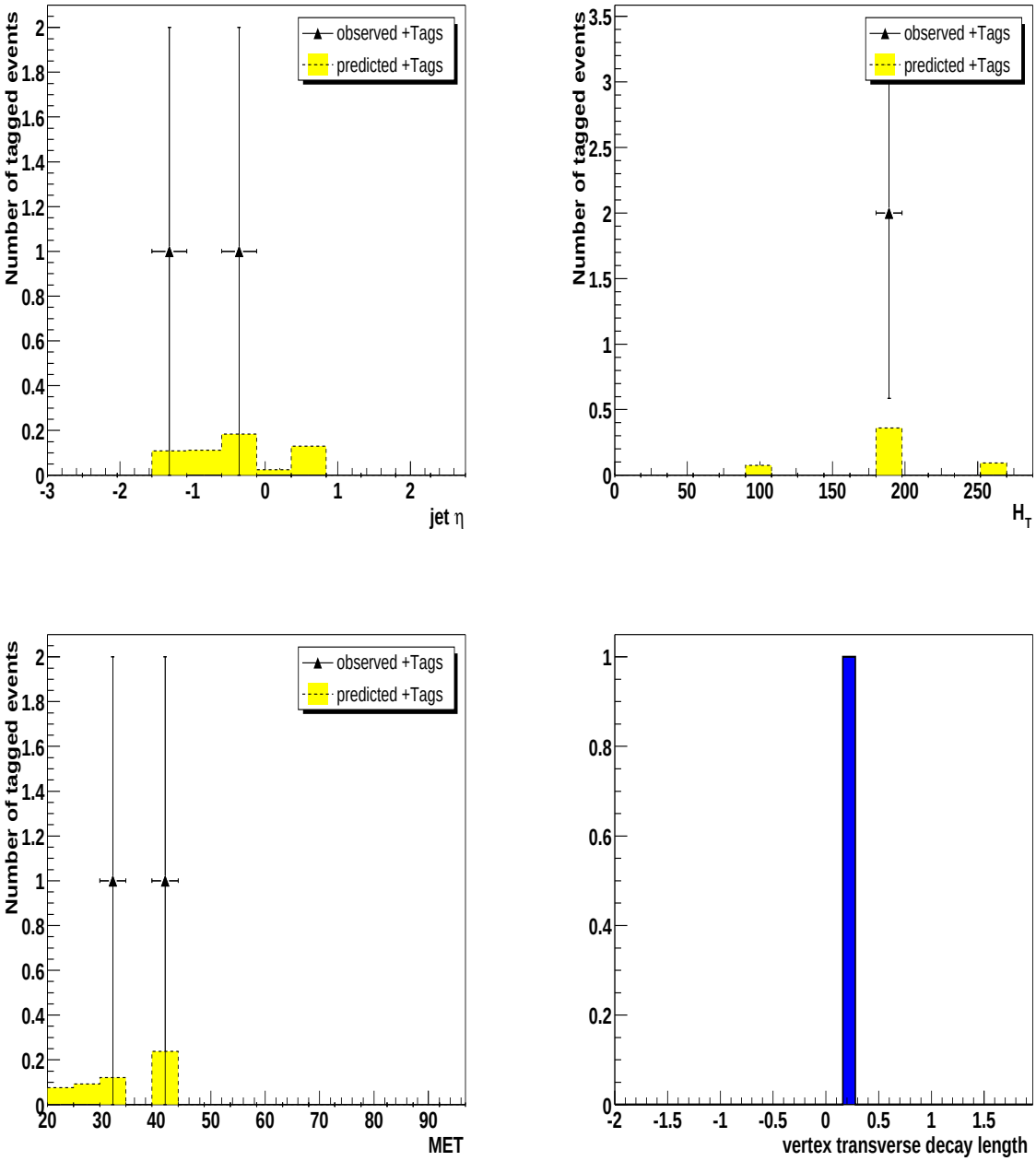

Figure 8.9: Kinematics of the tagged $W+ \geq$ 4jets sample. Comparison between distribution of η, H_T and $\not\!\!E_T$ for predicted background and observed tagged events and decay length of distribution of the tagged jets.

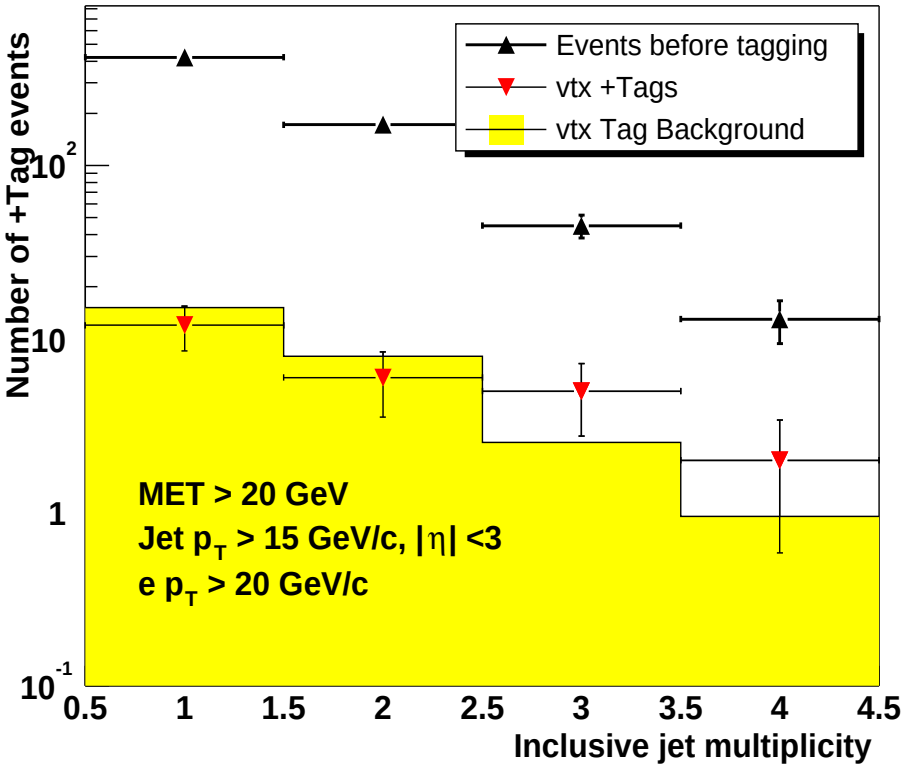

Figure 8.10: Observed number of tagged events (dots), and total predicted background (error band including the statistical uncertainty) in the e+jets sample.

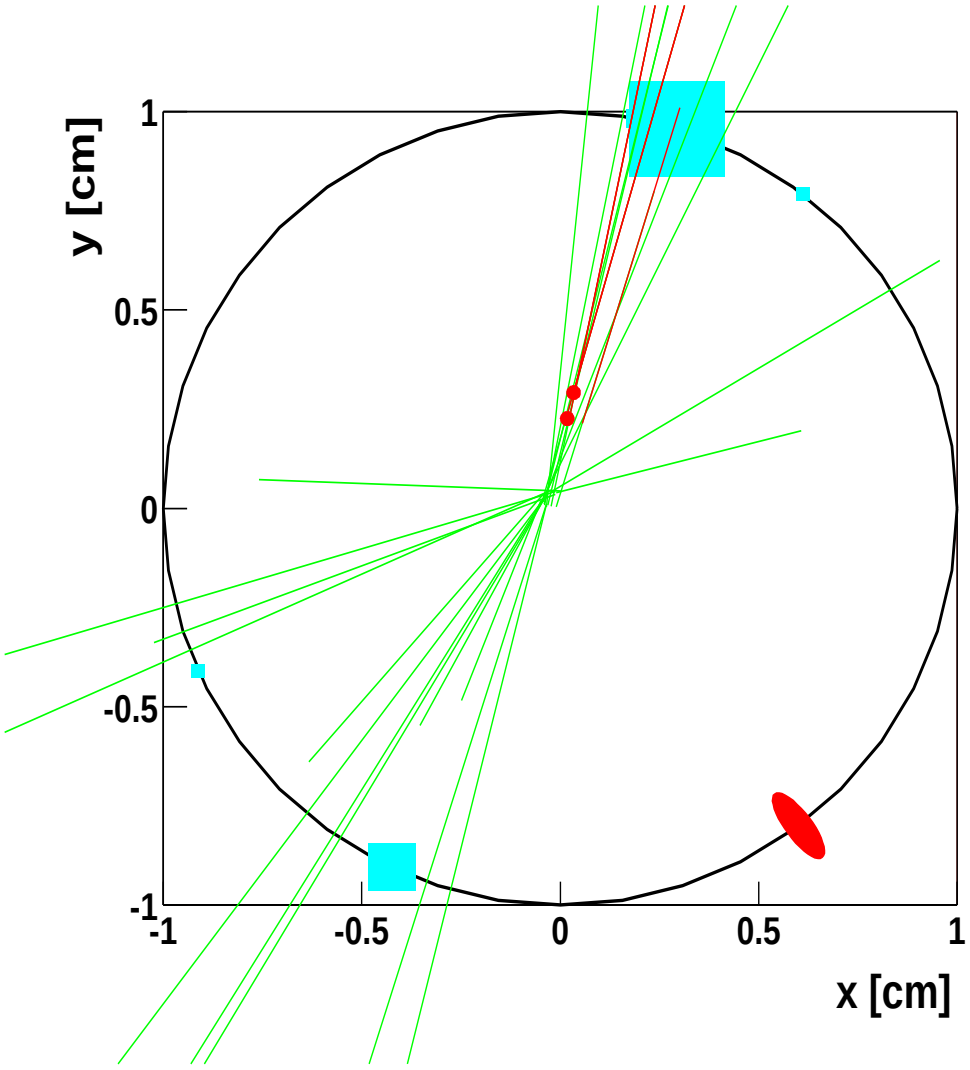

Figure 8.11: Event display of a single tagged event. Calorimeter jets are drawn as light grey boxes with its size proportional to p_T. Black lines correspond to all tracks within track-jets. Two secondary vertices are shown as dark circles and its attached tracks are plotted as dark lines. The dark ellipse corresponds to the electron.

Source	$W+ \geq 1$ jet	$W+ \geq 2$ jets	$W+ \geq 3$ jets	$W+ \geq 4$ jets
Background	15.2	5.7	1.3	0.5
Data	12	5	3	2

Table 8.3: Summary of the expected and observed number of tagged events in the W+jets sample as a function of jet multiplicity. The number of background events is expected to be an overestimate.

nevertheless fruitful Run I years. This Thesis has set the ground along two of these lines, the pursue of B physics through the full reconstruction of its secondary decay vertices, and the identification of top quark production via its most promising signature, the tagging of b-jets via displaced vertices. At the time of writing, Run II data taking is starting after a long shutdown period, allowing only for the preliminary physics results here presented. Within six months, however, extrapolation of the present instantaneous luminosity leads to expect a statistics comparable to the full Run I data taking, with an estimated sample of 30 $t\bar{t}$ events and 2000 fully reconstructed $B^{\pm} \to J/\psi K^{\pm}$ hadron decays, leading to exciting times in DØ for the years to come.

Bibliography

[1] Particle Data Group, K. Hagiwara *et al.* Phys. Rev. D 66, 010001 (2002).

[2] V. Barger and R. Phillips, *Collider Physics - Updated Edition*, Addison-Wesley Pub., 1997.

[3] R. Ellis, W. Stirling and B. Weber, *QCD and Collider Physics*, Cambridge University Press, 1996.

[4] V. Gribov and L. Lipatov, Sov. J. Nucl. Phys **15** (1972) 438; G. Altarelli and G. Parisi, Nucl. Phys. **B126** (1977) 298

[5] CTEQ, H.L. Lai *et al.*, Phys. Rev. D **51**, 1280 (1995).

[6] CTEQ, H.L. Lai *et al.*, Phys. Rev. D **55**, 1280 (1997).

[7] A.D. Martin *et al.*, Eur. Phys. J. **C4**, 463 (1998).

[8] S. Herb et al., Phys. Rev. Lett. **39**, 252, (1977)

[9] PYTHIA 6.3, hep-ph/0308153; T. Sjöstrand *et al.*, Computer Physics Commun. **135** (2001) 238

[10] HERWIG 5.9, hep-ph/9607393; G. Marchesini (Milano), B.R. Webber (Cambridge), G. Abbiendi (Padova), I.G. Knowles (Glasgow), M.H. Seymour (CERN), L. Stanco (Padova)

[11] ISAJET 7.69, hep-ph/0312045; F. Paige, S. Protopopescu, H. Baer and X. Tata

[12] "Run II Handbook", Fermilab beam division web page:
`http://www-bd.fnal.gov/runII/`

[13] The DØ Collaboration, "The DØ Upgrade: The Detector and its Physicsi", Fermilab-Pub-96/357-E.

[14] The DØ Collaboration, "The DØ Detector", Nucl. Instr. and Methods A **338** 185 (1994)

[15] J. Brzeezniak, et al., "Conceptual design of a 2-Tesla superconducting solenoid for the Fermilab DØ detector upgrade", Fermilab-tm-1986.

[16] M. Roco, "The Silicon Microstrip Tracker for the DØ Upgrade", DØ Internal Note ♯3553

[17] The DØ Collaboration. "DØ Silicon Tracker Technical Design Report", DØ Internal Note ♯2169

[18] The CFT upgrade web-page
`http://d0server1.fnal.gov/projects/SciFi/cft_home.html`

[19] K. Del Signore, et al., "The Central Preshower Detector: A Core Dump of Useful Information", DØ Internal Note ♯3647

[20] A. Gordeev, et al., "Technical Design Report of the Forward Preshower Detector for the DØ Upgrade", DØ Internal Note ♯3445

[21] S. Abachi *et al.* (DØ Collaboration), Nucl. Instr. Meth. Phys. in Res. A **338**, 185 (1994).

[22] The muon system upgrade web-page
`http://www-d0.fnal.gov/hardware/upgrade/muon_upgrade.html`

[23] A. Lo, et al., "Luminosity Monitor Technical Design Report",
DØ Internal Note ♯3320

[24] The DØ RunII trigger web-page
http://niuhep.physics.niu.edu/ blazey/upgrade.html

[25] http://www-d0.fnal.gov/computing/algorithms/#intro

[26] D. Adams, "Finding Tracks", DØ Internal Note ♯2958.

[27] G. Blazey, "Run II Jet Physics ", DØ Internal Note ♯3750.

[28] www-d0.fnal.gov/phys_id/emid/d0_private/certification/main_v1_9.html

[29] S. Anderson, et al., "Measurement of the $t\bar{t}$ cross section at $\sqrt{s} = 1.96TeV$",
DØ Internal Note ♯4116.

[30] O. Peters, "Muon Segment Reconstruction",
DØ Internal Note ♯3901.

[31] F. Deliot, "The Fit Algorithm in muo_trackreco"
http://d0-france.in2p3.fr/WORKING_GROUPS/MUONS/doc.ps

[32] M. Narain and F. Stichelbaut, "Vertex Reconstruction using the Impact Parameters Technique", DØ Internal Note ♯3560.

[33] A. Gelb (ed.), "Applied Optimal Estimation", MIT Press., Cambridge and London, 1971.

[34] R. Fruhwirth, "Application of Kalman Filtering to Track and Vertex Fitting", Nuclear Instruments and Methods in Physics Reasearch **A262** (1987), 444-450

[35] R. Luchsinger and C. Grab, "Vertex reconstruction by means of the method of Kalman filtering", Computer Physics Communications **76** (1993) 263-280

[36] http://hep.physics.indiana.edu/ chuluo/BsJpsiPhi/

[37] T. Muta, *Foundations of Quantum Chromodynamics*, World Scientific, 1998.

[38] www-d0.fnal.gov/phys_id/bid/d0_private/certification/certification.html

[39] O. Long, "A Proper Time Dependent Measurement of ΔM_D Using Jet Charge and Soft Lepton Flavor Tagging", PhD. Thesis, 1998

[40] B. Knuteson, M. Strovink, "The missing transverse energy resolution of an event", DØ Internal Note ♯3629.

[41] M. Bhattacharjee, et al., "JetEnergy Resolutions", DØ Internal Note ♯2887.

[42] F. Beaudette and J-F. Grivaz, "Electron identification and b-tagging with the road method", DØ Internal Note ♯4032.

[43] R. Van Kooten, "Muon tag overview, status, limitations, changes, p_{Trel} comparisons". DØ Internal talk on b-id workshop, December 2002.

[44] D. Bloch, et al., "Performance of the Jet Lifetime Probability method for b-tagging in DØ data", DØ Internal Note ♯4158.

[45] R. Demina, et al., "b-tagging with Counting Signed Impact Parameter method", DØ Internal Note ♯4049.

[46] G. Houk, "Identification of Top Quark Production Using Kinematic and B-Tagging Techniques in the Lepton+Jets Channels in $p\overline{p}$ Collisions at $\sqrt{s}$=1.8 TeV", PhD Thesis, 1996.

[47] R. Demina, et al., "Measurement of the $t\bar{t}$ cross section at $\sqrt{s} = 1.96\,TeV$ using lifetime tagging", DØ Internal Note ♯4141.